FUNCTIONAL ORGANIZATION OF THE HUMAN BRAIN:

HOW WE SEE, FEEL, AND DECIDE

A Dissertation

by

RICKY R SAVJANI

Submitted to the Office of Graduate and Professional Studies
of Texas A&M University
in partial fulfillment of the requirements for the degree of

DOCTOR OF PHILOSOPHY

Chair of Committee,	David M Eagleman
Co-Chair of Committee,	William Griffith
Committee Members,	Richard De La Garza
	Leif Peterson
	Stelios Smirnakis
Head of Program,	Warren Zimmer

May 2018

Major Subject: Medical Sciences

ABSTRACT

The human brain is responsible for constructing how we perceive, think, and act in the world around us. The organization of these functions is intricately distributed throughout the brain. Here, I discuss how functional magnetic resonance imaging (fMRI) was employed to understand three broad questions: how do we see, feel, and decide? First, high-resolution fMRI was used to measure the polar angle representation of saccadic eye movements in the superior colliculus. We found that eye movements along the superior-inferior visual field are mapped across the medial-lateral anatomy of a subcortical midbrain structure, the superior colliculus (SC). This result is consistent with the topography in monkey SC. Second, we measured the empathic responses of the brain as people watched a hand get painfully stabbed with a needle. We found that if the hand was labeled as belonging to the same religion as the observer, the empathic neural response was heightened, creating a strong ingroup bias that could not be readily manipulated. Third, we measured brain activity in individuals as they made free decisions (i.e., choosing randomly which of two buttons to press) and found the activity within fronto-thalamic networks to be significantly decreased compared to being instructed (forced) to press a particular button. I also summarize findings from several other projects ranging from addiction therapies to decoding visual imagination to how corporations are represented as people. Together, these approaches illustrate how functional neuroimaging can be used to understand the organization of the human brain.

DEDICATION

I would like to dedicate this work to my family without whom I would have only dreamed to study neuroscience.

ACKNOWLEDGEMENTS

First, I would like to thank my advisor Dr. David Eagleman for a million reasons. Here are just a few. In medical school, I knew immediately I wanted to study the human brain with MRI. I wanted to probe the brain to see how it functioned, how we can manipulate it, and what it could tell us about the world we live in and how we experience it. I came across Dr. Eagleman's website, which was a science candy-land, a place I knew I had to be. I immediately drove down to Houston to Baylor College of Medicine, and after a single meeting, Dr. Eagleman offered me the chance to work in his lab! Plagued with the inescapable imposter complex, I was worried that since I was not a Baylor student, such an opportunity would be impossible. However, Dr. Eagleman never treated me any differently, and believed in me from that very first day we met.

Reflecting back over the years, Dr. Eagleman has given me a singularly unique opportunity to work in so many disciplines in neuroscience: from deep brain recordings in DBS patients, to trying to decode my dreams while I slept in the scanner, to attempting to help Chicago city gangs cease violence. And those were just a sample of the projects that failed! Initially, I had much regret, as many of these projects did not crystallize. However, I realized how much I grew and learned from these "failures," that science thrives on experiments not working at first. I know now how much better equipped I am to attack these problems, and how much hungrier I am to solve them.

Personally, I would like to thank Dr. Eagleman for all of the sacrifices he made to help me succeed. Dr. Eagleman has garnered international recognition both for his science and his public speaking, books, and TV shows. As such, every day he is pulled in several directions with very interesting opportunities. I am ever grateful for the time he spent with me, because it was always at the expense of meeting with renowned scientists, venture capitalists, tech giants, billionaires, and movie stars alike. To forego those meetings to chat with a student shows how great of a mentor he is. I've also gotten to ride along on many experiences, including appearing in TV episodes, running a CT scan on a mummy, and dozens of other opportunities a traditional graduate student would never encounter.

Lastly, I would like to make an important statement. Academia, at times, can be harsh on public figures. Dr. Eagleman has not been immune to this onslaught. However, as a student who sat right next to his office for 5 years, I know how important an advocate to the public David is. Every single day students, professors, teachers, lawyers, doctors, and fans of all statuses come by the lab to say hello, to collaborate. That's how inspiring he is. That's how important it is to have such a good scientist represent us to the public. We should never forget that. I've learned so much about the art of science (how to present, how to engage an audience) just from merely being in Dr. Eagleman's presence. Working in Dr. Eagleman's lab was an opportunity to witness one of the few remaining Renaissance men. I've learned so much, and I sincerely thank Dr. Eagleman for everything he has given me. I'll never forget.

In a similar vein, I had the wonderful privilege to meet and work with Dr. David Ress. I'll never forget how we met. I had recently run out of funding for my project on real-time fMRI, and the scanners were no longer available for my use. Dr. Eagleman was graciously paying the $500/hour out-of-pocket, a situation that could not last. Dr. Ress caught wind of this, and sent me the following email at 10 pm on a Wednesday night:

Hi Ricky,
I heard rumors that your project was short of money to pay for scanning time. If this is still true, we might be able to work a trade. Please let me know if you are interested.
Cheers,
DR

I had no idea if Dr. Ress wanted me to mop the scanner floors at night, or if he wanted one of my kidneys… the possibilities were left to my wildest imaginations. However, he introduced me to one of the most beautiful structures in all of the brain, the magical butterfly revealed, the superior colliculus. I had such a great time working with him and discovering the map of how eye movements are represented in the human brain. My favorite was having dinner/coffee with Dr. Ress to hear the wonderful adventures he had climbing, cycling, and skiing the world. Dr. Ress also introduced me to MR physics, a field I want to pursue more and more in clinical years in radiology.

I would also like to thank my committee members. Dr. Griffith for having to Skype in on meetings, Dr. Peterson for his wonderful lessons in statistics, Dr. Smirnakis for his clinical background and philosophies of science, and Dr. De La Garza for numerous insights on addiction and life. I've been fortunate to have such a wonderful and supporting committee. I would also like to thank Dr. Ramiro Salas, who I have written several structural imaging papers together with. Most notably, I will never forget his advice on persistence, the way turtles lay their eggs!

There are two other faculty members I must acknowledge: Dr. Lisa Wilde and Dr. Brian Taylor. Dr. Wilde has shown nothing but love and support, offering me data, projects, and funding! Dr. Taylor has also introduced me to clinical MR physics, and I look forward to learning more from him over the next few years.

Last but not least, I would like to thank my friends, classmates, and family who supported me endlessly. I want to thank my basketball colleagues: Sri, Bo, Sam, Lance, Daniel, Ken, and the dozens of others who have blessed me with the opportunity to play with, allowing me to forget all of my troubles on the court. I would like to thank my brother Neal for his support and advice on a career path I am likely to start next. I deeply thank Hansa and Rohit (my parents) for providing me with everything from food to extra money to the love needed to complete a PhD. And I would be remised to leave out Simon, someone who I have talked to nearly every single day since college, my eternal best friend.

But there's one person who brings me to tears to think about all that she has done for me. Someone with the heart of an angel, the strength of a lion… someone I leaned on every step of the way. Every discovery, no matter how big or small, I ran first to tell her. Someone who knows me so well, knows everything I did and everything that I am. In a strange and beautiful end, she embodies all that is my thesis, and she taught me how to apply my work to real life: explore this beautiful world (see), love thy neighbor (feel), and live free (decide). To my wonderful fiancée Angie: I love you.

NOMENCLATURE

SC	Superior Colliculus
MRI	Magnetic Resonance Imaging
BOLD	Blood Oxygen Level Dependent

TABLE OF CONTENTS

Page

LIST OF FIGURES

Page

LIST OF TABLES

Page

CHAPTER I

INTRODUCTION

I had the great pleasure of conducting my PhD at the Baylor College of Medicine under the guidance of Dr. David Eagleman and Dr. David Ress. Over the last 5 years, I worked on a variety of projects with mentors across many disciplines throughout the Texas Medical Center, Houston, and beyond. In many ways, my PhD differed than the traditional route many students pursue in which they dive deeply into a single question to answer about the brain, in the case of neuroscience. I certainly had that experience, as well, but it was not limited to one question, but rather several about the functional organization of the human brain. As such, I have organized my thesis into three main questions: How we see, How we feel, and How we decide.

In the first chapter, I explore how we see. Together with Dr. David Ress, we studied how a deep midbrain structure, the superior colliculus (SC), controls saccadic eye movements. As your attention and gaze jumps from one target to the next (e.g., looking from the computer monitor to the clock on your wall), the SC is the structure driving these commands. The SC receives direct retinal input onto its superficial layers. The intermediate layer uses the overlying visual input to drive eye movements. And the deep layer integrates activity from multiple modalities (e.g., vision, audition, somatosensation). Together, the SC is a layered midbrain structure responsible for processing visual attention and conducting saccadic eye movements. The SC was well

studied in the 1970s by monkey electrophysiologists. They found that activity within the SC increases prior to execution of saccades (Mohler and Wurtz, 1976) and stimulating particular portion of the SC elicited eye movements of particular eccentricity and polar angle (Robinson, 1972). However, since that 1970s, little work has been done to understand the functional organization of ***human*** SC. Lesion studies have inferred the function of SC (and continue to provide valuable information Sereno et al., 2006; Biotti et al., 2016), and whole-brain imaging infers general functions performed by the SC (e.g., work from the Himmelbach lab (Himmelbach et al., 2007; Linzenbold et al., 2011; Linzenbold and Himmelbach, 2012; Himmelbach et al., 2013)). However, these techniques cannot delineate the intricate functions of the very tiny SC, especially laminar profiles as the human SC is only ~4 mm in depth. Dr. David Ress's lab has developed advanced MR imaging approaches that enable high resolution studies of subcortical structures in humans. These advances include spiral trajectories, high-resolution 1.2 mm voxels, multi-shot dual echoes, and optimizing T_e for subcortex (~40 ms). Nonetheless, getting high SNR images from functional activity within the SC is challenging. We spent > 1 year optimizing stimulus paradigms to elicit enough activity within the SC to be able to measure it. This meant, participants had to make on the order of 1000s of eye movements to get enough SNR to do functional mapping. We also had to avoid antisaccades and visual contamination to isolate activity evoked from eye movements of interest. Ultimately, we were able to find that eye movements along the superior-inferior visual axis are mapped across the medial-lateral anatomy of the SC. Further, the eye movement maps are in register with retinotopic topography and lie 1-2 mm deeper.

These studies conferred the organization of human SC is similar to that of monkey SC discovered in the 1970s. The approaches further enable studies in the awake, behaving human, which could unveil further functions of the SC with experimentation not possible or very challenging in the monkey. I enjoyed working with Dr. Ress very much and very interested in learning more MR physics as my trajectory in radiology continues. As I continue as a medical student, we would like to start a new study using a 3D display to conduct dichoptic experiments to see if we can measure ocular dominance columns in human SC.

In the second chapter, I describe how we feel. The brain has a particular set of networks that increases activity when a person feels pain (e.g., a shock or a stab). Interestingly, work over the last two decades has revealed that portions of these same brain regions increase activity when observing others in pain, as if the brain runs an emulation of other person's pain.(Botvinick et al., 2005; Hein and Singer, 2008; Jacoby et al., 2015; Singer et al., 2004; Valeriani et al., 2008). This empathic response, however, is modulated by beliefs about the victim. If the victim is of the same race membership.(Azevedo et al., 2013; Contreras-Huerta et al., 2013; Xu et al., 2009) or cheers for the same sports team(Cikara et al., 2011; Hein et al., 2010), people have heightened empathic responses for the victim. We were interested if this ingroup bias holds true for members of the same religious affiliation. Religion serves as a powerful divisive force across the globe. We scanned a large set of participants ($n > 135$) to observe this effect robustly. Generally, we found the ingroup bias holds true, that the empathy network shows

heightened brain activity for ingroup members compared to members of a different religion. Importantly, we did pit religions against each other in the analysis, as this would open many areas of contention that would not result in productive science about how the brain functions. Rather, we observed that regardless of a particular religious affiliation, people were more empathic towards members of the same religion. We were also interested to see if this bias could be altered or randomly generated. We constructed two different paradigms to address these questions. First, we assigned random outgroup religions to be "allies" with each participant's own religions. Together, the allies were declared to be at war with another three religions. Under this narrative, we did not find significantly heightened activity for allies; that is, allies were still considered as outgroup. Second, instead of using religions, we assigned participants randomly to belong to one of two groups: Augustinian or Justinian. Participants were given bracelets to identify themselves with the selected ingroup. However, we observed absolutely no ingroup bias under this circumstance. This result is in contrast to a recent finding that had participants assigned to random groups but told participants that group assignment was based on what type of problem solver they were (conclusive or sequential problem-solvers) (Ruckmann et al., 2015). Our studies reveal that the ingroup religious bias is more deeply rooted and cannot be so whimsically altered. This has important applications in the geopolitical scene that defines so much of how the world is constructed.

Lastly, in the third chapter, I discuss how we decide. The topic of free will has engaged neuroscientists, philosophers, and physicists for a long time. In the early 1980s, an experiment by Benjamin Libet showed activity rises in certain brain areas before an arbitrary decision (e.g., when to press a button) is made and before the participant is consciously aware that the decision has been made (Libet, 1985). John Dylan Haynes's Lab expanded this work to decode the decision-making using fMRI and two alternative choices. His group found that brain activity could be decoded well in advance (~10 s) of the conscious awareness of the decision (Soon et al., 2008; Kahnt et al., 2011; Bode et al., 2011, 2012, 2013, 2014). This study elicited several controversies documented in the literature. The experimental and statistical approaches employed leave open several questions regarding the interpretation of this brain activity: (a) Is a free will task really memory-less with respect to previous decisions?[5–7] (b) Is the underlying brain activity truly below conscious awareness?[8,9] and (c) Are the parametric assumptions of group MVPA searchlight analyses on linear decoding maps valid?[10] We attempted to address these questions in two approaches. First, we examined the neural differences between free decision-making and forced-decision making. We scanned participants for 15 minutes while they freely chose which of two buttons to press at random times of their choosing. Then, we had the participants press buttons at precise times. Unbeknownst to them, the timing and decision was exactly the same sequence they selected in the first 15 minutes. We found networks for fronto-thalamic brain activity to be increased when participants were making forced decisions compared to free decisions. The heightened activity could represent increased attentional resources allocated when awaiting

instruction, reflecting a relaxation of activity to allow for free decisions to be selected. Second, we are completing analyses to verify if the activity John Dylan Haynes's group discovered was in fact due to free decision-making. We constructed three different experimental paradigms: 1) an identical task as in Soon et al. 2008, 2) a forced decision making paradigm, and 3) a paradigm without a dual component task. We analyzed our data identically as Soon et al. 2008, and we found partial replication of the results, as well as decoding up to 10 s before decision awareness in novel areas like the caudate nucleus. Further, we ran null distributions to verify the parametric approach and found similar results. We attacked one more question on whether the decoding was due to non-randomness by decoding whether participants switched or stayed from the button previously pressed. We found positive predictive accuracies in brain regions aside from those involved in decoding the button press. In addition, we did not observe positive decoding accuracy in our forced control experiment, as expected. We also observed only weak decoding on the data acquired in the single task regime, indicating that some of the results may be due to the dual task nature in John Dylan Haynes's original work. This latter study is ongoing work we are still finalizing. Together, we are rigorously testing if decisions can truly be decoded from brain activity.

These three chapters form the thrust of my thesis and my oral presentation. However, I worked on several other projects during my time as a graduate student. I wanted to document them here, as well, for two reasons. First, many of the projects were unsuccessful, as a graduate student often faces. This document serves as a guide to my

future self (and other interested readers) to know and understand what I tried and what did not work. Second, the various side projects reflect the important connections I made with people throughout the medical center during my time here. Without these mentors, I would not have been equipped with the many tools I hold now. The topics are diverse ranging from cognitive functions in subthalamic nucleus in Parkinson's patient to decoding dreams to several studies on substance addiction. The depth of these topics also spans a broad range from published papers to ongoing ideas. Capturing them here serves as an important reflection for next steps.

Please enjoy the following chapters in any order. I hope that there is something to be gained for everyone reading across many disciplines in neuroscience.

CHAPTER II

HOW WE SEE

2.1 Introduction

Saccadic eye movements are controlled by a midbrain structure called the superior colliculus (SC). Electrical stimulation (Robinson, 1972) and neuronal recordings (Mohler and Wurtz, 1976) in the intermediate layers of monkey SC, have shown a retinotopically organized saccadic eye-movement map. Specifically, saccades along the superior-inferior visual field are mapped along the medial-lateral axis of the SC in monkeys.

In humans, studies to infer function of the SC have been largely limited to lesion studies and whole-brain imaging. Lesions have inferred the function of SC (and continue to provide valuable information Sereno et al., 2006; Biotti et al., 2016). However, it is rare to find human patients with focal lesions to the SC without comorbid complications. Further, the aspects of saccadic eye movements can recover even after direct lesions to monkey SC (Hanes et al., 2005). Whole-brain imaging infers general functions performed by the SC (e.g., work from the Himmelbach lab (Himmelbach et al., 2007; Linzenbold et al., 2011; Linzenbold and Himmelbach, 2012; Himmelbach et al., 2013)). However, these techniques cannot delineate the intricate functions of the small, especially laminar organization as the human SC is only ~4 mm in depth.

Previously, our lab has used high-resolution functional MRI to elucidate how visual attention is mapped on the superficial SC (Katyal et al., 2012, 2010; Katyal and Ress, 2014). Here, we expand those methods to image the intermediate layers of human SC to map the polar angle representation of eye movements.

2.2 Materials and Methods

2.2.1 Participants

We recruited five participants (4 males) to undergo several ~2 hour long scanning sessions. One to two imaging sessions were acquired for each participant as they made leftward and rightward eye movements separately, invoking primarily the contralateral SC. Each eye movement session consisted of 12-16 278.4-s runs. One to two scanning sessions were also acquired from each participant for visual stimulation retinotopic mapping. Visual stimulation experiments evoked activity from both SC in one session. Retinotopy sessions consisted of 14-16 228-s runs. Participants gave informed consent prior to scanning based on our approved protocol from the Baylor College of Medicine Institutional Review Board. Participants were also trained on the tasks prior to scanning, and an eye tracker was used to ensure eye movements and task performance was reliable.

2.2.2 Stimuli

Stimuli were generated using MATLAB R2015a (Mathworks, Natick, MA) and PyschToolbox-3 (Brainard, 1997) on a Windows 7 Dell PC. Stimuli were presented on a

32” LCD BOLD Screen (Cambridge Research Systems, Kent, UK) at the back of the scanner bore 1.3 m away from the participants’ eyes. The display was gamma corrected using an i1 Pro 2 spectrophotometer (X-Rite, Grand Rapids, MI).

Previous human studies of saccadic mapping in cortex have attempted to use phase encoding approaches (Connolly et al., 2015; Konen and Kastner, 2008; Schluppeck et al., 2005; Sereno et al., 2001); however, these designs had two critical limitations for imaging subcortical activity: 1) a very low duty cycle (1 saccade every 5 s) and 2) reverse saccades made immediately after forward saccades. The low duty cycle forces participants to fixate for the majority of time instead of making saccades, which dampens the measurable activity (**Figure 2.1A**). And performing anti-saccades may involve the release of inhibitory control exerted by frontal regions like the dorsal lateral prefrontal cortex (DLPFC) onto the colliculus (Condy et al., 2004), which could significantly alter topographic maps of the prosaccades (**Figure 2.1**).

To overcome these limitations, we designed a paradigm in which participants could perform many saccades in one direction while minimizing saccades in the opposing direction. Participants made saccades either to the left or to the right (activating primarily the contralateral SC) while we cyclically varied the vertical component of the saccade to correspond to the lower, horizontal, and upper visual field (**Figure 2.2**). Participants performed three 6° saccades guided by a green dot target in a static grid of 12 red dots. The static red dots were arranged with 4 dots separated by 6° along each of

the three principle axes (horizontal, 45° diagonal, and -45° diagonal). The use of a static grid reduces differential contrast effects from retinal slip; the use of green-red color contrast minimizes the effects of bottom-up contrast in target discrimination. Further, human SC has recently been shown to adapt to red-green contrast (Chang et al., 2016), so our static red-green grid reduces the evoked visual stimulation during saccadic eye movement measurements.

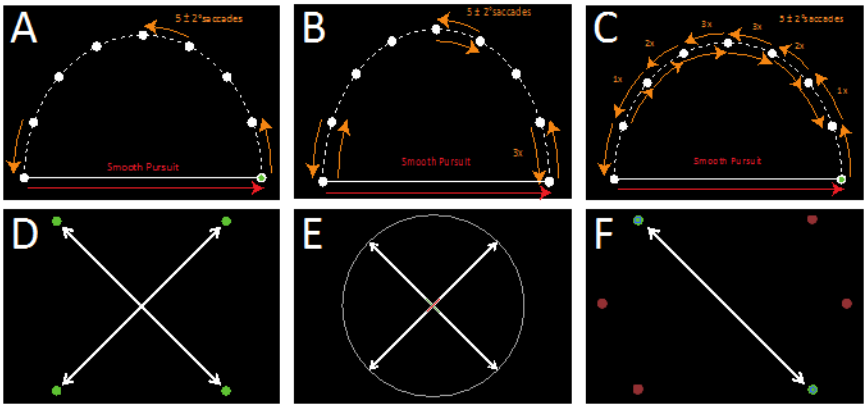

Figure 2.1 Evolution of Experimental Design

Related to Figure 2.2. Evolution of stimulus paradigms to evoke eye movement polar angle topography in human SC. A. Our first attempts to map the polar angle using a hemi-ellipse did not evoke significant activity, perhaps due to the amount of fixation time and non-blocked design. Attempts to increase the number of saccades by having participants jump back and forth from previous to next target 7 times (B) or a centrally weighted number of times (C) also did not yield significant activity in SC, likely due to the conductance of pro- and anti-saccades occurring right after each other. We next tried to use memory-guided saccades to elicit SC activity. In one attempt, we briefly flashed a pair of peripheral green dots (D) for 0.2 ms and participants rapidly performed saccades between the two remembered dots for 12 s followed by saccades in the orthogonal direction. Results were still weak, but slightly improved by using foveal cues: green and red lines flashed briefly at the center of the screen to cue the direction of the memory-guided saccades (E). Lastly, we used a static set of red dots with a pair turned green to cue the direction of the saccades. This reduced retinal slip and increase activity significantly, and ultimately led to the design used in our main finding.

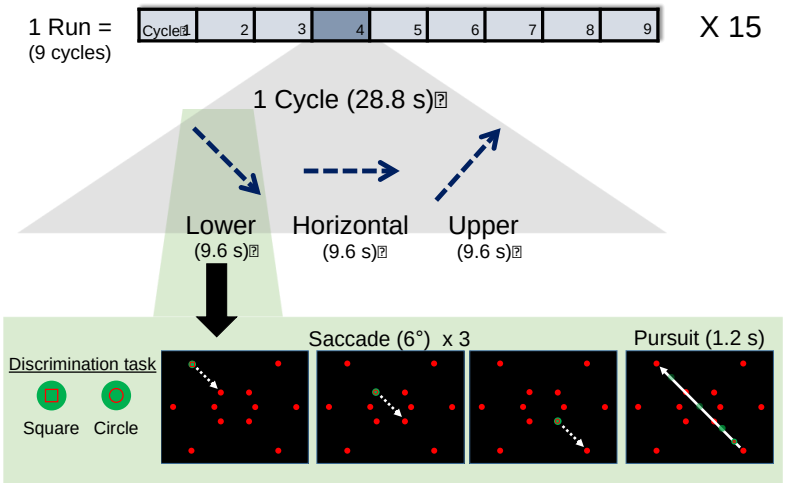

Figure 2.2 Experimental Setup

Participants performed visually-guided saccades to measure the polar angle representation of eye movements in the superior colliculus. Brain activity from primarily one SC in a session was measured by having participants perform saccades in one direction along the horizontal (right shown here). Each session consisted of 15 ~4.5 min runs, each of which consists of 9 cycles. In each 28.8 s cycle, the vertical component was varied along three principle axes: lower, horizontal, and upper visual fields. The stimulus screen showed a static grid of 12 red dots with one target dot turned green to indicate the saccade target. Participants made three 6° saccades along a principle axis, after which a 1.2 s visually-guided smooth pursuit was made back to the origin along that axis. Upon fixation onto target dots and during the smooth pursuit, participants performed an object discrimination task (square or circle) to keep attention engaged and improve reliability of eye movements.

One of the 12 red dots turned green to indicate the target to saccade to. Once the saccade was made, participants had to perform an object discrimination task (circle or square). This allowed attention to be engaged and saccades to be made more reliably. Participants responded via button press, which triggered the green do to move to the next target along the principle axis. After three saccades, the participants then performed a smooth pursuit (1.2 s) back to the first dot. Saccades and the pursuit were continued along the same axis for 9.6 s, and then participants performed another smooth pursuit to the start of the next

axis. During each smooth pursuit, the discrimination task had to be performed 0-2 times (truncated Poisson, $\lambda = 1$) at random times during the 1.2 s smooth pursuit, allowing attention to remain engaged and forcing eye movements to be restrained to the pursuit path. Participants performed 9 cycles in a single run (~4.5 min) and ~15 runs per session. Leftward and rightward saccades were run on separate sessions to measure the contralateral response of each SC independently.

Retinotopic maps were also acquired for all 5 participants using our previous visual stimulation paradigm (Katyal et al., 2010). Briefly, participants fixated at center while a wedge of moving dots rotated around the entire polar angle. As such, the entire polar angle retinotopy for both SC was measured in a single session. The rotating wedge consisted of 6 virtual sectors, and in one sector, the set of dots were moving either faster or slower. Participants performed the speed discrimination task with a staircase to keep attention engaged.

2.2.3 MRI Methods

Imaging was conducted on a Siemens (Erlangen, Germany) 3T Magnetom Trio scanner at the Core for Advanced Magnetic Resonance Imaging (CAMRI) at the Baylor College of Medicine. Eight 1.2-mm-thick quasi-axial slices (170-mm field of view) covered the entire SC with the prescription oriented roughly perpendicular to the local neuraxis. Functional data were acquired using a 3-shot spiral (Glover, 1999; Glover and Lai, 1998) dual-echo (both outward) sequence. We used a $T_R = 0.8$ s for each shot, yielding a 2.4 s

volume acquisition time for our 3-shots. T_E was set to 25 ms for the first echo and 40 ms for the second echo. The dual echoes were combined using a signal-weighted average, which yielded an increase in SNR of ~30% compared to the single echo.

A set of T_1-weighted structural images was obtained on the same prescription at the end of the session using a three-dimensional (3D) magnetization-prepared rapid gradient-echo (MPRAGE) sequence (0.7 mm isotropic voxels). These images were used to align the functional data to the segmented structural reference volume.

2.2.4 Image Data Analysis

Preprocessing- Image analysis was conducted using the mrVista software package (http://web.stanford.edu/group/vista/cgi-bin/wiki/index.php/MrVista) and custom modifications built on top of mrVista in our lab. The first 12 s of each retinotopy run were discarded to remove transient effects. Similarly, the first 19.2 s of each eye movement run were discarded to remove transients and to allow participants to engage in a regime of reliable eye movements. The following preprocessing was conducted on each of the two echoes for all runs (visual stimulation and eye movement), analogous to our previous pipeline (Katyal et al., 2010): slice-timing correction (zeroed at the middle slice), within-scan motion compensation (Nestares and Heeger, 2000), intensity-based between-scan alignment to the last scan in a session, and then averaging the multiple runs together to increase SNR. The two processed echoes were then combined using a signal-weighted average.

Surface Analysis- We segmented the brainstem (including portions of the thalamus) using a combination of automatic (e.g., active contour evolution) and manual approaches in ITK-SNAP (Yushkevich et al., 2006). A surface model was then built at the tissue-cerebrospinal fluid interface using a deformable surface algorithm (Xu et al., 2006). Functional data were then spatially aligned and resampled to the high-resolution T1 volume, averaged across runs, and visualized on the surface. A distance map was also computed from SC tissue voxels to the vertices of the surface to give a measure of the depth (s) of the tissue voxels.

Phase Mapping- A sinusoid at the stimulus repetition frequency (24 s for visual stimulation data, 28.8 s for eye movement data) was fit to the depth-averaged (0-1.6 mm for visual stimulation data, 0.8-1.2 mm for eye movement data) (Ress et al., 2007). The best fit sinusoid was found Fourier transform analysis to give measures of amplitude, coherence, and phase. Phase maps were projected onto the surface to visualize topography of visual stimulation and eye movements. P-values were generated by boot-strapping across the many depth-averaged runs for each participant.

ROI Generation- To define ROIs that depicted the topography of eye movements, we generated many elliptical ROIs. The phasic progression from medial to lateral was visually observed and then delineated with two vertices on the surface to define the start and stop of the putative eye movement maps. Surface projections of the SC were then flattened down to 2D, and the two vertices were transformed to the flat view. Then,

several (~20,000) elliptical ROIs were generated by varying 5 parameters: 1) size (15 – 60% of one entire SC hemisphere), 2) aspect ratio (3.5 to 7) 3) center x and 4) y-coordinates (each ± 2 pixels from the midline of the delineated phase progression), and 5) the elliptical angle (± 15° relative to the angle of the delineated phase progression). An exhaustive search was then conducted with following optimization criteria to maximize: 1) number of significant ($p < 0.2$) voxels, 2) geometric average p-value, 3) amount of phase coverage (median deviation), 4) degree of match between putative phasic angle and the elliptical ROI angle on the flat view, and 5) the variance explained and the 6) the closest matching slope of the linear fit between the mesh distance and the phasic progression. The five optimization criteria were multiplied together (un-weighted) to find the 4 best ROIs. ROIs were visually inspected for sanity, and generally the top fitting ROI was used for subsequent analyses.

Laminar Profile Analysis- We then examined the amplitude of the complex response as a function of laminar depth within the elliptical SC ROIs, similar to our previous approaches (Katyal et al., 2010, 2012; Katyal and Ress, 2014). Complex amplitude data was first averaged together across all runs for each participant. To correct for hemodynamic delay, phase normalization was performed for each run by dividing the complex amplitude of the profile with the mean phase within the respective elliptical ROI, restricted to the collicular surface where the data were strongest and most reliable. A boxcar-smoothing kernel (1.2 mm width in bin steps of 0.1 mm) was convolved with the average complex amplitude data as a function of depth; the magnitude of this

convolution was the laminar profile. The laminar profiles for both eye movement and visual stimulation experiments were normalized to range [0,1] for ease of comparison across participants.

We used bootstrapping to obtain confidence intervals on the laminar amplitude profiles in each participant and all participants combined for both visual stimulation and eye movement experiments. For each ROI, we calculated the complex amplitudes for each run to create an ensemble of complex amplitude datasets. We then formed averages by resampling this ensemble with replacement over 5,000 iterations, and calculated the laminar profile anew for each resampled average.

Centroids of the laminar profiles were calculated to quantify comparisons of depth between the attention and stimulation conditions using:

$$c = \frac{1}{\hat{A}} \int_{s_{min}}^{s_{max}} sA(s)ds$$

where $A(s)$ is the amplitude as a function of depth and $\hat{A}$ is the average amplitude. The integration limits s_{min} and s_{max} were set to 0 and 4 mm, respectively, as that is roughly the thickness of human SC. The centroid calculation was also bootstrapped across the ensemble of runs to obtain confidence intervals and p-values for differences between

centroid values for visual stimulation and eye-movement maps (fraction of bootstrapped centroids with eye movement values > visual stimulation values).

Retinotopy-Eye Movement Correlation- Within each optimal elliptical ROI for all participants, we measured how well phase maps for saccadic eye movements were in register with the phase maps for visual stimulation. The raw eye movement maps spanned the entire cycle (2π), and thus were first converted to visual field coordinates (90° around 0° for rightward eye movements, 90° around 180° for rightward eye movements). Visual stimulation phase data were corrected by estimating the hemodynamic delay, which we corrected by subtracting the mean off of the phase data and adding 180° for the left visual field.

We again used bootstrapping to obtain confidence intervals on the correlations for each participant and all participants combined. For each attention session, we calculated a run-by-run ensemble of depth-averaged complex amplitude datasets. We then performed our correlation analysis with the retinotopy data for 5,000 averages of the attention-condition runs, each average obtained by resampling the ensemble with replacement. The p-values corresponded to the fraction of the correlations yielding a fit with slope ≤ 0.

Eccentricity Measurements- In two participants, we obtained visual eccentricity measurements in both SC on separate scanning sessions (Halfen et al., manuscript in

prep). Eccentricity was obtained from the population receptive field (pRF) model of the stimulus of moving bars. The eccentricity was extracted from voxels within the elliptical ROIs generated above for the eye movement maps. The mean and spread of the eccentricity data were plotted as histograms. This allowed us to see how well the neural data represented the amplitude of the saccades performed (i.e., 6°).

2.2.5 Eye Movements

Eye movements were obtained with the SR EyeLink 1000 Plus (Scientific Research, Ontario, Canada) both outside of the scanner for training and inside the scanner during image acquisition. Inside the scanner, the infrared light and camera were placed beneath the LCD display and angled at the mirror allowing us to track the participant's right eye at ~130 cm lens-to-eye distance. Raw x,y position coordinates were sampled at 1000 Hz. Saccade reports were generated using the EyeLink Data Viewer (Scientific Research, Ontario, Canada) and further analyzed in MATLAB (Mathworks, Natick, MA, 2000). Saccades were detected using three minimum thresholds: position (> 0.15°), velocity (> 30°/s), and acceleration (> 9500°/s^2). Eye blinks were detected when the pupil diameter was too small (< 1 mm), obstructed, or not tracked, and any saccades during blinks were discarded from analysis. Polar plots were created to represent the saccades with the direction of the saccade as the polar angle and the amplitude of the saccade as the eccentricity, which was also visualized with histograms.

2.3 Results

2.3.1 Behavioral Performance

During the eye movement task, participants were able to perform the object discrimination task reliably (mean 81% across all sessions and participants, **Figure 2.3A**). The speed of the saccades were determined by the participants as the button response in the discrimination task triggered the onset of the next cue. Participants generally made saccades at a peak interval between 0.6 – 0.8 seconds (**Figure 2.3B**). During visual stimulation task, participants performed the speed discrimination task at a mean accuracy of 70.3% (**Figure 2.3C**), right around the staircase target accuracy, with a mean discrimination threshold of 1.6 °/s. The higher mean discrimination threshold was driven by two participants who had considerably less training/experience with the task than the other three participants (**Figure 2.3D**).

2.3.2 Eye Movements

We trained all participants on 2-3 runs before each eye movement mapping session (outside of the scanner) and quantified the reliability of eye movements prior to scanning (**Figure 2.4A**). Saccades were detected and visualized on polar plots to show the eccentricity and polar angle of each saccade. Also, saccades were color coded to represent the cycle timing to see how temporally the saccades along the three principle axes (inferior, horizontal, superior) were made. We were also able to obtain reliable eye tracking the scanner from two participants on both rightward and leftward eye

movement sessions (**Figure 2.4B**). Saccade amplitude histograms confirmed that participants were able to make 5-6° saccades.

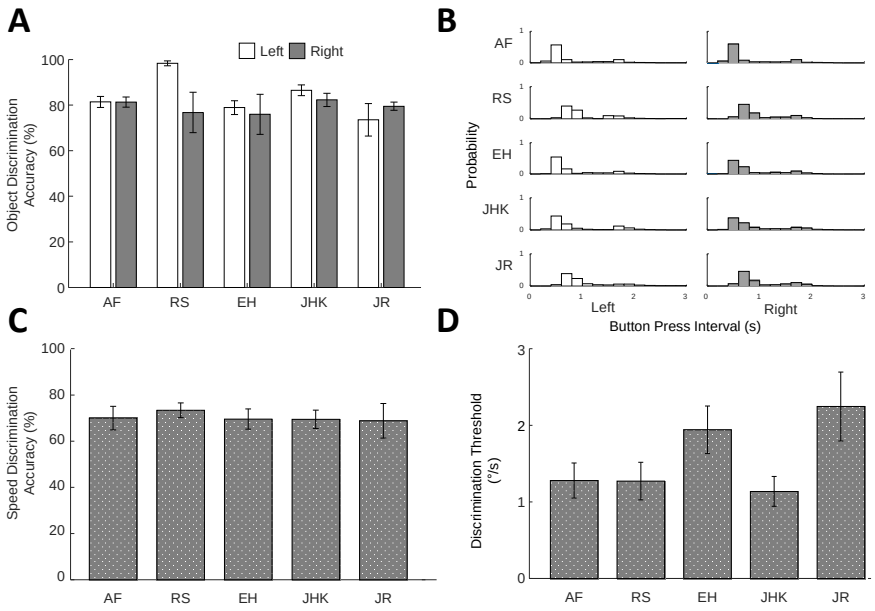

Figure 2.3 Behavioral Performance

Psychophysical performance measures show participants reliably performed both the object discrimination task during saccadic eye movements (top row) and the speed discrimination task during visual stimulation (bottom row). A. Participants were able to detect the object (circle or square) reliably at around 80%. B. Histograms showing the distribution of button press intervals. Histograms are bi-modal, with one mode around 0.6 – 0.8 s representing the speed of the saccades and a long-tailed mode at 1.2 – 1.5 s representing the smooth pursuit. Participants also performed the speed discrimination task at the 71% target accuracy (C) with a mean discrimination threshold of 1.6 °/s (D).

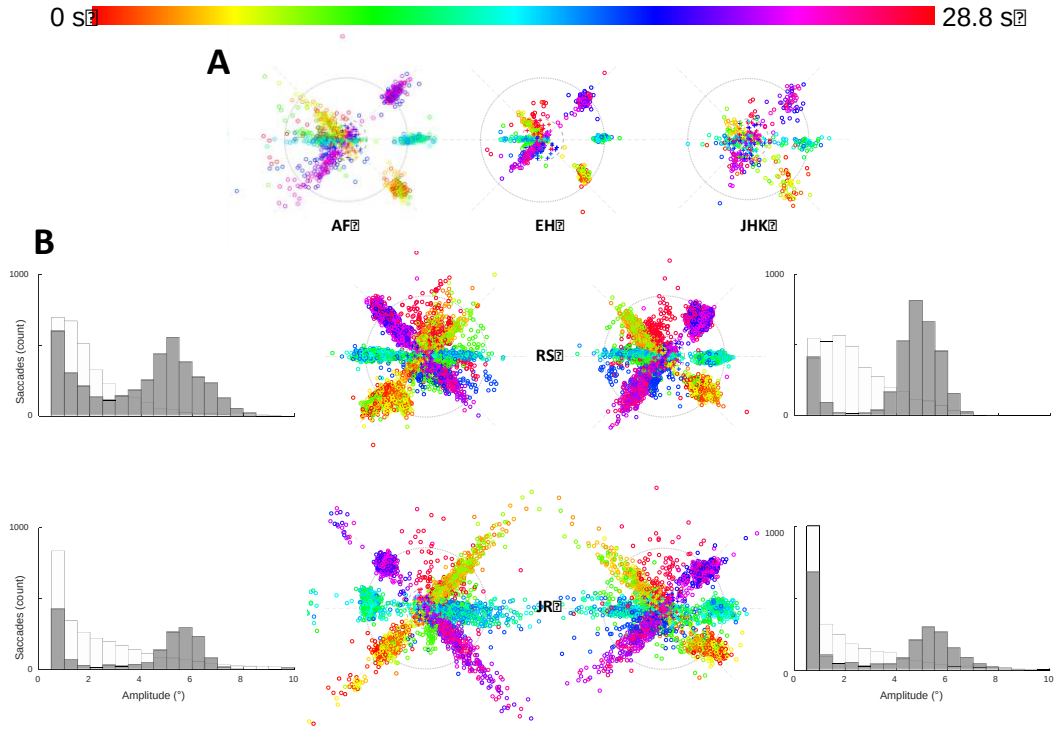

Figure 2.4 Reliability of Eye Movements

Eye tracking confirmed the reliability of eye movements participants were able to perform. A. Data from three participants show saccades outside of the scanner during a training session. Polar plots show the polar angle and eccentricity of each saccade detected, as well as the corresponding time during the 28.8 s cycle, represented as a color from the HSV color map. B. Data from 2 participants inside the scanner during image acquisition also show reliable eye movements during both leftward and rightward sessions. Histograms confirm peak eye movements around 5-6° in the cued direction (shown in gray). Long tailed distributions in the opposite direction (white) were also observed, as the smooth pursuits often contained variable saccades, but most were < 1°, which were easily separable from the cued saccades. Small correction saccades also contribute to the opposite direction saccades, as we observed participants to often saccade past the cued target and then make a small correction saccade back to the target.

2.3.3 Polar Angle Maps of Saccadic Eye Movements

Eye movements along the superior-inferior visual field were mapped along the medial-lateral axis of the SC in all 5 participants (**Figure 2.5**). Phasic activity was generally clumped into three zones: lateral, central, and medial corresponding to inferior, horizontal, and superior eye movements, respectively. In most participants, we also observed a rostral tilt in the lateral to medial phase progression. This tilt was in line with visual stimulation retinotopy, as well.

Our eye movement task involved making 6° saccades only in one horizontal direction, while smooth pursuing back in the opposite direction. This allowed us to see activation of primarily one SC at a time. The activity in the SC contralateral to the direction of horizontal eye movements was generally much stronger and showed more reliable medial-later phase progressions. However, in several participants, we observed medial-lateral phase progressions on the ipsilateral SC, sometimes in the reverse direction as the contralateral SC. One reason for this activity may be that the targets are still remembered during the smooth pursuit, and activity in monkey SC of both remembered and visually-guided saccade targets has been reported during such smooth pursuits (Dash et al., 2016). The reverse mapping in some participants may arise from small saccades during the smooth pursuits, particularly as the pursuit approaches the target end-point, and the participant saccades ahead of the pursuit. The ipsilateral SC activity may also arise from observed small correction saccades, as the participant often saccades passed the target

and makes an adjustment by saccading in the opposite direction to fixate back on the target.

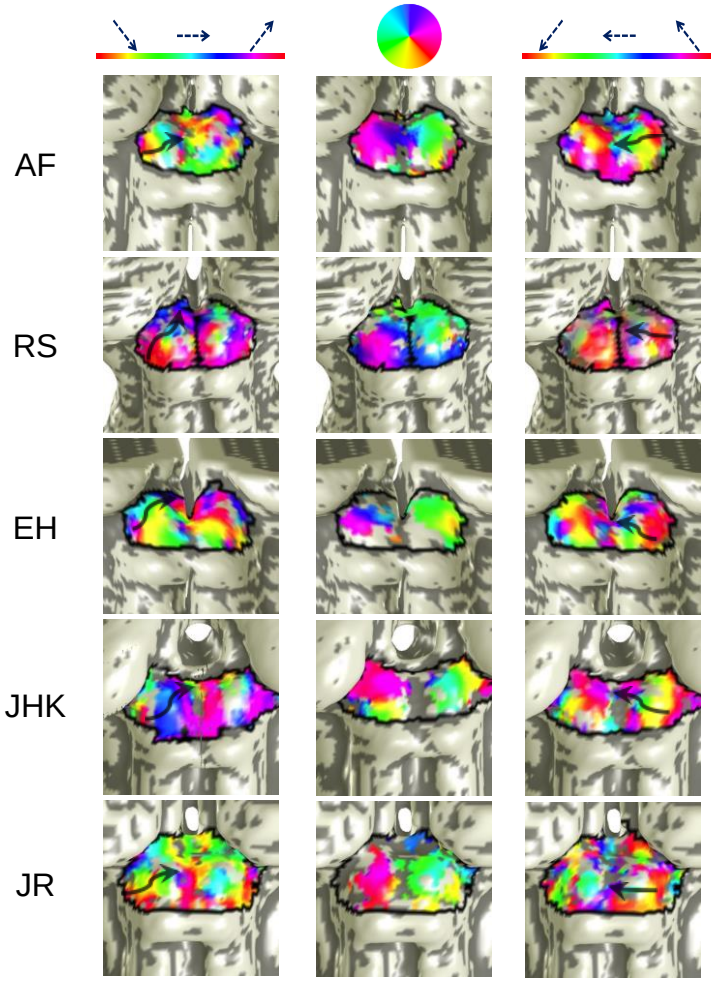

Figure 2.5 Topography of Saccades of SC

Eye movements along the superior-inferior visual field were mapped medial-laterally on the contralateral SC in five participants. The left column shows activation of the left SC as participants performed the eye movement task towards the right visual field, and the right column shows activation of right SC (leftward eye movements). Maps generally show three phases of activity: low phase medial (inferior eye movements), middle phase central (horizontal eye movements), and high phase medial (superior eye movements). The center column shows retinotopic topography for each participant elicited by visual stimulation.

2.3.4 Eye Movement Maps Correlated to Visual Stimulation Topography

Elliptical ROIs were first generated to delineate the medial-lateral phase progressions corresponding to the eye movements along the superior-inferior visual field (**Figure 2.6**).

Within the elliptical ROIs for each participant, we correlated the saccadic eye movement maps with the retinotopic visual stimulation maps (**Table 2.1, Figure 2.7**). Correlations were only significant for one SC in one individual (**Table 2.1**), but data approached significance when combined across all participants (left p-value: 0.163, right p-value: 0.0617).

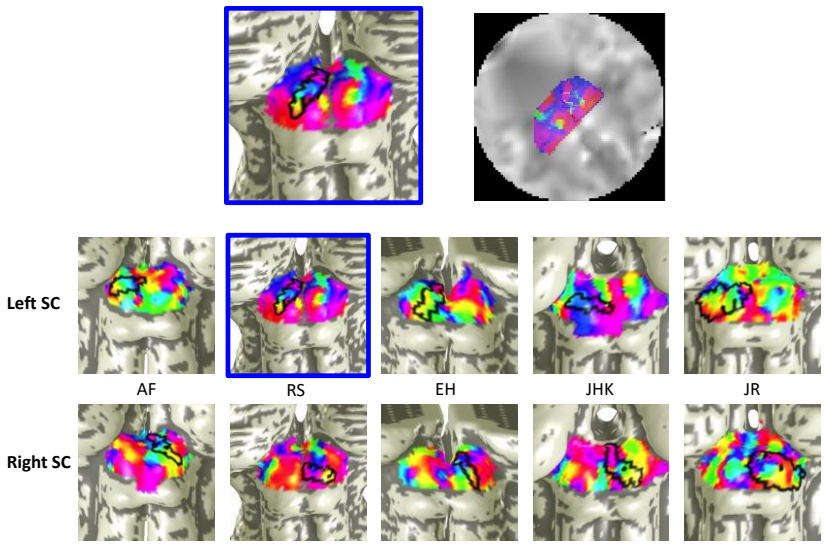

Figure 2.6 ROI Generation

Elliptical ROIs were optimally fit along the medial-lateral axis of the SC to isolate the eye movement regions for each participant on both SCs. The highlighted SC (blue box) shows the elliptical ROI on the surface mesh (black boundary, left) and in the flat view (white boundary, right), where the 2D elliptical ROIs were optimally found.

Table 2.1 Eye Movement and Visual Stimulation Correlations

Quantifications (R2, boot-strapped p-value, and slope) for eye movement and visual stimulation correlations for each and all participants for both SC.

	Left R^2	Left p-value	Left Slope	Right R^2	Right p-value	Right Slope
AF	0.58873	0.207	0.8263	0.54997	*0.0066	1.572
RS	0.52737	0.1678	1.7262	0.059043	0.3978	0.40487
EH	0.38232	0.5894	0.99059	0.070883	0.419	0.095239
JHK	0.069807	0.2844	0.75405	0.61038	0.3382	1.6273
JR	0.31734	0.3622	1.3559	0.070547	0.2974	0.41204
All	0.16228	0.163	0.94693	0.17679	0.0617	0.79896

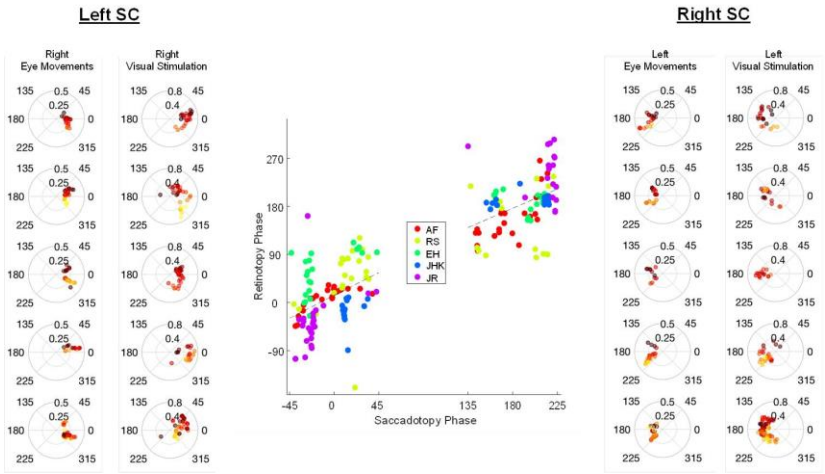

Figure 2.7 Eye Movements and Visual Stimulation Correlations

Saccadic eye movement phase maps correlated (weakly) with visual stimulation topography. Polar plots on the left and right columns show three pieces of information for eye movement and visual stimulation maps. The polar angle of each dot represents the phase from each significant ($p < 0.1$) voxel in the elliptical ROI. The r-axis the coherence of the sinusoidal fit for the voxel. And the color represents the distance on the mesh from the medial inter-collicular axis. Together, the polar plots reveal: 1) the medial-lateral phase progression of eye movements along the superior-inferior axis adjacent to the retinotopic progression, which visually appear in register. To further quantify this, we correlated the phase of the eye movements with visual stimulation maps across all participants for each SC (center plot). Correlations approached significance on both SC (left p-value: 0.163, right p-value: 0.0617). See Figure 2.9 for an exemplar participant (RS) that visually shows all maps along with eye movement maps from eye tracking.

2.3.5 Depth Profile

Laminar depth profiles extended deeper into SC for activity evoked by eye movements compared to visual stimulation (**Figure 2.8**). The left SC profile shows high activity for visual stimulation superficially that drops off almost completely 2 mm into the SC. In contrast, eye movement evoked activity begins to rise at 1 – 1.5 mm and peaks at ~3 mm. Similar though smaller differences are observed on the right SC. The centroid is also significantly shifted deeper for eye movement maps compared to visual stimulation maps for both left ($\Delta c = 1.767$, $p \sim= 0$) and right ($\Delta c = 0.9886$, $p = 0.0222$) SC. At the individual level, data were only significant in 3/10 SC (**Table 2.2**).

We also computed depth profiles on 3 ROIs (medial, central, lateral) rostral-caudal midline of the colliculus, which were drawn using 3 mm radius independent of either phase map (**Figure 2.10**). Eye movement maps were significantly deeper for left lateral and medial ROIs, as well.

Table 2.2 Depth Profiles

Quantifications of laminar profile centroid shifts (Δc) for eye movement maps compared to visual stimulation maps for each individual participant.

Subject	ΔC Left SC	p-value Left SC	ΔC Right SC	p-value Right SC
AF	1.249	*~0	1.351	*0.002
RS	-0.547	0.793	-0.208	0.364
EH	1.249	0.273	0.995	0.282
JHK	1.988	*0.005	0.282	0.480
JR	-0.009	0.508	0.458	0.419

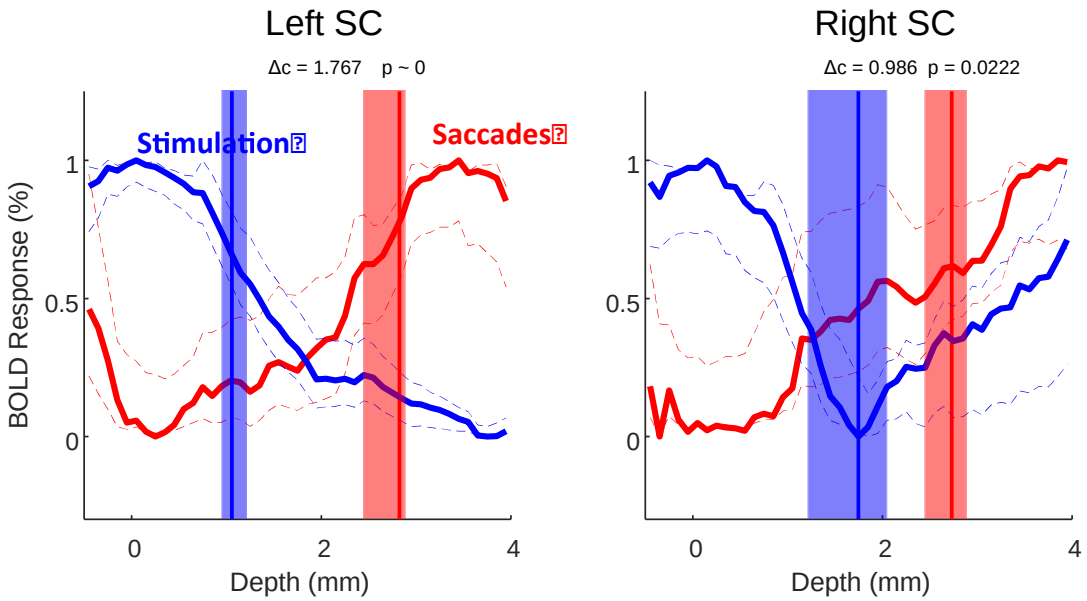

Figure 2.8 Depth Profiles

Saccadic eye movement maps lie deeper in SC than visual stimulation maps. Laminar depth profiles for both left and right SC show the activity evoked by eye movements (red) lies deeper in SC than activity evoked by visual stimulation (blue). Data are combined across all 5 participants for left and right SC. Dotted lines represent 68% confidence intervals bootstrapped across all runs and participants. The centroid is significantly shifted deeper for eye movements for both left and right SC (shaded rectangles show bootstrapped confidence intervals for centroid calculations).

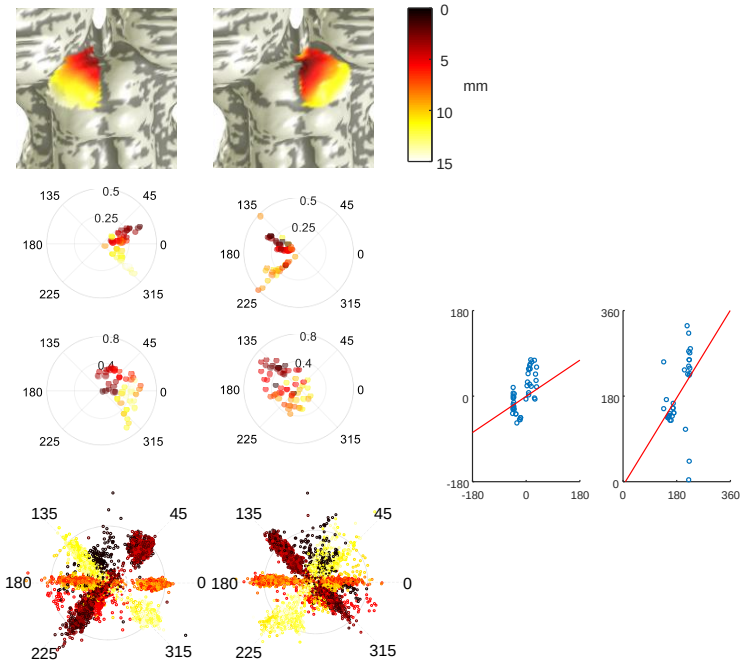

Figure 2.9 Exemplar Participant

Related to Figure 2.7. An exemplar participant (RS) showing a full set of mesh distance maps (top, left), saccadic eye movement polar plots (second row, left), visual stimulation polar plots (third row, left) and corresponding eye movement plots (bottom, left). Phase and color progressions are visually in register with all plots. Retinotopic and eye movement correlations for the individual are shown on the right.

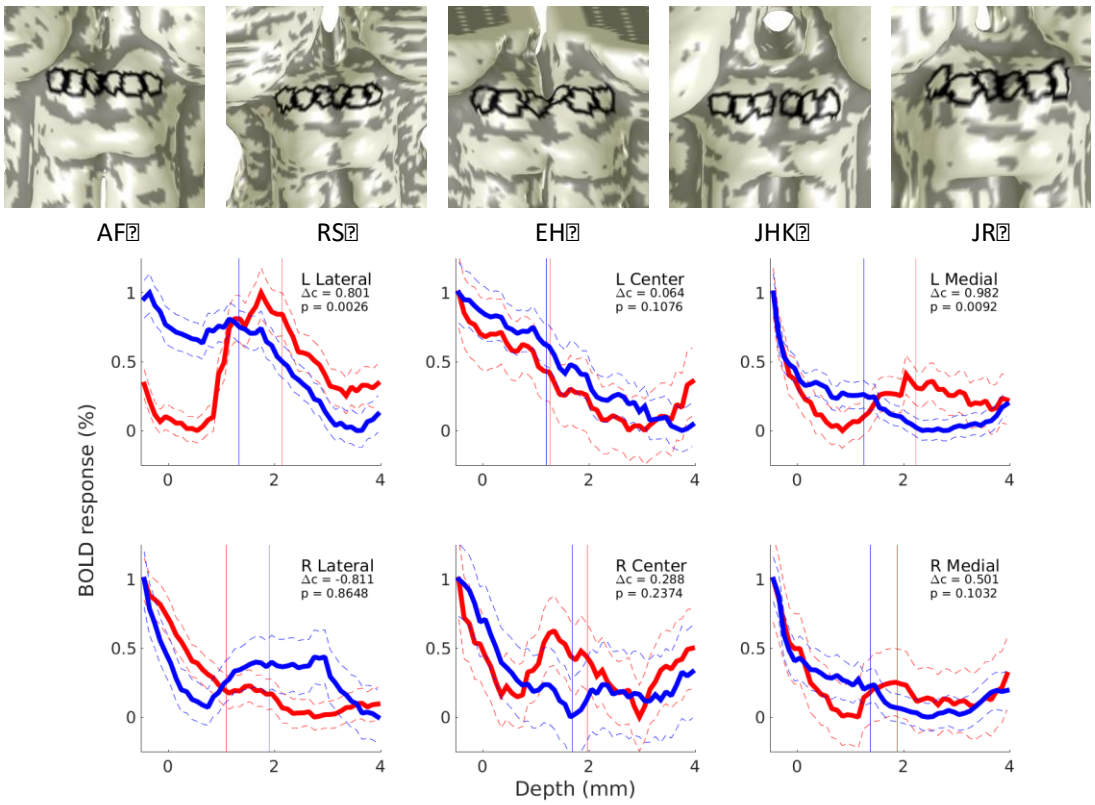

Figure 2.10 Depth Profiles in ROIs

Related to Figure 2.8. Laminar profile depth analysis reveals activity evoked by saccadic eye movements extends significantly deeper into the left SC compared to activity evoked by visual stimulation in ROIs drawn independently of either map. Lateral, central, and medial ROIs with 3-mm radius were drawn on each SC for all participants (top row). Laminar profiles and bootstrapped confidence intervals for eye movement maps (red) and visual stimulation maps (blue) are plotted. Vertical bars represent the centroids of the laminar profiles, which were significantly deeper for the left lateral ($p = 0.0026$) and left medial ($p = 0.0092$) SC ROIs.

2.3.6 Eccentricity Maps

We quantified the eccentricity of the eye movements in two participants (AF, EH) from the neural data within the elliptical ROIs derived from the eye movement maps (**Figure 2.11**). The eccentricity in one participant (AF) closely matched the eye movement profile from training (**Figure 2.3**), with the neural data overestimating the eccentricity just by ~1-2°. The other participant (EH) also showed the neural data to overestimate the eye movements by 3-4°.

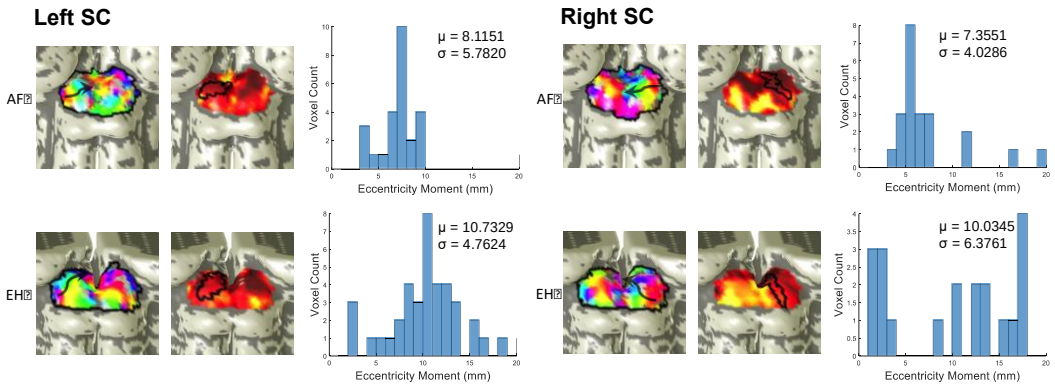

Figure 2.11 Eccentricity of Eye Movements

The eccentricity of saccadic eye movements derived from the neural data were slightly larger than the eccentricity of the actual eye movements (derived from eye-tracking, see Figure 2.3). One participant (AF, top row), the eccentricity peaked at ~6-7° on both sides. The mean was brought up by just a few voxels with much higher eccentricity. In the other participant (EH, bottom row), the eccentricity within the elliptical ROI contained more spread and peaked higher (~10°) than the actual 5-6° eye movements made.

2.4 Discussion

We used high-resolution functional MRI to map the polar angle representation of saccadic eye movements onto the human SC. We found eye movements along the superior-inferior visual axis were mapped medial to lateral on the anatomy of the SC. Eliciting these maps required a novel paradigm in which participants could make saccades along principle direction and then making a smooth pursuit back to the origin of the axis. Doing so isolated forward saccades from reverse saccades, while still allowing participants to make many saccades in an experimental session. This construct was not immediately obvious to us, and was only discovered many failed paradigms that evolved over time (**Figure 2.11**).

We found the saccadic eye movement maps in human SC to be in rough alignment with the overlying retinotopic topography. When we plotted the phase data from the two maps against each other, the slopes were all positive for every participant for each SC. However, the variance explained was often not extremely high (R^2 ranged from 0.05 to 0.6) and only one SC out of 10 had a bootstrapped p-value < 0.05. This may be in part due to the fact that the polar angle visual stimulation maps were acquired on the both hemifields simultaneously. We corrected the phase maps by mean centering the data appropriately, but perhaps exciting the visual field with the precise cycle and order of the saccadic eye movement stimuli would have enhanced the correlations. For example, such experiments in monkey were done in which individual neurons had their receptive

fields mapped by stimulation as well the elicited saccades by electrical stimulation showed a very precise correlation between the two maps (Schiller and Stryker, 1972).

The depth profiles show that the saccadic eye movement maps lie 1-2 mm deeper than visual stimulation maps on both SC. Data were significant for only 3/10 participants individually. This is often observed as many sessions are needed to obtain the resolution to resolve the laminar profiles, as we previously encountered when comparing attentional maps to visual stimulation maps (Katyal et al., 2010).

Neural eccentricity measurements were quite close to (but slightly overestimated) the 5-6° saccades in one participant (AF) but much more severely overestimated in the other participant (EH). We are not sure what precisely caused these higher eccentricity representations in the neural data. The phase progressions for saccadic eye movement maps are large and do traverse rostrally as the maps move medially in several participants. The more caudal eye movement maps lie laterally and seem to be at higher eccentricities in the neural data. The precise correlation between neural eccentricity and saccadic eye movements might be better elucidated by running the stimulus paradigm at various eccentricities (i.e., making saccades at 3° 6° 9° 12°) and seeing if the neural eccentricity matches each experiment.

In summary, our techniques allowed us to measure the functional topography of eye movements on the human SC. This required using high-resolution functional MRI to

reliably image the subcortex, as well as a novel experimental paradigm that allowed participants to make many saccades and isolate saccades to one principle direction. The functional organization of the eye movement maps were in register with retinotopic projections but were deeper in SC, similar to the organization observed in monkey SC. With this finding, we can now study more aspects of subcortical vision (e.g., ocular dominance columns) to understand the function of the human SC and how it may differ from non-human primate and rodent SC.

CHAPTER III

HOW WE FEEL

3.1 Introduction

When seeing someone in pain, observers tend to show neural activation patterns similar to if they had experienced pain themselves. We found that this empathic response was increased when participants viewed a painful event occurring to a hand labeled with their religious affiliation than a different affiliation. This neural ingroup bias was not seen with randomly assigned teams or alliances, suggesting that differential empathy may require some semblance of non-arbitrariness.

3.2 Materials and Methods

3.2.1 Participants

We recruited 135 participants (29.2 +/- 8.9 years, 63 males, 108 right-handed) with normal or corrected-to-normal vision from the Houston, TX metropolitan area. All participants were told they were being recruited for a study on memory; the study (and the deceptive research) was consented prior to the study in accordance with Baylor College of Medicine approved IRB, and participants were compensated for taking part in the experiments. Data from 8 participants were excluded due to errors on MR image acquisition or reconstruction, and 22 participants were excluded from analysis due to excessive head motion (absolute mean displacement > 3.0 mm), leaving 105 participants in total for analysis.

3.2.2 Behavioral Questionnaires

First, we asked participants their religious affiliation, as specifically as possible (they could declare ‘agnostic’ or ‘atheist’). Next, participants completed 5 brief surveys that quantified empathy and degree of religiosity: (1) Balanced Emotional Empathy Scale (BEES) (Mehrabian, 2000), (2) Davis Emotional Empathy Interpersonal Reactivity Index,(Davis, 1980) (3) Right Wing Authoritarianism Scale (Altemeyer, 1981), (4) Religious Conviction (Dawkins, 2008), and (5) Religious Orientation (Gorsuch and Venable, 1983).

3.2.3 Stimuli

All stimuli were programmed in MATLAB with PsychToolbox (Brainard, 1997). Participants viewed the stimuli on a back-projected screen while lying supine in the scanner.

All experiments were structured identically. First, participants viewed trials in which 6 hands appeared on the screen, each of which were similar in skin tone and apparent age, but was differentiated by an arbitrary bracelet that simply helped to give each hand a unique identity (**Figure 3.1A**). Two to four seconds later, one hand was randomly ‘selected’ by the computer by the addition of a red border around the image. After 6 seconds, the selected image moved into the middle of the screen and became a video. The video, lasting 2.3 seconds, either showed the hand being stabbed with a syringe needle or touched with a cotton swab—events that are visually similar in angle-of-

approach and timing, but quite different in terms of emotional impact. Because each participant saw multiple stabs and touches in the course of an experiment, we filmed stabbing and touching events from several different angles to reduce desensitization. In most versions of the experiment, except as where noted below, participants began by observing 6 stab trials and 6 touch trials; the contrast of these two baseline conditions allowed us to localize the pain matrix in fMRI. Observations were separated by a blank screen of at least 8-12 seconds inter-trial interval (ITI).

Next, for the remainder of the experiment, religious group labels were presented on top of each hand. The following 60 trials were identical to the first 12 except that each hand was labeled with a religion or group.

To examine whether small changes in the ITI or the number of hands would affect our results, we ran three slightly different versions of this experiment:

1) 6 hands, ITI 8-12 s, 6 religions, 12 baseline trials, 60 religion trials (n = 38 participants, including 10 agnostic)
2) 6 hands but 3 Christian and 3 atheist (to boost and balance # of ingroup trials), ITI 8-12 s, 2 religions, 12 baseline trials, 60 religion trials (n = 11 participants, including 4 agnostic)
3) 4 hands, ITI 14-18 s, 4 religions, 8 baseline trials, 56 religion trials (n = 23 participants, including 5 agnostic)

Our analysis found that these parameter variations did not influence our conclusions, so we combined these groups, each of which allows us to define ingroups and outgroups.

We constructed two more separate versions of the experiment on separate sets of participants to address religious ingroup bias and whether it could be manipulated rapidly.

In experiment 2 (allegiance), we studied the effects of allies. We arbitrarily pitted two groups of religions against each other: a participant's religion was allied with two other random religions who were now at war with 3 other random religions. For this we used 6 hands, ITI 10-14 s, 6 religions, 12 baseline trials, 60 religion trials (n = 19, including 5 agnostic).

In experiment 3 (arbitrary assignment), participants were randomly assigned to one of two made up groups (Augustinian or Justinian). In this experiment, we randomly assigned participants to the Augustinian or Justinian group before the fMRI portion of the experiment began. Specifically, participants began by tossing a coin: they were told that if they tossed a heads, they would be Augustinian, if tails, a Justinian. Participants thus knew that the assignment was arbitrary and up to chance. They were next handed a bracelet for their team (either Augustinian or Justinian), which they were instructed to put on. This was intended to both remind them of their team and bond them to it. We here used 6 hands, ITI 10-14 s, 2 groups, 12 baseline trials, 60 group trials (n = 14).
In each experiment, participants were told that the purpose of the study was to examine the effects of pain on memory. They therefore believed they were watching labeled hands being stabbed to see how the witnessed pain helped them to remember which hand

had been selected on any given trial. To buttress this impression (as well as to quantify alertness), we asked participants on a random 20% of trials to report which religion was associated with the selected hand 10-14 seconds after the trial. This deception (approved by our IRB) was necessary to keep participants naïve to the purpose of the experiment.

3.2.4 MR Image Acquisition

Data were acquired on a Siemens 3T Trio (Erlangen, Germany) scanner. First, high resolution T1-weighted scans were acquired using an MPRage sequence (0.4785 x 0.4785 x 1.0 mm voxels). Functional image acquisition details were as follows: echo-planar imaging, gradient recalled echo; repetition time (TR) = 2000 ms; echo time (TE) = 40 ms; flip angle =90°; 64 x 64 matrix, twenty nine 4 mm axial slices, yielding functional 3.4 mm x 3.4 mm x 4.0 mm voxels, one ~30 minute run.

3.2.5 Preprocessing.

fMRI data processing was carried out using FEAT (FMRI Expert Analysis Tool) Version 6.00, part of FSL 5.0.9 (FMRIB's Software Library, www.fmrib.ox.ac.uk/fsl). The first two volumes from every participant's functional run were discarded. The following pre-statistics processing was applied: motion correction using MCFLIRT (Jenkinson et al., 2002); slice-timing correction using Fourier-space time-series phase-shifting; non-brain removal using BET (Smith, 2002); spatial smoothing using a Gaussian kernel of FWHM 5mm; grand-mean intensity normalization of the entire 4D dataset by a single multiplicative factor; highpass temporal filtering (Gaussian-weighted

least-squares straight line fitting, with sigma=30 s). All first level analyses and model fitting were conducted in the functional space.

For group level analyses, parameter estimates and contrasts of beta weights were registered to the MNI152 template brain. Registration to high-resolution structural images was carried out using FLIRT (Jenkinson et al., 2002; Jenkinson and Smith, 2001) (full-search, boundary based registration, BBR). Registration from high resolution structural to standard space was then further refined using FNIRT nonlinear registration (Andersson, 2007a, 2007b) (full-search, 12 DOF, warp resolution 10 mm).

3.2.6 GLM Analysis

A general linear model (GLM) was fit to each participant's time-series data using FSL FILM (FMRIB's improved linear model) with local autocorrelation correction (Woolrich et al., 2001). Six standard motion regressors and individual motion outlier (RMS intensity difference to middle volume, *fsl_motion_outliers*) regressors were added to the model. For each trial condition (baseline, ingroup, outgroup, and/or ally) a set of regressors were included for both stab and touch trials separately, corresponding to the onset of the video of the hand being stabbed or touched. In addition, a regressor for hand selection for each condition was also included, corresponding to the time when the particular group of hand was selected. A regressor marking the trial onset across all trials, a regressor for the times questions were asked, and regressor for times buttons

were selected for the answers were also included. For each regressor, a temporal derivative regressor was also fit to allow for slight offsets of peak timings.

3.2.7 FIR Model

A finite impulse response (FIR) model was separately built for extracting fMRI time series to plot the hemodynamic response functions (HRFs) (**Figure 3.1C**). For each video onset, a set of 12 impulses were modeled from -8 s to + 16 s to capture the nature of the response to each trial. Each trial condition (baseline, ingroup, outgroup, and/or ally) were modeled separately for both stab and touch in order to extract HRFs for each condition. Regressors for questions, answers, and trials onsets were also included and were modeled with the standard double gamma HRF.

3.2.8 Group Analysis

First, we identified the pain matrix by contrasting the initial 6 stab trials from the initial 6 touch trials (baseline stab – baseline touch, **Figure 3.1B**). We used FSL FEAT mixed effects modeling (FLAME 1; **Figure 3.1B**) with outlier de-weighting for the group-level contrasts.

Next, we used whole brain search to identify regions outside of the pain matrix which responded more when ingroup hand was stabbed painfully. We used non-parametric statistics via permutations testing (FSL *randomize* (Winkler et al., 2014)) to perform whole-brain ingroup – outgroup searches. Contrasts between ingroups and outgroups

were conducted on all participants who had definable ingroups and outgroups (n=67; agnostics were excluded since they had no ingroup).

Within these two networks, parameter estimates were extracted and converted to percent signal change (FSL *featquery*).

3.3 Results

When watching another person get hurt, neuroimaging reveals activation of brain areas involved in the perception of one's own pain (Botvinick et al., 2005; Hein and Singer, 2008; Jacoby et al., 2015; Singer et al., 2004; Valeriani et al., 2008). Importantly, this empathy-related response is not constant: it is modulated by one's beliefs about the person being hurt. For example, there is a diminished response in the empathy network if the observer believes the pain-recipient has acted unfairly in a simple economic exchange (Singer et al., 2006). A similar diminishment occurs when the observer is told that the victim is receiving a large monetary compensation for undergoing the pain (Guo et al., 2012).

Modulation of empathy-associated regions also occurs with group distinctions: people are generally more empathic toward members of their ingroup than toward members of an outgroup. This neural ingroup bias has been demonstrated for one's preferred sports team (Cikara et al., 2011; Hein et al., 2010) as well as racial group membership (Azevedo et al., 2013; Contreras-Huerta et al., 2013; Xu et al., 2009). Beyond neural activity, the ingroup bias translates to actions: members of an ingroup are more likely to

help a fellow ingroup member (Hein et al., 2010). These biases have important practical considerations, from jury decision-making to bystander behavior in emergency situations.

Using functional magnetic resonance imaging (fMRI), we investigated how the neural ingroup bias might extend to religion affiliation. First, we localized empathy-related brain regions. Each participant observed a collection of hands on a screen; one hand was randomly selected and then either stabbed with a needle, or touched with a cotton swab (**Fig. 3.1A**). The whole brain contrast of *stab* > *touch* trials yielded 8 significant clusters (**Fig. 3.1B**), which we refer to collectively as the *empathy network* (**Fig. 3.1C**). This network is consistent with previous findings, containing both affective (insula, anterior cingulate) and sensorimotor (lateral occipital, fusiform, supramarginal) components.

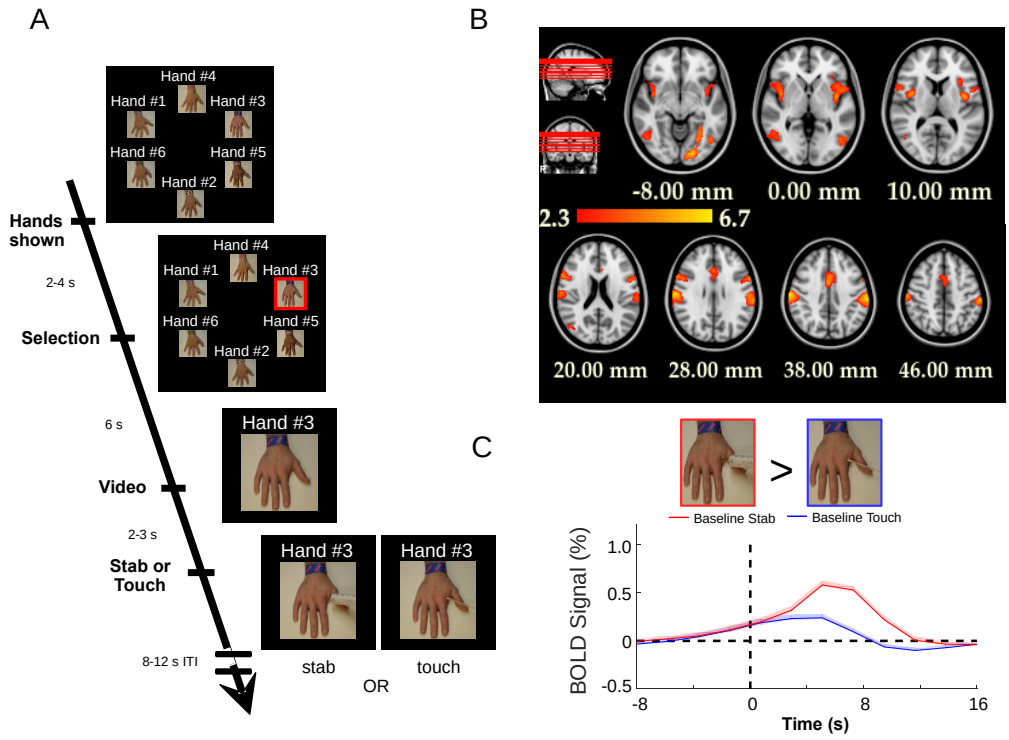

Figure 3.1 Localizing Empathy Network

Seeing another's hand in pain localizes a network of areas involved in empathy. **A**. Participants (n = 105) were shown several different hands on the screen. One hand was selected randomly, and then a video was shown of that hand either stabbed with a syringe needle or touched with a cotton swab. **B**. The contrast of stabs and touches reveals 8 significant clusters of activation weighted by z-statistics (Z>2.3 and FWE-corrected cluster significance threshold of p<0.05). **C**. The hemodynamic response to the stab (red) and touch (blue) trials averaged across the empathy network. See **Table 3.1 and Fig. 3.2** for more detail

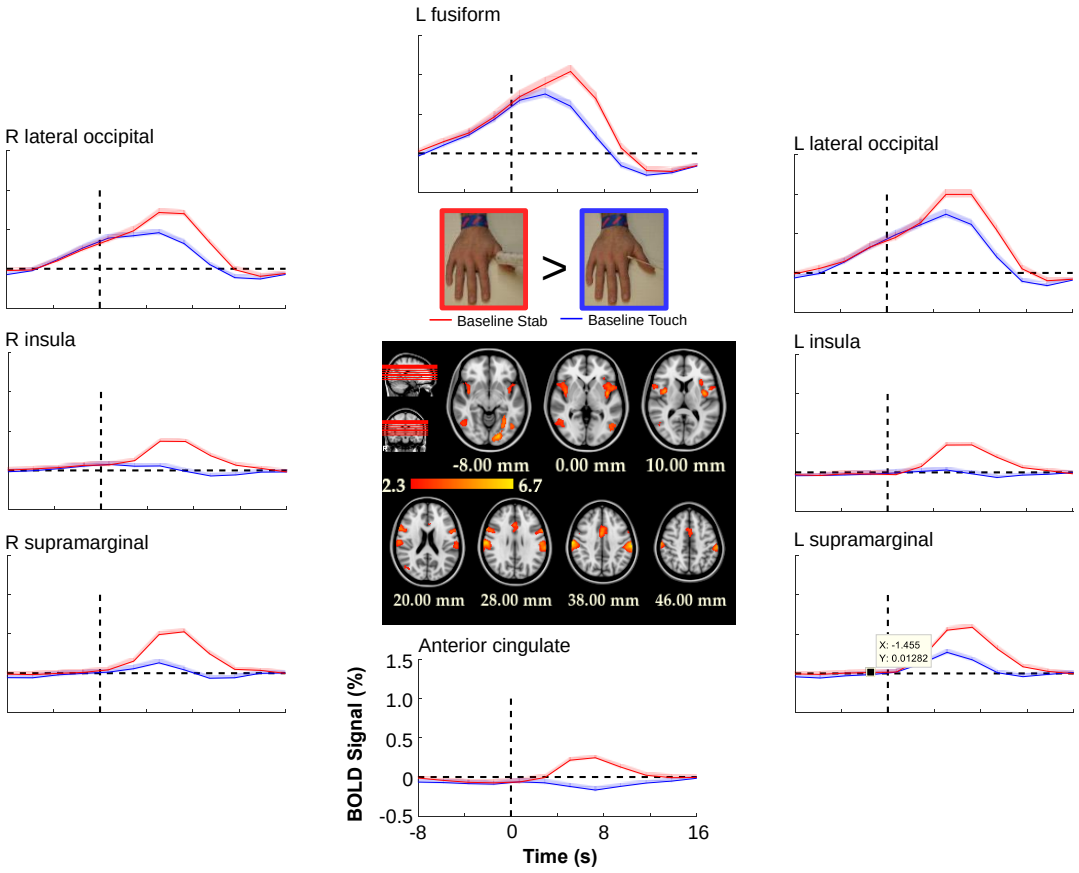

Figure 3.2 Empathy Network Hemodynamics

The average time series for each of the 8 clusters of the empathy network show that hemodynamic responses for observing painful stab trials (red) are greater than observing non-painful touch trials (blue). Time 0 is the onset of the stab or touch video. The time series were derived from a separate GLM model fit with 12 finite impulse responses (FIRs) from -8 to +16 seconds around the time of the video onset of the stab or the touch. Time series units are in percent signal change from baseline. See **Table 3.1** for coordinates of activation (n = 105).

Table 3.1 Empathy Network Coordinates

MNI Coordinates from empathy network for pain (from Figure 3.1). Coordinates represent the center of gravity of the z-statistic for each cluster.

Cluster	Voxels	P	X (mm)	Y (mm)	Z (mm)
left insular cortex	1347	2.86E-06	-44.5	5.29	8.49
right insular cortex	1276	5.25E-06	48.4	7.83	10.8
left supramarginal	1043	4.09E-05	-58.4	-26.1	33.9
right supramarginal	1022	4.96E-05	61	-21.4	32.2
ant. cingulate cortex/SMA	907	0.00015	-0.587	9.79	36.1
left fusiform gyrus	862	1.03E-09	-23.7	-70.7	-12.7
right lateral occipital cortex	520	0.00827	49.5	-61.7	0.421
left lateral occipital cortex	306	0.000124	-47.5	-68.5	-0.993

We next assessed if the neural empathic response could be modulated by replacing the text labels of the hands (e.g. Hand #3) with religious affiliations: Christian, Muslim, Hindu, Jewish, atheist, and Scientologist (**Fig. 3.3A**). For each participant, their self-reported religion was defined as *ingroup*, and the other religions were defined as *outgroup*. The average response magnitude in the empathy network was significantly higher for ingroup trials compared to outgroup trials for both *stab* ($p = 0.012$, corrected) and *touch* ($p = 0.036$, corrected) trials (**Fig. 3.3B,C**, $n = 67$; **Fig. 3.4, 3.5** for statistics and re-sampling). There was a positive correlation between participants' scores on the Balanced Empathy Emotional Scale and activity in the left insula (**Fig. 3.3E, Fig. 3.6, Fig 3.7**); however, there was no correlation between activity in the empathy network and participants' strength of religious belief. A whole brain contrast for ingroup greater than

outgroup (combining stab and touch trials) yielded three clusters beyond the empathy network: the mPFC, posterior cingulate/precuneus, and superior temporal gyrus (**Fig. 3. 3D,F**, **Fig. 3.8, 3.9**). These areas are involved in self-referential thought and mentalizing. There were no significant voxels in the contrast outgroup > ingroup.

Next, we investigated the modulability of the observer bias. The 6 religions were divided into 2 teams, and the participant was told the two teams were at war with each other. Thus, two outgroup religions were now on the same 'team' as the participant's ingroup religion. We found that the neural response to these 'allies' was not significantly different from the response to the outgroup members, indicating that a fictitious alliance scenario was not sufficient to reduce the neural ingroup bias (**Fig. 3.10, 3.11**). In a final experiment, participants were randomly assigned (by coin flip visible to the participant) to one of two groups: Augustinian or Justinian. They were given a bracelet with their group name, and told that the Augustinians and Justinians were two warring tribes. They then ran the same paradigm as previously except the hands were labeled Augustinian or Justinian instead of with religious affiliations. Participants showed no neural bias between ingrf2coup tribe and outgroup tribe trials (for either stabs or touches) (**Fig. 3.12, 3.13**). This finding somewhat conflicts with recent evidence that ingroup bias emerges when participants were deceived into believing they belonged to one of two types of problem solvers (Ruckmann et al., 2015). One possibility for the difference in results is that we did not use deception to assign groups; it was clear to our participants that group assignment was random.

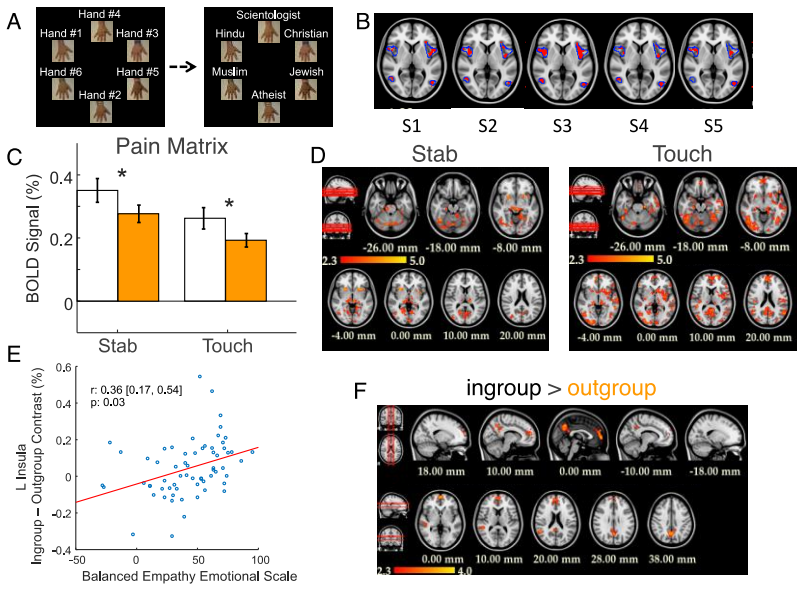

Figure 3.3 Ingroup vs Outgroup

Within the empathy network, BOLD activity to either stabs or touches was larger for ingroup-labeled hands than for outgroup hands. A. Participants (n = 67) watched painful stabs and non-painful touches to hands labeled with their same religion (ingroup) or a different religion (outgroup). B. Within the empathy network, participants showed greater activation for their ingroup than outgroup, for both stab and touch trials. C. Ingroup – outgroup contrast parameter estimates of the left insula correlated significantly with individual scores on the Balanced Empathy Emotional Scale (r = 0.36, 95% confidence interval 0.17 to 0.54, raw p = 0.004, corrected for number of ROIs p = 0.03). D. A whole brain search for ingroup > outgroup differences (combining stab and touch trials) yielded three clusters beyond the empathy network: the mPFC, posterior cingulate/precuneus, and superior temporal gyrus. There were no significant voxels in the contrast outgroup > ingroup F. After parametrically controlling for repetition suppression (Fig. 3.7) and combining across stab and touch trials, the whole-brain ingroup > outgroup contrast yielded three significant clusters: the anterior cingulate, posterior cingulate/precuneus, and superior temporal gyrus. There were no significant voxels in the contrast outgroup > ingroup. See Table 3.2

Table 3.2 Whole Brain Ingroup Bias Coordinates

MNI Coordinates from whole brain search for voxels that respond greater to witnessing ingroup pain compared to outgroup pain (from **Figure 3.3**). Coordinates represent the center of gravity of the z-statistic for each cluster.

Cluster	Voxels	P	X (mm)	Y (mm)	Z (mm)
right sup. temporal gyrus	964	6.9E-05	2	2.02	54.4
precuneus/post. Cingulate	850	0.00021	1.52	-56.5	34.2
anterior paracingulate	628	0.00214	54	-35.9	6.32

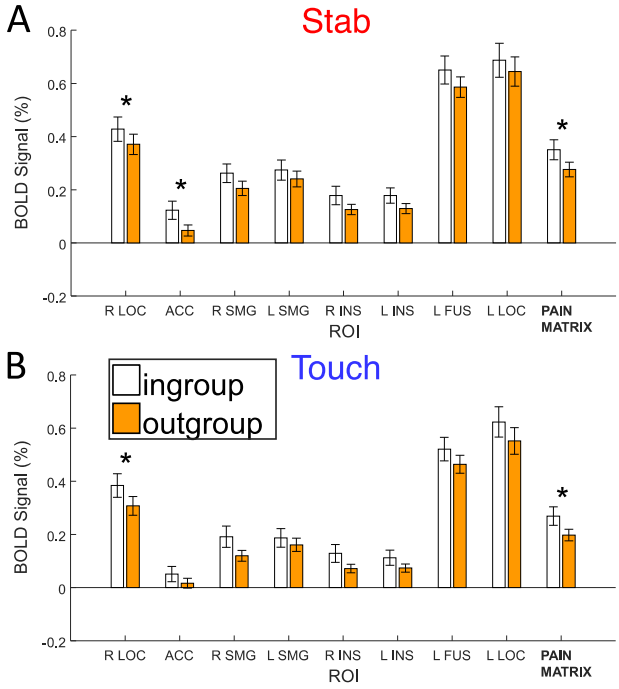

Figure 3.4 Empathy Netowrk Ingroup Bias

Parameter estimates from the clusters of the empathy network show heightened responses when an ingroup hand gets either painfully stabbed (A) or non-painfully touched (B) compared to the same action of an outgroup hand. Asterisks represent significant ingroup – outgroup effect ($p < 0.05$, Holm-Bonferroni corrected for the number of ROIs in the empathy network) as computed by permutations testing. Stab distributions in red; touch in blue.

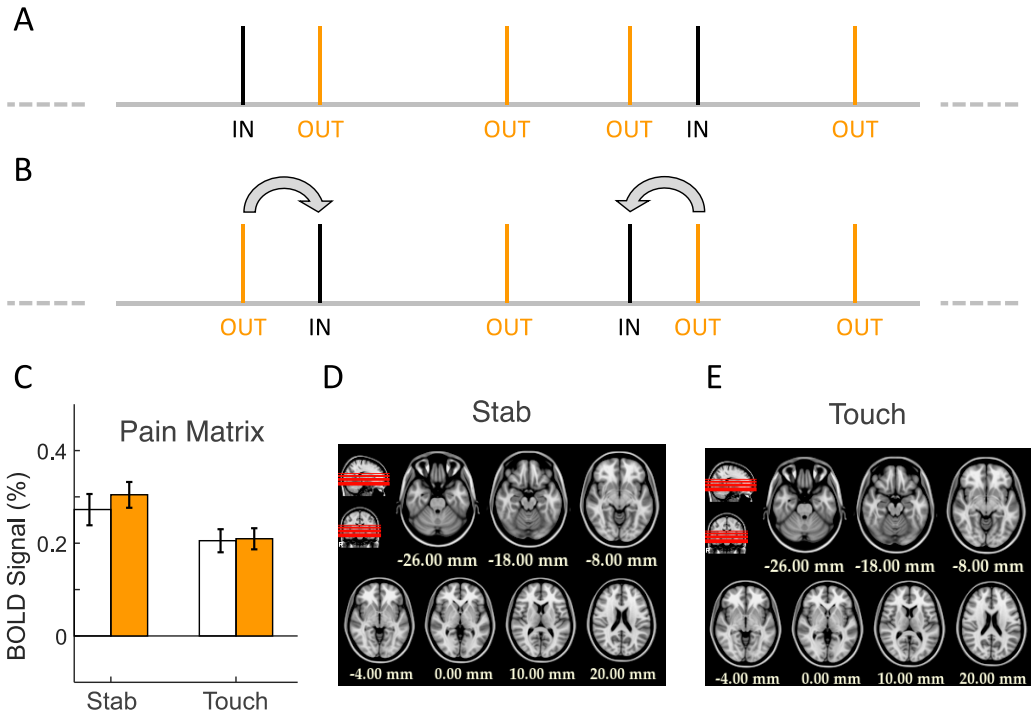

Figure 3.5 Control Experiment

To account for frequency effects (there were more ingroup trials), we ran a control analysis in which ingroup trial labels were swapped with the closest matching outgroup trial labels. The results show no significant ingroup effect, indicating that the main results were not due to an imbalanced number of trials. **A**. The stick diagram represents a schematic of the true timing of ingroup and outgroup trials. Condition type (stab or touch) labels are not shown here for simplicity. **B**. Trials constituting the ingroup condition were swapped with the temporally closest matching outgroup trials (stimulus type – pain or touch – was conserved). **C**. With the ingroup trials swapped, the group effect of the empathy network is no longer observed (stab: $p = 0.9215$, touch: $p = 0.5894$, permutations testing). Further, whole-brain search for ingroup > outgroup effects yield no significant voxels for either stabs (**D**) or touches (**E**).

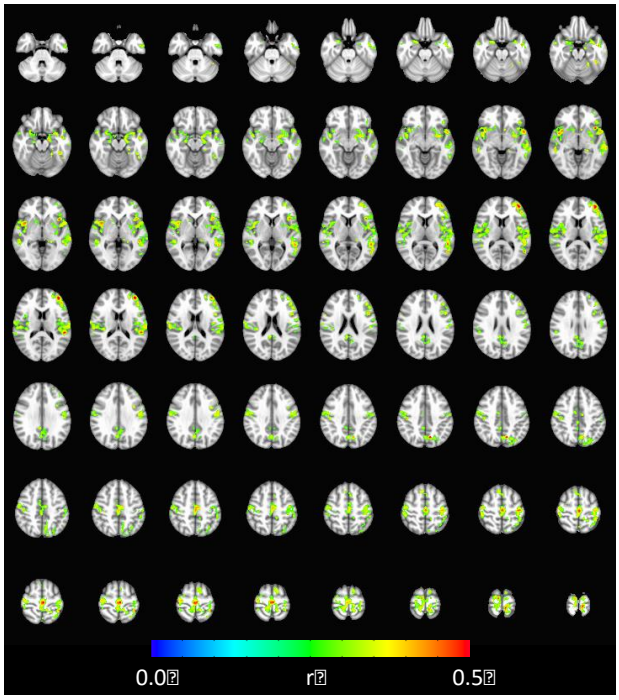

Figure 3.6 Correlation with Behavior

Individual empathy ratings - as measured by the Balanced Empathy Emotional Scale (BEES) scores - were significantly correlated to the neural activity differences between ingroup and outgroup conditions in several brain regions, including bilateral insula, left inferior frontal gyrus, and left superior temporal gyrus (n = 67). Thresholds for correlations were computed using permutation testing (FSL *randomise*, threshold-free cluster enhancement (tfce), $p < 0.05$, FWE corrected).
However, Whole-brain searches did not yield any significant voxels for correlations between ingroup – outgroup contrast parameter estimates and each of 1) intrinsic religiosity, 2) religious conviction, 3) Davis Emotional Empathy Interpersonal Reactivity Index – Empathy Concern (EC) and 4) Perspective Taking (PT). Further, we also did not observe any correlations with baseline stab – touch contrast parameter estimates and any of the 5 behavioral measures. This is in contrast to previous reports showing significant empathy correlations in painful – non-painful contrast parameter estimates and BEES and Davis EC measures.(Singer et al., 2004) Singer et al. (2004) elicited empathic responses in a group of 16 participants by administering pain to a loved one sitting next to him/her in the scanner. Perhaps the elicited empathic response was stronger under this context and correlated better to behavioral empathy questionnaires, as compared to our baseline contrast measures in 12 trials (6 painful, 6 non-painful) in 105 participants. Further, we chose not to plot any correlations derived from these whole-brain searches, as the topic of the "non-independence error" has been scrutinized heavily.(Lazar, 2009; Lieberman et al., 2009; Nichols and Poline, 2009; Vul et al., 2009a, 2009b).

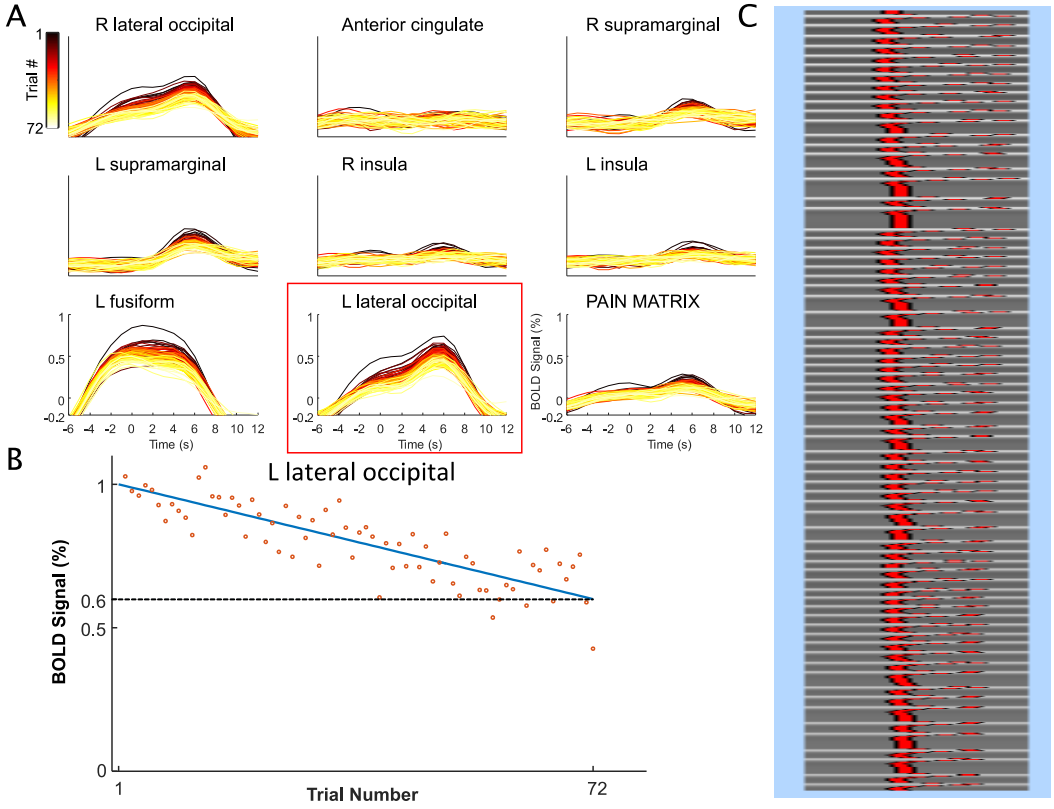

Figure 3.7 Repetition Suppression

Repetition suppression effects are observed within the clusters of the Pain Network across the 72 trials, so we designed a parametric modulation regressor to refine the GLM model. **A.** A separate GLM model was fit to the data with a regressor for each trial, regardless of the trial type (e.g., stab or touch, ingroup or outgroup). The peri-stimulus HRF was drawn for the spatial average of each of the 8 clusters within the pain network and across the entire pain network. The heatmap colors each trial from 1 (black) to 72 (yellow). **B**. A linear regression model was fit to the left lateral occipital cluster, a cluster that showed high degree of repetition suppression effect. The linear model predicts a 40% repetition suppression effect from the 1st trial to the 72nd trial. **C**. The model from the left lateral occipital cluster was used to create a regressor to parametrically model and account for the effect of the repetition suppression in subsequent analyses. A separate GLM model was built identical to the original but included the participant specific regressor in an attempt to account for repetition suppression effects to localize ingroup – outgroup effects.

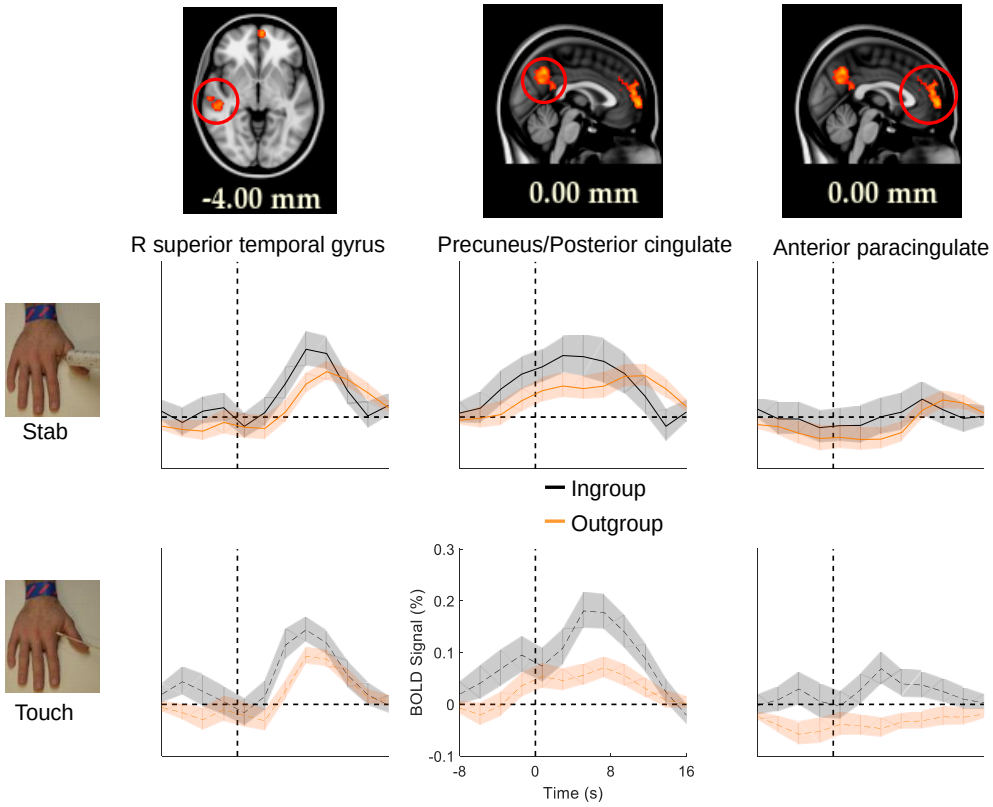

Figure 3.8 Whole Brain Ingroup Bias

The average time series of each of the 3 clusters of the ingroup – outgroup whole brain search. Time series units are in percent signal change from baseline. The time series were derived from the FIR GLM model fit used in **Figure 3.3**. The top row of traces show the time series for the ingroup stab (black) and outgroup stab (orange) trials. The bottom row of traces analogously shows the ingroup and outgroup differences for touch trials. Within these clusters, the ingroup > outgroup effect appears to be greater for touch trials than stab trials. (n = 67).

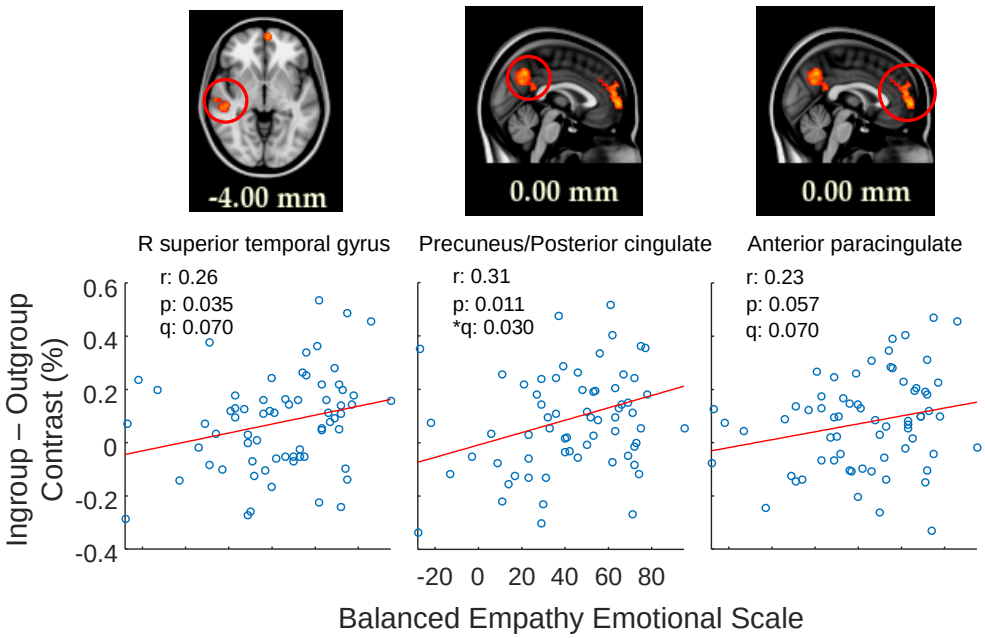

Figure 3.9 Whole Brain Correlations

The strength of the ingroup – outgroup activation difference in the 3 clusters found in the whole-brain search correlated positively with the empathic BEES score, with a significant correlation within the precuneus/posterior cingulate. Shown below each cluster is the scatter plot of the BEES score and the ingroup – outgroup contrast parameter estimate (averaged across stab and touch). Pearson correlation coefficients (r), p-values (p), and Holm-Bonferroni corrected p-values (q) are shown for each plot.

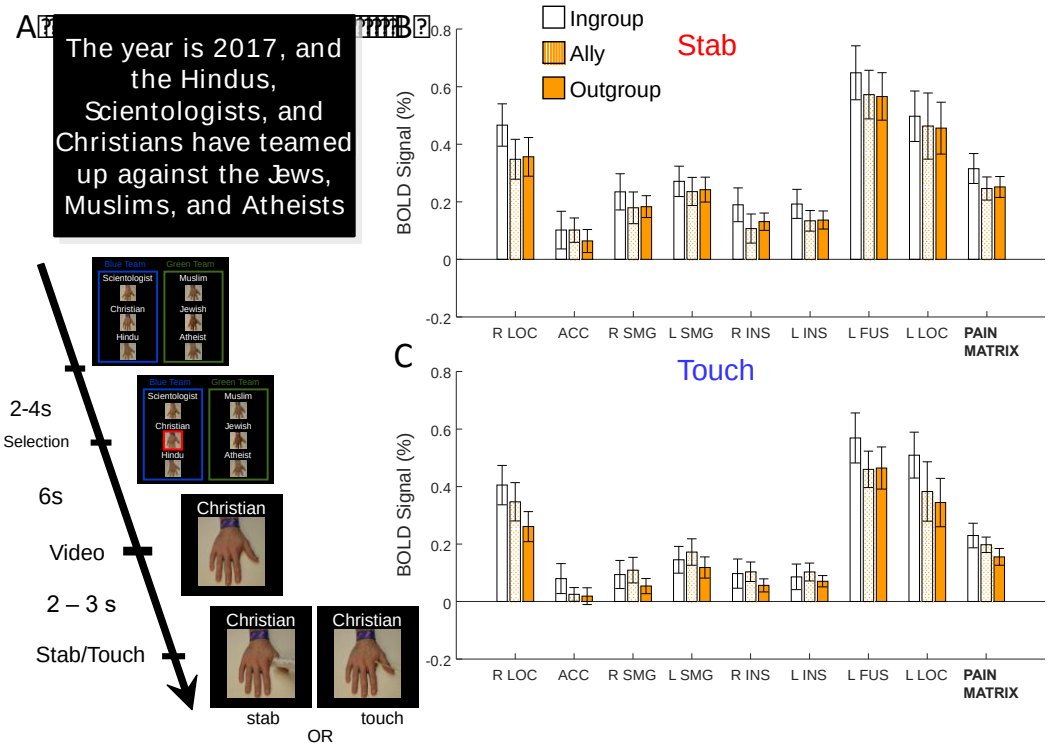

Figure 3.10 Empathy Network Allies

Manipulating allegiances does not robustly alter brain responses within the empathy network. **A**. Participants (n = 14) were told that two random religions had formed an allegiance (allies) with their own religion fighting against 3 other random religions (outgroup). Team membership was indicated at the start of each trial via both labels and colors. A random hand was selected and either painfully stabbed or non-painfully touched, as in the original experiment. Parameter estimates for each condition for each ROI within the empathy network are shown for both stab (**B**) and touch (**C**) trials. Ally parameter estimates were not significantly different from those of the outgroup (see **Figure 3.11**).

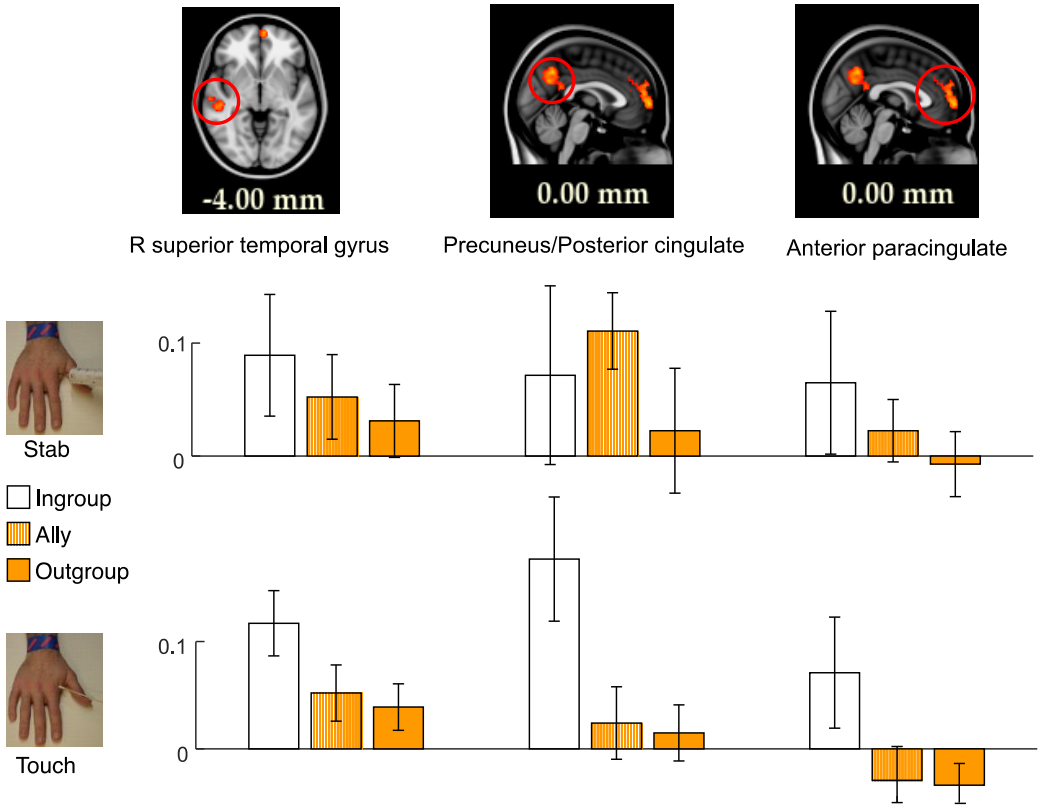

Figure 3.11 Whole Brain Allies

Manipulating allegiances does not robustly alter brain responses within brain regions that show ingroup – outgroup differences. Parameter estimates for each condition for each of the three ROIs are shown for both stab (top row) and touch (bottom) trials. Ally parameter estimates were not significantly different from those of the outgroup.

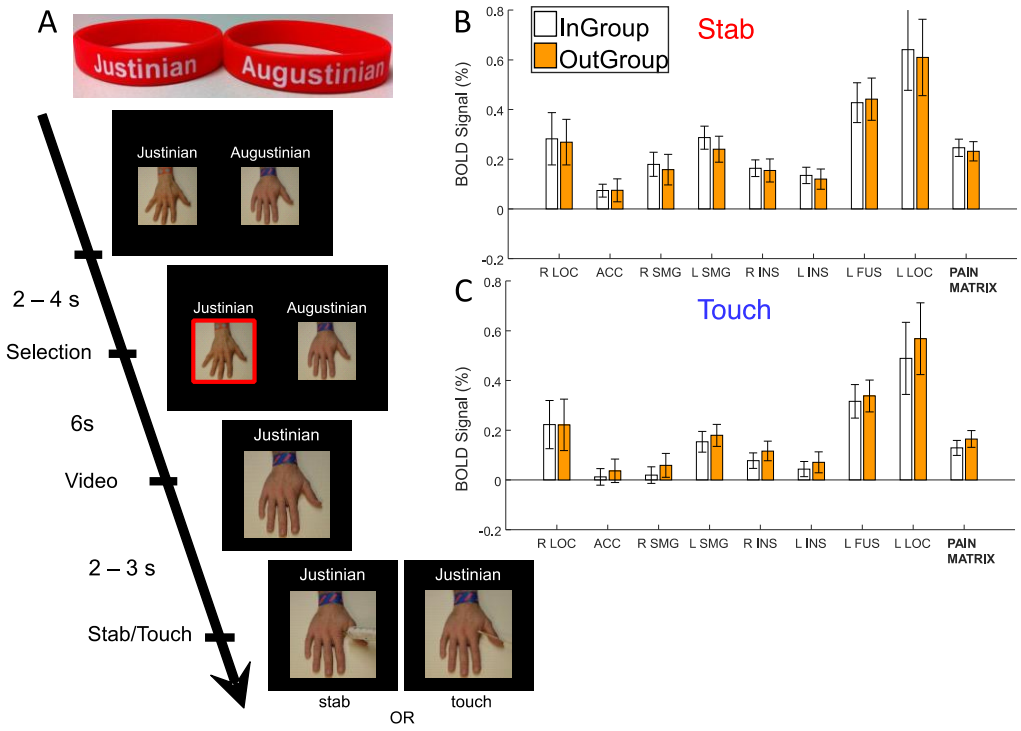

Figure 3.12 Arbitrary Group Assignment

Randomly assigning group membership does not invoke group allegiances within the empathy network. **A**. We devised an experiment where participants (n = 14) were participants were randomly assigned to one of two groups: Augustinian or Justinian. Participants were given bracelets to wear on their wrists during the scan. Two hands were labeled, one from each group, and a random hand was selected and either painfully stabbed or non-painfully touched, as in the original experiment. Parameter estimates for each condition for each ROI within the empathy network are shown for both stab (**B**) and touch (**C**) trials. Ally parameter estimates were not significantly different from those of the outgroup.

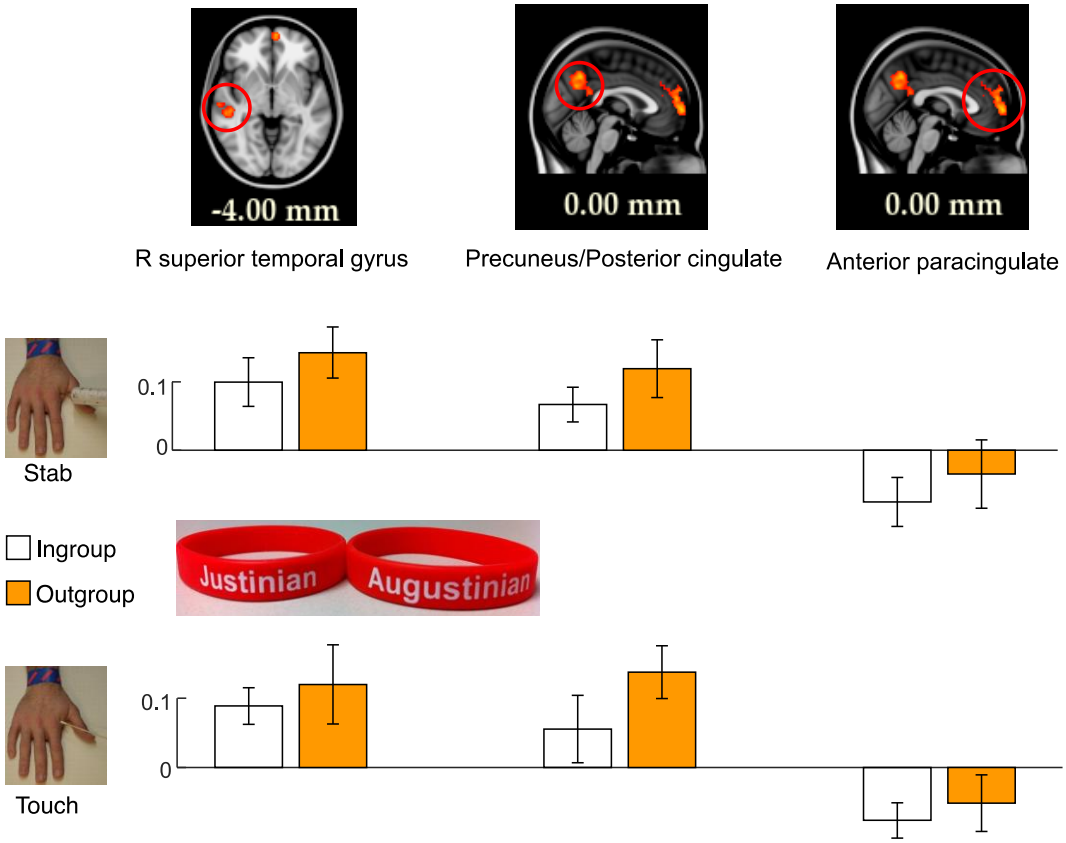

Figure 3.13 Arbitrary Group Assignment Whole Brain

Randomly assigning group membership does not invoke group allegiances within brain regions that show ingroup – outgroup differences in the original experiment. Parameter estimates for each condition for each of the three ROIs are shown for both stab (top row) and touch (bottom) trials. Ingroup parameter estimates were not significantly different from those of the outgroup.

Our results expand upon previous findings, demonstrating for the first time that a neural empathy bias is present in religious affiliations. The ingroup bias was elicited simply by changing the text label written above a hand, without any other group information. Further, the strength of the ingroup bias correlated with an individual's empathic rating, not their intrinsic religiosity or their religious conviction. That is, the more a person reports the ability to empathize with another, the stronger the ingroup bias. In addition, the ingroup bias was found to exist in many areas of the brain beyond the empathy network, including the mPFC and putamen, regions that are also active when confronted with images of hated people (Zeki and Romaya, 2008). Taken together, our study highlights that religious affiliation forms a deep-rooted alliance that cannot be easily manipulated or arbitrarily formed.

CHAPTER IV

HOW WE DECIDE

4.1 Introduction

Neuroimaging has long been used to examine the cascade of neural activity leading to human decision making. One approach is to directly contrast free decisions and cued (forced) decision. That is, how does brain activity differ when actively making a choice versus simply executing an instruction? Here, we designed an experiment to isolate and compare the neural signatures of both conditions.

Although the prefrontal cortex is hypothesized to play a unique role in free decision-making, the details remain unclear. Functional magnetic resonance imaging (fMRI) has previously shown areas in the medial prefrontal cortex, such as the rostral cingulate zone, to be more activated in free trials compared to forced trials (Demanet et al., 2013; Forstmann et al., 2006). Others have found the anterior insula and frontal poles to play a role in free decision making, with evidence suggesting that greater activity within these regions is required to overcome conflicting biases (Orr and Banich, 2014). In contrast, studies using magnetoencephalography (MEG) have failed altogether to find any differences in frontal brain regions in free vs. forced decision making (Garcia Dominguez et al., 2011; Kostelecki et al., 2012). Experimental evidence has not converged to localize the frontal circuitry involved in free decision making.

The use of two conventions in prior approaches may explain why experiments have failed to consistently localize brain activity. First, previous studies (Demanet et al., 2013; Forstmann et al., 2006; Frith et al., 1991; Garcia Dominguez et al., 2011; Hyder et al., 1997; Kostelecki et al., 2012; Orr and Banich, 2014; Thimm et al., 2012) have used a paradigm that restricted the timing of free decision-making. In those studies, the free and forced conditions were randomly interleaved, such that a participant could not know in advance whether to make a free decision or a forced decision (e.g., a button press in either hand). Specifically, a cue would instruct the participant either to make a free choice or follow a forced choice, and then the participant would have to respond accordingly. Under that experimental construct, participants were explicitly told precisely when to act freely, rather than making the decision on their own—thus calling into question what is implied by 'free'. In such circumstances, decision-making was compressed to a limited time just prior to execution of the decision. Although there are clear advantages to interleaving event types and controlling the timing of events (e.g., removing attentional effects, balancing trial types), such an experimental design fails to allow participants to engage in a more natural version of making a choice.

Second, several previous studies have modeled pre-decision activity, cue onset, decision onset, and decision execution—all combined into one single event. One study, for example, assumed a canonical double-gamma hemodynamic response function (HRF) to model all the events, from cue onset to task execution (Orr and Banich, 2014). With such a model, the blood oxygen level dependent (BOLD) effect for decision-making

cannot be adequately distinguished from task execution. Thus, this design prohibits analyses of how brain activity differs when freely selecting an action versus when being forced to select.

One recent experimental paradigm for free decision making overcomes those limitations (Bode et al., 2011; Soon et al., 2008; Soon et al., 2013). In this design, participants select the time of their decision. Participants are not instructed when to make the free decision, but instead are allowed to make and execute the decision at a time of their choosing. Second, the analysis uses finite impulse response (FIR) functions to model the BOLD effect from times ranging from 10 seconds before through 14 seconds after the decision execution. The FIR approach does not assume the shape of the activity in the general linear model (GLM), thus allowing the true shape of the hemodynamics to be fitted for each event type before the decision is executed. Using this paradigm, studies have found that patterns of brain activity in the frontal cortex up to 10 s prior to a freely-selected decision can partially predict the binary decision a participant will make. While the interpretation of these results is an area of active debate (e.g., whether the activity is truly below conscious awareness, (Miller and Schwarz, 2014) whether unbalanced transitions between binary decisions gives rise to above-chance prediction accuracies, (Allefeld et al., 2013; Lages et al., 2013) and whether the signal is due only to random fluctuations (Schurger et al., 2012)), their design allowed adequate engagement in and modeling of free decision making.

To address the previous limitations, we have developed an fMRI paradigm to hone in on the differences between freely selected and forced button presses. Specifically, participants experience two 15-minute experimental blocks. In the first block, they freely select both the timing (when) and the side (left or right) of a button press (free condition). To simplify the experiment, we do not ask participants to report the timing of their decision (as done previously (Soon et al., 2008)), a request which forces them to simultaneously perform two tasks: (1) decide when to press which button, and (2) remember the timing of their conscious decision to button press. That is, by removing the additional task of remembering and reporting the timing of the decision, we remove a cognitive burden from the participants, such that the measure of interest (i.e., binary decision making) is isolated. In our paradigm, participants are instructed to make decisions naturally as they come. Further, we removed the enforced inter-trial interval (ITI), such that participants can press whenever they felt the urge. In our second 15-minute block, participants are told which button to press (left or right), and when (forced condition). To balance the exact timing and sequence of decisions, we replay the identical sequence of presses that participants chose in the free condition. In this way, the two blocks provide and exact (but unremembered and undetected) match across free and forced conditions. Then, we perform event-related analyses on these two regimes of behavior.

Previous findings during free decision making seem to suggest that we would either observe an increase in BOLD activity in frontal regions (Demanet et al., 2013;

Forstmann et al., 2006; Orr and Banich, 2014) or no difference at all between free and forced conditions (Garcia Dominguez et al., 2011; Kostelecki et al., 2012; Soon et al., 2008). However, given that our experiment allowed participants to freely select the timing of their decisions (without additionally being asked to remember and report that timing), and that our FIR model allowed us to directly test for differences in brain activity between the conditions (agnostically in every voxel), our design and analysis methods can shed new insight on the how the brain reaches decisions.

4.2 Materials and Methods

4.2.1 Participants

We recruited 37 healthy participants (28.7 ± 7.0 years, 24 males, all right handed). All participants gave informed consent as approved by our IRB at the Baylor College of Medicine.

4.2.2 Imaging Acquisition Details

All participants were scanned on a Siemens 3T Trio Magnetom (Erlangen, Germany) scanner at the Baylor College of Medicine's Center for Advanced Magnetic Resonance Imaging (CAMRI). Scanner acquisition parameters for the structural T1 MPRAGE sequence were as follows: **voxel size**: 1x1x1 mm, **slices**: 192 transversal slices (1 mm thick with 0.5mm gap), **phase encoding direction**: R-L, **FOV**: 245 (A-P) x 215 (R-L) mm, **matrix size**: 256 (A-P) x 215 (R-L), **TR**: 1.2 s, **TE**: 2.66 ms, **echo spacing**: 6.5 ms, **flip angle**: 12°, **duration**: 4:30, **bandwidth**: 210Hz/Px. Scanner acquisition parameters

for the functional EPI scan were as follows: **voxel size**: 3.4x3.4x4.0 mm, **slices**: 37 transversal slices (4 mm thick with 0 mm gap), **phase encoding direction**: A-P, **FOV**: 220 (A-P) x 220 (R-L) mm, **matrix size**: 64 (A-P) x 64 (R-L), **TR**: 2.0 s, **TE**: 25 ms, **echo spacing**: 0.45 ms, **flip angle**: 90°, **bandwidth**: 2604 Hz/Px, **slice acquisition**: interleaved.

4.2.3 Experimental Task-Free Press

To investigate the neural underpinnings of freely-chosen binary motor decisions, participants were scanned for 15 minutes while freely choosing to press a button with either the left or right hand (**Figure 4.1**, left panel). Participants were specifically instructed as follows (modified from Soon et al. 2008):

"For the next 15 minutes your **only** task is to press either the left or right button whenever you feel the urge to press a button. The time and choice of a press is completely up to you, but it should be executed without hesitation once you've decided which button to press. Please do not make button selections based on any kind of pattern and avoid any form of preplanning. Try not to be too eager to initiate a button press after a previous button press. Do not maintain a constant state of readiness for the movement but instead stay as relaxed as possible until you feel the urge to press. When you press a button, an arrow pointing in the direction you pressed will appear."

4.2.4 Experimental Task-Forced Press

To further investigate the neural basis of forced decisions, we then scanned participants in the same functional EPI run in the *forced* condition for 15 minutes (**Figure 4.1**, right panel). In the forced condition, participants were instructed which button to press *and* when. Unbeknownst to the participant, the exact sequence of buttons and times of button presses each participant selected in the *free* condition served as the sequence of cued buttons and timings in forced condition. This allowed the frequency and timing of button presses to be matched exactly in both blocks. The specific instructions given to each participant were as follows:

"Now, an arrow pointing to the left or right will randomly flash on the screen. When it appears, press the button on the side where the arrow is pointing. For example, if the arrow points left, press the left button immediately."

All stimuli were presented using MATLAB (Mathworks, Natick, MA) and the Psychophysics Toolbox extensions.(Brainard, 1997; Pelli, 1997)

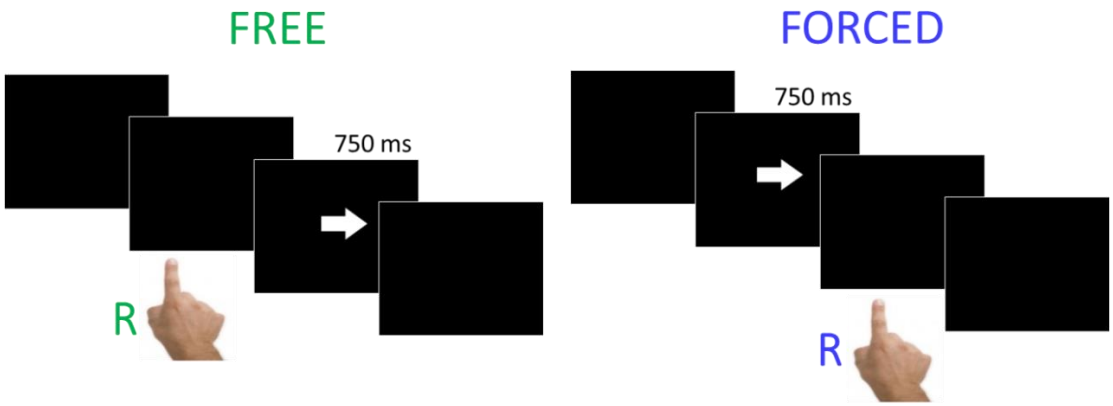

Figure 4.1 Experimental Design

In the *free* condition, participants freely chose to press the left or right button at the time of their choice. In the *forced* condition, participants were instructed which button to press when. The cue lasted for 750 ms, and participants were required to press the instructed button within 2000 ms of the cue onset. In the *forced* condition, unbeknownst to the participant, the exact sequence of commands matched their previous selections in the *free* condition. Both blocks were performed for 15 minutes each, in the same functional EPI run with the *free* condition always occurring first.

4.2.5 Behavioral Analysis

To ensure that each participant pressed the left and right buttons with minimal bias, we computed a lateralization index (after Soon et al., 2008). Specifically, the lateralization index (*I*) was computed as:

$$I = \frac{L - R}{L + R} \qquad (1)$$

A positive index indicates a bias towards left button presses, whereas a negative index indicates a right button press bias. Any participant with a lateralization index greater than 0.3 in either direction was discarded from further analysis.

4.2.6 fMRI Data Pre-Processing

All fMRI data were analyzed using the software package FSL 5.0.5 (FMRIB, Oxford, UK)(Jenkinson et al., 2012; Smith et al., 2004; Woolrich et al., 2009) and MATLAB (Mathworks, Natick, MA). Pre-processing was carried out using FSL FEAT. Pre-processing parameters included: motion correction (*mcflirt* (Jenkinson et al., 2002)), linear slice timing correction, 6 mm FWHM spatial smoothing, 0.02 Hz high pass filtering, brain extraction (*bet*(Smith, 2002)), and time-series pre-whitening. The first 2 volumes of the functional run for each participant were discarded to allow the scanner to reach steady state. Motion and intensity outliers were computed using *fsl_motion_outliers* and added as regressors of no interest to the GLM model. In addition, any participant with instantaneous absolute motion > 3 mm was rejected from further analysis. Functional image registration to the high resolution T1 anatomical image was carried out using linear boundary based registration (FSL *flirt (bbr)*(Jenkinson et al., 2002; Jenkinson and Smith, 2001)). Structural image registration to the MNI152 2 mm isotropic template brain was carried out using non-linear warping (FSL *fnirt*). All first level analyses were carried out in the original function space, and then the transformation matrices were combined to transform contrast and variance parameter estimates from functional space to the MNI152 2 mm isotropic template brain.

4.2.7 fMRI First Level GLM Analysis

fMRI first-level general linear model (GLM) analysis was also carried out using FSL *FEAT*. The hemodynamic response of interest was the 10 s preceding the button press. Because the shape of the hemodynamic response function (HRF) prior to button press was unknown, we used 13 finite impulse response (FIR) functions to model activity from 10 s prior to button press to 14 s after button press, just as in Soon et al. 2008. This set of FIR functions was used to model each button press type (Free L and R, and Forced L and R), resulting in 52 regressors of interest. In addition, the same set of FIR functions were used to model any incorrect button presses in the *forced* condition, as well as the instruction blocks at the start of the experiment and the time in-between the *free* and *forced* conditions blocks. These were treated as regressors of no interest.

4.2.8 fMRI Group Analysis

We compared how the HRF differed between free and forced conditions in the time preceding the button press. To this end, we computed the area under the curve (AUC) from -10 s to 0 s for every gray matter voxel (masked with MNI gray matter probability atlas, thresholded at minimum of 25%) for both free and forced conditions. Because the distribution of the AUCs was unknown and possibly not Gaussian, we used non-parametric permutation methods via FSL's *randomise*.(Nichols and Holmes, 2002) We used one-sample, one-way tests for both directions (*free* AUC – *forced* AUC and the inverse). We used FSL *randomise* threshold free cluster enhancement (TFCE) and controlled the family-wise error rate at $p < 0.05$. All contrasts were performed using

10,000 permutations to build a robust null distribution. We then calculated percent signal change for each FIR within any regions that showed differences between free and forced conditions (FSL *featquery*, weighted average on t-statistic value of significant ROIs). Finally, the change in the BOLD signal from -10 to +14 s was computed from the ROIs.

4.3 Results

4.3.1 Behavioral Results

The mean lateralization index for all participants was -0.052 ± 0.117 (see **Figure 4.2** for raster plots of all button presses for each participant). Only one participant was discarded because of a lateralization index greater than|0.3|. The mean time between button presses across all remaining participants was 22.0 ± 20.0 s. One participant pressed buttons much more rapidly than all other participants. We did not anticipate this given the instructions, and thus did not set any a priori thresholds for inclusion/exclusion. We posthoc decided to remove any participants pressing with a mean interpress interval less than 4 s, as this led to many accumulated errors in the *forced* condition. As a result, one additional participant was removed, who pressed on average every 3.85 s. Thus, from the 37 participants recruited, 2 were rejected due to behavioral performance.

4.3.2 fMRI Results

Two additional participants had head movement greater than 3 mm and were discarded from further analysis. In addition, we were unable to achieve successful alignment of the

functional EPI run to the structural T1 volume for one participant, and this participant was also discarded from analysis.

The remaining 32 participants' data were run in the group AUC analysis. The *forced* > *free* contrast yielded significant ROIs (**Figure 4.2A**, FWE corrected, $p < 0.05$). The bilateral ventrolateral prefrontal cortex (VLPFC), thalamus, and anterior insula all had greater areas under the curve from -10 s to button press (0 s) in the *forced* condition compared to the *free* condition. The FIR parameter estimates were averaged over all participants from within all significant voxels in this contrast, with a spatially weighted average on the thresholded t-statistic. The curves reveal significantly higher AUC for forced compared to free. The difference in both AUC analyses was greater for the right button presses (**Figure 4.3B**). Further, the general difference in the shapes of the curves between *free* and *forced* conditions was seen in specific ROIs of the significant voxels found (**Figure 4.4**). There were no differences prior to button press found in the motor and premotor areas via the AUC analysis and via visual inspection of the BOLD traces (**Figure 4.4**)

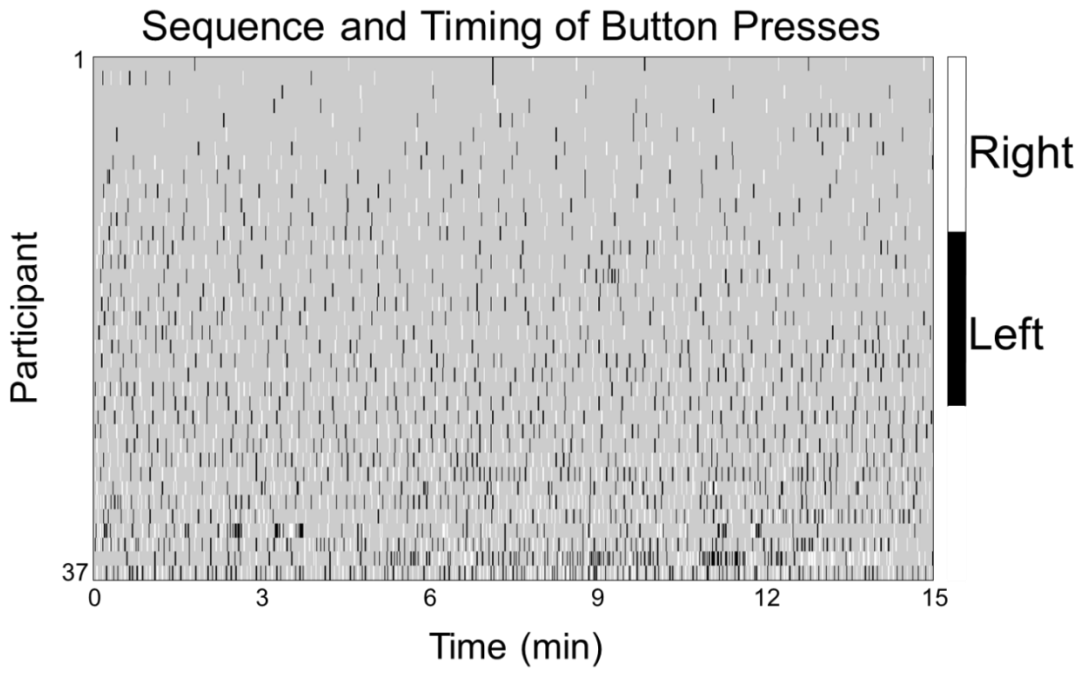

Figure 4.2 Sequence and Timing of Button Presses

The raster plot shows the variability in the timing and selection of button presses for each of the 37 participants during Free Press. Data are sorted from top to bottom in ascending order by total number of button presses.

A

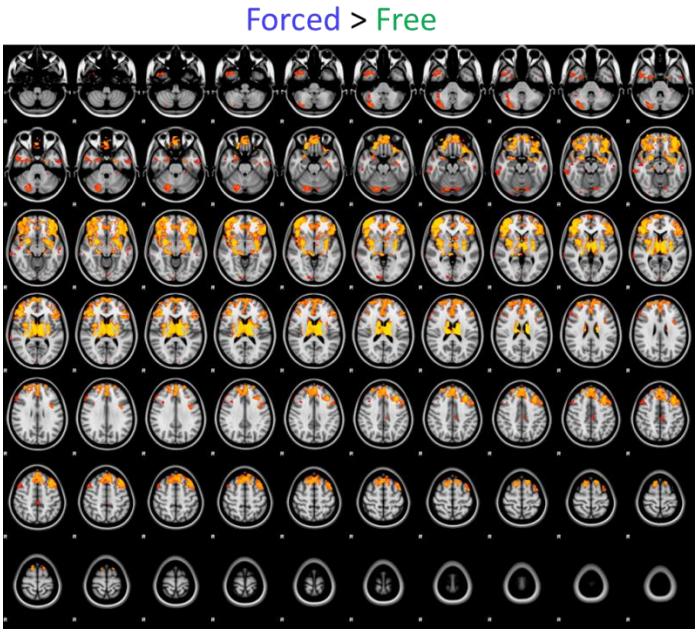

B

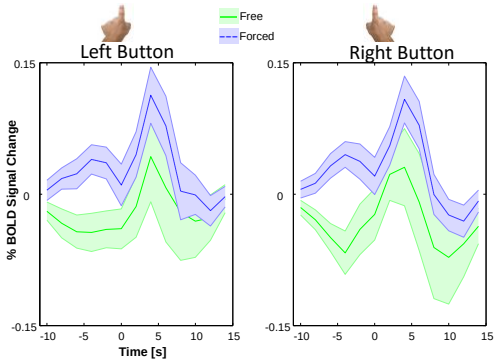

Figure 4.3 Forced > Free

Brain regions showing greater area under the curve (AUC) before the button press in the forced condition compared to the free condition. (A) Horizontal slices revealing the voxels showing significantly greater AUC in forced than free. Data are collapsed across left and right button presses (see **Table 4.1** for peak cluster coordinates). AUC differences were computed by non-parametric permutations testing and corrected with FWE ($p < 0.05$) with threshold-free cluster enhancement (TFCE). Free > Forced did not yield any significant ROIs. (B) The hemodynamic responses are shown pre- and post-button presses for *free* (green) and *forced* (blue) conditions. The traces are drawn from the weighted spatial average of all voxels that met significance.

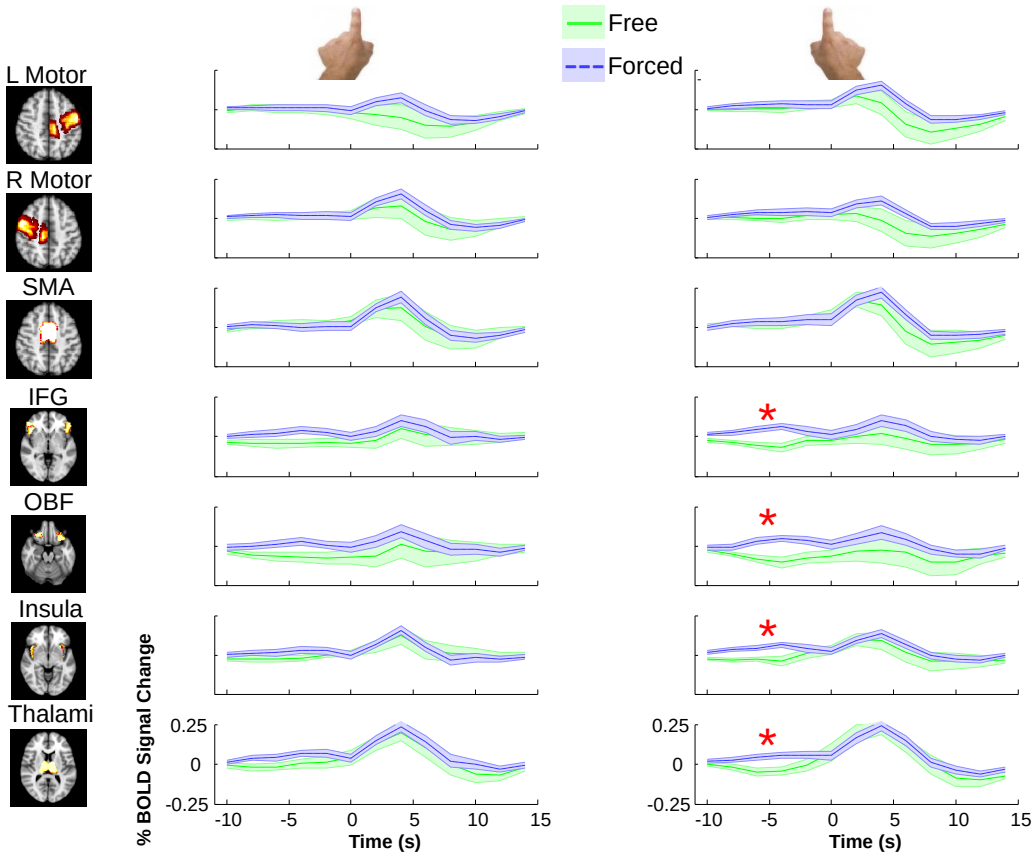

Figure 4.4 Forced > Free ROIs

BOLD traces reveal diverging hemodynamic activity in Free Press vs. Forced Press prior to button press. The first column shows the brain regions (ROIs) the BOLD traces in the next two columns are drawn from. All ROIs were first extracted from the Harvard-Oxford Cortical (or Subcortical) Structural Probability Atlases. The probability maps of the first three regions (Left Motor Cortex, Right Motor Cortex, and Supplemental Motor Area) were used to create spatially weighted average BOLD traces from within the ROIs. The latter four regions (Inferior Frontal Gyrus, Orbitofrontal Gyrus, Insula, and Thalami) were first used to select the regions that overlapped with the significance of Free Press > Force Press (Figured 2). Then, the thresholded p-values from within each overlapping region was used to generate the weighted spatially weighted averaged BOLD traces. The BOLD traces are drawn separately for Free Press (Green) and Forced Press (Blue), with the envelopes representing S.E.M. Columns are also separated by left button (middle column) and right button (right column) presses. The asterisks in red indicates that the right hand button presses showed significant differences in AUC prior to button press in Free Press vs. Forced Press.

Table 4.1 Forced > Free Coordinates

MNI Coordinates of cluster peaks for forced > free AUC contrasts. Also reported are the mean and max z-statistic for the contrast, as well as the number of voxels in each cluster

Cluster Index	x	Y	Z	MEAN Z STAT	MAX Z STAT	VOXELS
8	**22**	**77**	**38**	**3.06**	**6.14**	**25114**
7	**25**	**37**	**16**	**3.29**	**4.64**	**1026**
6	**9**	**47**	**29**	**2.96**	**5.27**	**271**
5	**71**	**59**	**21**	**3.25**	**3.67**	**127**
4	**45**	**16**	**39**	**3.32**	**3.98**	**121**
3	**74**	**54**	**31**	**3.29**	**3.79**	**112**
2	**47**	**51**	**58**	**3.76**	**4.3**	**92**
1	**57**	**44**	**21**	**4.41**	**4.61**	**19**

4.4 Discussion

We examined the neural differences between freely made and forced (cued) binary decisions. Our study for the first time allowed participants to select both the time and choice of their decision, without any confounding cognitive tasks (e.g., Libet Clock, Stroop task, inter-trial intervals). Further, the *forced* condition was intentionally balanced so that the exact sequence of button presses participants selected in the *free* condition was replayed as the cues in the *force* condition. Participants were not told of this replay, and no participants reported detecting of the replay on post-scan interviews when participants were debriefed.

Our results show that the BOLD signal function from -10 s to 0 s of execution of the decision differ significantly in the *free* and *forced* conditions. In particular, the area under the curve is significantly greater in the *forced* condition in bilateral frontopolar cortices, thalami, and anterior insula. When analyzing left and right button presses separately, these regions are only significant during right button presses (not shown). However, when collapsing across left and right button presses, the difference in the area under the curves was more pronounced. There was a general bias towards right button presses (mean laterality index across all participants of -0.052), and all of participants were right handed. Perhaps the bias in lateralization index and the effect of the dominant hand gave rise to stronger separation of the curves with right presses.

Previous evidence showed the AUC in the frontopolar cortices under *free* condition would be greater than *forced* condition (Orr and Banich, 2014); however, we observed exactly the opposite. Orr and Banich (2014) showed that freely made decisions in their voluntary task switching paradigm resulted in stronger activation within the frontopolar and anterior insular regions as compared to forced decisions. However, their analysis did not separate cues from decision making from task execution. By presenting the conditions in blocks rather than in interleaved trials, we were able to make inferences on the entire BOLD effect of freely making decisions. Thus, our results show that these frontal regions are more activated when forced to make decisions during the time up to 10 s prior to decision execution.

Of additional interest is the greater activation of the thalamus and basal ganglia in the times prior to button press in the *forced* condition. To our knowledge, neuroimaging studies have not reported the involvement of the thalamus in comparing free and forced decision making(Demanet et al., 2013; Forstmann et al., 2006; Garcia Dominguez et al., 2011; Kostelecki et al., 2012; Orr and Banich, 2014; Thimm et al., 2012). Previous studies interleaved trials, removing the arousal component of decision making in their studies, which may have also removed thalamic involvement under free conditions as participants were required to attend to stimuli to know when to make their decisions. But thalamic involvement may be involved with more than just attention or arousal. Thalamic activation is greater in moral decision making when directly contrasted with neutral decision making (Sommer et al., 2010). Further, during a Stroop task, cognitive control is engaged by a network involving the prefrontal cortex, striatum, and thalamus (similar to our AUC analysis in *forced* > *free*), which must hyper-activate in chronic cocaine abusers to gain similar task performance as controls (Mayer et al., 2013). Our results may elucidate further the involvement of the cognitive control network and its temporal response that leads to decision making.

The BOLD signal revealed an interesting difference between the two block types. In the *forced* condition, starting from -10 s, the percent signal change increased from baseline and peaks at -4 s. This may represent increased cognitive inhibition as participants suppressed decision making processes. Then, at -4 s, the signal began to drop back down

to baseline by 0 s. This could represent relaxing of the cognitive inhibition as the participant readies him/herself for an upcoming cue. However, since the time of the cue remains unknown in each trial for each participant, this result and potential interpretation is a bit surprising. Further, the opposite is observed in Free Press: from -10 s to -4 s, the signal decreases and then increases from -4 s to 0 s. That is, cognitive inhibition decreases as the participant searches for which button to select; then, as the participant begins finalizing the decision choice, the cognitive inhibition is increased until the time of execution. This interpretation could provide an increased understanding how people make decisions when freely deciding compared to when being explicitly instructed.

We additionally performed an AUC analysis for the time after decision execution [+2 s +14 s]. We employed the same non-parametric permutations testing approach as with the AUC prior to button press. We did not find any significant regions when looking at right and left button presses separately or when collapsing across button press type. Using the AUC method for the time after the button press, is confounded by the undershoot of the HRF. From the BOLD signals plotted in **Figure 4.2**, it is clear that the HRF peaks higher after *forced* presses. Because participants were required to press the button within 2000 ms of onset of the cue, this difference in amplitude could be simply due to the fact that participants may have pressed the buttons more vigorously and rapidly during *the* forced condition to stay within the allotted time.

While the AUC analysis clearly shows separation of the BOLD signal for our identified ROIs, this analysis does not fully address the shape of the BOLD signal curves. To compare the conditional differences in the BOLD response modeled with multiple basis functions, we computed a 3-way mixed effects ANOVA (AFNI's(Cox, 1996) *3dANOVA3 –type 4*) with fixed effects as (1) condition (*free* and *forced*, 2 levels) and (2) FIR basis functions (-10 s to 0 s, 6 total levels for before button press) with (3) the participants modeled as a random effect (n = 32). We found very similar significant ROIs using this approach as we found with using AUC and FSL's non-parametric permutations testing (data not shown).

One limitation of our study is the inability to perform a mixed design in which events and blocks could be modeled simultaneously. We used 15 minute long blocks for *free* and *forced* conditions in part to allow natural decisions and also so that the exact sequence and timing of button presses could be matched without the participants realizing the design. However, this did not permit us to model differences at the block level because such long blocks are below the frequency of the high pass filter (< 2 Hz). Modeling the blocks without the highpass filter would not remove low frequency oscillations due to scanner drift.

Another limitation in our study is that participants were not making decisions completely independently from trial to trial. Our data, like Soon et al. (2008), deviates significantly from a binomial process (e.g., coin flip). Our participants were more likely to switch

(i.e., higher transition probabilities) from one button press to the other than to repeat the button press. Whether this non-random behavior influences deciphering brain activity involved in free decision making is being actively questioned.(Allefeld et al., 2013; Lages et al., 2013) The implication could be that our participants may have been exerting cognitive efforts during *free* condition in an attempt to achieve randomness. Even though participants did not achieve 'true randomness', this confound could play a role in the differences between *free* and *forced* conditions. However, our study matched the exact sequence in per participant basis such that the laterality is matched identically in both blocks, which helps to control this confound behaviorally.

Our study examined the cognitive processes giving rise to binary decisions in two different blocks: when freely making decisions and when forced to execute an instruction. By matching the exact sequence and timing across blocks, we were able to separate the temporal nature of the BOLD signal before a decision was made and executed in each block. Our results expose a network of bilateral prefrontal areas, basal ganglia, and thalamic regions that have increased activity in the forced condition compared to free condition. Further, the timing of the BOLD signal before the button press may indicate that cognitive control can increase (or decrease) to prevent (or allow) decision making prior to execution. Our findings shed new light on the cognitive processes giving rise to freely made decisions.

CHAPTER V

THE ADDICTED BRAIN[*]

5.1 Characterizing White Matter Changes in Cigarette Smokers via Diffusion Tensor Imaging

5.1.1 Introduction

Although the effects of cigarette smoking have been well studied in several organ systems, the effects of chronic tobacco use on brain structures have not been well characterized. Particularly, DTI has yielded inconsistent findings on white matter structural changes caused by nicotine use. Some data indicate chronic cigarette smoking increases FA in several white matter regions, including bilateral fronto-parietal regions (Liao et al., 2011), portions of the corpus callosum (Hudkins et al., 2012; Paul et al., 2008), and the right prefrontal lobe (Hudkins et al., 2012). On the other hand, other findings suggest that smoking decreases FA within the corpus callosum (Lin et al., 2013; Umene-Nakano et al., 2014) and left prefrontal cortex (Zhang et al., 2011). Several confounds may give rise to these inconsistent DTI findings including variable sample sizes, dissimilar inclusion criteria for smokers and matched controls, differing image acquisition and registration protocols, and varying statistical approaches.

---

[*] Reprinted with permission from "Characterizing White Matter Changes in Cigarette Smokers via Diffusion Tensor Imaging" by Savjani RR, Velasquez KM, Thompson-Lake DG, Baldwin PR, Eagleman DM, De La Garza R 2nd, Salas R, 2014. *Drug and Alcohol Dependence*. 145, 134-142, Copyright 2014 by Elsevier Inc.

[*] Reprinted with permission from "The role of neuroscience in drug policy: Promises and prospects" by Ormachea PA, Savjani RR, De La Garza R, Eagleman DM, 2016. *The Journal of Science Law*. 2, 1-15, Copyright 2016 by The Journal of Science Law.

Nonetheless, human imaging evidence does suggest the timing and volume of nicotine exposure exerts consistent effects on white matter characteristics. Over the long term, the total amount of nicotine consumed (or the severity of dependence) correlates negatively with FA in several brain regions (Hudkins et al., 2012; Liao et al., 2011; Lin et al., 2013; Paul et al., 2008; Umene-Nakano et al., 2014; Zhang et al., 2011). For example, Lin et al. 2013 found that the more years participants smoked, the lower the FA. Further, some studies have attempted to explain the variance in previous findings by a temporal model: nicotine exposure during adolescence increases FA values initially, but then chronic smoking throughout adulthood decreases FA (Hudkins et al., 2012; Paul et al., 2008). Over the short term, acute nicotine exposure via a nicotine patch can increase FA within the corpus callosum, but only in participants with a low level of cotinine (Kochunov et al., 2013), a biomarker of nicotine exposure. These studies highlight that it is important to study a wide range of participants with varying smoking histories as well as controlling for acute nicotine exposures.

In the present study, we examined the effects of nicotine on white matter characteristics using four novel approaches. (1) To improve detection of white matter brain regions implicated, we acquired images with a greater number of diffusion gradient directions (71) than has been previously used in an attempt to more accurately fit the tensors in the DTI model. (2) We expanded whole-brain TBSS analyses to include not only FA measures as have been used previously (Lin et al., 2013; Umene-Nakano et al., 2014; Zhang et al., 2011) but also all standard tensor metrics as well as a crossing fiber model

(Jbabdi et al., 2010) to better agnostically characterize the white matter alterations that arise from smoking. (3) We used probabilistic tractography to define participant specific tracts and compared DTI metrics within these tracts between smokers and healthy controls. (4) Finally, in a cohort of participants, we scanned smokers under two separate conditions: after smoking *as usual* and after abstinence (24 hours). Although DTI metrics have been perceived to measure anatomically stable chronic characteristics, recent studies have shown acute changes after different manipulations (Hofstetter et al., 2013). DTI metrics have also been shown to change acutely as a result of nicotine administration via patch (Kochunov et al., 2013), but no DTI study to date has compared the same smokers while abstinent (asked to not smoke) and sated (allowed to smoke normally). Collectively, these approaches allowed us to further characterize the white matter changes in cigarette smokers.

5.1.2 Materials and Methods

5.1.2.1 Participants

This study was approved by the Baylor College of Medicine institutional review board and participants were compensated for their time. 32 non-smokers and 30 cigarette smokers participated in the study. Participants were recruited from the greater Houston metropolitan area via advertisements. During phone screening callers who did not identify as treatment seeking, and smoked ≥ 10 cigarettes a day for at least one year were eligible for in-person screening. Non-smokers could not have smoked ≥ 5 cigarettes in their lifetime. Smokers were participant to an in-person screening interview and

exclusion criteria for smokers included: other non-tobacco substance dependence, diagnosis of any AXIS I disorder according to the Mini-International Neuropsychiatric Interview, and a positive illicit drug urine toxicology at time of screening. Smokers were also required to give an exhaled breath carbon monoxide (CO) of ≥ 10 ppm on the day of smoking as usual, and ≤ 5ppm on the day of abstinence. CO levels were measured using a CO meter (Micro+ Smokerlyzer Monitor, Bedfont Scientific, Kent, England). Thirty cigarette smokers took part in the DTI scan when abstinent; of these, 15 participants returned to perform another identical DTI scan in which they smoked as usual prior to the scan.

To assess the level of nicotine dependence of smokers, we used the Fagerstorm Test for Nicotine Dependence (FTND), which consists of 6 questions with a mixture of multiple choice questions (scored 0 to 3) and yes/no questions (Scored 0 or 1). The total score range is from 0-10, with 0 being lowest dependence and 10 being highest. The FTND was administered when smoking as usual.

5.1.2.2 Imaging Acquisition Details

All participants were scanned on a Siemens 3T Trio Magnetom scanner at the Baylor College of Medicine's Center for Advanced Magnetic Resonance Imaging (CAMRI). Scanner acquisition parameters for the DTI sequence were as follows: **voxel size**: 2x2x2 mm, **slices**: 61 transversal slices (2 mm thick with no gap), **phase encoding direction**: A-P, **FOV**: 256 x 256 mm, **TR**: 9.4 s, **TE**: 91 ms, **matrix size**: 128 x 128, **echo spacing**:

73 ms, **diffusion directions**: 71 unique directions at b_0 = 1000 s/mm^2 with 8 repetitions at b_0 = 0 s/mm^2, **duration**: 12:32 m. Due to FOV and slice selection, the cerebellum and posterior occipital lobes were not fully captured for every participant.

5.1.2.3 Tract-based Spatial Statistics (TBSS)

To perform an unbiased, voxel-by-voxel analysis to identify WM regions with significantly different FA between non-smokers and smokers, we performed tract-based spatial statistics (TBSS) via FMRIB Software Library [FSL v5.0.4] (Jenkinson et al., 2012; Smith et al., 2006). The Neuroimaging in Python Interfaces and Pipelines (Nipype) (Gorgolewski et al., 2011) was used to carry out the analyses and facilitate preprocessing. Raw diffusion weighted images (DWI) images were preprocessed first by correcting for motion artifacts by linearly registering each DWI volume to the first b_0 = 0 volume using FSL FLIRT (Jenkinson et al., 2002; Jenkinson and Smith, 2001) with 6 degrees of freedom (DOF) and appropriately rotating the b-vectors(Leemans and Jones, 2009). Second, the images were corrected for eddy current distortions using FSL's FMRIB's Diffusion Toolbox FDT (Behrens et al., 2003) *eddy_correct*. Next, the 8 b_0=0 volumes were averaged and then brain extracted (FSL *bet* (Smith, 2002)) to generate a brain mask. Diffusion tensors were fitted to the brain extracted DWI using FSL FDT (Behrens et al., 2003) *dtifit*. After preprocessing, all participants' FA data were aligned into a common space using the nonlinear registration tool FNIRT (Andersson, 2007a, b), which uses a b-spline representation of the registration warp field (Rueckert et al., 1999). Next, the mean FA image was created and thinned to create a mean FA skeleton which

represents the centers of all tracts common to the group. Each participant's aligned FA data was then projected onto this skeleton and the resulting data fed into voxel-wise cross-participant statistics. In addition to FA, TBSS was performed independently on axial diffusivity ($Da = \lambda_1$), radial diffusivity ($Dr = [\lambda_2 + \lambda_3]/2$), and mean diffusivity ($MD = [\lambda_1 + \lambda_2 + \lambda_3]/3$).

Between group comparisons were performed using permutations testing methods via FSL's *randomize* (Bullmore et al., 1999). All contrasts were run with 10,000 permutations and FSL's threshold-free cluster enhancement (TFCE) for clustering. Multiple-comparisons were corrected by controlling family-wise error (FWE), with significance thresholded at $p < 0.05$. Ethnicity, education, gender, and age were demeaned and entered as covariates in the GLM to isolate the effects of tobacco use. Furthermore, to explore how DTI measures correlated with these covariates directly, we also ran regressions with the individual covariates. Any regressions yielding significant voxels were then explored further to determine the effects of the covariates on their interaction with smoking status.

In addition to performing TBSS on traditional tensor measures (FA, Da, Dr, and MD), we also performed TBSS on crossing fiber measures. Tensor measures such as FA ignore information about fiber bundles and their orientations at each voxel. Recently, TBSS models have been extended to incorporate crossing fibers to measure relative structural integrity of multiple fibers along their principal direction at each voxel (Jbabdi

et al., 2010). We used Bayesian sampling techniques (FSL *bedpostx*, default parameters) to build up the distribution of diffusion parameters on the basis of Markov Chain Monte Carlo (MCMC) sampling (Behrens et al., 2007). To compare fibers consistently across participants, we used FSL *tbss_x* to align two fiber bundles at each voxel. We then proceeded to perform spatial statistics on each of the two fiber bundles, adjusting for covariates identical to the approach with tensor measures discussed above.

We also examined the impact of smoking dependence severity (as measured by FTND) on the TBSS. First, we used the FTND score as a regressor in the TBSS model described above for smokers to find voxels that correlate with FTND. Second, we ran a separate TBSS analysis on smokers with FTND > 3 to exclude participants with lesser nicotine dependence. All descriptive statistics were completed using MATLAB™. For all statistics with FTND and DTI, ethnicity, education, gender, and age were adjusted as regressors of no interest, as in all TBSS analyses.

5.1.2.4 Probabilistic Tractography

While TBSS performs agnostic voxel-wise comparisons on major WM tracts common to all participants, we also looked at particular tracts hypothesized to be implicated in nicotine dependent individuals. Specifically, we examined participant-specific tracts that connected to the frontal cortex from nucleus accumbens, habenula, and motor cortex.

To generate the seed masks, we first used the Harvard-Oxford Cortical and Sub-cortical Structural probability atlases to generate seed masks for the nucleus accumbens (thresholded at > 25%) and precentral gyrus (thresholded at > 75%). These thresholds

were selected to best isolate the two structures, as well as to use similar number of voxels in each seed (~1000 voxels). For the habenula, we isolated the center voxel in each participant's T1 anatomical image, drew a sphere with a radius of 3 mm around the voxel, and used boundary based linear registration (FSL *epi_reg*) to map the habenula ROIs into DWI space. For the target ROI, we generated a frontal cortex mask by including any coronal slices anterior to the temporal poles in MNI space. Each seed and target ROI was created for both hemispheres.

We then used probabilistic tractography (FSL *probtrackx2*) to find the WM tracts connecting each of the 6 seeds to the ipsilateral frontal cortex target ROI. We used default parameters for *probtrackx2* (5000 sample pathways, 0.2 curvature threshold, 2000 termination steps, 0.5 mm step length) and also incorporated 2 crossing fibers (*bedpostx*). Tractography was performed in participant's native diffusion space by back-projecting via inverting the non-linear transformations from diffusion to MNI space created by TBSS (FSL *tbss_deproject*). For each participant, each of the 6 generated tracts were first confined to white matter using the individual participant's white matter mask (generated by segmentation by FSL *fast*) and then thresholded to probabilities greater than 0.5% of the probabilistic index of connectivity (i.e., 0.005 * fdt_paths / waytotal). For each participant and tract, we then computed the spatially averaged FA within the thresholded tract and ran group statistics using a GLM model analogous to the model we used in TBSS. Thus, we could compare differences in FA within our hypothesized tracts between controls, abstinent smokers, and sated smokers.

5.1.3 Results

5.1.3.1 Participants

Demographics for age, gender, race and smoking characteristics are shown in **Table 5.1**. Although we invited all 30 smokers to return for the second scan in which they smoked as usual prior to the scan, only 15 returned for the second scan. Further, the FTND of the 15 participants who did return, had significantly greater FTND than the 15 participants who did not return (two-sample, two-way t-test: $p = 0.0020$, t-stat = 3.4099). The other smoking metrics (years of smoking, cigs/day, and exhaled CO) did not significantly differ between the two groups.

Table 5.1 Demographics

Demographic Information and Smoking Severity Measures

	Controls Mean ± SD	**Smokers Mean ± SD**	
Education (years)	15.44 ± 2.6	13.47 ± 1.73 ***	
Gender	14 M: 18 F	17 M; 13 F	
Race	15 Caucasian 10 African Am 1 Asian Am 6 Hispanic	8 Caucasian 14 African American 0 Asian American 8 Hispanic	
Age (years)	35.97 ± 13.75	39.03 ± 9.90	
Yrs of smoking	N/A	21.15 ± 9.52 (obtained from 20 participants)	
FTND	N/A	5.37 ± 2.57	
Cigarettes/Day	N/A	15.23 ± 7.68	
Exhaled CO (ppm)	N/A	15.17 ± 7.52 (smoking as usual)	3.21 ± 1.72 (abstinent 24 h)
Time since last cigarette (hrs)	N/A	2.33 ± 3.51 (smoking as usual)	26.92 ± 7.12 (abstinent 24 h)

5.1.3.2 TBSS

5.1.3.2.1 Covariate Interactions

Significant correlations were found between FA and two demographic covariates: gender and age. When gender was used as a covariate, females had several regions with significantly greater FA than males, and age negatively correlated with FA for several voxels throughout the brain ($p < 0.05$). Importantly, to test if gender and/or age had different impacts on smoking status, we regressed the age and gender covariates separately for smokers and non-smokers. No significant interactions were found between the two groups for either age or gender, indicating that the impact of gender and age are not significantly different for smokers and non-smokers.

5.1.3.2.2 FTND

When FTND was regressed against FA in smokers, no voxels were found that had significant positive or negative correlation with FTND ($p > 0.25$, t-test, FWE corrected).

5.1.3.2.3 Controls vs Smokers (abstinent 24 h)

Smokers (abstinent 24 h) had significantly decreased FA ($p < 0.05$, t-test, FWE corrected) compared to controls in several brain regions (**Figure 5.1**). This reduction in FA in abstinent smokers was seen in the left and right splenium of the corpus callosum, with a larger region on the left side that extended more inferiorly. Reductions in FA were also found in smokers with bilateral anterior limb of the internal capsule. To better quantify the effect size of the reduction, we computed the mean of four DTI metrics (FA,

MD, Dr, Da) within all significantly different voxels found by TBSS on FA (**Figure 5.2A**). Within these regions, FA and Da decreased, while Dr and MD increased in smokers compared to controls. The mean FA within these regions in smokers correlated negatively with the number of years of regular smoking ($r^2 = 0.27$, $p < 0.05$). We also observed a positive trend in correlation of Dr and the number of years of regular smoking (**Figure 5.2B**) that approached significance ($r^2 = 0.18$, $p = 0.054$). These correlations were run on data from 20 out of the 30 smokers from whom information on years of regular smoking was obtained. The correlations were weak, suggesting that many other factors may influence white matter disruptions; however, the correlation strengths and directions are consistent with previous findings (Lin et al., 2013).

5.1.3.2.4 Other DTI Metrics: Controls vs Smokers (abstinent 24 h)

TBSS analysis also revealed changes in non-FA DTI metrics in abstinent smokers compared to controls. Smokers had higher Dr within the corpus callosum and internal capsule bilaterally (**Figure 5.3**). Further, modeling the DTI data with 2 crossing fibers shows significant differences between smokers and controls in both fiber directions. Smokers showed decreases in anisotropy of the major fiber (F1) within notably large portions of the left corpus callosum (**Figure 5.4**). Smokers also showed decreases in anisotropy of the second fiber (F2) within several anterior brain regions (**Figure 5.5**). TBSS for Da and MD did not yield any significantly different voxels.

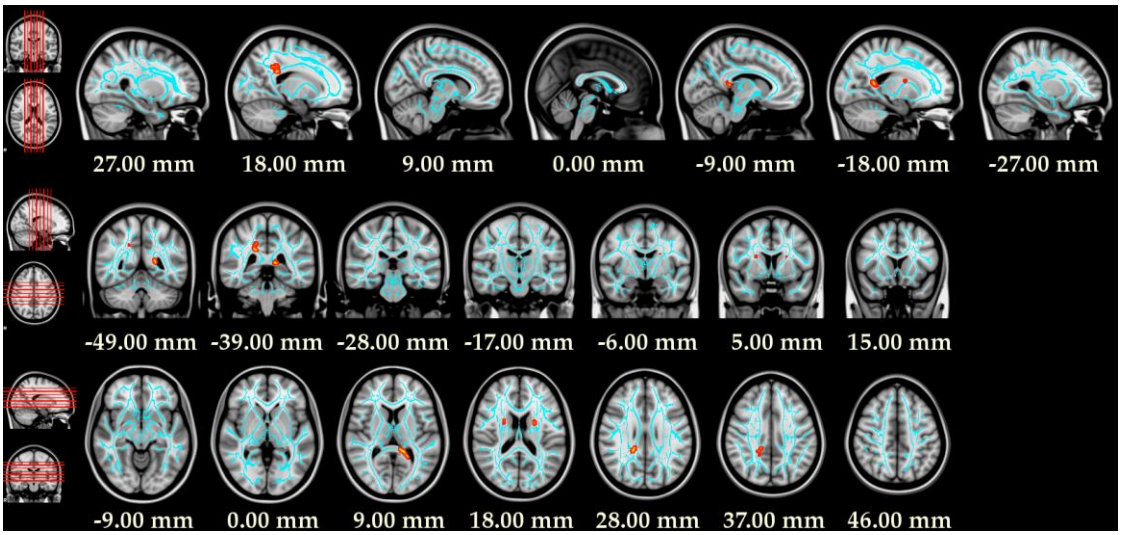

Figure 5.1 Fractional Anisotropy Deficits in Smokers

TBSS results reveal that smokers have decreased FA in the L and R splenium of corpus callosum and the L and R anterior limb of internal capsule. Ethnicity, education, gender, and age were adjusted for as additional covariates in the GLM. Anatomical labels were derived from the JHU ICBM-DTI-81 White Matter Labels. The light blue indicates the skeletonized WM in which the voxel-wise TBSS was performed. The red-yellow shows significant voxels ($p < 0.05$, FWE controlled) with the voxels filled along the WM tracts for easier visibility. Brain images are in radiologic convention (right hemisphere appears on left).

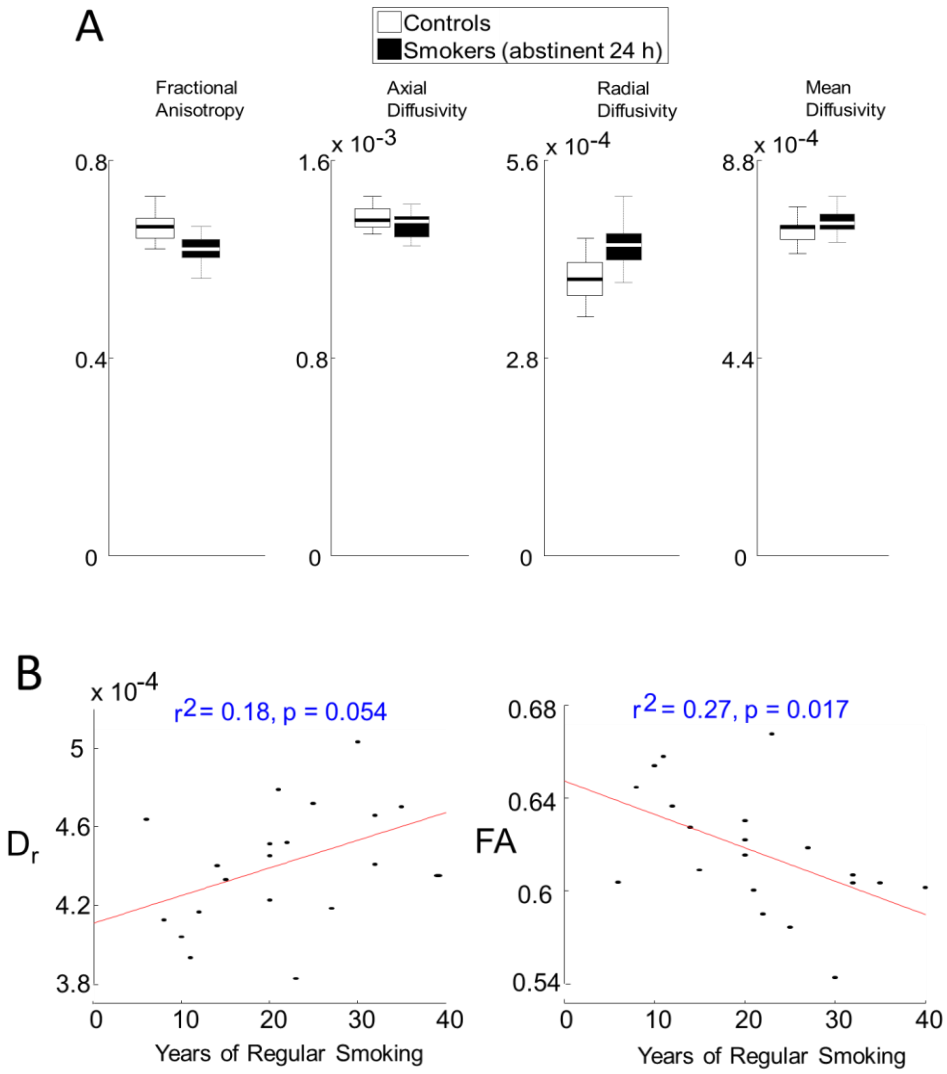

Figure 5.2 Impact of Smoking

WM regions with significantly lower FA in smokers also show changes in other DTI measures. A. FA was decreased, Da was decreased, Dr was increased, and MD was increased in smokers compared to non-smokers. Significance testing was not computed here to avoid circularity. The box and whisker plots show group statistics of the averaged DTI metrics from each tract: median within the box, the 25th and 75th percentiles at the bounds of the box, the extremes of the data not outliers as whiskers, and the outliers in red crosses. B. Correlations of DTI metrics with severity of smoking revealed a negative correlation of FA and duration of smoking and a positive correlation with Dr and duration of smoking. Data is from 20 of the 30 smokers from which years of regular smoking was obtained. These characteristic correlations are highly consistent with Lin et al (2013), even though our brain regions differ.

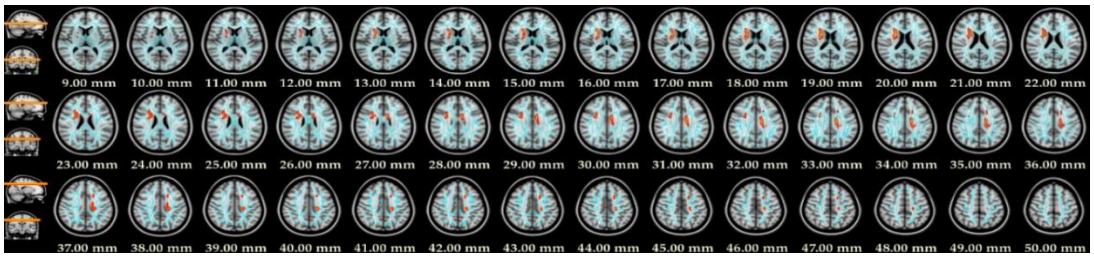

Figure 5.3 Radial Diffusivity Changes in Smokers

TBSS results reveal smokers have increased Dr diffusely in corpus callosum and bilateral internal capsule. Ethnicity, education, gender, and age were adjusted for as additional covariates in the GLM. Anatomical labels were derived from the JHU ICBM-DTI-81 White Matter Labels.

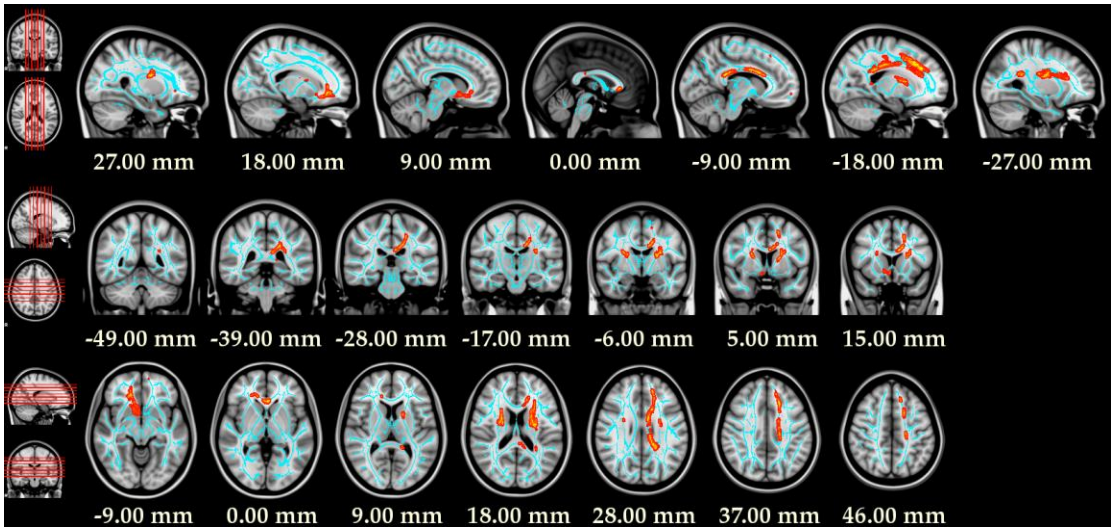

Figure 5.4 Major Fiber Changes in Smokers

TBSS results reveal smokers have significantly decreased anisotropy along the major fiber (F1) in the L body of the corpus callosum (top row), the bilateral anterior limb of the internal capsule (middle row), and the L forceps minor (bottom row). Ethnicity, education, gender, and age were adjusted for as additional covariates in the GLM. Anatomical labels were derived from the JHU ICBM-DTI-81 White Matter Labels or the JHU White-Matter Tractography atlas.

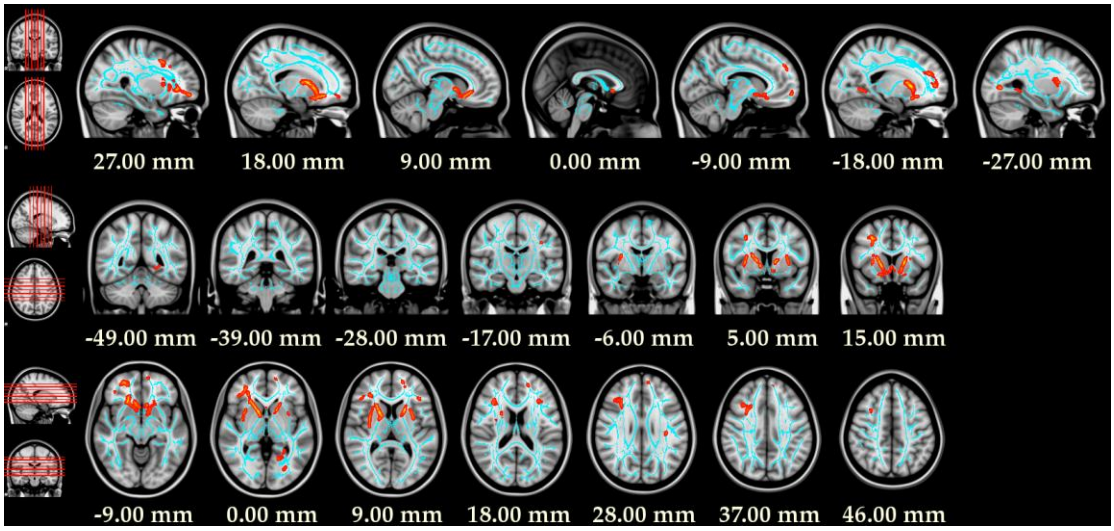

Figure 5.5 Secondary Fiber Changes in Smokers

TBSS results reveal smokers have significantly decreased diffusivity along the second anisotropy (F2) in bilateral anterior internal capsule (top row), the L inferior fronto-occipital fasciculus (middle row), and the R genu of the corpus callosum (bottom row). Ethnicity, education, gender, and age were adjusted for as additional covariates in the GLM. Anatomical labels were derived from the JHU ICBM-DTI-81 White Matter Labels or the JHU White-Matter Tractography atlas.

5.1.3.2.5 Sated vs Abstinent Smokers

No differences in FA, MD, Dr, or Da were found via TBSS between smokers who smoked as usual (sated) and smokers who abstained for 24 hours (abstinent).

5.1.3.3 Probabilistic Tractography

5.1.3.3.1 Controls vs Smokers

Several differences between abstinent smokers (24 h) and controls were observed within the frontal-projecting white matter tracts (**Figure 5.6**). When abstinent, smokers had lower FA in the right fronto-motor tract compared to controls ($p < 0.05$, GLM t-contrast

control - smoker). When smoking as usual, smokers had lower FA compared to controls in left fronto-accumbal, right fronto-motor, and right fronto-habenula tracts ($p < 0.05$, GLM t-contrast control - smoker). When smoking as usual, smokers also had lower FA compared to abstinent smokers in right fronto-accumbal and right fronto-habenula tracts ($p < 0.05$, paired t-test).

5.1.3.3.2 Hemispheric Asymmetry in Smokers (abstinent 24 h)

Previous studies (Lin et al., 2013) have shown asymmetrical disruptions in white matter as a result of smoking, with more disruptions in FA appearing on the left hemisphere. Our probabilistic tractography results also show that smokers (abstinent 24 h) have lower FA in the left fronto-habenula and left fronto-accumbal tracts compared to the right sided tracts ($p < 0.05$, paired t-test). However, control participants did not show any such asymmetry (**Figure 5.7**).

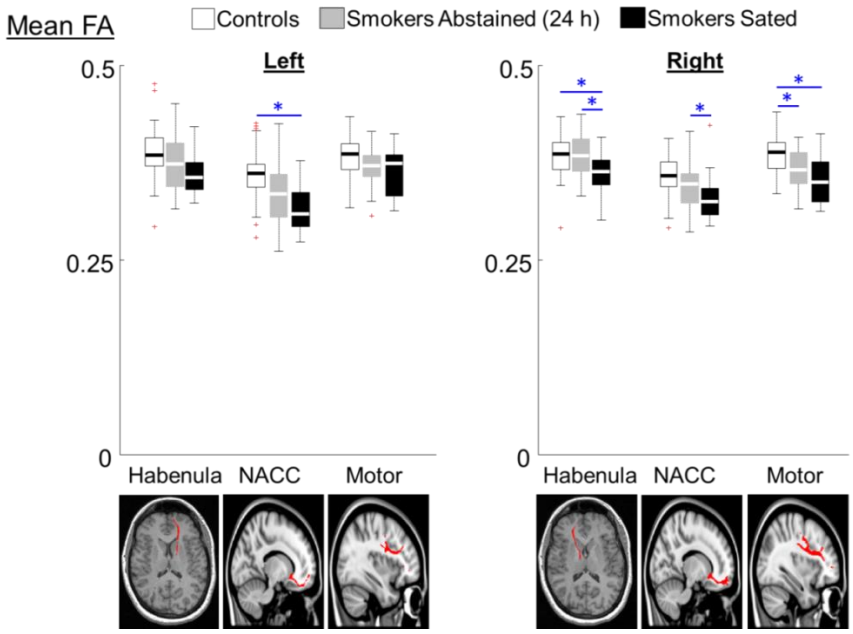

Figure 5.6 Tractography

Chronic tobacco use causes decreases in FA within frontal projecting tracts, which show further decreases in FA when smokers have recently smoked. Probabilistic tractography was used to find specific tracts projecting to the frontal cortex originating from 3 ROIs: habenula, nucleus accumbens (NACC), and pre-central gyrus (motor). Tracts from a representative participant are shown on the bottom row of images corresponding to the ROI seeds. Above each image is the distribution of FA across participants within that tract. The box and whisker plots show group statistics of the averaged FA from each tract: median within the box, the 25th and 75th percentiles at the bounds of the box, the extremes of the data not outliers as whiskers, and the outliers in red crosses.

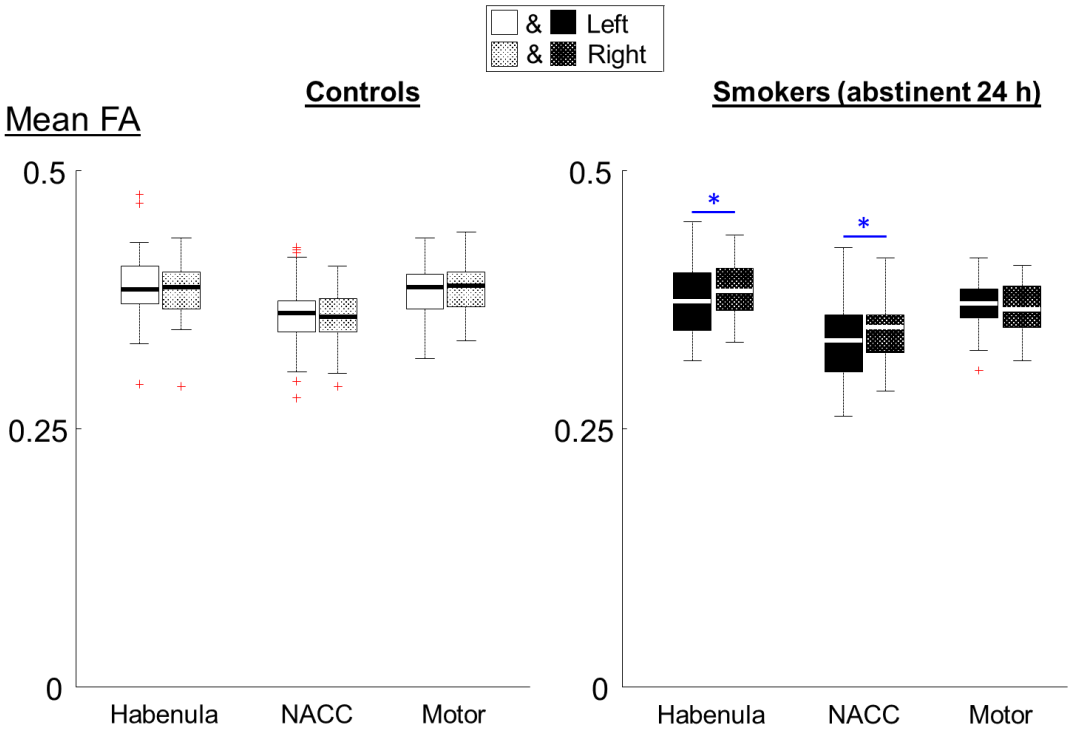

Figure 5.7 Asymmetrical Hemispheric Differences

Nicotine users show asymmetrical hemispheric differences in FA along fronto-habenula and fronto-accumbal tracts. Nicotine users showed significantly lower FA (*: $p < 0.05$, paired t-test) along the L habenulo-frontal and accumbo-frontal tracts compared to the corresponding right hemispheric tract. Controls showed no hemispheric asymmetries along any of our measured tracts. The box and whisker plots show the group statistics of the averaged FA from each tract: median within the box, the 25th and 75th percentiles at the bounds of the box, the extremes of the data not outliers as whiskers, and the outliers in red crosses.

5.1.4 Discussion

Our approaches yield three new pieces of evidence characterizing white matter disruptions from nicotine use: (1) Using TBSS, we found abstinent smokers compared to controls have decreased FA, increased radial diffusivity (Dr), and decreased anisotropy within aligned fiber bundles in several brain regions, including the corpus callosum and anterior internal capsule. (2) We found structural connections between the frontal cortex and two reward-related brain areas (the nucleus accumbens (Balfour, 2002, 2004; Di Chiara et al., 2004) and the habenula (Salas et al., 2009; Velasquez et al., 2014)) to be implicated in chronic nicotine smoking, and these disruptions were further exaggerated by acute smoking. (3) We found specific hemispheric asymmetries within frontal projecting tracts observed in chronic smokers but not in healthy controls, suggesting the white matter disruptions in the left hemisphere to be more susceptible to the effects of nicotine than the right hemisphere. Collectively, our study uses recent DTI approaches to better characterize the adverse effects of nicotine on white matter characteristics in the brain.

First, using TBSS we found decreased FA within regions of the corpus callosum, in line with some previous studies (Lin et al., 2013; Umene-Nakano et al., 2014) and refuting others (Hudkins et al., 2012; Paul et al., 2008). Also using TBSS, we found Dr was increased in the corpus callosum in smokers (abstinent 24 h) compared to controls, a result that was previously not found (Umene-Nakano et al., 2014) or not explicitly searched for using TBSS (Lin et al., 2013). We also built a model that incorporated

crossing fibers (Jbabdi et al., 2010) and found large decreases in anisotropy along the first fiber direction in the entirety of the left corpus callosum and decreased anisotropy in several frontal WM regions in bilateral frontal regions. Such a model had not been tested for nicotine dependence, and our analysis with this model supports previous studies reporting left sided corpus callosum disruptions in smokers (Lin et al., 2013). Further, by aligning fiber orientations and running TBSS on each fiber bundle individually, we were also able to elucidate decreases in anisotropy in anterior internal capsule and frontal regions, a result not previously reported in TBSS analyses on FA only. Our data also recapitulated correlations of FA and years of nicotine use previously seen across several studies (Hudkins et al., 2012; Liao et al., 2011; Lin et al., 2013; Paul et al., 2008; Umene-Nakano et al., 2014; Zhang et al., 2011). Although the directionality of the correlations are consistent with the literature, all studies including our own have used relatively small sample sizes. The strength of these mild correlations might be increased by: (1) using an order of magnitude greater number of smokers, (2) adjusting for further demographic and biological data (e.g. socioeconomic conditions, genetic predispositions), and (3) acquiring better estimates of total lifetime volume of nicotine exposure. In sum, our TBSS data further elucidate the changes seen within the corpus callosum and the anterior limb of the internal capsule seen in cigarette smokers but not in controls.

Second, the probabilistic tractography within our 3 hypothesized tracts (fronto-accumbal, fronto-habenular, and fronto-motor) revealed a general trend of decreasing

FA in smokers who abstained from smoking for 24 hours, compared to controls. These changes were further exacerbated when smokers smoked as usual (sated). Even though our TBSS analysis did not reveal any differences between smoking as usual and abstinent smokers, we found the right fronto-habenula and fronto-accumbal tracts to be decreased further when smokers recently smoked. We also found 3 of the 6 tracts to show significantly lowered FA in sated smokers compared to controls. Using participant-specific tracts to perform statistics rather than common group approaches like TBSS can reveal more subtle differences that can wash away in spatial normalization. Further, we also found evidence for hemispheric asymmetry in which the left hemisphere contained more disruptions in smokers but not controls, a result supporting previously observed findings (Lin et al., 2013). Although previous studies found significant correlations between FTND and DTI metrics (Hudkins et al., 2012; Paul et al., 2008; Zhang et al., 2011), our data did not show such correlations using two different approaches.

Third, our probabilistic tractography results support our hypothesis that acute effects of nicotine enhance the observable chronic disruptions in DTI in smokers in some regions. The opposite hypothesis, for smokers to show increases in FA after recent use, is also plausible and has been previously observed in the genu of the corpus callosum after recent nicotine administration (Kochunov et al., 2013) and in smokers who recently began smoking (Hudkins et al., 2012; Liao et al., 2011; Lin et al., 2013). Support for this hypothesis stems from the presence of functional nicotinic acetylcholine receptors

(nAChRs) within the white matter of the brain (Ding et al., 2004; Kochunov et al., 2013; Pimlott et al., 2004; Vizi and Lendvai, 1999) and/or glial swelling (Hudkins et al., 2012; Opanashuk et al., 2001), which could account for acute exposure to nicotine increasing FA values. Our results show that smokers who were sated had decreases in FA compared to the same smokers when they abstained for 24 hours within particular frontal projecting tracts. Since our TBSS results showed no difference between sated and abstinent smokers, it is possible that acute nicotine exposure affects only specific WM tracts. Further, smokers exhibited greater disruptions in the left compared to right tracts. Although we did not hypothesize such a laterality difference selectively in smokers, the greater DTI changes in the left hemisphere may parallel lateralization of dopaminergic systems. Dopaminergic dysfunction is characteristic in Parkinson's disease, in which greater nigrostriatal damage is seen on the left hemisphere (Scherfler et al., 2012) and in which stronger left lateralized functional connectivity is associated with a decreased risk for Parkinson's disease (Ellmore et al., 2013). This interpretation is further supported that smoking propensity can be altered in humans via dopaminergic agonists and inverse agonists (Caskey et al., 2002). Interestingly, we also did not hypothesize the fronto-motor tracts to differ significantly from controls or between abstinent and sated smokers. However, disruptions in motor coordination have been observed in rats with prenatal exposure to tobacco extracts (Khalki et al., 2012), suggesting the motor circuit may also be implicated in nicotine use. Further, nicotine exposure may induce changes to networks throughout the frontal cortex, giving rise to our observed changes in all three frontal projecting tracts.

An alternative interpretation of the data is that the white matter changes in the abstinent smokers is related to acute withdrawal of nicotine rather than chronic nicotine exposure. This seems plausible, as 24 hours without a cigarette certainly induces withdrawal symptoms. However, we did not find significant differences in the paired TBSS analysis of smokers in sated vs. abstinent conditions. Further, our probabilistic tractography data show that when sated, the FA measures decline further rather than reversing, as would be expected if the effect was due to withdrawal. That is, we did not observe FA measures to restore towards the level of controls when smokers recently smoked. Nonetheless, a further investigation parametrically modulating the duration of abstinence and observing the effects on DTI metrics might further substantiate our findings.

The characteristics of the altered DTI metrics in smokers may elucidate the biological underpinnings of the impact of nicotine on white matter. Smokers were found to have an increase in radial diffusivity compared to controls without significant decreases in axial diffusivity, suggesting the disruptions observed in smokers are more likely related to dysmyelinated axons rather than axonal injury (Song et al., 2003; Song et al., 2002; Song et al., 2005). This finding is consistent with rodent studies that revealed gestational nicotine exposure decreased myelin gene expression in both adolescent and adult rats in regions including the prefrontal cortex, basal ganglia, and the nucleus accumbens (Cao et al., 2013a; Cao et al., 2013b).

Our study has four important limitations. First, our DTI sequence prevented imaging of the cerebellum and the posterior occipital lobe, limiting inferences from these regions. Further, incomplete imaging of the cerebellum could prevent optimal image registration. Second, we did not scan control participants twice to measure the test-retest reliability of the imaging as well as the analysis approaches. This is a growing concern in DTI imaging, and TBSS approaches are participant to imperfect test-retest reliability (Madhyastha et al., 2014). Third, we did not randomize the days that smokers were abstinent. Due to participation in a separate study (a virtual reality session prior to scanning), all participants had been abstinent for over 24 hours on the first day they were scanned. Further, the 15 participants who did return for the second scan while smoking as usual had significantly greater FTND. This may limit the implications of the effects of acute nicotine exposure on DTI metrics to smokers who have a greater dependence on nicotine. Fourth, there are a multitude of factors that could additionally or partially explain differences in DTI metrics between controls and smokers. Our covariates accounted for linear trends in the data; however, non-linear effects of age and education in particular were not removed. Further, we did not assess other indices of health including but not limited to: diabetes, blood pressure, hypertension, and cardiac disorders. Thus, our study cannot state that tobacco plays any causal role on these observed changes, only that a correlation was observed.

5.1.5 Conclusions

Our study investigated the effects of nicotine use on white matter characteristics using a variety of approaches. By using multiple directions in our DTI image acquisition and incorporating crossing fibers into our TBSS analysis, we provide a more complete picture of white matter disruptions in chronic smokers, including regions of decreased FA in the corpus callosum. Further, our probabilistic tractography data reveals decreases in FA in smokers in white matter tracts projecting to the frontal cortex from the nucleus accumbens, habenula, and the motor cortex. Disruptions were greater on the left side in smokers vs. non-smokers, and decreases were generally exaggerated by acute exposure to cigarette smoking. DTI may help elucidate the addictive potential of nicotine and how it interacts with cortical and subcortical white matter. Fortunately, there is some evidence that quitting smoking for > 20 years restores disruptions in white matter characteristics (Gons et al., 2011), suggesting these disruptions may not be permanent. Mapping what the disruptions are and how they can recover could be instrumental in therapeutic development.

5.2 Characterizing the Full Sympathetic Response to Drug Cues

5.2.1 Introduction

One the biggest challenges in drug addiction therapy is finding an objective marker to quantify the level of success for drug therapies. Currently, the two best indicators of treatment performance are: 1) the number of days a participant is able to abstain from drug use and 2) participant questionnaires asking for craving status. The abstinence criteria is heavily debated topic but the federal agencies have mandated a minimum of 2 weeks abstinence is required before a treatment can garner FDA approval. Even if therapies can reduce usage or alter dependence, if the abstinence criteria is not met, the drug will unfortunately not be approved. Reduction without elimination of drug usage could still hold very beneficial, much the way weight loss programs don't require complete abstinence from unhealthy foods. The binary measure of abstinence does not forecast if physiology has been altered and dependence has been reduced, beyond the abstinence observed during the treatment regimen. Further, most therapy programs have a contingency management baked into them, which has shown to be one of the most effective behavioral therapy regimens (Knapp et al., 2007). But, contingency management can artificially inflate abstinence during treatment regimens, which may not be reflective of abstinence rates as soon as the therapy ends. Participant questionnaires are not objective markers and vary drastically between days, participants, and experimenters.

To this end, we are investigating the complete sympathetic nervous system response to drug cues in order to quantify craving states in crack cocaine users. The sympathetic nervous system response includes increased heart rate, increased blood pressure, increased galvanic skin response (GSR) via increased conductance (decreased resistance), pupillary dilation, and decreased skin temperature. Several labs have investigated some of these measures independently (e.g., (Ehrman et al., 1992)) in the early 1990s and found cocaine users exhibited heightened sympathetic responses when shown drug-related stimuli. The claim is that the cue or conditioned response may trigger a withdrawal state.

However, reports slightly later discussed that these cue responses did not correlate with motivational states (Robbins et al., 1997). Here, we are investigating examining closer the full sympathetic response by measuring the temporal response of 4 measures on effector organs simultaneously with well-controlled baseline conditions. We hypothesize that the timing of each response is variable across the different measures, and capturing the temporal profile will be essential. Further, most previous studies used a block design, measuring responses to long chunks of videos or stimuli. Here, we are employing an event-related design that can allow us to study the temporal profile of each measure in response to single, briefly flashed images. Together, these measurements may allow us to predict better the mental states from physiological measurements. Work is currently ongoing and unpublished as of yet.

5.2.2 Materials and Methods

5.2.2.1 Stimuli

The most critical component of measuring the sympathetic response is to find a well-matched control to get a baseline response to a briefly flashed image. For pupillometry, this proves challenging to match the visual properties of the images in control images. Many previous approaches used phase-scrambled images, images which take an FFT of the original image, randomly scramble the phase, and bring the image back to the spatial domain. However, these images often appear very unnatural and do not preserve local contrast features (**Figure 5.8**).

Instead, we used diffeomorphic transformations to allow us to use color, scrambled images that are much better matched to the original image (Stojanoski and Cusack, 2014). These images much better preserve local features and allow control on much to scramble the original image (**Figure 5.9**).

In our experimental design, we first flashed the warped image for 250 ms followed by an inter-trial interval of 6 – 10 s. Then, we flashed the true image next. Images were randomly selected from a set of cocaine or cocaine paraphernalia images or natural images. We showed 20 images of each type, making for 40 images and 40 warped images. Experiment time was ~15 minutes. Participants were not asked to perform any task to minimize motion during data collection. Afterwards, participants rated the degree to which each cocaine image elicited craving using a visual analog scale (VAS) for 0 (no

response) to 100 (maximum craving response). Participants were required to give a negative urine sample (no cocaine in system for last 72 hours) to ensure a minimum satiety across participants.

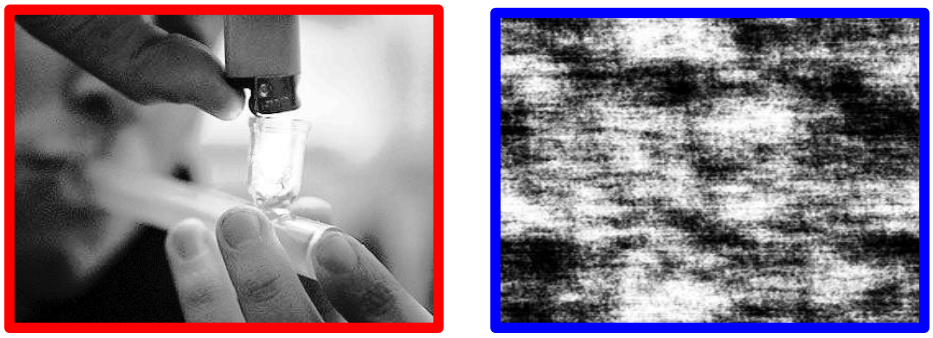

Figure 5.8 Phase Scrambled Images

Phase scrambled images do not preserve image statistics.

Figure 5.9 Diffeomorphic Transformations

Diffeomorphic transformations all just the high-level content of images to be distorted without destroying critical image statistics to measure pupillometry.

5.2.2.2 Physiological Measurements

We are measuring 4 sympathetic responses in crack cocaine users in response to cocaine images:

1) Heart rate variability
2) Skin conductance (GSR)
3) Skin Temperature
4) Pupillary dilation

Heart Rate Variability- Heart rate was measured using a pulse oximeter BIOPAC (Goleta, CA) Pulse Oximeter Trans, Finger Transducer – TSD123A and amplifier (BIOPAC Pulse Oximeter Amplifier – OXY100C) sampled at 200 Hz. Heart rate variability was computed as follows:

$$HRV = std(Peak - to - Peak\ time)$$

The peak-to-peak times were computed by finding the local maxima (**Figure 5.10**).

Skin Conductance- Skin conductance (or GSR) was measured using the BIOPAC Galvanic Skin Response Amplifier – GSR 100C and BIOPAC Skin Conductance Trans, AgCl GSR Electrodes – TSD203. Electrolytic gel (BIOPAC Gel 101) was applied to sensor leads. GSR was continuously sampled at 200 Hz.

Skin Temperature- Skin temperature was measured using the BIOPAC Skin Temperature Amplifier SKT 100C and the BIOPAC Fast Response Thermistor, TP –

TSD202A. The thermistor was taped to the participants' right forearm, and data were sampled continuously at 200 Hz.

Biopac Data Acquisition- The above three measures were all acquired with the BIOPAC MP150 Data Interface using AcqKnowledge 3.9.1 software on a Windows XP laptop.

Pupillometry- Eye movements and pupillometry were obtained with the SR EyeLink 1000 Plus (Scientific Research, Ontario, Canada). Raw position and pupil diameter were sampled at 1000 Hz. Saccade reports were generated using the EyeLink Data Viewer (Scientific Research, Ontario, Canada) and further analyzed in MATLAB (Mathworks, Natick, MA, 2000). Eye blinks were detected when the pupil diameter was too small (< 1 mm), obstructed, or not tracked, and any saccades during blinks were discarded from analysis.

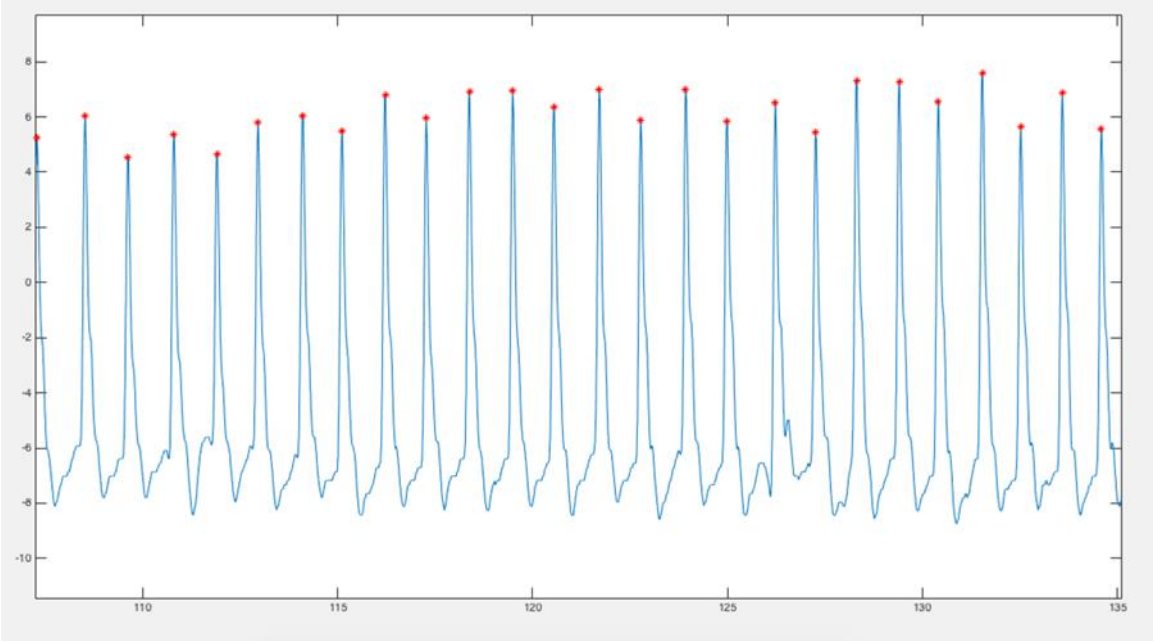

Figure 5.10 Heart Rate Variability

Finding local maxima peaks of the heart rate pulses to compute HRV.

5.2.3 Results

Preliminary data from 5 participants show minor changes in the physiological response of drug cues compared to natural images (**Figure 5.11-14**).

5.2.4 Discussion

The data from 5 participants are preliminary and do not yet show a consistent heightened sympathetic response to cocaine cues. Work is ongoing to collect data from more participants and to refine approaches.

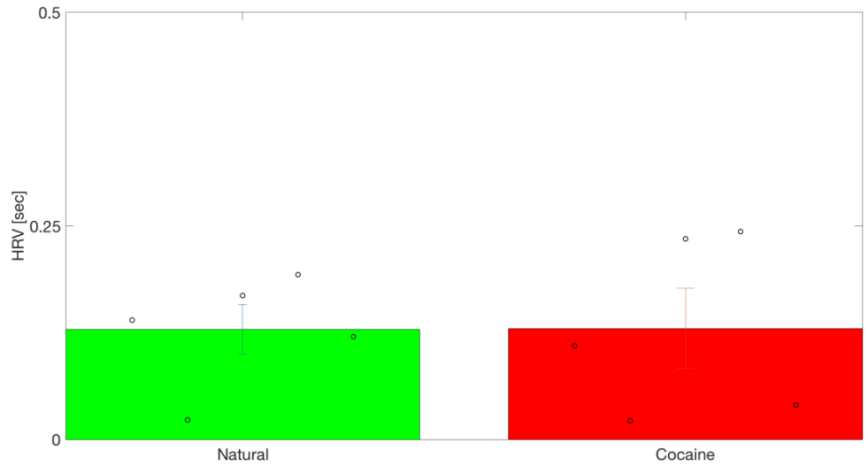

Figure 5.11Heart Rate Variability Differences

Minor changes in heart rate variability were detected in participants shown cocaine vs. natural images.

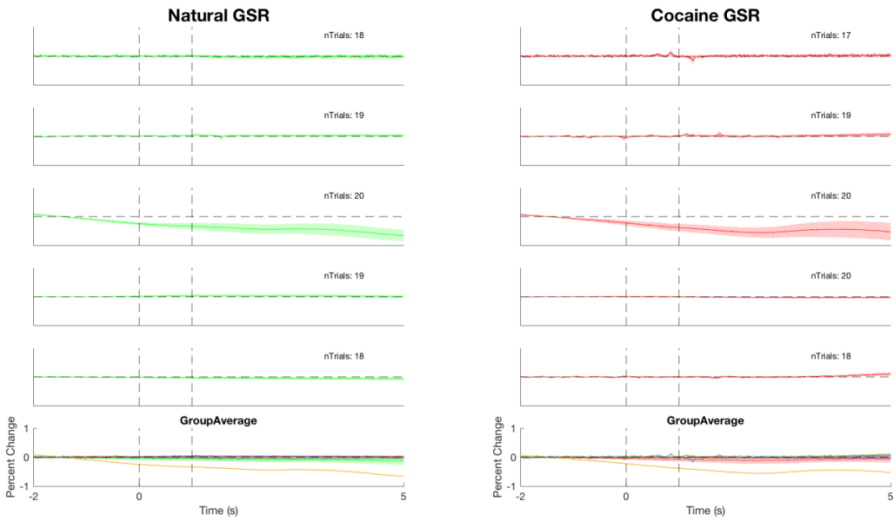

Figure 5.12 Galvanic Skin Response

Minor changes in galvanic skin response were detected in participants shown cocaine vs. natural images.

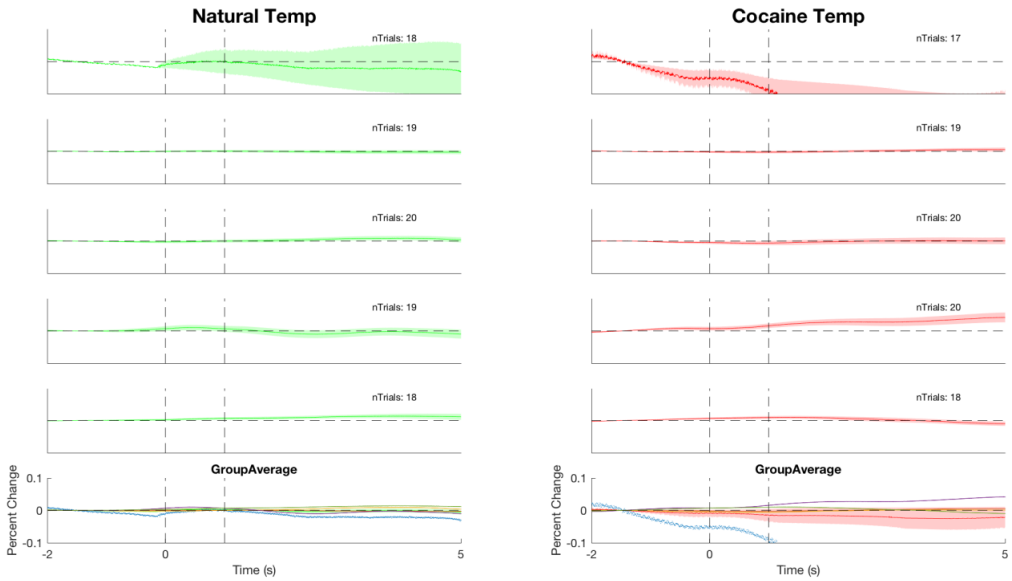

Figure 5.13 Skin Temperature

Minor changes in skin temperature measure in participants shown in cocaine vs. natural images.

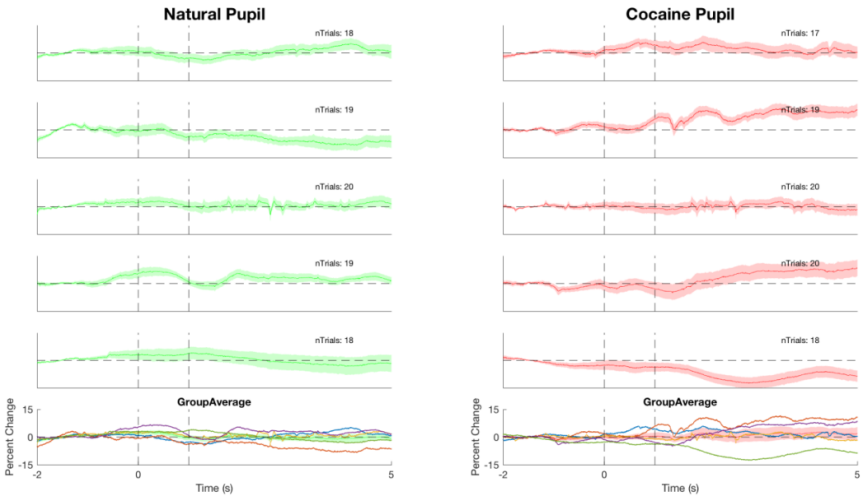

Figure 5.14 Pupillometry

Minor changes in pupillometry measurements in participants shown in cocaine vs. natural images.

5.3 Real Time fMRI Feedback

5.3.1 Introduction

Crime intersects with mental health at a precarious crossing: drugs. Controlled substance abuse impacts the criminal justice system profoundly.

Starting locally, I indexed and categorized all publicly available criminal record data from 1977 to 2010 in Harris County in Houston, TX. What I found was incredibly clear: charges for controlled substances account for more crimes than any other type of violation since 1990 (**Figure 5.15A**) with 19.4% of all crime involving controlled substances (**Figure 5.15B**).

Is charging, arresting, and incarcerating people for possession of controlled substances effective in preventing future crimes? To answer that, I used the unique person identifier to compute recidivisms for each crime type and found a striking result**:** people charged for controlled substances were more likely to repeat the same offense than any other crime type: controlled substance charges account for 28.1% of all recidivism in Harris County, TX **(Figure 5.15C).** The criminal justice system is funding an expensive endeavor to incarcerate controlled substance abusers (Office of National Drug Control Policy, 2012) but is not deterring future re-offenses (Cid, 2009; Vieraitis et al., 2007).

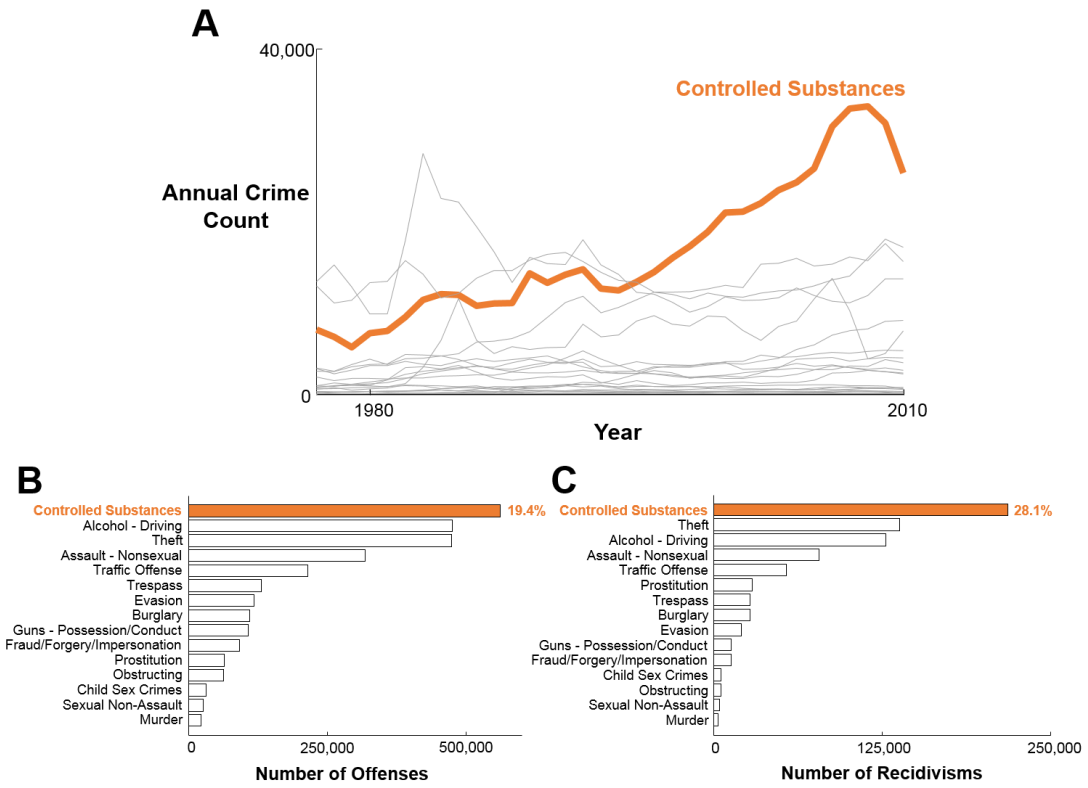

Figure 5.15 Drugs and Crime

Criminal charges involving controlled substances have been increasing annually (A) and account for the majority of all offenses (B) and recidivisms (C) in Harris County, TX from 1977 – 2010. Recidivism here is defined as the number of multiple offenses for the same crime type committed by the same individual on different dates. (Publicly available criminal record data were categorized and aggregated in house by the Institute of Neuroscience and Law).

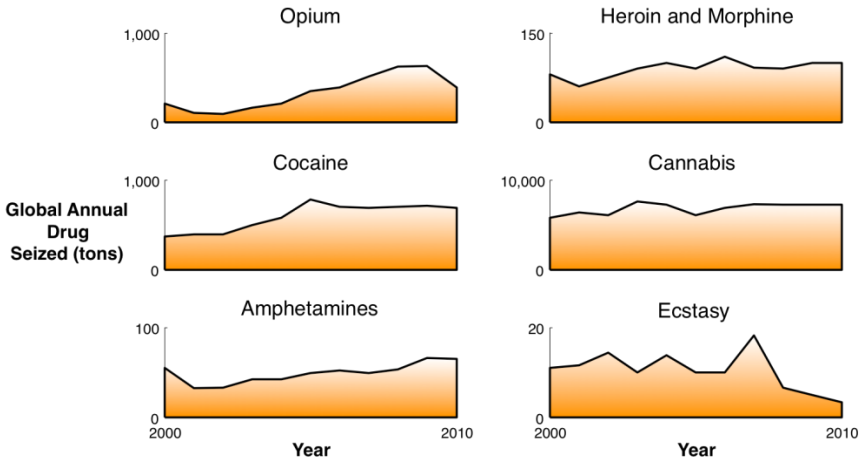

Figure 5.16 Drug Seizures

Annual global seizure of illicit drugs has remained stagnant or increased from 2000 - 2010, suggesting a steady market demand and little to no deterrent effect on illicit drug production (Data from UNODC World Drug Report 2012).

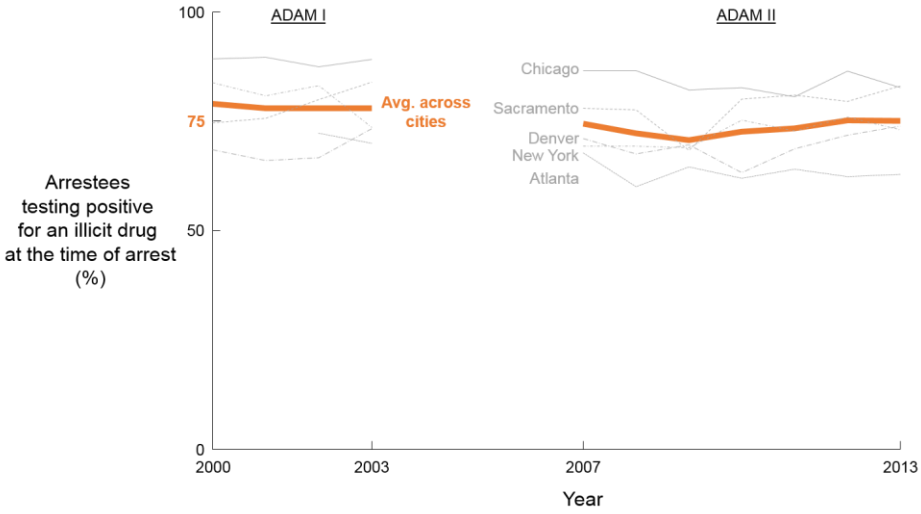

Figure 5.17 Drug Arrests

When individuals are arrested for a criminal offense, controlled substances are present in a vast majority of arrestees at the time of arrest. (Data from the Arrestee Drug Abuse Mentoring, ADAM II (Office of National Drug Control Policy, 2014)).

The “war on drugs” has also failed on the supply side. The global seizure rate of various narcotics has remained stagnant or increased annually over the decade from 2000 – 2010 (**Figure 5.16)** (UNODC, 2012). Seizing one source of supply often leads to an outburst of another source (Eagleman and Correro, 2010; Jarvik, 1990).

Further, substance use itself may be criminogenic. The Arrestee Drug Abuse Mentoring (ADAM) program performed a urinalysis on all arrestees in 5 different cities across the country (Office of National Drug Control Policy, 2014). They found on average about 75% of arrestees tested positive for at least one controlled substance at the time of arrest. This trend remained constant across all cities from 2000 – 2013 (**Figure 5.17**).

Drugs are integrally involved in the criminal justice system. Drug-related arrests account for the most crimes and recidivisms, drug supplies remain omnipresent, and drugs are detected in the system in the majority of arrestees. However, there are a lack of effective interventions for those addicted to illicit drugs. No Federal Drug Administration (FDA) approved therapies exist for people addicted to cocaine, a drug linked with increased risk-taking behaviors (Canavan et al., 2014; Hulka et al., 2014; Inciardi and Surratt, 2001; Wechsberg et al., 2012).

The social, behavioral, and psychiatric fields have tried many different behavioral interventions aimed to help addicts abstain from cocaine use. A systematic, retrospective review of 27 different psychosocial therapies involving over 3,500 participants

attempted to identify an effective strategy for reducing cocaine use (Knapp et al., 2007). Of the various behavioral regimens analyzed in the review (e.g., Cognitive Behavioral Therapy, Community Reinforcement Approach, Supportive-Expressive Psychodynamic Therapy), not one therapy adequately addressed cocaine addiction. Pharmacotherapy and behavioral interventions have all failed to offer a way out of cocaine addiction and abuse. With few options, the criminal justice system is forced to deal with the abundance of controlled substance related activities and crimes and is often left no choice but to incarcerate drug users.

A central mission for the NIJ in FY2015 is to seek "*alternatives to incarceration, their consequences and cost effectiveness.*" Over decades of research, neuroscience and neuroimaging have shed light on the brain of a cocaine addict, elucidating areas of the brain circuitry that have gone awry in cocaine addicts. Modern advances in imaging allow us to capture the activity of the entire brain via functional magnetic resonance imaging (fMRI) in real-time. Thus, I propose to build and test a neuroscientific rehabilitative regimen using innovative methods of biofeedback to help cocaine addicts decrease use and prevent crime, relieving the largest burden the criminal justice system faces.

5.3.2 Materials and Methods

Social and behavioral science experiments attempt to measure and manipulate behavior by either subjective (e.g., self-report) or psychophysical (e.g., 2 alternative forced choice) experimental feedback from the participants. But **what is lacking is a direct objective measure reflecting an individual's cognitive state.** If physiological activity of high-level cognition could be accurately and rapidly measured, we could more closely understand and guide therapeutic interventions to alter behavior.

5.3.2.1 Real-time fMRI Feedback

Traditional fMRI allows us to measure the brain activity in humans as they are participating in a particular task. For example, we can see what areas of the brain are activated when viewing images of cocaine. Modern computational advances enable this information in real-time as the participant performs the task inside the scanner. Information about real-time brain activity is not limited to the experimenter, but can also be displayed to the participant in the scanner. Just as a music student uses the sound of his instrument to learn how to play the guitar, a cocaine participant could use his own brain activity as feedback to learn how to overcome cocaine craving (**Figure 5.18**).

The principle behind rt-fMRI technology dates back nearly two decades (Cox et al., 1995), but the technique has only been realized recently with advances in modern computing power (Sulzer et al., 2013). Neuro-feedback via rt-fMRI has been previously applied successfully to help modulate chronic pain (deCharms et al., 2005), depression (Linden et al., 2012), and anxiety (Brühl et al., 2014) (rt-fMRI applications reviewed

comprehensively elsewhere (Bagarinao et al., 2006; Caria et al., 2012; deCharms, 2008, 2007; Weiskopf et al., 2007, 2004, 2003)). But research is only beginning to probe the utility of this tool as a therapeutic approach to drug addiction. A handful of preliminary studies have shown cigarette smokers were able to decrease participantive craving for cigarettes (Canterberry et al., 2013; Hanlon et al., 2013; Hartwell et al., 2013; Li et al., 2012); however, no studies to date have been able to assist addicts with dependence to cocaine, a much more severe and consequential disorder to the criminal justice system.

Understanding the neuropsychiatric bases for cocaine addiction is essential for developing targeted therapies. Presentation of cocaine-associated stimuli elicits increased activation of the anterior cingulate cortex (ACC) (Childress et al., 1999; Garavan et al., 2000; Goldstein et al., 2007; Kilts et al., 2001; Maas et al., 1998; Wexler et al., 2001), amygdala (Bonson et al., 2002; Childress et al., 1999; Grant et al., 1996; Kilts et al., 2001), insula (Bonson et al., 2002; Kilts et al., 2001; Naqvi and Bechara, 2009), nucleus accumbens (Kilts et al., 2001), caudate (Garavan et al., 2000), and ventral tegmental area (VTA) (Goldstein et al., 2009) – what I will summarize as a craving network (**Figure 5.18A**, **red**). Recent neuroimaging studies indicate that addicts who are instructed to cognitively inhibit their cravings for cocaine can transiently lower activity within regions of this network (Volkow et al., 2010). Such findings open the way for a therapy that can quantify and directly assist addicts in decreasing activity in this craving network (Parvaz et al., 2011).

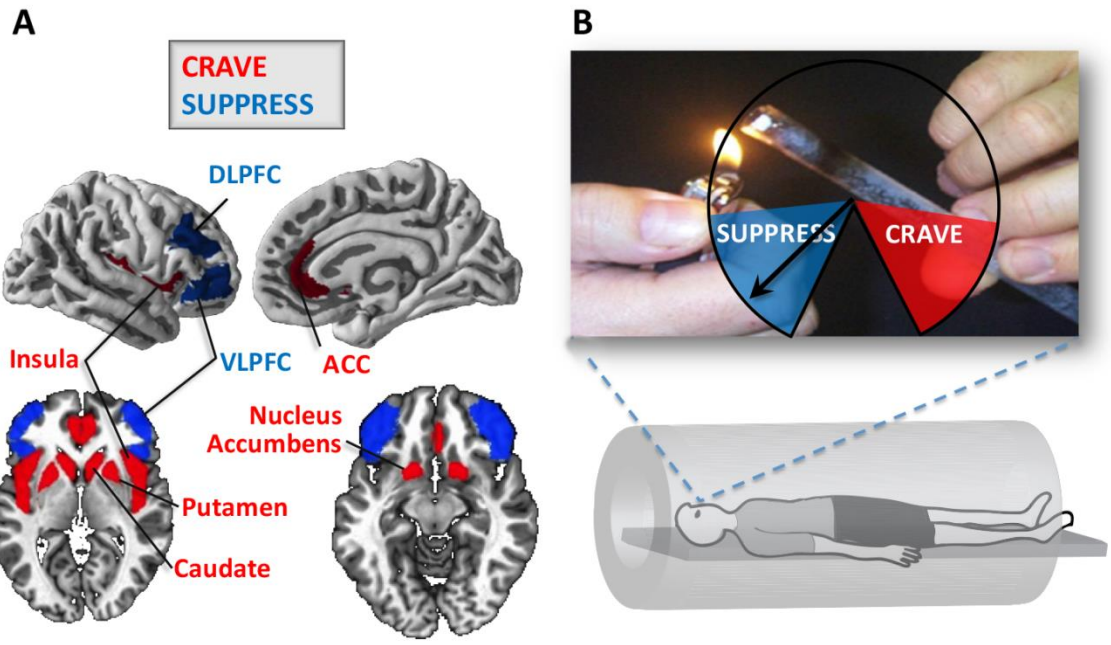

Figure 5.18 Real-time fMRI Neurofeedback

Real-time fMRI neurofeedback as a technique to control craving for cocaine abusers. A. The therapy guides addicts to decrease activity in brain regions involved in craving (red), while also increasing brain activity brain regions involved in suppressing cocaine craving (blue). B. Crack cocaine abusers are shown images of the drug and associated paraphernalia while in an MRI scanner. Participants are instructed to suppress their craving, and feedback representing the ratio of activities in the craving and suppression networks is shown in the form of a meter on the screen. The end goal of this therapy is to strengthen cognitive control, fortifying participants with the capacity to overcome their craving when faced with enticing environmental drug cues.

Increasing activity in a "suppression" network may also prove therapeutic (**Figure 5.18A**, **blue**). The prefrontal cortex (PFC) is involved in suppressing urges in cocaine addicts (Volkow and Fowler, 2000). Cocaine addicts show abnormal evaluations of futures (Coffey et al., 2003; Konova et al., 2012) and cognitive inhibition (Barros-Loscertales et al., 2011a; Fernandez-Serrano et al., 2012; Lane et al., 2007), and these are underpinned by deficits in inhibitory prefrontal circuitry, as measured by functional

(Barros-Loscertales et al., 2011a; Garavan et al., 2008; Hester and Garavan, 2004; Kaufman et al., 2003) and structural (Barros-Loscertales et al., 2011b; Ersche et al., 2013, 2011; Franklin et al., 2002; Moeller et al., 2005; Schlaepfer et al., 2006) neuroimaging. Directly stimulating PFC via optogenetics in rats (Chen et al., 2013) and via repetitive transcranial magnetic stimulation (rTMS) in humans (Camprodon et al., 2007) results in decreased cocaine cravings. Remarkably, addicts who are able to successfully abstain from cocaine abuse show an intact inhibitory control network indistinguishable from non-users (Bell et al., 2013), indicating these inhibitory networks may be recoverable. This suggests that strengthening the prefrontal networks may aid in successful cocaine abstinence.

The brain networks involved in craving and suppressing must be isolated for each participant individually. I can leverage tasks known as functional localizers to isolate the specific brain regions. In the crave localizer, participants are presented blocks of images of cocaine and other blocks of images of natural scenes (**Figure 5.19A**). A contrast can be performed to determine which brain areas activate more when the participant is viewing and actively craving cocaine images compared to when just viewing natural scenes. This isolates the craving network. To localize the suppression network, participants perform a task that requires cognitive suppression and engagement of the frontal cortex (**Figure 5.19B**). This localizer is known as the continuous perform GO-NOGO task, in which participants must press a button every time a new image is presented (GO); however, when any image is a repeat of the immediately previous

image, the participant must withhold from pressing (NOGO) (Bell et al., 2014). By contrasting successful NOGO trials from GO trials, I can isolate the regions of the brain involved in cognitive suppression specific for each individual.

Once the corresponding brain regions have been localized for both craving and suppressing, I can now perform the feedback runs. The participant in the scanner will be shown images of cocaine and asked to suppress their cravings. Average brain activity within the *crave* and *suppress* networks can be computed for each individual at each image acquisition (every 2 seconds). I can summarize how much a participant is craving or suppressing at any given instant with the relative ratio of craving activity to suppressing activity (**Figure 5.20**).

This ratio at every image acquisition can be displayed to the participant in the form of a speedometer, thus providing feedback to the participant of how well they are suppressing. I do not instruct the participant to use any particular strategy to successfully suppress. Rather, participants iterate over their mental space until they can converge on a strategy that allows their brain activity in their suppression network to override the craving network. Such an implicit method allows a diversity of possible strategies tailored for each individual; some participants may think the impact cocaine as had on their family, others may reflect on the financial consequences, and still others may remember the horrors of incarceration. Each individual explores which strategy works best and hones that approach to fight cocaine cravings.

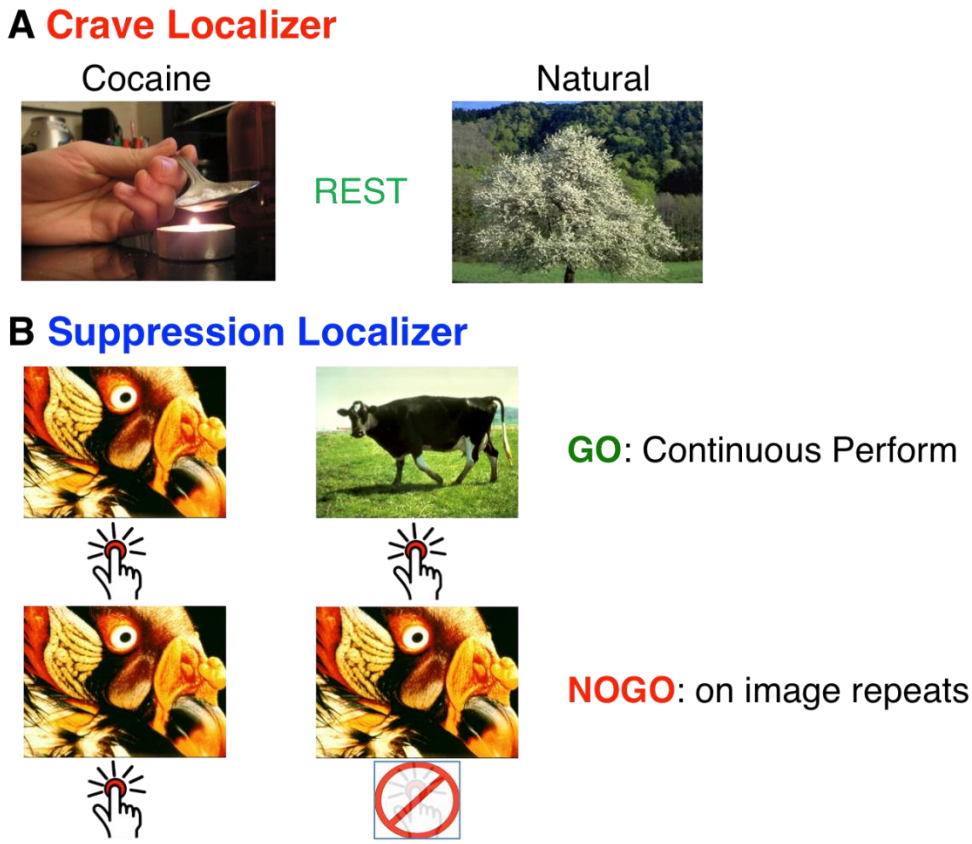

Figure 5.19 Experimental Localizers

Functional localizers are used to isolate the brain regions involved in craving and suppressing for each individual participant, enabling targeted therapy. A. To localize the brain regions involved in craving, participants will view blocks of cocaine images and blocks of natural scene images. By contrasting the two blocks, we can determine which regions of the brain are involved in craving. B. To localize the brain regions involved in suppressing, participants perform a GO-NOGO task (Bell et al., 2014). Neutral images (from International Affective Picture System [IAPS](Lang et al., 2008)) are presented every 1 s, and the participant must press immediately following every image presentation (GO). But he participant must inhibit pressing when the image is repeat of the previous image (NOGO). Contrasting successful NOGO and GO trials localizes the suppression network.

$$\frac{CRAVE - SUPPRESS}{CRAVE + SUPPRESS}$$

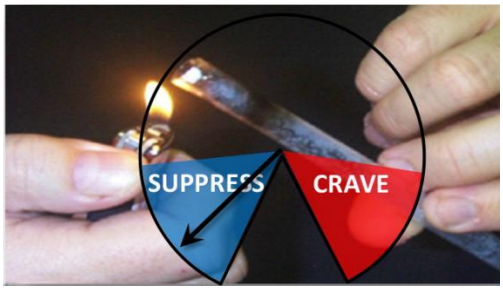

Figure 5.20 Neurofeedback

The relative ratio of the brain activity in the crave and suppress networks is used to control the position of the arrow on the speedometer that the participant sees in the scanner.

I plan to recruit 15 chronic cocaine dependent users to enroll in a longitudinal 3-week study. Participants will come to the Baylor College of Medicine every Monday, Wednesday, and Friday for three weeks to undergo scanning at the Center for Advanced Magnetic Resonance Imaging (CAMRI). Each day, participants will first run the localizer tasks and then perform 5 consecutive 5-minute runs of the feedback. I can then measure how each participant progresses in their ability to suppress cocaine cravings. In addition, I will perform urinalysis before scanning every day to check whether patients are able to stop using cocaine.

5.3.2.2 Potential Concerns

Cocaine-dependent participants are often difficult to recruit longitudinally. Further, the risk of relapse may hinder longitudinal recruitment. To address these issues, I will implement the following measures of contingency management, which have shown promise in aiding with successful reduction in cocaine use (Knapp et al., 2007). (1)

Contingency management for abstinence: Patients will be required to give a urine sample at the start of each day. If the urine is clean of all illicit drugs, the patient will be awarded a $5.00 bonus each day the urine analysis is negative. (2) Contingency management for suppression during task: Contingency management will be built into the experimental design. The longer the patient is able to suppress cravings, the more points she will earn. These points will accumulate and be redeemed for extra cash payment each day for a maximum of $5.00 extra/day. These two contingency management approaches will encourage patients to abstain from cocaine use and to find ways to maintain suppression of their cravings during the task.

I have completed the entire 3-week study in one participant, establishing feasibility of this approach. First, the participant was able to abstain entirely from cocaine for the duration of the study. The participant expressed great financial need and was committed to remain clean to earn the additional contingency management incentives. Second, the participant's ability to suppress improved over time (**Figure 5.21**). She did, however, encounter some potential relapses in craving on the last day when she was unable to successfully suppress cravings. Nonetheless, she was able to develop and employ a cognitive strategy to help her overcome cocaine cravings.

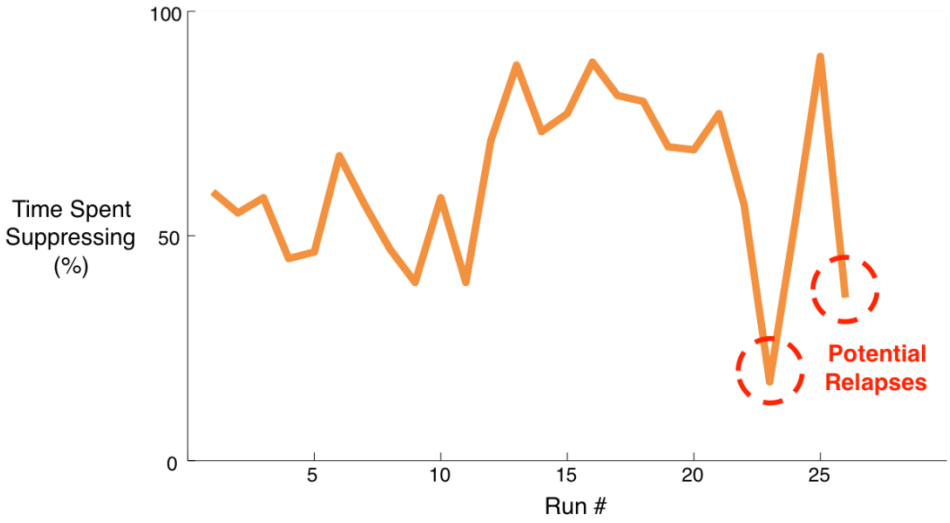

Figure 5.21 Longitudinal Assessment

Preliminary data: A cocaine-dependent individual showed an ability to suppress her cocaine cravings via rt-fMRI over a longitudinal 3-week study. Her time spent suppressing increased dramatically just before run # 15. However, towards the end of the study, the participant seemed to relapse and was unable to move the meter consistently to the suppression side. Despite these cognitive relapses, the participant was still able to abstain from cocaine entirely for the duration of the study, as measured by urinalysis.

5.3.3 Potential Impact

Controlled substances enter the criminal justice system from every angle (**Figures 5.15-17**). To reduce crime, we must offer people with substance use disorders something that science and medicine have failed to provide: a way to reduce illicit drug dependence. I am proposing to build a behavioral therapy that leverages physiological signs to guide cocaine-dependent individuals to learn how to suppress their cravings. In turn, this regimen can help people reduce cocaine use, alter fundamental decision-making, and ultimately reduce crime and the burden on the criminal justice system (**Figure 5.22**).

In my previous work, I have shown alterations in the structure of the brain due to cigarette smoking (Savjani et al., 2014). I utilized diffusion tensor imaging (DTI) to measure disruptions in connections between brain circuits. My preliminary data now show a weakened connection in inhibitory circuitry in 16 cocaine-dependent participants (**Figure 5.23**). Further, I can employ DTI to objectively determine if feedback therapy will help restore structural changes, facilitate reductions in cocaine use and thus reduce crime.

Figure 5.22 Experimental Training

Reducing crime requires fundamentally guiding people suffering from substance use disorders to learn how to suppress their cravings.

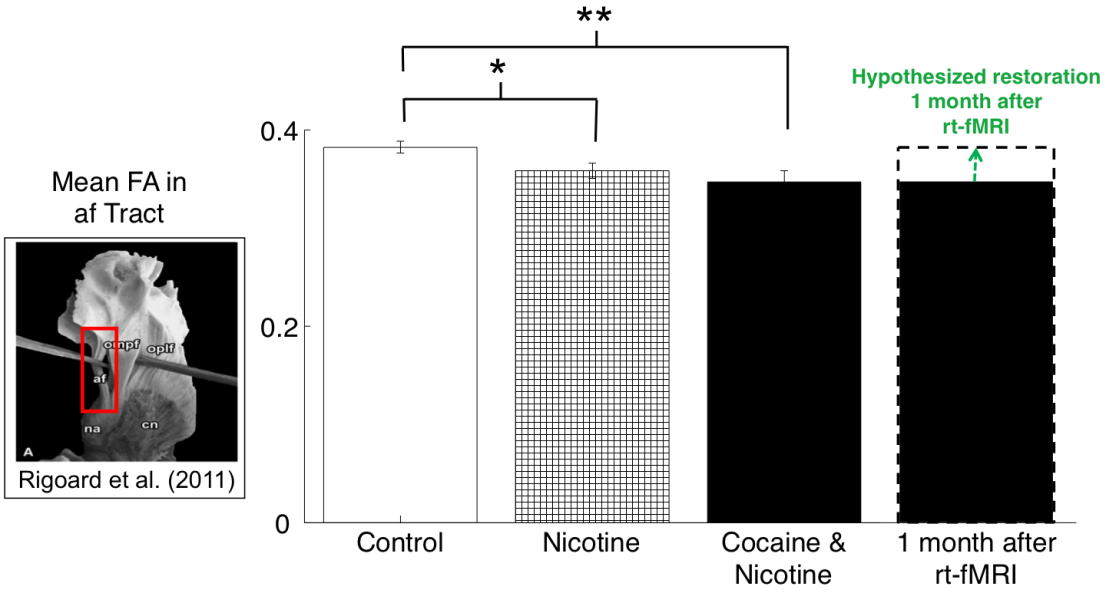

Figure 5.23 Structural Restoration After Training

Cigarette smoking and cocaine use are linked with measurable brain alterations, which might serve as a metric Chronic cigarette smokers have significantly decreased FA within accumbo-frontal (af) WM tracts (* $p < 0.05$), and cocaine dependent patients show further decreases in FA compared to controls (** $p < 0.01$). Via the rt-fMRI therapy, cocaine-dependent individuals may be able to restore the deficits within the af tract, allowing better top-down control of cocaine craving. Picture inset: af tract identified by fiber dissection in a human specimen (Rigoard et al., 2011)

CHAPTER VI

THE DAMAGED BRAIN

6.1 Introduction

One of the greatest challenges in military veterans is to find quantitative, objective markers of traumatic brain injury (TBI) using non-invasive techniques. Neuroimaging provides such an opportunity but has thus far failed to robustly diagnose many patients with mild TBI experiencing symptoms including memory and concentration problems. Even when hundreds of neuroimaging exams are acquired in the civilian population, machine learning approaches on those exams yield prediction accuracies below 70% (Mitra et al., 2016). The approaches lack the statistical power to be of diagnostic value. Further, the military population is more complex with several comorbidities, even in patients without TBI (e.g., post-traumatic stress disorder (PTSD), depression, substance abuse).

Brain imaging studies, however, can still enhance understanding of the pathophysiological changes associated with TBI. Gray matter cortical thickness has been one measure used to characterize several neuropsychiatric conditions such as Alzheimer's Disease and Williams Syndrome (Thompson et al., 2005). Cortical thickness measures are beginning to provide some insight on brain morphological changes following a TBI. In animal models, rats who were subjected to repeat weight-drop showed reduction in cortical thickness directly beneath the zone of impact by 46%

two weeks after injury(Goddeyne et al., 2015). In humans, young adult civilians with recurrent sports TBI showed thinning in insula, right middle temporal gyrus, and right entorhinal area (List et al., 2015). Further, changes after TBIs suffered from motor vehicle collisions resulted in frontal cortex thinning 3 months after injury (Wang et al., 2015). How long these changes in direct cortical thickness measures persist is not exactly known, and at least one study was not able to detect changes after 1 year (Dean et al., 2015).

To date, only three studies to our knowledge have explored cortical thickness in military TBI populations, and all studies had significant comorbidities (Wilde et al., 2015). In one study, patients had significant hearing loss and associated thinning in Heschl gyrus (Tate et al., 2014), and in another study, significant PTSD and lifetime stress were confounding factors (Corbo et al., 2014). PTSD was also found to play additive role in cortical thinning in patients with comorbid TBI (Lindemer et al., 2013). These comorbidities make it difficult to make inferences about the effects of TBI alone on cortical thickness, highlighting the need for well-controlled studies. Further, given the large heterogeneity across individuals, it may be difficult to find consistent group differences in averaged univariate cortical thickness measures alone.

An alternative approach is to see if patterns of structural brain metrics can predict demographics, such as age. Recent work has revealed potential accelerated brain aging after TBI in the civilian population. Using a gray matter model built from T1-weighted

MRI images alone from a large cohort of healthy controls, participants with TBI were predicted to be 4.66 years older than their actual age (Cole et al., 2015). This over-prediction of age was unique to participants with TBI and was not seen in a test set of healthy controls scanned on the same scanner.

Here, we sought to see if accelerated brain aging occurs after military mTBI. We measured cortical thickness using Advanced Normalization Tools (ANTs) (Avants et al., 2011), which has previously been shown to be one of the most accurate tools in predicting brain age from T1-weighted images in healthy controls, even outperforming the commonly used FreeSurfer (Fischl and Dale, 2000) across many measures of error (Tustison et al., 2014), a potential advantage over previous studies in military TBI (Corbo et al., 2014; Tate et al., 2014). We built 4 models to predict brain age from cortical thickness measures in military patients with TBI and military patients without TBI, an important control to attempt to isolate the effects of TBI on brain aging in the veteran population.

6.2 Materials and Methods

6.2.1 MRI Acquisition

The T1-weighted images for the veteran test sets (both participants with TBI and controls) were acquired on a Siemens 3T TIM Trio using a 3D MPRAGE sequence with the following parameters: TE=2.8 ms, TR=2530 ms, TI=900 ms, flip angle = 10°,

FOV=256x256x220 mm, Matrix=256x256x220, NEX=1, Bandwidth=180Hz/pixel, iPAT=2, resolution=1.0x1.0x1.0 mm.

Diffusion weighted imaging (DWI) data were acquired to facilitate multi-modal template construction. DWI Data were imaged using a single shot twice-refocused spin-echo echo-planar sequence in the axial plane with the following parameters: TE=82 ms, TR=8700 ms, FOV=256x256 mm, matrix = 128x128, slice thickness/gap = 2.0/0.0 mm, NEX = 1, b-value=1000 s/mm2, Bandwidth=1396 Hz/pixel. Diffusion gradients were applied along 64 directions.

6.2.2 Healthy Control Training Set

We trained age prediction models from cortical thickness measurements derived from previous sets of healthy control populations. Building models with a large number of participants from a variety of scanners and differing protocols allows construction of robust age-prediction models. Particularly, we used cortical thickness measurements derived from four publicly available data sets: Information eXtraction from Images (IXI), Nathan Klein Institute (NKI), Multi-Modal MRI Reproducibility Resource (MMRR), and Open Access Series of Imaging Studies (OASIS). The cortical thickness pipeline had already been previously run on each of these data sets (Tustison et al., 2014), and the processed data was retrieved online (https://github.com/ntustison/KapowskiChronicles). To build our model, we restricted the age in all datasets to be within 18 to 60 years, as our military population was

confined to within this age range, and the aging process may vary greatly at the extremes. Ultimately, we were able to use 762 healthy control participant data (36.32 ± 12.54 years-old; 373 Males) to train our models with to predict age from cortical thickness measures.

6.2.3 Participants

The TBI test set consisted of 92 participants (29.67 ± 7.02 years [range: 22-57]; 88 males) with TBI (89 mild, 3 severe) experienced in the Iraq and Afghanistan wars (Operation Iraqi Freedom/Operation enduring Freedom; OIF/OEF). The military control test set consisted of 34 OIF/OEF veterans without TBI (31.15 ± 9.17 years [range: 22-55]; 30 males). All participants were scanned at the Iowa City VA Medical Center with an identical scanning protocol.

6.2.4 Constructing a Multivariate Population-Specific Template

The TBI test set consisted of 92 participants (29.67 ± 7.02 years [range: 22-57]; 88 males) with TBI (89 mild, 3 severe) experienced in the Iraq and Afghanistan wars (Operation Iraqi Freedom/Operation enduring Freedom; OIF/OEF). The military control test set consisted of 34 OIF/OEF veterans without TBI (31.15 ± 9.17 years [range: 22-55]; 30 males). All participants were scanned at the Iowa City VA Medical Center with an identical scanning protocol.

6.2.5 Constructing a Multivariate Population-Specific Template

A multivariate population-specific template was built using 10 random participants without TBI (**Figure 6.1**). Both the T1-weighted images and the diffusion-weighted images (DWI) were used in construction of the template. Using the DWI images for multivariate template construction allows dense features within the white matter to be used for the registration. The DWI images were processed using FMRIB Software Library [FSL v5.0.9] (Jenkinson et al., 2012; Smith et al., 2004) and batched and parallelized using the Neuroimaging in Python Interfaces and Pipelines (Nipype) (Gorgolewski et al., 2011) with customized scripts we previously built (Savjani et al., 2014). First, raw DWI images were motion corrected by linearly registering each DWI volume to the first b0 = 0 volume using FSL flirt (Jenkinson et al., 2002; Jenkinson and Smith, 2001) with 6 degrees of freedom (DOF) and appropriately rotating the b-vectors (Leemans and Jones, 2009). Second, the images were corrected for eddy current distortions using FSL's FMRIB's Diffusion Toolbox FDT (Behrens et al., 2003) eddy_correct. Third, the b0=0 volume was brain extracted (FSL bet (Smith, 2002)) to generate a brain mask. Diffusion tensors were fitted to the brain extracted DWI using FSL FDT (Behrens et al., 2003) dtifit. The fractional anisotropy (FA) volume was then registered to the participant's T1 anatomical scan (**Figure 6.2**) using ANTs (antsIntermodalityIntraparticipant.sh). The registered FA volume (relative weight 1.0) and the T1 anatomical scan (relative weight 1.25) were then used to build the multivariate template via ANTs (antsMultivariateTemplateConstruction2.sh (Avants et al., 2010)).

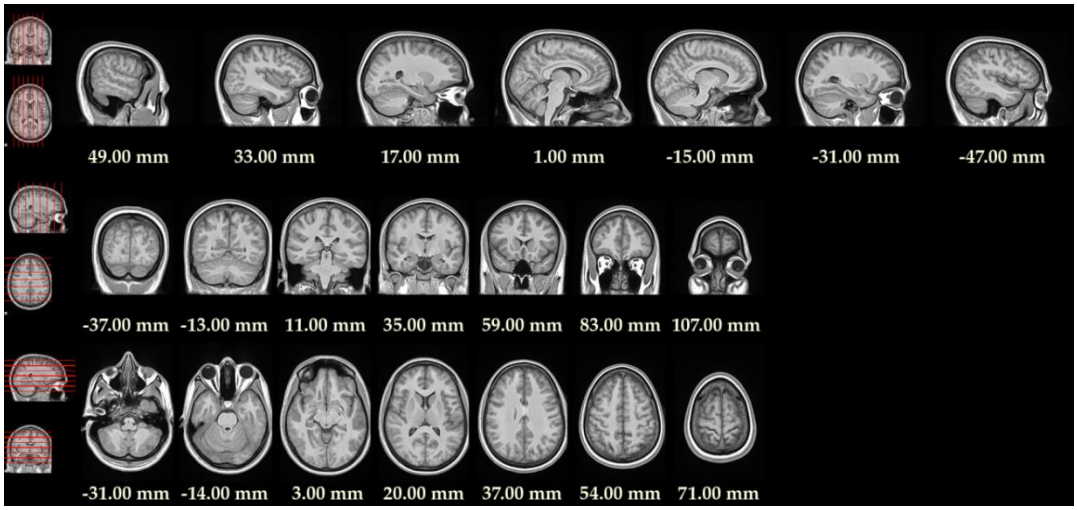

Figure 6.1 Brain Template

We used a population-specific template for military participants.

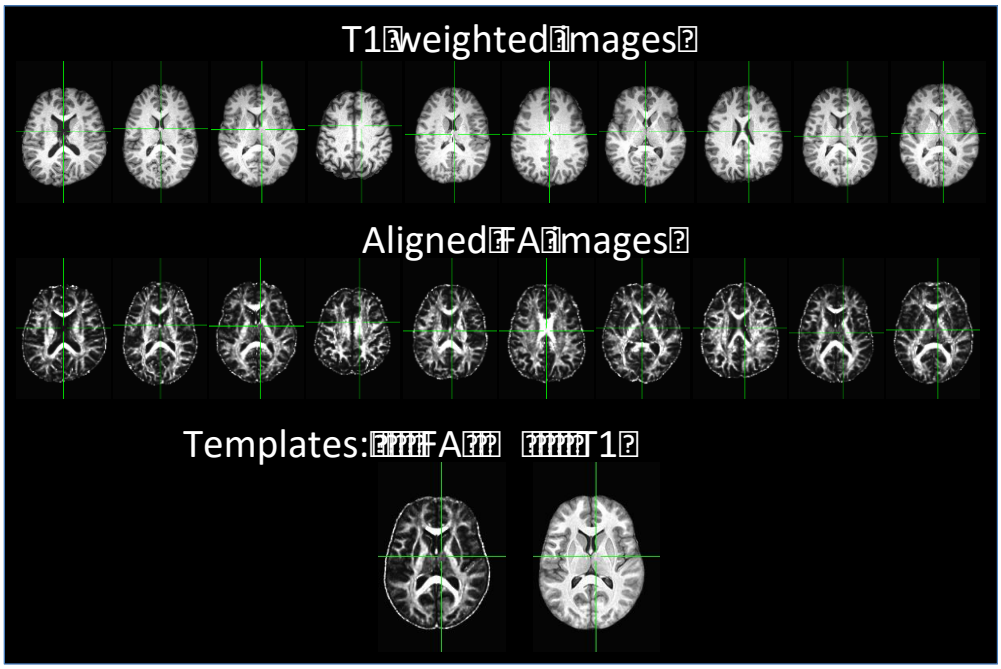

Figure 6.2 Multivariate Template

We constructed a multivariate template from FA and T1 volumes in 10 participants without TBI.

6.2.6 Building Template Priors

Brain tissue priors were built for our population-specific template brain (**Figure 6.3**) using the same approach used for the healthy control templates (Tustison et al., 2014) (we used the general guidelines found in this example: https://github.com/ntustison/antsCookTemplatePriorsExample). First, template-based brain extraction (*antsBrainExtraction.sh*) was performed on our template brain using the OASIS template, which was well-matched to our anonymized, defaced T1 dataset in our veteran patients. Then, 20 of the OASIS participants who had manually-drawn cortical labels (Klein and Tourville, 2012) (http://www.mindboggle.info/data.html) were registered to the template, and the labels were fused (*antsJointLabelFusion.sh* (Wang et al., 2013)). The fused labels allowed for construction of 5 main template priors: gray matter, cerebrospinal fluid (CSF), deep gray matter, brain stem, and cerebellum. The white matter was not adequately labeled in the original datasets, so the template brain was segmented (*antsAtroposN4.sh*). The white matter posterior was used to generate the remaining prior needed for deriving the cortical thickness pipeline.

6.2.7 Cortical Thickness Measurements with ANTS

We derived cortical thickness measures with ANTs from our military participants with a near-identical procedure that was previously used for the healthy control participants (Tustison et al., 2014). Briefly, the cortical thickness pipeline (*antsCorticalThickness.sh*) was run for each participant using our population-specific template priors. Then, multi-atlas label fusion (MALF, *antsJointLabelFusion.sh*) was run on each participant to get

cortical labels (31 for each hemisphere, 62 total) for each participant using the same subset of hand-labeled OASIS participants describe above. Then, the thickness was averaged for each of the 62 cortical labels, giving 62 scalars for each participant representing the average cortical thickness in each brain region. Finally, the total intracranial volume for each participant was also computed using each participant's brain extracted mask (ANTs: *LabelGeometryMeasures*).

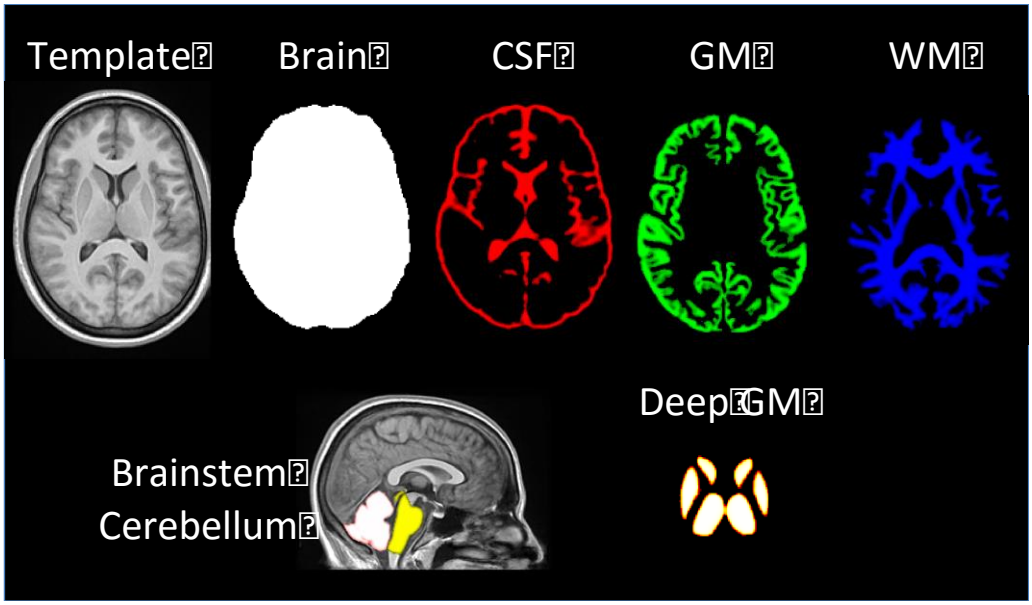

Figure 6.3 Brain Tissue Priors

Brain tissue priors for the population-specific template for military patients were created. These template priors were needed to run cortical thickness analysis in ANTs.

6.2.8 Models for Predicting Brain Age

Using the healthy control data (n = 762), we built four regression models in MATLAB (version 8.6 R2015b, The Mathworks Inc., Natick, MA) to predict age from cortical

thickness: linear regression (LR), support vector regression (SVR), Gaussian process regression (GPR), and random forest regression (RFR). In each model, the features consisted of the 62 average cortical thickness measurements (in mm) for each labeled brain region, as well as the gender and the total intracranial volume, yielding a total of 64 features for each participant.

The LR model (MATLAB *fitlm*) was identical to the model used in the study comparing ANTs to FreeSurfer.(Tustison et al., 2014) The model is:

$$AGE \sim VOLUME + GENDER + \sum_{i=1}^{62} T(DKT_i) \quad (1)$$

where T(DKTi) is the average thickness value in a given cortical brain region. The SVR model (*fitrsvm*) was trained with a linear kernel, and the features were standardized (z-scored) prior to model fitting. The GPR model (*fitrgp*) was inspired by the civilian TBI study (Cole et al., 2015), and the model was trained with standardized features, a linear basis function, and with the fully independent conditional approximation prediction method. And lastly, the RFR model (*TreeBagger*) was trained using 200 trees and default options, similar to the implementation in R used previously (Tustison et al., 2014).

6.2.9 Model Comparison via Cross-Validation

In order to get reliability measures for each of the four models we trained, we performed model comparison using cross-validation (Tustison et al., 2014). We randomly split the

healthy control training data into halves, one set used for training the models and the other for testing. We computed the root-mean-square error (RMSE) on the predicted ages for each model. We repeated this procedure on 10,000 permutations and plotted RMSE densities for each model to facilitate visual comparison.

6.2.10 Predicting Age in the Military Patients

All four regression models were trained on the full healthy control training data. The models were then used to predict age in the veteran population, for participants with TBI and for participants without TBI. We then computed the predicted age difference (PAD) (Cole et al., 2015) by subtracted the predicted age from the patient's actual age. We finally compared the PAD for patients with TBI and compared them to the PAD of patients without TBI.

6.3 Results

6.3.1 Cortical Thickness Measures and Labels

For each participant in our military participant population (n = 126), we computed cortical thickness (**Figure 6.4**) and performed MALF to get cortical labels (**Figure 6.5**). We then averaged the cortical thickness across each label (62 cortical brain areas) for each patient, yielding 62 scalar values for each patient. We then added two additional features: total intracranial volume and patient gender, which yielding a feature matrix of 126 patients by 64 features.

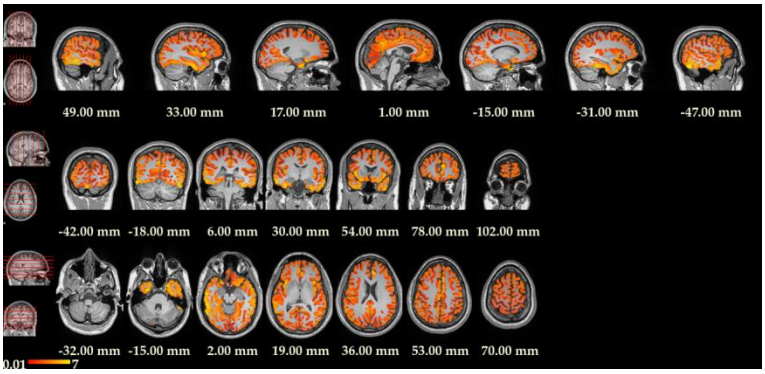

Figure 6.4 Cortical Thickness

Cortical thickness for a representative military participant is shown here. Thickness is represented as a Red-Yellow colormap from 0.01 to 7.00 mm

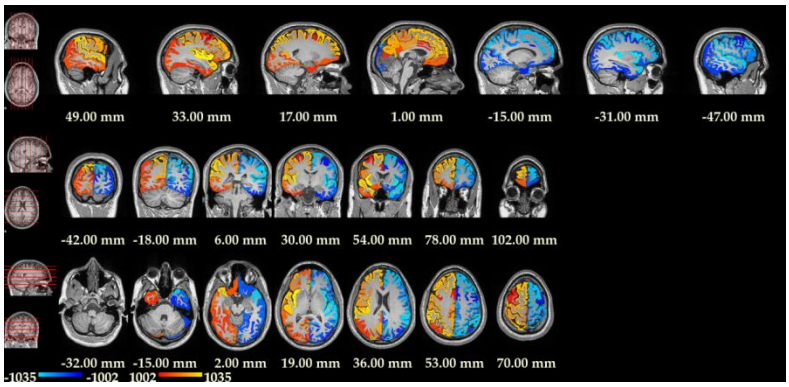

Figure 6.5 Cortical Labels

Cortical labels for a representative military participant. Cool colors are on the left hemisphere, and hot colors are on the right hemisphere. Each hemisphere has 31 cortical labels.

We then plotted the mean and standard deviations of the cortical thicknesses for all labels for left and right hemisphere and comparing participants with TBI to participants without TBI (**Figure 6.6A**). By visual inspection, it appeared that the means thicknesses in several brain regions were slightly lower in participants with TBI compared to those

without. To see if this was the case, we computed the multivariate Hotelling's T^2 test (using R: "Hotelling" package (Curran, 2013)) comparing the cortical thicknesses between the two groups for each hemisphere separately. We computed the null distributions by randomly permutating participants across labels (TBI or no TBI) with 10,000 permutations and then computed scaled T^2 stat and p-values. We did not find significant differences ($p >> 0.05$) at the group level in cortical thicknesses between patients with TBI and those without (**Figure 6.6B**).

6.3.2 Training and Evaluating Models on Healthy Control Data

We then trained the 4 regression models using the previously processed data (Tustison et al., 2014) on healthy controls from publicly available datasets. This allowed us to construct models that could take in cortical thickness measures from our patient population and predict age. We first plotted the actual age vs. the predicted age for each model (**Figure 6.7**). All models show general linear positive correlation.

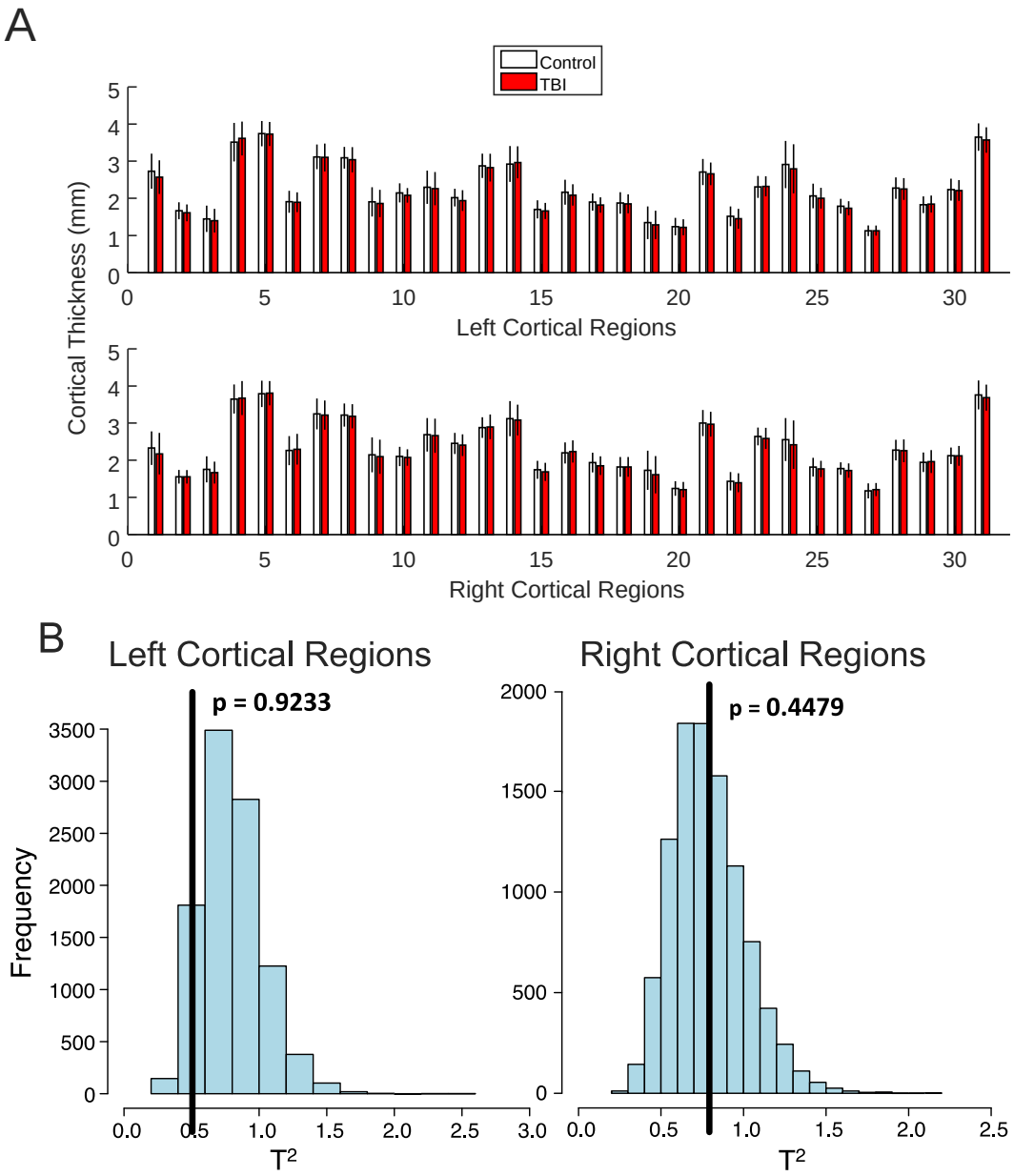

Figure 6.6 TBI vs. Control: Cortical Thickness

Mean cortical thicknesses do not differ between participants with TBI and participants without TBI. A. Mean ± std for each of the 31 cortical brain regions for left (top) and right (bottom) hemispheres plotted for participants with TBI (red) and without (white). B. Multivariate Hotelling's test reveals no significant difference in either hemisphere in cortical thickness between patients with TBI and without TBI. Blue bars show the histogram of scaled T2 statistic of 10,000 null permutations, and solid black lines show observed scaled T2 statistic.

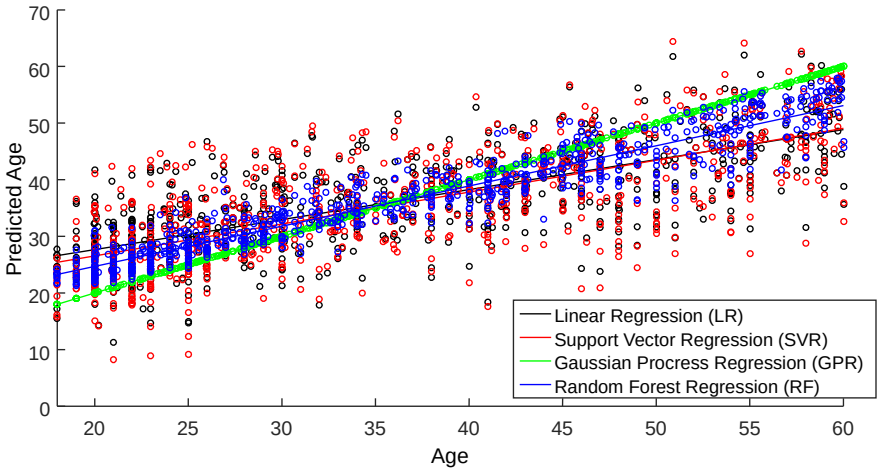

Figure 6.7 Model Training

Cortical labels for a representative military participant. Cool colors are on the left hemisphere, and hot colors are on the right hemisphere. Each hemisphere has 31 cortical labels.

Then, in order to examine which features the models were utilizing to make age predictions, we computed the absolute value of the beta weights (LR, SVR, and GPR) or the mean increase error (RF) and plotted the ranked values (**Figure 6.8**). The mean increase error for the RF model measures the increase in prediction error if the values of that feature are permuted across the out-of-bag observations, averaged across all 200 trees (*OOBPermutedPredictorDeltaError*).

To help visualize the important brain labels driving the LR age model, we overlaid the significant ($p < 0.05$, two-way one-sample t-tests) signed beta weights onto the population-derived template brain (**Figure 6.9**). Decreases in cortical thicknesses in several frontal areas predicted an older age.

We then performed model comparison by cross-validating each model on 10,000 random half-splits and computing the RMSE on each permutation (**Figure 6.10**). The RMSE was the lowest for the RF model, intermediate for the GPR model, and higher for the LR and SVR models.

6.3.3 Predicting Age in the Military Population

The fully trained models were then used to predict age in the military population. The predicted age difference (PAD) was significantly ($p < 0.05$, two-sample, one-way t-tests) greater for participants with TBI compared to those without for all 4 models (**Figure 6.11**). The t-tests were run with permutations testing (n = 10,000 permutations). The LR, SVR, and GPR models had median PAD at close to zero for participants without TBI, and median PAD scores greater than zero for participants with TBI. The RF model, however, predicted greater ages for both participant groups, but still a greater PAD for participants with TBI. All four models suggest a process of potential accelerated aging in military participants with TBI.

To check for systematic biases at different ages, we created Bland-Altman plots for each model for both participants with TBI and without TBI separately (**Figure 6.12**). These plots show that the age tends to be over-predicted in participants with TBI in the mid-30s to mid-40s.

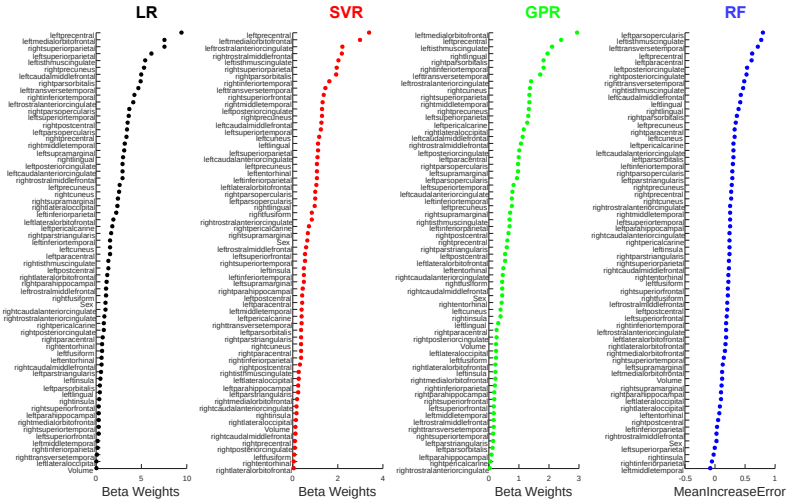

Figure 6.8 Model Evaluation

Feature importance for all 4 models. Absolute value of beta weights are shown for the linear, support vector, and Gaussian process regression models, and the average error increase is shown for the random forests model.

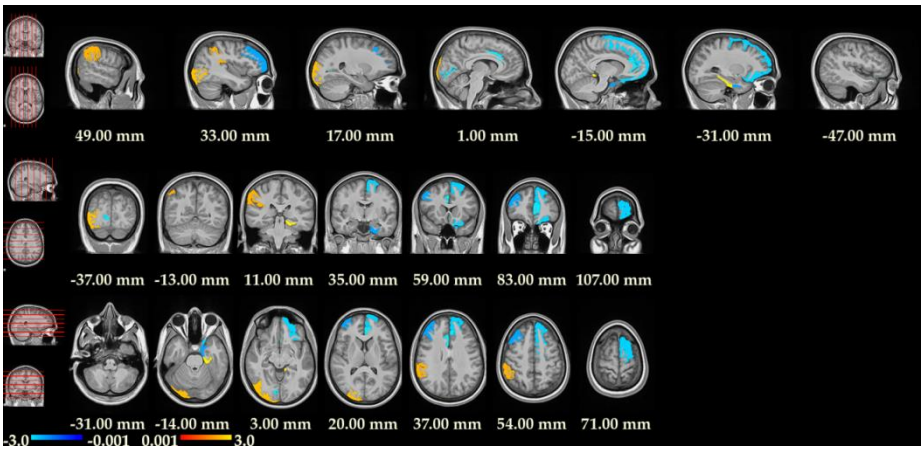

Figure 6.9 Beta Weights

Significant ($p < 0.05$) beta weights for the linear regression (LR) model. This included 7 regions where the thickness negatively correlated with age (cool colors: left caudal middle frontal, left isthmus cingulate, left precentral, left rostral anterior cingulate, left transverse temporal, right parsorbitalis, right precuneus) and 3 regions where the cortical thickness positively correlated with age (hot colors: left medial orbitofrontal, right inferiortemporal, right superiorparietal).

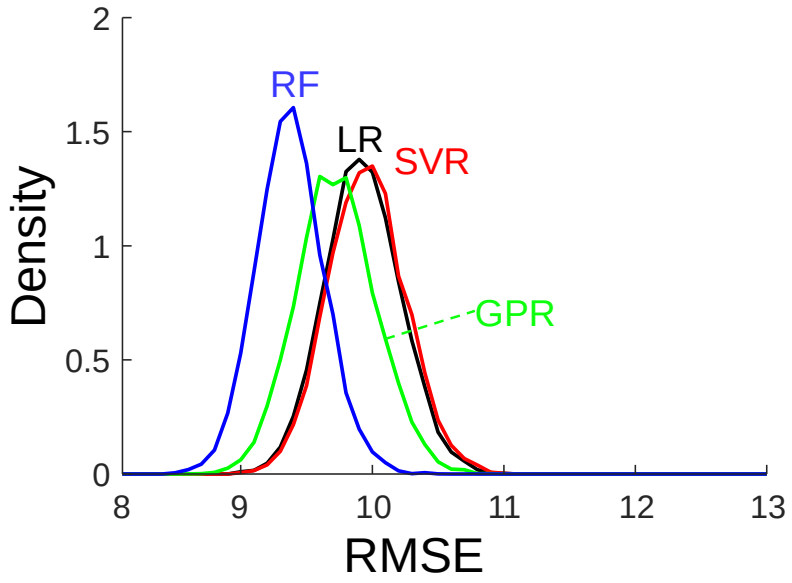

Figure 6.10 Model Performance

Model comparison on training data using 10,000 permutations of random half-split cross validation.

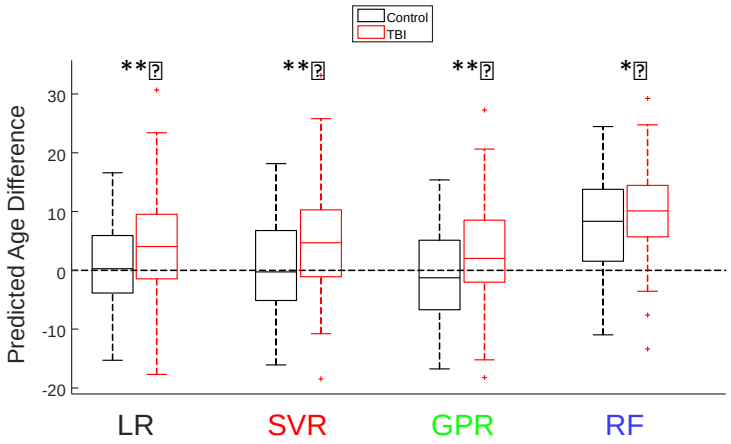

Figure 6.11 Model Testing

All 4 models predict higher age difference for participants with TBI compared to participants without TBI. *: $p < 0.05$ and **: $p < 0.01$ in two-sample one-way t-test using permutations testing with 10,000 permutations (LR: $p = 0.0050$; SVR: $p = 0.0027$; GPR: $p = 0.0040$; RF: $p = 0.0313$).

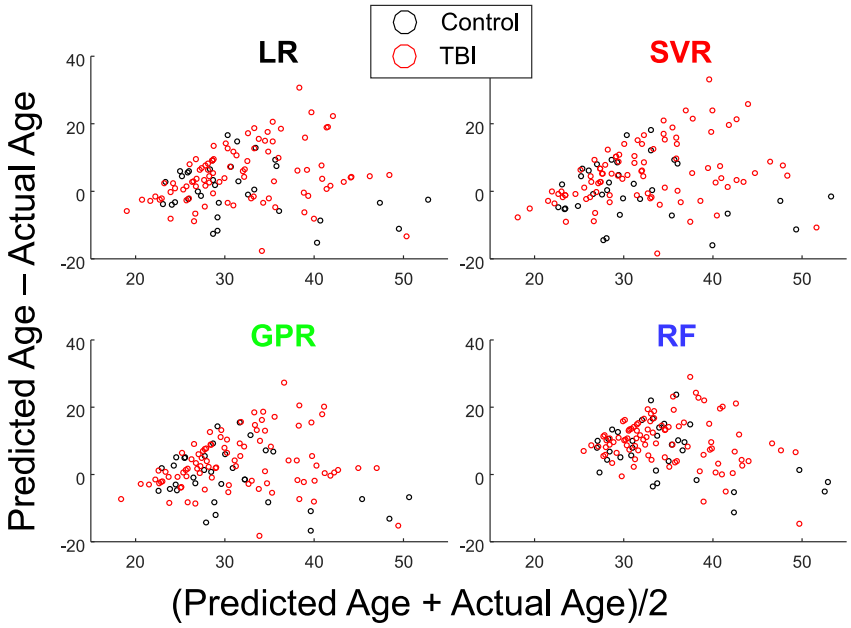

Figure 6.12 Bland-Altman Plots

Bland-Altman plots for each model. The ages of military participants with TBI (red) appear to have predicted age differences at mean ages in the mid-30s to mid-40s.

6.4 Discussion

Finding objective *in vivo* markers of combat-related TBI has proven challenging. The heterogeneity of the trauma to the head combined with the individual differences in patient morphology, genetics, and functional recovery obscure the ability to reliably detect parenchymal alteration and predict outcomes. Here, we used population (rather than individual) effects to probe the pathophysiology of military TBI. Specifically, we examined if participants with combat-related TBI had an altered trajectory on brain age, as compared to a comparison group of veterans who did not experience TBI. Our data and analysis indicate that military TBI may be associated with accelerated brain aging in

that decreases in cortical thickness were greater in the participants with TBI. More severe TBI itself has been implicated in cortical thinning, likely as a result of neuronal loss using histopathological analysis, particularly in patients with diffuse axonal injury (Maxwell et al., 2010). Additionally, aging is associated with decreased cortical thickness, particularly in the frontal lobes (Fjell et al., 2009; Fotenos et al., 2005).

Our approach builds upon two seminal studies. First, Cole et al. (2015) showed that a Gaussian process regression model trained on healthy controls over- predicted the age of civilian participants with TBI but not on healthy controls scanned on the same scanner (Cole et al., 2015). Our data extends this finding to the military population, showing that the GPR model, as well as three other models, all over-predict age in veterans with TBI. Importantly, we also scanned and predicted age in *military controls* in whom all models predicted ages that were significantly less than that of participants with TBI. This is an important finding, as the military arena introduces many stressors with psychiatric sequela (e.g., PTSD, depression, substance abuse) that could potentially lead to altered brain morphology (Li et al., 2016; Wolf et al., 2015). Our data show that TBI in previously deployed veterans is associated with increased brain aging, more than in deployed veterans who did not experience a TBI. It is important to note, however, that we cannot conclude causality; that is, it is unknown whether the TBI (either alone or in combination with other factors and comorbidities (Liu et al., 2012)) actually induced accelerated brain aging. Nevertheless, these findings are provocative because of concerns related to the long-term effects of combat exposure; such concerns have also

been documented in former athletes with repeated exposure to multiple concussive blows manifesting cortical thinning disproportionate to age (McKee et al., 2009; Omalu et al., 2011; Tremblay et al., 2013).

Second, our approach used cortical thickness derived from ANTs to predict age. We found this approach compelling, particularly after Tustison et al. (2014) showed that ANTs outperforms FreeSurfer when predicting in age in healthy controls (Tustison et al., 2014). By averaging cortical thickness across labeled brain regions, we explicitly reduced the number of dimensions and did not rely on kernel operations (Cole et al., 2015) or create black-box decoders. This allowed us to compute the relative contributions of each cortical region for each model (**Figure 6.8**) to understand and verify which brain regions were driving age prediction, which is an extension of previous work. Thinning in many frontal brain regions predicted greater brain age (**Figure 6.9**) in the healthy control training set, a well-known finding (Jernigan et al., 1991; Raz et al., 1997; Salat et al., 2004; Sowell et al., 2003) replicated here. Brain age was over-predicted using these strongly weighted frontal brain regions, suggesting that finer examination of frontal areas including volume and connectivity may help to build better models and better understand the pathophysiology of TBI.

We trained 4 different models that each showed an over prediction of age in the military TBI participants. There were, however, differences in the model behaviors. The cross-validations indicated that the RF model had distinctly the lowest RMSE, yet the RF

model over predicted the age of the military participants without TBI, not just the participants with TBI, a performance unique to this model. Perhaps this actually represents aging closer to ground truth, and the RF model is able to capture the other comorbidities associated with military service. Nonetheless, the RF model still had a greater PAD for participants with TBI compared to those who did not.

6.5 Conclusions

We used cortical thickness measures derived using ANTs to assess group differences in military participants with and without TBI. Four different regression and machine learning models each predicted the age to be greater in participants with TBI compared to their actual age. Further, the predicted age difference was significantly greater in military participants with TBI compared to military participants without TBI, and the use of veteran controls is a strength of the current study Our results extend previous work by showing that military TBI is associated with accelerated brain aging.

CHAPTER VII

SOCIAL NEUROSCIENCE[*]

7.1 Are Corporations People Too? The Neural Correlates of Moral Judgments About Companies and Individuals

7.1.1 Introduction

As individuals organize into groups, the collective unit gains its own representation. For example, corporations like Microsoft and AT&T come to embody a distinct entity, separate from the people who comprise them. Little is known about how our brains process information about collective units such as corporations. As an organization comes to form an identity, a question arises: are corporations and their actions regarded as social beings or as inanimate objects? Though this question has been largely ignored in the cognitive neuroscience literature, it has become an important topic in legal systems and public opinion. For example, the American legal system has extended the rights of individuals to corporations ("corporate personhood") and held corporations, as a collective unit, liable ("corporate liability"). In a controversial decision in *Citizens United v. Federal Election Commission* (2010), the United Sates Supreme Court granted corporations the right to free speech. This decision stemmed from the court's opinion that the rights of individual citizens, ensured under the First and Fourteenth

---

[*] Reprinted with permission from "Are corporations people too? The neural correlates of moral judgments about companies and individuals." by Plitt M, Savjani RR, Eagleman DM, 2015. *Social Neuroscience*. 10, 113-125, Copyright 2015 Routledge Taylor & Francis Group.

Amendments, extend to corporations as well (Kang, 2010). More recently, the United States Supreme Court further extended corporate rights, allowing for-profit organizations to be exempt from a law that violates the owners' religious beliefs (Burwell v. Hobby Lobby, 2014).

The recent legal and popular attention to this topic motivates a further question: does corporate personhood parallel an underlying similarity in the way human brains represent corporations and individuals? Indirect evidence suggests that the mechanisms that determine our reactions to the behavior of large groups and to the behavior of individuals could overlap or even be identical. For example, people are equally likely to reciprocate favorably if given positive reinforcement from either a corporation (e.g., corporate sponsorship)(Harvey et al., 2010) or an individual (e.g., cooperation in game theory) (Rilling et al., 2002). Further, overlapping networks of brain activity are engaged whether the reciprocity is towards corporations (Harvey et al., 2010) or people (Rilling et al., 2002).

On the other hand, social reasoning areas of the brain are observed to decrease in activity if an entity is objectified. For example, the superior medial prefrontal cortex (SMPFC), a key component in social cognition(Amodio and Frith, 2006), is less active in impersonal moral or non-moral reasoning than personal moral reasoning (Greene et al., 2001) and, interestingly, while viewing dehumanizing images of homeless people and drug addicts (Harris and Fiske, 2006) or highly sexualized images of women (Cikara et al., 2011).

Collectively, these studies raise an open question of whether people objectify corporations or view them as a social being. No studies to date have directly compared how the brain responds when judging positive, negative, or neutral actions of corporations and the actions of individuals. To this end, we performed a vignette-based functional magnetic resonance imaging (fMRI) experiment. While in the scanner, participants rated their emotional response to short vignettes about the actions of people or corporations. In these vignettes, people or corporations performed pro-social actions (e.g. donating to charity), anti-social actions (e.g. lying or breaking the law), or neutral actions (e.g. buying a printer). To establish a control condition, a third category of vignettes described objects.

The brain invokes reciprocal inhibition, allowing people to think either socially or objectively (Jack et al., 2012). Moral emotional decision making tasks have been shown to strongly activate circuits involved with theory of mind (ToM) (Greene and Haidt, 2002; Hein and Singer, 2008; Jack et al., 2012; Knabb et al., 2009; Krauss, 2010; Mar, 2011; Moll et al., 2002; Moll et al., 2008), representing the thoughts and actions of other people. During non-social tasks, however, regions of the ToM network deactivate, and regions associated with working memory and objective reasoning such as the dorsolateral prefrontal cortex (DLPFC) and large portions of the parietal lobe including the intraparietal sulcus become more active (Greene et al., 2001; Jack et al., 2012). Given this apparent mutually exclusive framework, we hypothesized the actions of corporations to evoke inherent social reasoning processes. Specifically, we hypothesized

that participants would not only rate the actions of corporations and people similarly but also that the neural responses to reading vignettes of these two types would be very similar. Further, we hypothesized that vignettes about both people and corporations would elicit greater activity in the ToM network than vignettes about objects.

7.1.2 Materials and Methods

7.1.2.1 Participants

Forty two adults (19 males) aged 26.86±7.42 years (mean±SD) with 17.1±1.92 years of education normal or corrected-to-normal vision and no history of current or past mental or neurological illness were recruited from the Houston, TX metropolitan area to take part in the experiment after giving written consent in accordance with the Institutional Review Board at Baylor College of Medicine. Two participants were excluded from all analyses for failure to follow instructions during the in-scanner task An additional 10 participants did not meet head movement standards described below and were removed from all fMRI analyses, leaving 30 participants (15 males, age 28.6±8.18 years, 17.23±2.14 years of education) that were included in the GLM and MVPA analyses. In order to maximize statistical power, all 40 participants (18 males, age 27.33±7.45 years, 17.18±1.91 years of education) that successfully completed the experiment were included in the behavioral analyses.

7.1.2.2 Paradigm

Passive and active viewing of short, emotionally laden vignettes has successfully been used to investigate moral emotional reactions to situations of moral violations, moral dilemmas, empathic responses, and decisions of culpability (Buckholtz et al., 2008; Casebeer and Churchland, 2003; Greene et al., 2001; Moll et al., 2002; Schaich Borg et al., 2008; Young et al., 2007). Although other paradigms, such as the viewing of emotionally laden images and faces, have been used to investigate moral emotions, the vignette paradigm is the only one that lends itself to judgments about an abstract entity such as a company or organization (Decety and Lamm, 2006; Greene and Haidt, 2002; Moll et al., 2008; Thielscher and Pessoa, 2007).

7.1.2.3 Stimuli

We constructed 75 vignettes. 30 of these described the actions of people ("person" vignette; mean 45.63 words), of which 10 were about pro-social or positive actions (such as donating to charity), 10 were about anti-social or negative actions (such as lying or breaking the law), and 10 were of a neutral *valence* (such as painting a room or buying a printer). Each of these 30 Person vignettes was matched with a vignette about a company ("company" vignette; mean 44.73 words) with only minor details of the vignette changed for plausibility. The names of persons in the vignettes were randomly chosen on each trial from a list of 15 popular male names, and company names were randomly chosen on each trial from a list of 15 names generated from an online company name generator (www.company-name-generator.com). The additional 15 vignettes ("object"

vignette; mean 47.6 words) were adapted descriptions from wikipedia.org of nouns generated from a random noun generator (www.desiquintans.com/noungenerator.php). See **Figure 7.1A** for example vignettes. Participants were asked to think of each of the vignettes as independent events. We refer to the company, person, and object vignettes as the *agency* axis, and the positive, negative, or neutral vignettes as the *valence* axis. The length of the vignettes did not significantly differ across the *agency* (p=.92) or *valence* axis (p=0.74). See Experimental Procedures for a list of all 75 vignettes.

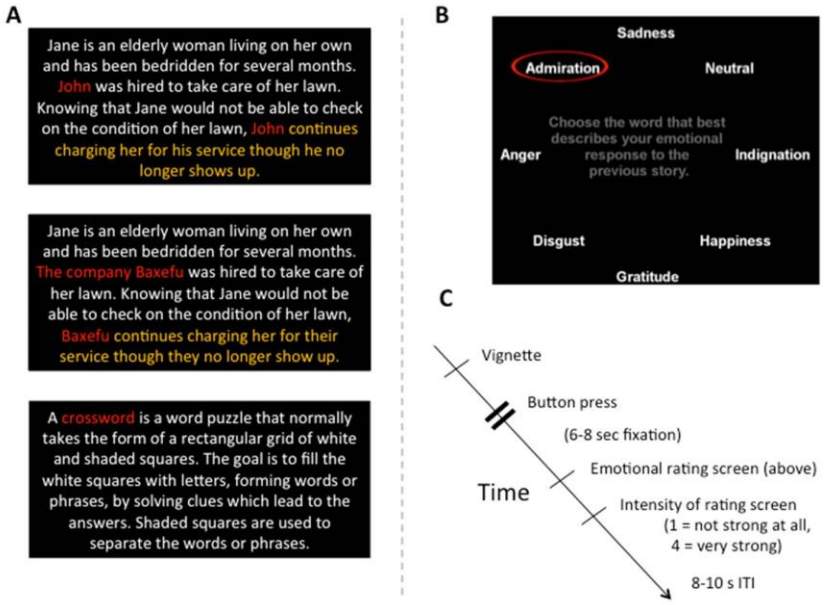

Figure 7.1 Experimental Paradigm

Experimental paradigm. **A.** A representative pair of matched "person" (top) and "company" (middle) vignettes are shown with the agency manipulation highlighted in red and the valence manipulation highlighted in yellow. Participants did not see any such highlighting, and each participant only saw one vignette from a matched pair. An "object" vignette (below) is also shown. **B.** An example emotion rating screen that participants saw between each trial. **C**. Schematic of a single trial.

7.1.2.4 Extended Procedures

While in the MRI scanner, participants read a total of 45 vignettes, 15 each of the company, person, and object conditions, during a single EPI run. The company and person vignettes were matched such that half of the participants were randomly presented with the company version of the vignette and the other half was presented with the person version. This was done to ensure that vignettes were matched without having any individual participant read the same story twice with different *agency*. The company and person vignettes included 5 positive *valence*, 5 negative *valence,* and 5 neutral *valence* vignettes per *agency*.

During each trial the participants first saw a randomly drawn vignette from the available pool of 45. Once the participant finished reading the vignette, he/she pressed a button to move forward. This vignette screen was followed by a fixation cross for 6-8 seconds. After fixation, participants were prompted to choose the word that best described their emotional response to the previous vignette from a list of 8 words ('happiness', 'disgust', 'anger', 'admiration', 'sadness', 'indignation', 'gratitude', 'neutral') placed at random, evenly spaced positions along a circle (**Figure 7.1B**). These emotions were selected from lists of basic and moral emotions in a previous study investigating disgust (Moll et al., 2005). The list of emotions in our current study does not reflect the full extent of moral or basic emotions in Moll et al (2005) but reflects the range of emotions expected from the stimuli in the current study. Participants used two buttons to scroll through choices before confirming that choice with a third button press. Following this emotional

rating, the participants rated the intensity of their emotional reaction on a scale of 1-4, with 4 being the most intense. On 25% of trials, participants additionally had to answer a true/false question about the content of the previous vignette to ensure sustained attending and understanding. Each trial was followed by a fixation period of 8-10 seconds. See **Figure 7.1C** for a schematic of an experimental trial.

7.1.2.5 fMRI Data Acquisition and Pre-Processing

High-resolution T1-weighted scans were acquired on a Siemens 3.0 Tesla Trio scanner using an MPRage sequence. Functional run details were as follows: hyperscan echo-planar imaging, gradient recalled echo; repetition time (TR) = 2000 ms; echo time (TE) = 40 ms; flip angle = 90°; 64 x 64 matrix, 34 4 mm axial slices, yielding functional 3.4 mm x 3.4 mm x 4.0 mm voxels.

7.1.2.6 fMRI GLM Data Analysis

General Linear Model analysis was performed using SPM8 (www.fil.ion.ucl.ac.uk/spm/software/spm8) with motion artifact removal using the Art toolbox (www.nitrc.org/projects/artifact_detect). Images were created using Mango (http://ric.uthscsa.edu/mango).

Motion Correction was carried out by co-registering data to a mean functional volume. Images in which head motion exceeded a cutoff (>1 mm of translation or rotation between consecutive TRs) were regressed out of the model. Images that were outliers

(>3 standard deviations from mean) in global brain activation were also regressed out. Additionally, any participant whose head movement exceeded 3 mm at any point in the scan was removed from analysis. Ten participants were completely removed from the GLM analysis for head movement exceeding 3 mm, leaving 30 total participants analyzed. Note, we did not exclude the 10 participants with excessive head motion from the behavioral analysis, as head motion only impacted image quality.

The average of the motion-corrected images was co-registered to each individual's structural MRI using a 12 parameter affine transformation. EPI images were spatially normalized to the MNI template (2 mm x 2 mm x 2 mm voxels) by applying a 12 parameter affine transformation, followed by a nonlinear warping using basis functions (Kao et al., 2005). Images were then smoothed using a 6 mm isotropic Gaussian kernel and highpass filtered in the temporal domain (filter width of 128 s).

To identify regions of interest of increased activation, we performed a general linear model (GLM) regression. Regressors were defined from the onset times and durations of all vignettes, emotional rating screens, and questions (separated by *valence* and *agency* condition). Additionally, the timing of participants' button presses and head movement parameters were included in the GLM as effects of no interest to account for motor responses and head movements. The events were convolved with SPM's canonical HRF (characterized by 2 gamma functions) to create the regressors used for analysis. After performing the regressions, we formed 12 contrasts of β values; family wise error

correction to a p-value of 0.05 was performed for all contrasts by non-parametric methods (10,000 permutations) using SnPM8 (http://warwick.ac.uk/tenichols/snpm).

7.1.2.7 Multi-Voxel Pattern Analysis

In addition to the standard GLM univariate analysis, we employed multi-voxel pattern analysis (MVPA) using a linear support vector machine (SVM) to search for patterns of activity that could successfully decode *agency* and *valency* separately. The MVPA analysis could also provide insight on how brains might differentially process emotional content when considering the actions of persons as compared to companies.

7.1.2.8 MVPA Preprocessing

The MVPA analysis was performed independently of the GLM. As such, we started with the raw data and built a separate preprocessing pipeline for MVPA analysis. The raw functional data for each of the 30 participants was preprocessed using AFNI (http://afni.nimh.nih.gov/afni) (Cox, 1996). The preprocessing pipeline consisted of linear slice timing correction, EPI to anatomical alignment, anatomical to Talairach alignment via non-linear registration (3dQwarp), re-sampling to 3 x 3 x 3 mm, and volume registration to the first volume. We then performed additional preprocessing steps using the PyMVPA python package (http://www.pymvpa.org) (Hanke et al., 2009a; Hanke et al., 2009b). We carried out fifth-order polynomial de-trending and z-scoring (normalizing) on each voxel independently over time. Lastly, we used a

Talairach probability atlas to select only grey matter voxels with probability greater than 20% for each aligned functional dataset.

7.1.2.9 MVPA Trial and Time Selection

Because participants' functional data were structurally aligned to Talairach space, we combined all participants and all trials into one large data set. This greatly increased the ability to train a classifier, as each participant individually only saw 5 trials of each *valence* (positive, negative, neutral) for each *agency* of interest (person and company). By combining all participants, our pattern analysis could be performed on an average of 139 trials for each *agency*-specific *valence* (see **Table 7.1**). Not all trials for each participant were kept. We used artifact detection to identify individual trials that entailed too much motion (>4 STD in fMRI signal intensity or >1 STD in motion) and rejected those specific trials from the MVPA analysis. We also ensured that each participant had at least 3 trials in each category after removal of artifact trials. As a result of this criterion, we rejected 1 participant who did not have the adequate number of trials, leaving a total of 29 participants on which we performed the MVPA analysis. Further, because participants had variable reading times, we aligned to the time the participant finished reading the vignette (indicated by button press) with 4 volumes (8 s) on either side.

Table 7.1 Number of Trials

Number of trials per condition for all participants combined for 3-class valency SVM.

TRIAL TYPE	# OF TRIALS
People Positive	141
People Negative	138
People Neutral	140
Company Positive	137
Company Negative	139
Company Neutral	137

7.1.2.10 MVPA Pattern Classification

We constructed several linear support vector machines (SVM) using PyMVPA (LinearCSVMC, implemented via LIBSVM) to classify *valency* (i.e., positive, negative, vs. neutral vignettes) and *agency* (person vs. company vignettes) separately. For all classifiers, we used a one-way ANOVA to select for 5,000 task-related features to pass to the SVM. We used leave-one-participant-out cross-validation to train and test the SVM for all analyses. The strength of the margin for each fold was estimated from the normal of the selected features. For the first classifier, we used all 9 volumes

surrounding the button press to create a 2-class SVM to decode on a trial-by-trial basis the *agency* (i.e., person or company). Separately, we used a 3-class SVM to decode *valency* (i.e., positive, negative, or neutral) within each *agency*. To dissect the 3-class SVM further, we computed the confusion matrices of the *valency* classification. Finally, we conducted a temporal analysis and created a set of 3-class SVMs to decode *valency* for each of the 9 time points surrounding the button press separately. This allowed us to determine *when* the decoding accuracy was strongest. We also plotted the sensitivities (SVM weight vectors) for each voxel and projected the sensitivities overlaid on the Talairach template. In addition to overall prediction accuracy, the sensitivity maps allowed us to infer which areas in the brain are implicated in classifying *valency*.

7.1.3 Results

7.1.3.1 Behavior

All 40 participants who successfully completed the experiment were kept in the behavioral analysis. In the scanner, participants correctly answered questions about the vignettes with an accuracy of 87%, indicating appropriate attentiveness and comprehension of the vignettes. Vignette reading times for the three conditions of *agency* were as follows: *person* $\mu=12.7 \pm 4.6$ s, *company* $\mu=14.0 \pm 4.9$ s, and *object* $\mu=13.2 \pm 5.3$ s. Although the difference between reading times was significant ($F=9.06$, $p<.001$), this difference is less than a single TR (2 s), suggesting the difference should not significantly affect our results. Participants answered in line with expectations about the intended *valences* of the vignettes (**Figure 7.2**).

We then evaluated the differences in reported emotional ratings and intensity as a function of agency. Emotional ratings of vignettes significantly differed across the agency categories, showing that participants describe their emotional responses to vignettes differently for each of the three agency categories (χ^2 =589.15, p<10e-116; **Figure 7.3A**). All pairwise comparisons (e.g. person vs. company) showed significant differences in emotional ratings as well. These post-hoc comparisons were made using a Bonferroni correction for the repeated tests (p<.0025). Since object vignettes were not designed to have valence manipulation, we only compared intensity ratings for company and person trials. There was no main effect of *agency* category on emotional intensity (F=.02, p=.88; **Figure 7.3B**). There was, however, a significant main effect of *valence* on emotional intensity ratings (F=62.7, p<.001) and a significant interaction between the *valence* and *agency* for emotional intensity (F=3.36, p<.05; **Figure 7.3B**). In this crossover interaction, we find that pro-social actions performed by people evoke a more intense positive emotional response than pro-social actions by companies, and anti-social actions by companies elicit more intense negative emotional responses than the same actions performed by people. This finding gives evidence for a negativity bias towards companies on which we elaborate in a later portion of the results.

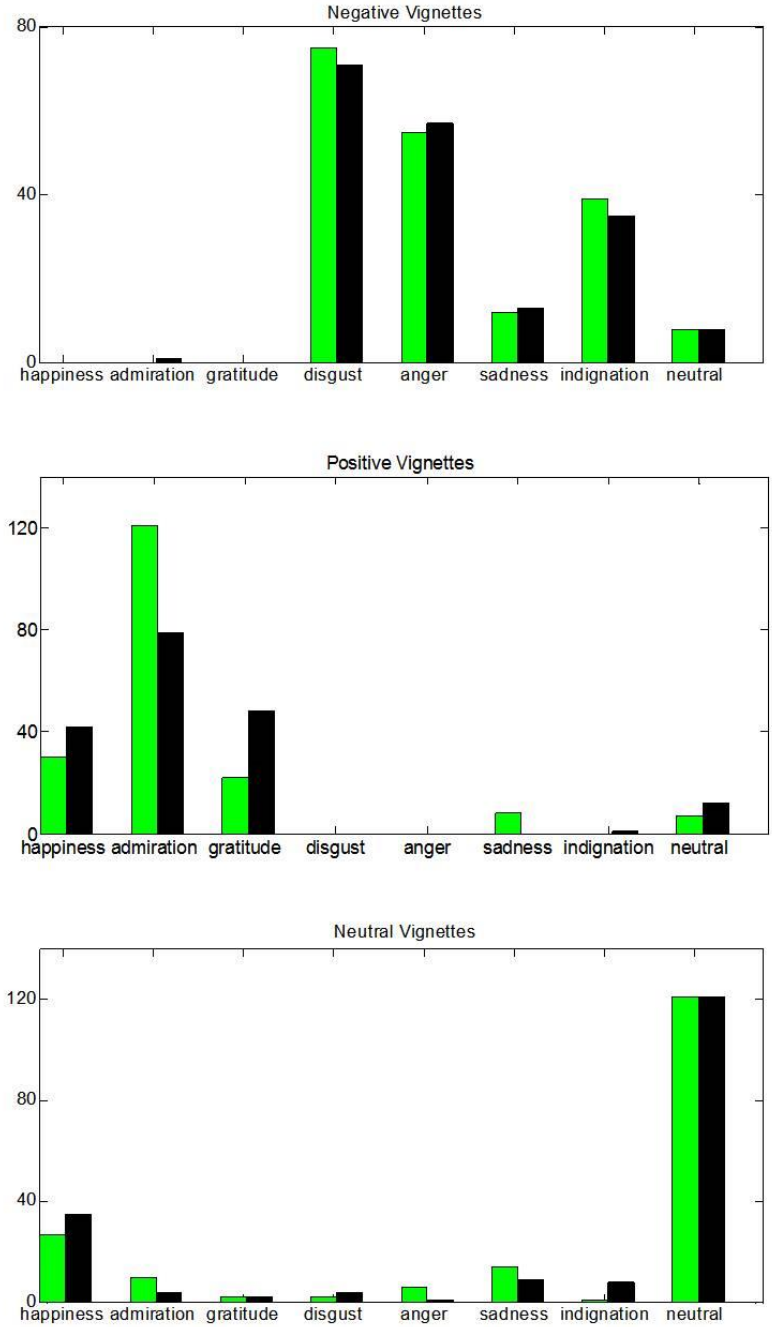

Figure 7.2 Emotional Responses

Emotional responses for company (black) and person (green) vignettes. The word chosen is on the horizontal axis and the height of the bar indicates a count of responses across participants.

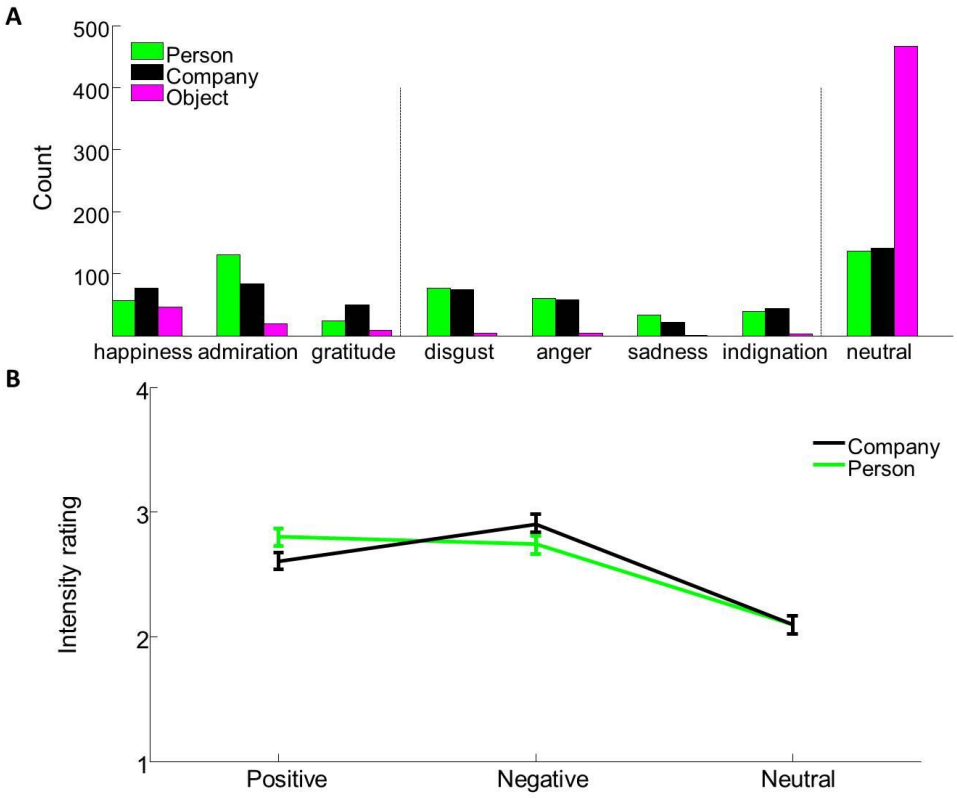

Figure 7.3 Participant Ratings

Participants reported different emotional ratings to person and company vignettes. A Histograms of emotional responses for all three agency manipulations. Emotional responses significantly differed across agent categories ($\chi 2$ =589.15, p<10e-116). All pairwise comparisons were also significant (Bonferroni corrected p<.01) B Ratings of emotional intensity are plotted against intended valence category for person and company trials separately. Intensity ratings show a main effect of vignette valence (F=62.7, p<.001) and an interaction of vignette valence and agency (F=3.36, p<.05). There was no main effect of agency on emotional intensity.

7.1.3.2 fMRI

To determine regions responsible for the processing of *agency*, we contrasted GLM beta estimates for person vs. object and company vs. object (**Figure 7.4**, and **Table 7.2**). Areas that showed greater activation to companies or persons more than to objects included the bilateral superior temporal pole (TP), bilateral angular gyrus (AG), posterior cingulate cortex (PCC), SMPFC, and bilateral cerebellum. An additional region in the midbrain responded with greater activity to person than to object vignettes. Several regions in the left hemisphere showed greater activity to objects than to either person or company vignettes: the left inferior frontal gyrus (L IFG), the left inferior parietal lobule (L IP), and the left inferior temporal gyrus (L ITG). In addition, left pars opercularis (L PO) showed greater activity to objects than to person vignettes. BOLD traces drawn from these regions reveal that the significance of the TP, AG, and possibly SMPFC are due to an increase in BOLD activity for persons and companies, while the significance of L PO and L ITG are due to an increase in BOLD activity for object vignettes. In the PCC, however, a depression of activity in the object condition drives significance, and in the L IFG and L IP there is a depression of the BOLD response for the person and company conditions.

No regions survive our non-parametric permutations testing method for family-wise error (FWE) correction in the direct comparison of persons and companies.

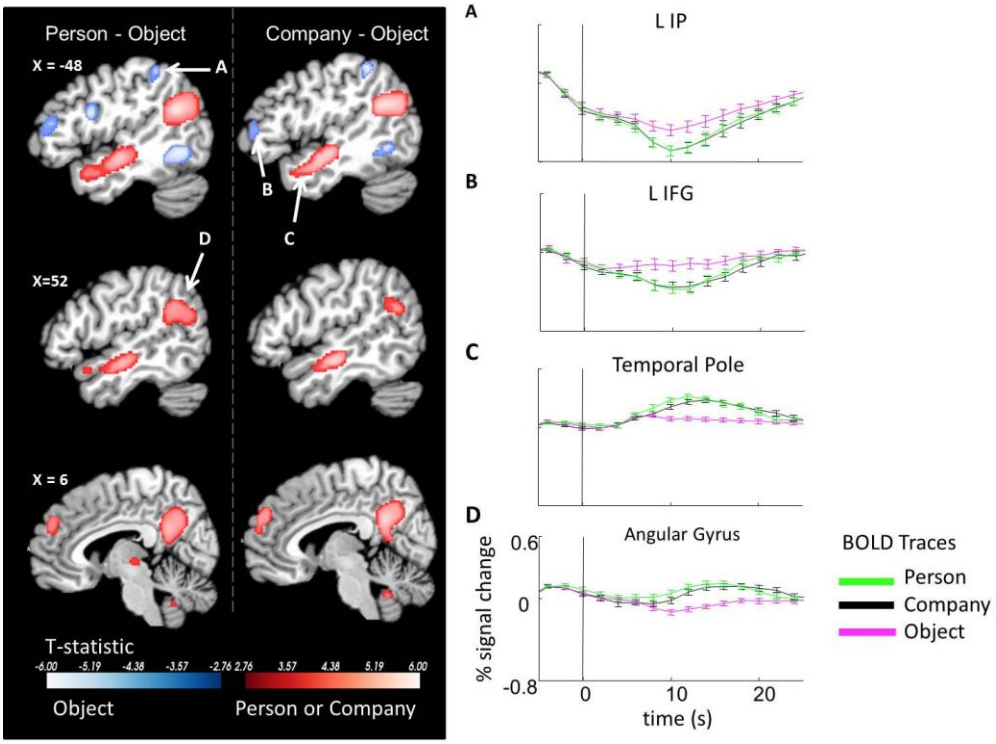

Figure 7.4 Social Networks

Vignettes about persons and companies elicit similar activity within social networks when compared to stories about objects. The left column of brain images depicts the contrasts of person>object (red colors) and object>person (blue colors). The right column of brain images depicts the contrasts of company>object (red colors) and object>company (blue colors). All contrasts are shown with family-wise error (FWE) correction at $p<0.05$. BOLD traces drawn from example regions of interest (ROIs) are shown to the right. The person and company BOLD activity show similar patterns in all ROIs. Time=0 s corresponds to the vignette onset.

Table 7.2 Coordinates of Activation

List of coordinates and statistics for significant region in GLM contrasts

		Coordinates of peak t-statistic				
contrast	**regions**	**x**	**y**	**z**	**peak t-statistic**	**number of voxels**
person > object	R Cerebellum region 9	6	-56	-42	5.3349	15
	L Cerebellum region 9	-6	-54	-42	5.2746	14
	L Temporal Pole	-58	-12	12	9.3871	669
	R Temporal Pole	56	-4	-16	10.3454	468
	Midbrain	0	-20	-4	5.4855	27
	R Angular Gyrus	56	-54	22	7.5676	677
	L Angular Gyrus	-50	-56	22	9.6119	935
	Posterior Cingulate	2	-52	24	7.8388	1077
	R Medial Prefrontal Cortex	12	62	16	5.111	21
	Superior Medial Prefrontal Cortex	4	50	28	5.5416	175
object>person	L Inferior Temporal Gyrus	-54	-62	-10	7.1581	258
	L Orbitalfrontal Lobe	-26	34	-14	5.0141	15
	L Inferior Frontal Gyrus	-46	36	12	7.73259	356
	L Brodmann Area 44	-48	6	20	7.1328	101
	L Inferior Parietal Lobule	-58	-36	44	6.4229	139
company>object	R Cerebellum 9	8	-52	-38	6.0121	48
	L Temporal Pole	-60	-10	-12	9.0272	560
	R Temporal Pole	56	-4	-16	8.2349	402
	Posterior Cingulate Cortex	0	-50	26	7.7595	1055
	R Medial Prefrontal Cortex	12	62	14	4.4849	6
	Superior Medial Prefrontal Cortex	-10	58	28	6.9258	451
	L Angular Gyrus	-56	-60	22	8.4072	745
	R Angular Gyrus	56	-56	22	6.6599	280
	L Medial Prefrontal Cortex	-12	40	46	5.137	13
object>company	R Orbitalfrontal Cortex	24	42	-16	5.5306	5
	L Inferior Temporal Gyrus	-56	-60	-10	5.9608	100
	L Inferior Frontal Gyrus	-46	44	8	6.1566	292
	L Inferior Parietal Lobule	-54	-40	48	5.5381	153
positive>negative	L Cerebellar Tonsil	-36	-64	-42	4.7184	10
	R Cerebellar Tonsil	36	-54	-42	5.1647	14
	R Cerebellum region 1	40	-68	-40	5.3209	7
	R Dorsolateral Prefrontal Cortex	42	48	12	5.5802	83
	R Anterior Cingulum	10	32	24	5.0323	24
	Posterior Cingulate Cortex	0	-30	26	7.6269	456
	Precuneus	-8	-70	38	7.7823	967
	Middle Cingulum	0	24	34	4.9674	26
	R Posterior Parietal Lobe	38	-66	46	4.8977	10
negative>positive	Superior Temporal Gyrus	-54	-34	-4	4.78	4

To ferret out any more subtle differences between persons and companies, we performed a multi-voxel pattern analysis (MVPA). We attempted to decode corporation and person trials using a 2-class SVM combining all valences and feeding the 9 timepoints around the button press to the SVM. However, our overall prediction accuracy was only 54.93%, (chance = 50%, p=0.0082, χ^2), indicating *agency* was difficult to decode. Thus, we ran a separate 3-class SVM in an attempt to decode emotional *valence* separately in person and company conditions. The overall prediction accuracy for both person and company trials was computed by using all 9 timepoints around the button press in an SVM, and the *valence* was decoded. This yielded a prediction accuracy for person trials of 50.60% (chance = 33.33%, p < 7.6e-11, χ^2) and a prediction accuracy for the company trials of 44.07% (chance = 33.33%, p < 2.8e-13, χ^2). We then computed a time series analysis decoding using each time point separately. This showed that the peak prediction accuracy occurred 4 s before the vignette ended (**Figure 7.5A**). Although the time series analysis shows similar decoding accuracy for person and company trials, the confusion matrices for these SVMs provides further evidence for differential emotional processing of these two trial types as seen in the analysis of the emotional responses (**Figure 7.5B**). The prediction accuracies for negative, neutral, and positive vignettes within the person condition were of similar magnitudes. However, for company vignettes, the SVM was much more successful in classifying positive vignettes than negative or neutral company vignettes. SVM sensitivity maps for the 3-class SVMs for company and person trials at -4 s are shown in **Figure 7.6**.

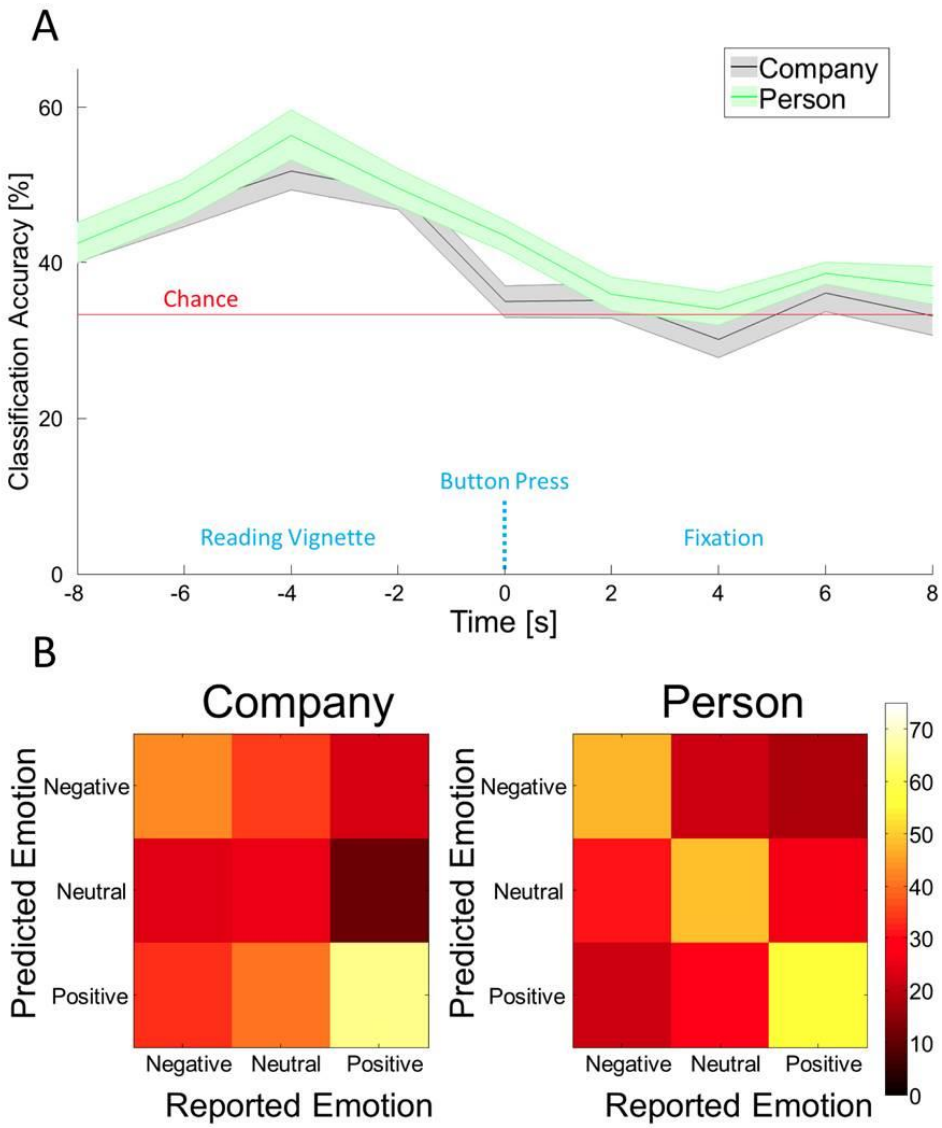

Figure 7.5 Decoding Analysis

Neural decoding of negative and neutral emotions is weak in Company trials but not in Person trials. A Time series analysis of decoding accuracy is similar in person and company trials. Peak prediction accuracy occurs 4 seconds before participants finished reading vignettes. Shaded regions indicate ± 1 SEM. Horizontal red line indicates chance level performance (33.33%). B Confusion matrices for person and company trials suggest a difference in emotional processing. Columns indicate the true valence condition of the trial, and the rows represent the SVM-predicted valence of the trial. Colors indicate the percent of trials that were classified with that label. The diagonals of the graph indicate the proportion correct in each trial type.

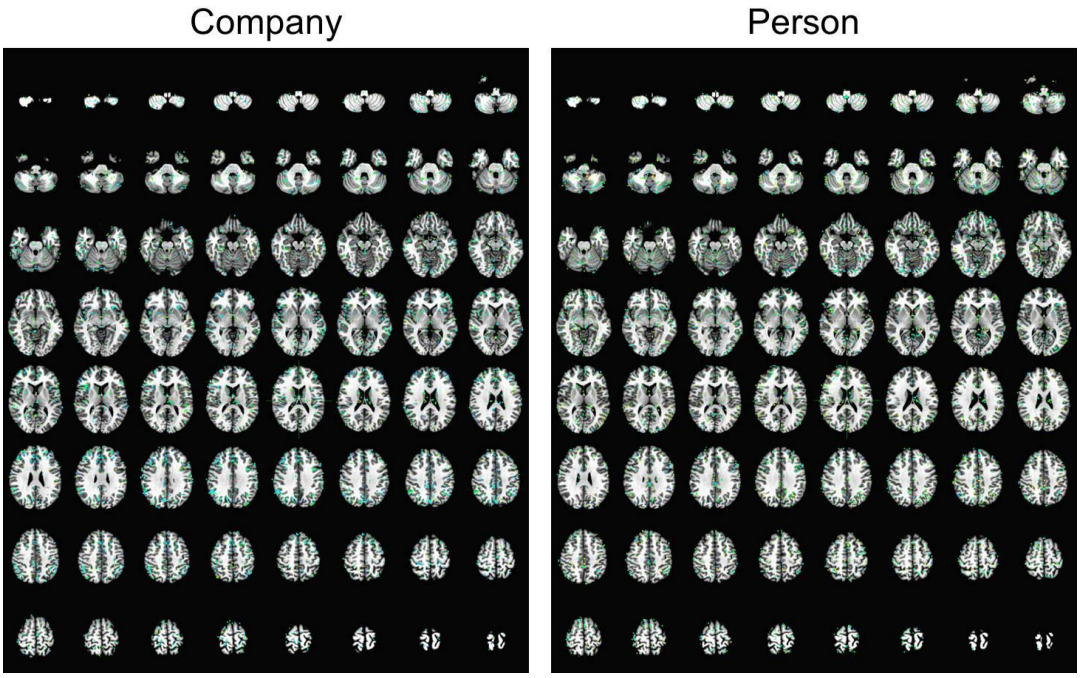

Figure 7.6 Sensitivity Maps for Classifiers

Sensitivity maps for SVM classifiers for company at the peak decoding time (4 s prior to vignette end) reveal how voxels were weighted in the SVM. Feature selection using a one-way ANOVA was first used to pre-select 5,000 voxels. The weights of these voxels were scaled using an L1-norm and are shown overlaid on the Talairach brain template.

To determine the regions that may underlie this difference in decoding accuracy for person and company emotions, especially the neutral vignettes, we returned to the GLM analysis and collapsed person and company vignettes into one group and then separated the *valence*. Collectively the positive vs. neutral and negative vs. neutral contrasts yielded the same regions as the positive vs. negative contrasts, so we will consider only the latter comparison (**Figure 7.7**). The right dorsolateral prefrontal cortex (R-DLPFC), right anterior cingulum (R AC), PCC, precuneus, mid-cingulum, right posterior parietal lobe, and bilateral cerebellar tonsil showed greater activation to positively *valenced*

vignettes. Only a small cluster of the superior temporal gyrus showed greater activity to negative vignettes. BOLD traces in these regions show no significant differences between the company and person trials within either the positive or negative trial subtypes. Within the neutral vignettes, however, person vignettes showed consistently higher BOLD activity than company vignettes. The BOLD activity from neutral person vignettes resembled the BOLD activity for positive vignettes, and the BOLD activity for neutral company vignettes resembled BOLD activity from negative vignettes, providing additional evidence for a negativity bias towards companies on a neural level.

7.1.4 Discussion

We found that the networks that underlie our ability to understand the actions of companies and people substantially overlap. That is, corporations are neurally represented as social beings rather than inanimate objects. Vignettes about corporations and people gave rise to largely similar neural responses, but there appears to be important differences in the emotional processing of these stories. Varying emotional responses between these vignette subtypes taken together with neural decoding using SVM classification and region of interest analysis suggests a negativity bias towards corporations. Not only did we see a bias against companies when rating positive and negative vignettes, but the neural response during neutral vignettes suggested a predisposition to judge companies more negatively. The neural response to a neutral vignette about a company was more similar to a negative vignette than to a positive vignette. This bias was not found in the neutral person vignettes.

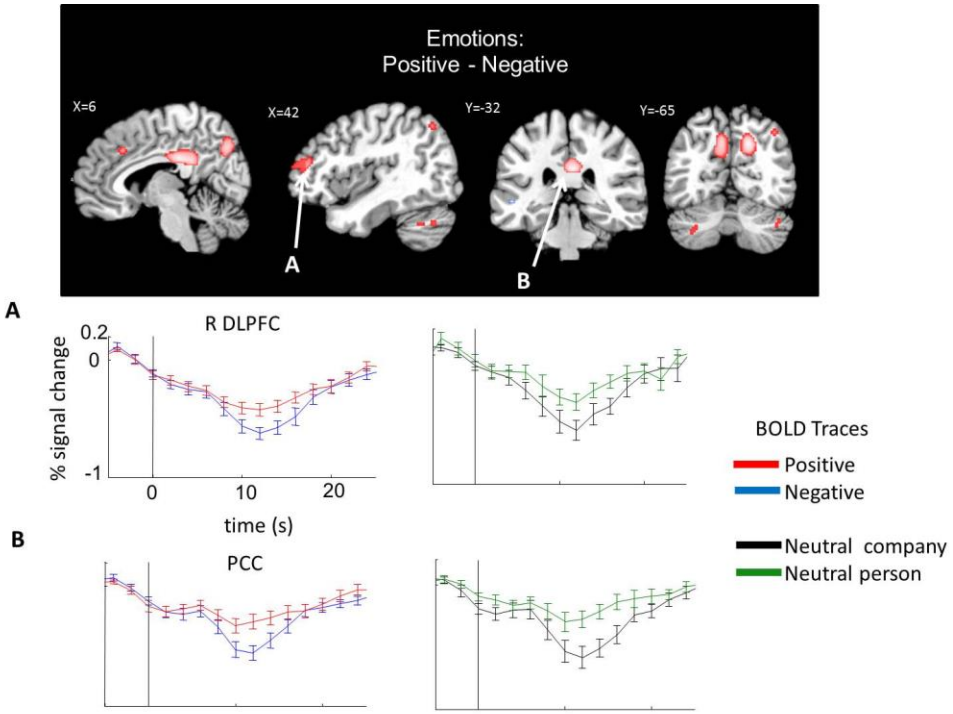

Figure 7.7 Brain Hemodynamics

No differences are seen between company and person agency when participants read positive and negative vignettes. However, neutral person trials consistently elicit significantly greater activity than neutral company trials. A contrast of all positive > negative trials revealed large medial regions such as the anterior cingulate cortex (ACC), posterior cingulate cortex (PCC), and the precuneus (FWE <0.05). Traces are drawn from the labeled ROIs. The plots on the left depict for each ROI negative and positive BOLD activity averaged for person and companies. The plots on the right depict for each ROI neutral vignette BOLD activity for person and companies. Time=0 s corresponds to vignette onset. Positive and negative as well as neutral company and person BOLD traces shown are significantly different by repeated measures ANOVA.

When contrasted with objects, people and company both elicited activity in a widely cited “mentalizing network” of brain regions responsible for representing the actions and thoughts of others. A meta-analysis of 63 ToM studies finds a strikingly similar network to our agent > object contrasts (**Figure 7.2**), including the SMPFC, PCC/precuneus,

bilateral TPJ, bilateral STS, and bilateral temporal poles (Mar, 2011). A similar network of regions appears crucial for social cognition and moral decision making (Greene and Haidt, 2002; Hein and Singer, 2008; Moll et al., 2008).

Activation of this mentalizing network of activity suggests that people apply similar mechanisms of moral reasoning and perspective taking when evaluating the actions of corporations and people alike. The brain can operate under two distinct states with antagonistic networks: a "social reasoning" network (e.g., interacting with other people) and "mechanical reasoning" (e.g., doing physics problems) (Jack et al., 2012). Our results show that both person vignettes and corporation vignettes activate this social reasoning network, while vignettes about objects activate the mechanical reasoning network. In other words, people do not treat corporations as physical entities but rather as social beings. Further, this social reasoning network allows people to form representations of the others, giving rise to decisions about morality and justice (Robertson et al., 2007).

Other neuroimaging evidence has further characterized this mentalizing brain network beyond the simple social vs. non-social distinction. Activation of the thalamus and ventromedial/orbitofrontal activation has been implicated in particularly negative moral emotions (e.g., disgust) (Moll et al., 2005). Additionally the cerebellar regions seen in our agent > object contrasts (**Figure 7.4**) have been shown to be functionally connected to the other regions of the mentalizing network (Buckner et al., 2011). The sum of the

functions within these regions gives rise to the ability to understand the personal and social behavior in both individuals and corporations alike. Our strongest evidence of corporate personhood stems from activation of the SMPFC in both corporations and individuals when each was contrasted to objects (**Figure 7.4**). The medial prefrontal cortex is critical to many social functions such as discriminating emotion, processing reward and punishment, representing and updating the value of future outcomes, and predicting the mental states of other organisms and cartoons (Amodio and Frith, 2006; Mitchell et al., 2005). Crucially, corporation vignettes did not down-regulate the SMPFC, as dehumanization studies have found (Cikara et al., 2011; Harris and Fiske, 2006). Our results show that vignettes involving corporations activate this frontal region just as person vignettes do.

Our MVPA investigated whether emotional judgments about corporations and individuals could be decoded in patterns of activity distributed spatially across the brain. We found prediction accuracies were highest in company vignettes for positive trials, whereas in people all three emotions were decoded with similar accuracies (**Figure 7.5**). This suggests that the brain might respond uniquely to pro-social behavior of a company. Alternatively, the neutral and negative vignettes might elicit indistinguishable neural responses in company trials. Further evidence for the latter interpretation was seen in the GLM analysis (**Figure 7.7**). In regions captured by the positive vs. negative contrasts, neither positive nor negative vignette BOLD traces differ between people and corporations; however, the neutral traces drawn from these regions are significantly

different. The person neutral traces resemble the positive traces while the company neutral traces resemble the negative traces. Collectively, these results give neural evidence for a negativity bias towards corporations that we see in our analysis of participants' emotional ratings. Such biases towards corporations have been previously noted in the literature outside of neuroscience. For example, participants in psychology studies view unethical behavior by corporations as more predictive of a corporation's future behavior than refraining from unethical behavior or displaying pro-social behavior (Folkes and Kamins, 1999). The bias we find here provides a basis for further investigation of emotional processing in decision making about corporations.

It is possible that in an alternative experiment, the ToM network could be activated for inert objects. Several studies have been able to ascribe human behavior to inanimate objects (e.g., walking with point-light patterns) (Beauchamp et al., 2003; Grossman et al., 2000; Grossman and Blake, 2001), and the ToM network activates when these inanimate objects engage in social interactions (Martin and Weisberg, 2003). This evidence suggests that the brain is capable of abstracting constructs and developing high-level frameworks of social interaction. Our evidence supports this model, suggesting that corporations can also be abstracted and mentalized as social beings.

Regions that displayed greater activation to objects (L IFG, L IP, L ITG, and L PO) than to either people or companies have been seen a variety of studies. For example, similar regions are activated in non-social reasoning including mechanical reasoning (Jack et al.,

2012), non-moral reasoning (Greene et al., 2001), motion discrimination and multisensory integration during tactile stimulation (Pasalar et al., 2010; Van Boven et al., 2005), visual and non-visual working memory (Pessoa et al., 2002) (for review see (D'Esposito et al., 2000)), and semantic and syntactic reasoning (Costafreda et al., 2006; Friederici et al., 2003; Hirshorn and Thompson-Schill, 2006; Moss et al., 2005; Poldrack et al., 1999). The left IP and in particular the left intraparietal sulcus have additionally been implicated in tasks involving object manipulation. Imagined, observed, and pantomimed tool use as well as point-light displays of tools preferentially activate the left intraparietal sulcus (Beauchamp et al., 2003; Moll et al., 2000). Vignettes from the object condition that contain information about tools and other objects (e.g. scissors, staplers, tractors) may be responsible for the observed activation of this region.

Our study gives rise to two additional questions to further probe the neural and emotional responses to the actions of corporations versus individuals. First, our study took a broad approach to observe the effects of three different *agents* (person, company, and object) under three different *valences* (positive, negative, and neutral) in a single fMRI run. Future work will examine negative corporation and person trials to further elucidate our observed negativity bias towards corporations. To this end, we will use multiple short runs to generate robust classifiers for MVPA (Coutanche and Thompson-Schill, 2012) to perform cross-validation on independent runs of data within participant. Second, we assessed here only the emotional responses to different vignettes. Future work will also examine how participants would choose to punish negative behavior and

reward positive behavior differently in individuals and corporations. This study will allow us to differentiate the actions participants take from their emotional response. It should be noted that company vignettes occasionally mentioned individual people (e.g., as the recipient of the action of a company, see Jane in **Figure 7.1A**). The strong activation of the ToM network observed in this experiment could be due to the mentioning of individuals in these vignettes. Future work should fully isolate corporations or the collective unit being studied from the individuals with whom they often interact.

As mentioned above, ToM activity has been elicited by other non-human entities such as "socially interacting" basic shapes (Martin & Weisberg, 2003). Therefore, we cannot conclude that corporations or companies represent a special case of ToM network activation. We did not test participants' judgments or brain activity with any other type of collective, such as charities, educational institutions, or government organizations. It is likely that the same networks will be strongly activated when contemplating the actions of other such collective groups.

Lastly, this study does not provide a scientific justification or grounding for court decisions such as *Citizen's United vs. Federal Elections Committee* (2010). There are numerous political, legal, and economic reasons why corporations ought or ought not to be granted the rights of individuals; these are beyond the scope of this study. Rather,

this study concludes that judgments about both individuals and corporations are underpinned by remarkably similar neural mechanisms.

7.1.5 Conclusions

We investigated how participants judge the actions of corporations compared to the actions of individuals. Our results showed that participants elicited the same networks of brain activity in response to the actions of corporations and individuals alike. Analysis of the emotional responses to these vignettes, on both a behavioral and neural level, revealed a slight negativity bias towards corporations in which participants' appear predisposed to judge the actions of companies more harshly. Collectively, our results support our hypothesis that corporations are viewed as social beings.

7.2. PSAP

Social forces drastically influence our decision-making behaviors. For example, adolescents will be more likely to make riskier decisions (e.g., run a run red light) when they are simply being watched by their peers (Chein et al., 2011). Social influences can also cause people to make better decisions, a successful approach utilized by the organization CeaseFire in urban Chicago. Gang violence has plagued Chicago recently, and CeaseFire deploys “community elders” to scenes to prevent outbreaks when tensions escalate and violence is imminent.

My first fMRI experiment involved studying these social interactions on behavior and quantifying neural correlates of these differences. Particularly, I studied how aggression could be modulated under different social influences. I used a well-studied aggression task called the Point Subtraction Aggression Paradigm (PSAP) (Cherek, 1981). I modified the task to be used during an fMRI scan and to be modulated by social influences. In this test, the participant was told that he would be paired anonymously with an opponent who is another participant; however, this opponent was actually just a computer. The participant had two response buttons—pressing one resulted in the accumulation of money (Button A) and pressing the other reduced the money of the other party (Button B). Pressing Button B was classified as an aggressive response. During the game, at random times, the computer reduced the participant’s money, as though the opponent pressed his Button B. At this point, the participant may or may not retaliate by pressing his Button B any number of times, allowing us to document the

participant's aggressive response. This pattern was varied over the length of the game, and aggressive responses were measured.

To measure the effect of social influences, we ran the study under two different paradigms. Participants were recruited in pairs (e.g., spouses, close friends, well-liked classmates). Participants were ostensibly told that they would be playing a game with each other while both were being scanned ("hyperscanning"). In reality, one participant was placed in the scanner, while his/her peer waited. The experiment consisted of 3 parts. In the first part, the participant in the scanner trained on the PSAP task. Then, either his/her peer would be shown via a live webcam feed while he/she played 10 minutes of the PSAP task or a video of a (mock) police officer (**Figure 7.8-9**). After 10 minutes, the other stimulus (peer or officer) would be shown while the participant played the PSAP game. Order was counter-balanced across participant pairs. When the peer was observing, he/she was simply watching a YouTube video to Animal Planet and was told nothing more about the study. Meanwhile, the live video feed was shown to the participant in the scanner, who believed that his/her peer was watching the PSAP game.

Unfortunately, we did not find significant behavioral differences or neural signatures in 10 participants (5 pairs). Participants were not more likely to respond aggressively in either condition (**Figure 7.10**).

We also performed event contrasts on student > officer and officer > student on provocations and aggressive responses, but did not find significant brain regions to differ.

These negative results may (at least in part) be due to the fact that the deception may not have been convincing enough to undergraduate/graduate students generally familiar to the idea of deceptive research. We had engaged conversations with Dr. Gary Slutkin at CeaseFire and initiated projects, but they did not reach fruition.

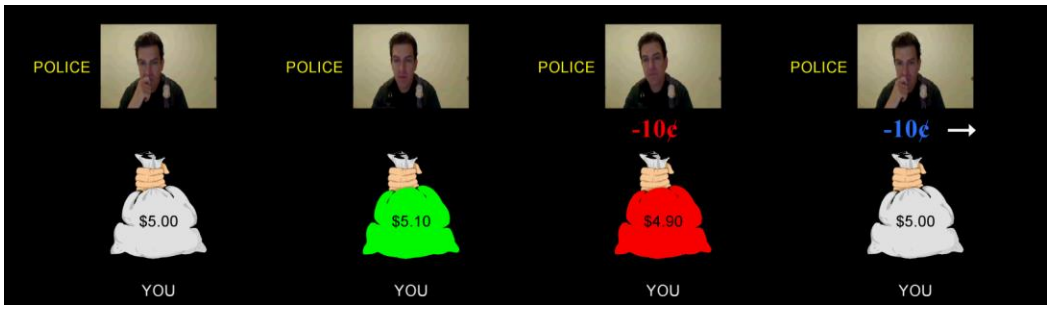

Figure 7.8 Police Observer

PSAP task is played while being "watched" by a police officer.

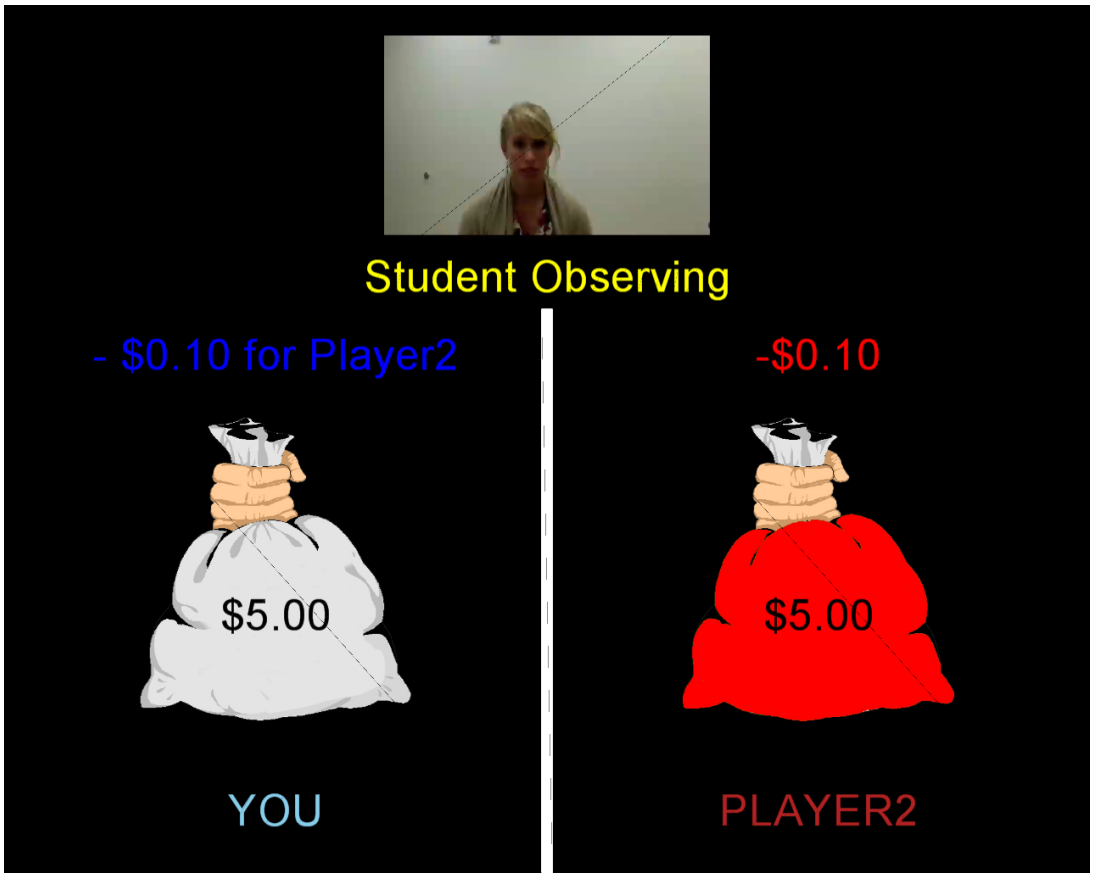

Figure 7.9 Student Observer

PSAP task played while being "watched" by a peer.

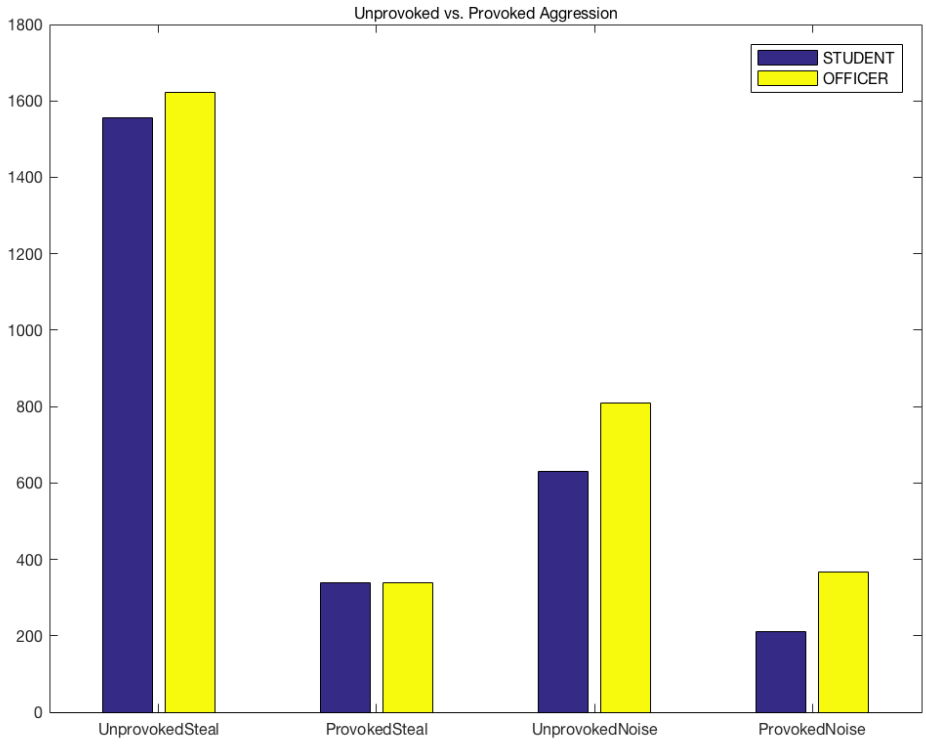

Figure 7.10 Behavioral Responses

Behavioral counts on the number of provoked or unprovoked aggressive responses. In this version of the paradigm, participants could also inject painful noise to the headphones of their peers, and were also susceptible to being delivered noise by the other player (aka computer).

CHAPTER VIII

BRAIN PHYSIOLOGY

8.1 Introduction

The basal ganglia play a key role in modulation of motor output. However, their role in sensory integration and higher cognitive function is not well elucidated. For example, patients who suffer a stroke to the subthalamic nucleus will experience contralateral hemibalismus, but it is unknown if the patient will suffer from any subtler cognitive integration deficits. Intraoperative deep brain stimulation (DBS) provides the only window to measure the human electrophysiology of these subcortical nuclei. In the operating room, prior to the insertion of the stimulating electrode, recording microelectrodes are inserted into the target nuclei to provide electrophysiological confirmation that the right nucleus has been reached. It is during this time while the recording electrodes are still in place that stimuli can be presented to the patients and the responses of human deep brain nuclei can be measured. The targets of the deep brain stimulation include the subthalamic nucleus (STN) and the globus pallidus internus (GPi) in Parkinson's disease and dystonia, and the ventral intermediate nucleus (Vim) in Essential Tremor.

There are at least two pressing hypotheses regarding potential cognitive roles of basal ganglia nuclei: 1. the perception of time (Allman and Meck, 2012; Teki et al., 2011), and 2. the processing of emotional stimuli (Bruck et al., 2011). Evidence to support the

involvement of basal ganglia in time perception has come from both pathology and neuroimaging. Behavioral testing in Parkinson's disease patients has revealed deficiencies in interval timing (Merchant et al., 2008). In addition, functional magnetic resonance imaging (fMRI) of healthy participants has been used to show the involvement of the putamen and other basal ganglia nuclei in rhythm and beat perception (Grahn and Brett, 2007). There is at least one body of evidence suggesting the role of emotional prosody processing is involved in the STN (Bruck et al., 2011).

We propose to find the fundamental electrophysiological evidence for cognitive roles of basal ganglia nuclei. We will use the hypothesis in the literature to drive our own hypothesis. However, there exists a challenge with electrophysiology of single units: the behavioral or neuro-imaging studies utilize the aggregation of thousands or even millions of neurons to collect data from. In electrophysiology, we are recording from single units consisting of often less than 5 detected neurons. As a result, there exists no particular guarantee that the set of individual cells we observe will indeed be involved in the putative cognitive tasks.

To tackle this challenge, we have created two key innovations. First, we have developed an online analysis system, capable of spike detection, sorting, and hypothesis testing all within the OR to determine if cells we are recording from indeed respond to particular stimuli. If they do, we can perform more trials to increase our sample size. If the cells do not respond, then we can drive the recording electrodes to another depth in the hopes of

finding more responsive cells. This methodology will maximize our chances of finding cognitively involved neurons within basal ganglia structures. Second, we have developed a psychophysical battery of tests consisting of several cognitive modalities. Each test can be run in whole or in batches, depending on the responses of the cells we measure. In this way, we can avoid measuring from un-informative cells for a long duration. With these two innovations, we hope to elucidate electrophysiological basis of time perception and emotional processing in the basal ganglia **(Figure 8.1, Figure 8.2, Figure 8.3, Figure 8.4, and Figure 8.5)**.

8.2 Materials and Methods

The following stimuli were used to present various emotional stages to the patients:

1) Faces with staged emotions (happy, sad, neutral) (Belhumeur, 1997)
2) Digitized sounds with quantified valence and arousal levels (Lang, 1999)
3) Custom neutral words spoken with particular emotions (happy, neutral, angry)
4) Presented words of varying emotional content (happy, sad, neutral)

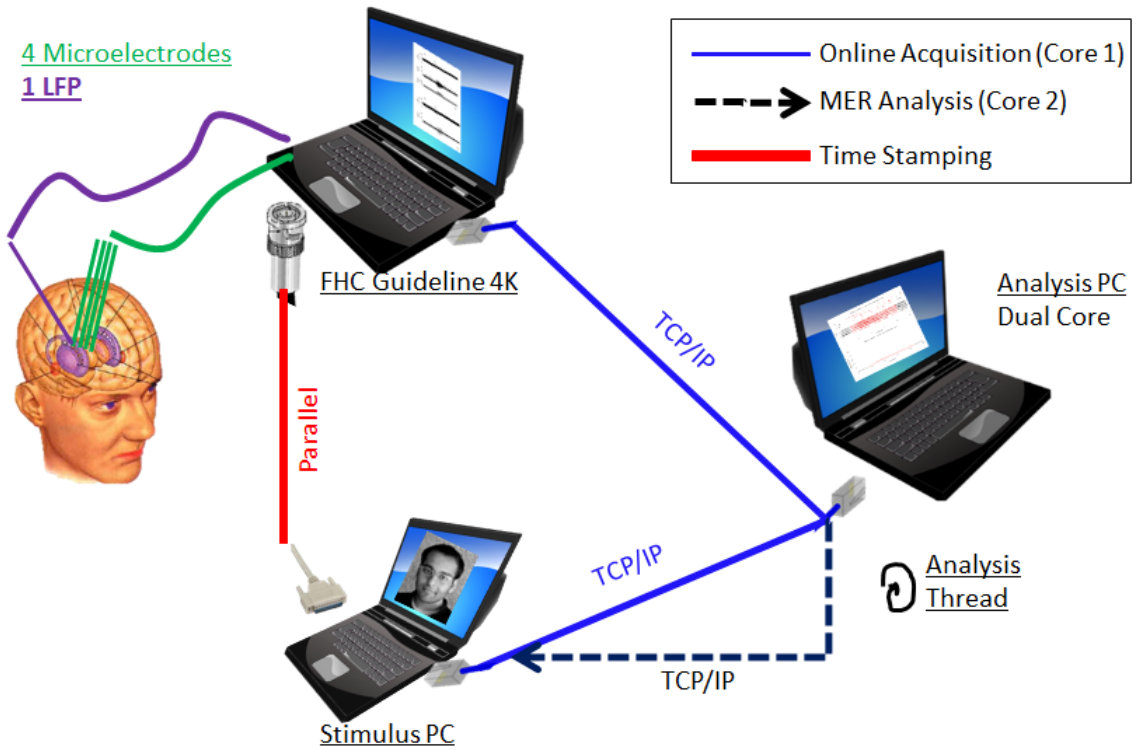

Figure 8.1 Operating Room Online Analysis Diagram

Prior to insertion of the stimulating electrode, 4recording microelectrodes are inserted at target nucleus. One of these electrodes also has a low-pass filter and pre-amplifier allowing simultaneous acquisition of the local field potential (LFP). This LFP electrode is represented as another electrode (in purple), although it is indeed acquired from one of the 4 microelectrodes. These electrodes, along with microphone data from speech, are passed to the FHC Guideline 4000 system. Stimuli are presented from another stimulus PC, and the timestamps are written to the FHC system via a parallel port connection (red connection). Using TCP/IP and a one of two cores, data from the FHC PC and stimuli categories from the stimulus computer are sent to a dual core analysis PC (blue connection). Once the end of a task completed, the analysis PC will analyze the MER data on another core in parallel. The analysis computer will generate PSTH plots and Raster Plots as well as compute hypothesis testing for each condition over all trials. The plots, the p-values, and the effect sizes are then sent back to the stimulus computer (yellow connection) for the researcher to make real-time decisions about which tests to run, all inside the operating room.

Figure 8.2 Adaptive Psychophysical Battery

Representations of the various domains of our psychophysical battery. The battery is adaptive, allowing us to run any or all of these domains directly dependent on the responsiveness to the particular stimuli. The emotional stimuli are displayed as faces, sounds, semantic words, and emotional expressions of words.

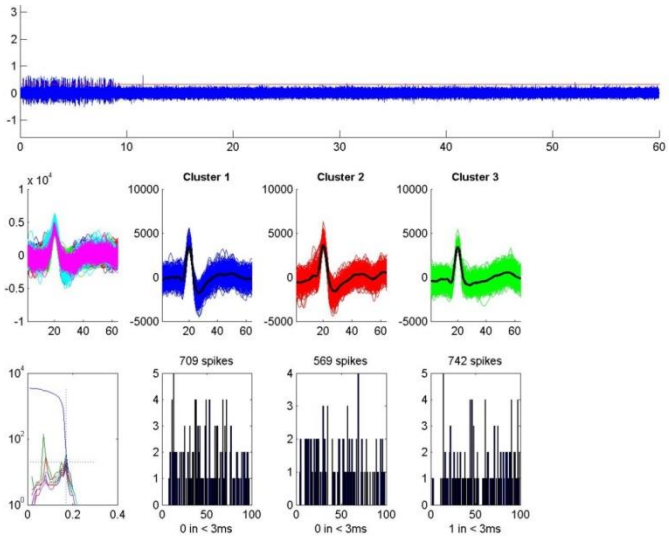

Figure 8.3 Spike Sorting

A sample output of the WaveClus (Quiroga et al., 2004) algorithm's spike sorting. The top panel shows the raw z-scored voltage output from a single microelectode recording. After spike detection, the algorithm clusters spikes into different representative neurons. In middle panel, all clusters are overlaid on top of each other. The three clusters are then shown to the right. In the bottom panel, parameters of cluster size and temperature can be selected on the left, if using supervised learning. The plots on the right show histograms of the counts of the inter-spike intervals (ISI) for each cluster. The total number of spikes is also displayed on top each histogram.

8.3 Results

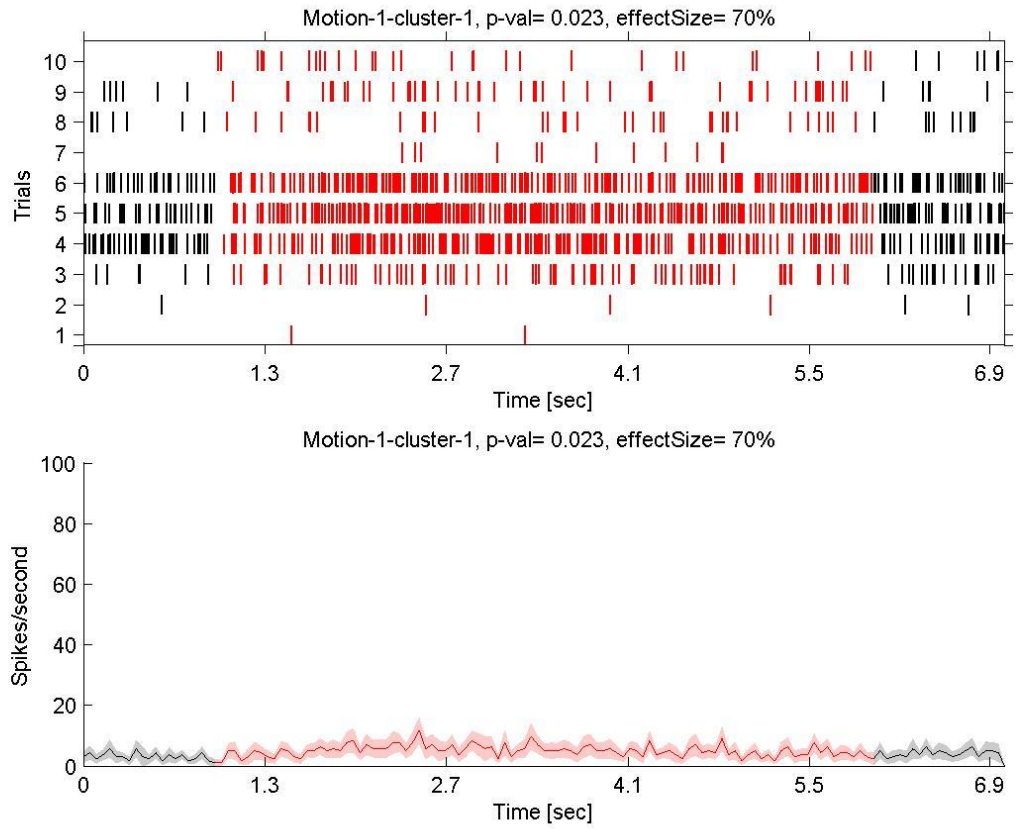

Figure 8.4 Peristimulus Time Histograms and Raster Plots

On the top panel, a raster plot is shown for a particular stimulus category for each trial. On the bottom panel, the peristimulus time histogram (PSTH) is shown for the corresponding raster plot. The window for the PSTH was 50 msec. In both plots, red color is used to indicate the time while the stimulus was on (1 – 6 seconds in this example). Between each plot, the task, the electrode number, and the cluster number are displayed (Motion-1-cluster-1 indicates Motion was the task, electrode 1 was the channel, and cluster 1 was the cluster for this channel). Also, the p-value for the Wilcoxon Sign Rank test and the effect size are displayed. These values are computed by comparing the spike rate during stimulus onset to one second after stimulus offset to the spike rate during one second before stimulus onset to stimulus onset. The effect size is computed simply by calculating the percent of trials in which the spike rate in the stimulus/post-stimulus period was greater than the pre-stimulus (baseline) period.

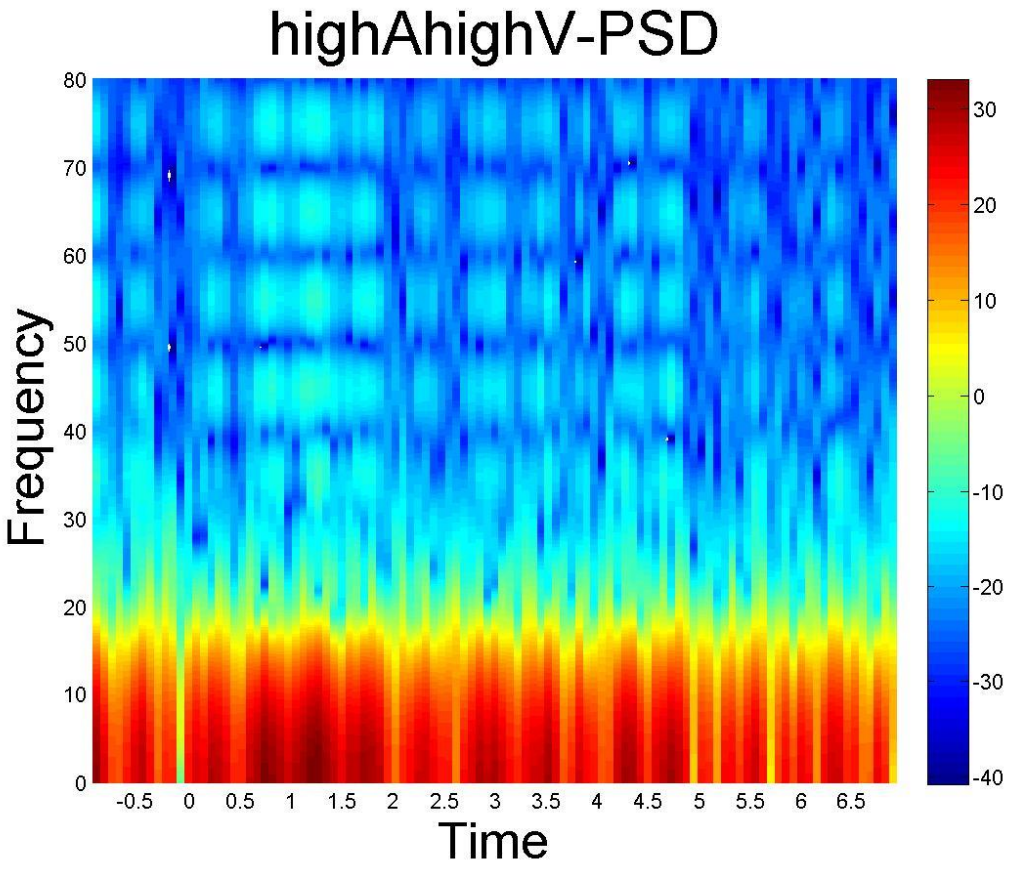

Figure 8.5 Local Field Potential Power Spectral Density

A sample output of LFP analysis. The stimulus was a high arousal, high valence sound (highAhighV) presented for 6 seconds. Time is shown on the x-axis, with stimulus onset at zero seconds. The times are binned into 100 ms windows with 25% overlap. Frequency is shown on the y-axis ranging from 0-80 Hz in steps of 0.1 Hz. For each time frequency coordinate, the power is shown in color, with the color bar shown on the right.

CHAPTER IX

DECODING AND ENCODING THE BRAIN

9.1 Introduction

Jack Gallant and his group at UC Berkeley made an instrumental step in decoding fMRI signal evoked by natural movies (Nishimoto et al., 2011). For the first time, the noisy, low temporal resolution blood-oxygen-level-dependent (BOLD) contrast was able to predict quite accurately which one of millions of movies the participant watched at a given time. In addition to identification, Gallant and his group were able to *reconstruct* the video participants watched by harnessing 18 million different YouTube videos and two powerful filtering approaches. Although seemingly impressive, Gallant's groups used a rather simple ranking framework to match the BOLD response of a watched video to the top predicted BOLD responses of randomly selected videos. In our first aim, we propose to employ much more rigorous image processing algorithms than global matching. We will employ local reconstruction frameworks that will enable us to piece-wise rebuild a video, voxel-by-voxel. This framework will not only improve the quality of video reconstruction, but the robustness of our framework will also be much more fruitful for extending the model to our next two aims: imagination and dreaming.

Imagination poses an interesting challenge for constructing an encoding model because, unlike with presented stimuli, we do not know precisely what participants were actually imagining, the ground truth. Formisano's group tried to tackle the challenge by training

participants to imagine particular scenes when presented with a particular auditory cues (de Borst et al., 2012). Using EEG and fMRI separately, Formisano's group elucidated a temporal flow of information that starts with the anterior frontal regions and synchronizes with right and central frontal regions, perhaps conducting both retrieval and integration of an imagined scene. Formisano, however, only utilized natural scenes, neglecting the spectrum of possibilities in imagination. James Haxby's group revealed the cortical networks involved in categorizing biological classes (Connolly et al., 2012). This emerging body of neuroimaging urges us to create a robust encoding model for imagination that takes the temporal dynamics, the classes, and the functional ROIs into account. With such an approach for imagination, we will construct a neural search engine, a technology that enables us to YouTube search with simply our minds.

Lastly, one of the most interesting frontiers in neuroscience is to understand sleep, both its physiology and its underlying evolutionary motive. Traditionally, electroencephalography (EEG) has been the gold standard for staging sleep, due largely to its temporal precision and ability capture oscillations that characterize sleep stages. However, even combined EEG-fMRI studies pose serious constraints on sleep studies, with the EEG scalp surface electrodes causing severe discomfort for participants, reducing both the quality and quantity of sleep attainable in the scanner. In light of this, very recent work by Laufs begun to enable automatic sleep staging using just the BOLD signal (Tagliazucchi et al., 2012). They were able to build a classifier that is independent of the participant, and they have shown classification accuracy for each sleep stage of

80% on two independent participants. To increase accuracy and reliability further, we will also utilize two additional technologies: pulse oximetry and a novel video-based staging of sleep. We will then be able to characterize the neural correlates of each stage of sleep, and in particular, decode dreams in REM sleep. Furthermore, we can begin to identify the influences of sleep by studying how decoded dreams correlate with visual activities prior to sleep. We aim to provide evidence for the fundamental question of why we sleep and dream.

9.2 Preliminary Studies and Rationale

We have begun to acquire fMRI data of two participants watching videos while in the fMRI scanner. Each participant watched 2 hours of randomly pulled 10 second YouTube videos. We hypothesize much more semantically driven influences to play a role in visual processing than has been previously proposed. Thus, we have designed two distinct MRI protocols: 1.) 18 coronal slices fast sequence (1 s repetition time, TR) originating at the occipital pole to capture occipital poles and 2.) 37 horizontal slices (2 s TR) to capture the whole brain. This will drive our discovery of the correct features to utilize in developing the optimal encoding models. Our preliminary studies on imagination have shown promise for a unique encoding model. (**Figure 9.1)** Two participants watched a series of short videos and were asked to imagine the exact videos they watched after a brief pause. The whole brain scans showed strong correlation between the watched and imagined video within voxels in visual area as well as frontal and parietal regions. This whole brain correlation provides key insight for developing

optimal encoding. We also observed a strong correlation between the imagined video and the corresponding watched video. In both participants, we were also able to identify the imagined video to its corresponding watched video with an accuracy 10 times higher than chance.

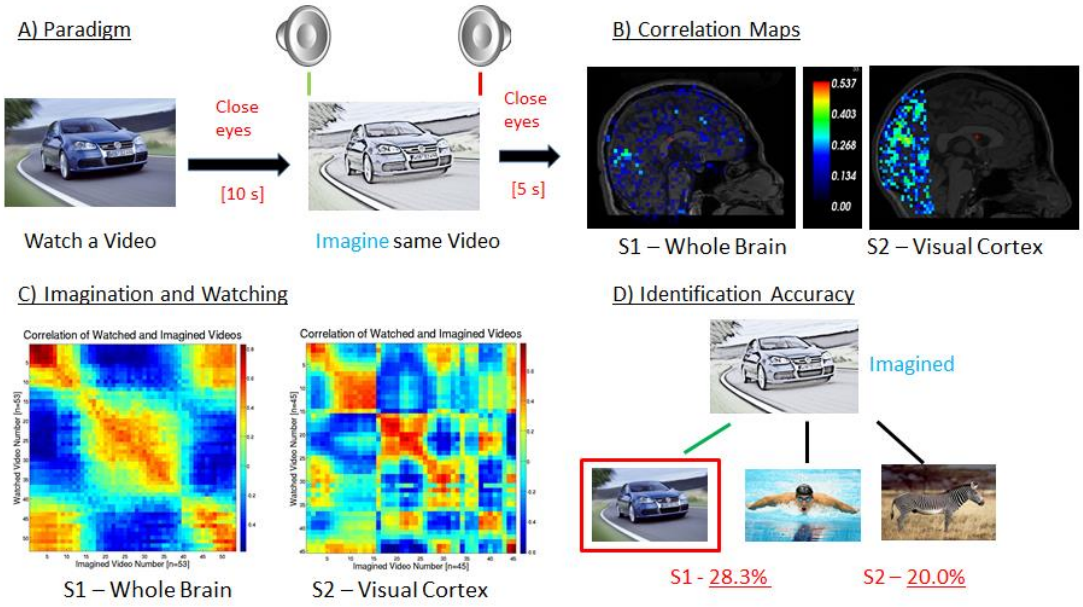

Figure 9.1 Video Decoding

A) Paradigm. Participants watch a clip, wait ten seconds with eyes closed, and then a sound cue instructs the participants to begin imagining the same video they just watched. A second distinct tone is played to cue the participant to stop imagining. 5 second inter-stimulus interval. B) Correlation Maps. The Pearson correlation coefficient between the watched video and the corresponding imagined video for every voxel in each participant's brain scan. C) Imagination and Watching. Pearson Correlation Coefficient for every imagined video across all watched video. D.) Identification Accuracy. Probability of selecting the correct watched video for all imagined videos.

We have also utilized a primitive physiological measure, heart rate, and HD video camera to capture the moments of REM sleep. Previous studies have shown that sympathetic innervation to the heart increases as humans transition from non-REM (NREM) to REM sleep (Bonnet and Arand, 1997). As such, the heart rate increases and becomes more variable as the participants enter REM sleep. We utilized our MR-compatible pulse oximeter to monitor a participant's heart rate as he slept for a period of time in the scanner. To provide another non-obtrusive way to estimate REM, we used a high-definition camcorder to record the eyes as the participant slept. We then correlated the time-frequency spectrum of the luminance change within the eyeball region in the video to the participant's heart rate (**Figure 9.2**).

9.3 Research Design and Methods

The most direct innovation will arise from applying novel image analysis techniques to the fMRI data **(Figure 9.3 and Figure 9.4)**.

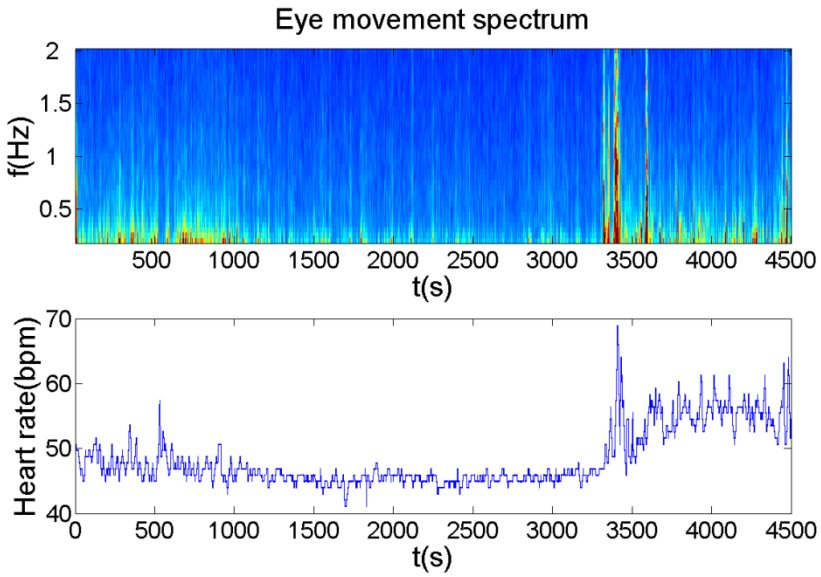

Figure 9.2 Sleep Staging

Top panel shows how different frequency components of the eye movement evolves with time, by analyzing the time-frequency spectrum of the luminance change within eye ball region. Participant woke up around 3400 sec, inducing the higher activity in high frequency. The activity in high frequency before 1000 sec likely involves REM sleep, as demonstrated by the covariation with heart rate (lower panel) and was confirmed by visual-checking of the eye-movement video.

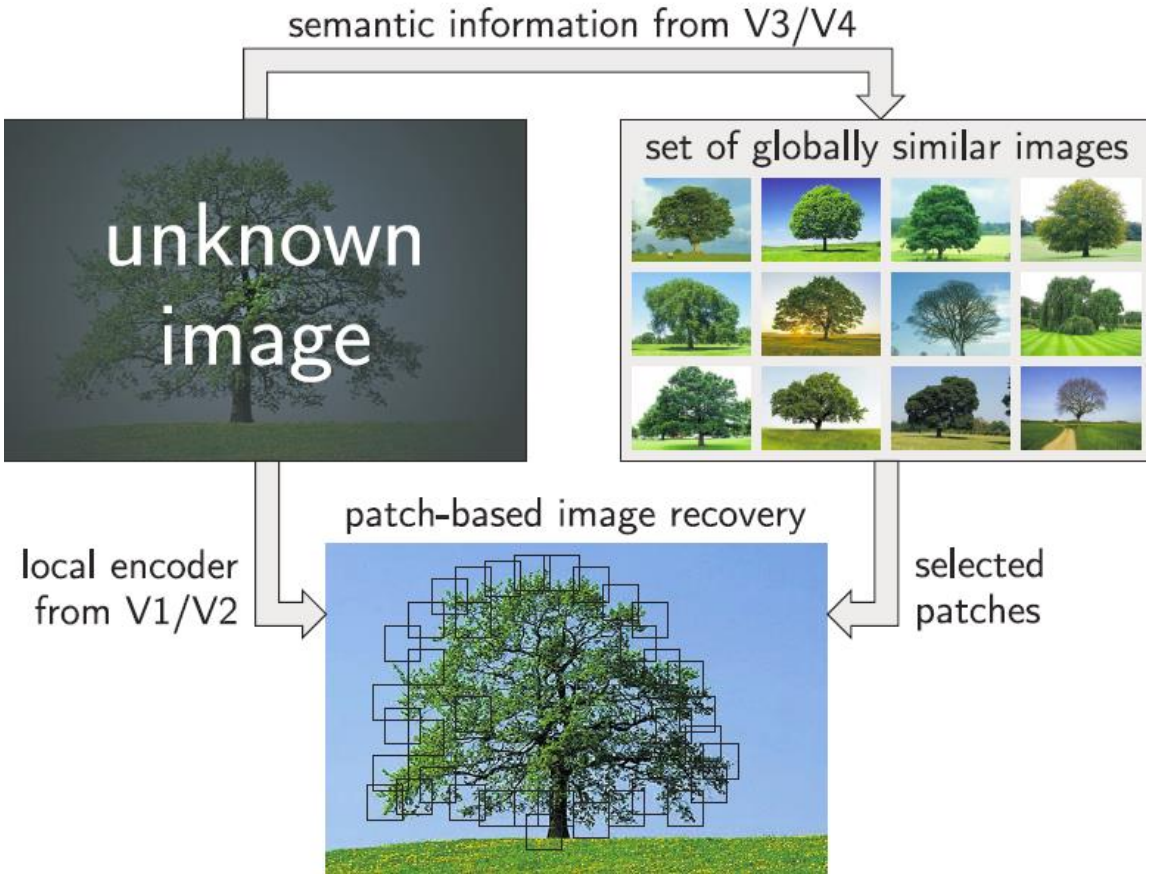

Figure 9.3 Semantic Analysis

Proposed image/video reconstruction algorithm that fuses semantic information from higher areas of the visual cortex with local information found in early visual cortex. The key steps of the algorithm involve selecting similar images from a corpus using semantic information and uses local patches from these images to construct the unknown stimulus.

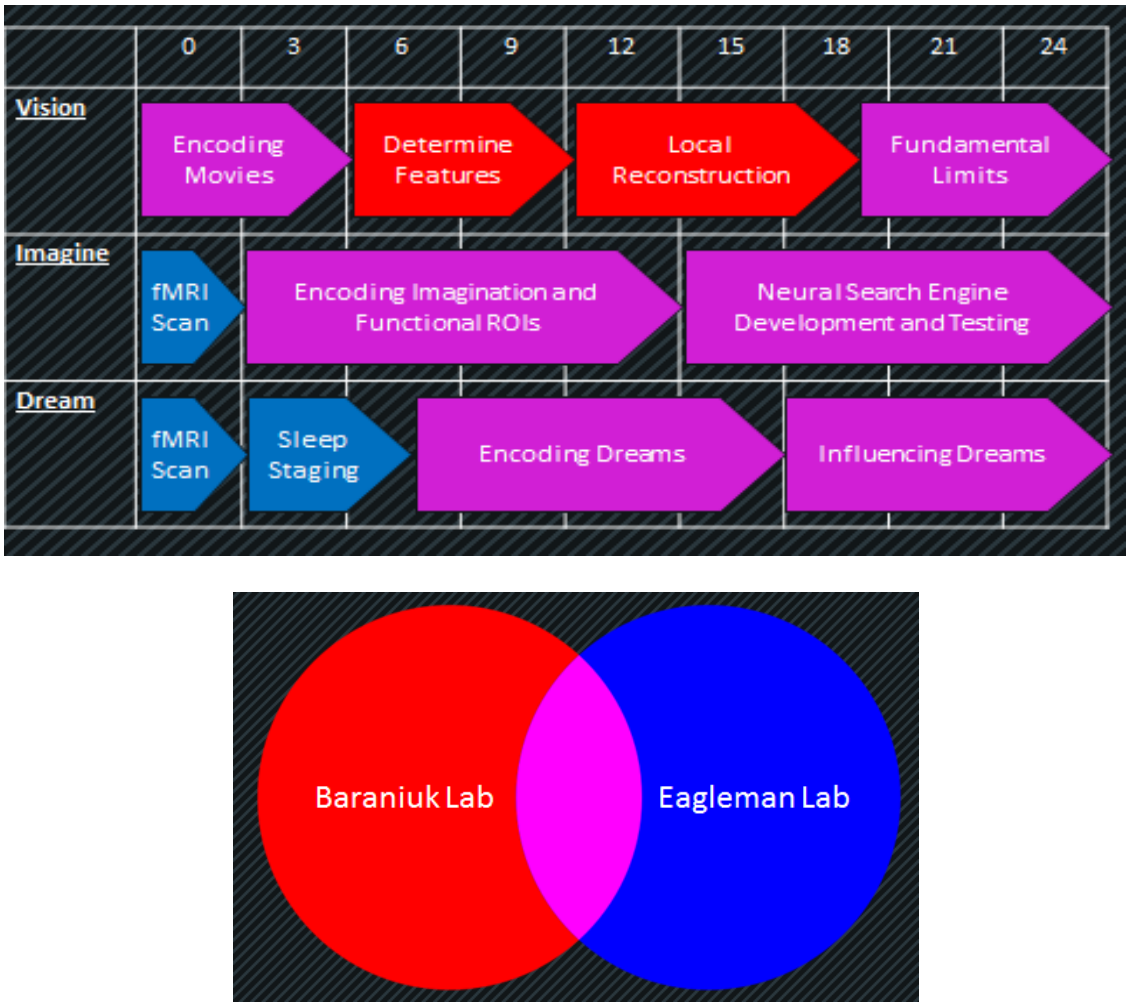

Figure 9.4 Project Milestones

Project's quarterly proposed timeline.

9.4 Specific Aims

9.4.1 Specific Aim 1: Improve Neural Visual Reconstruction With Novel Image Processing Techniques and Machine Learning

We will critically improve a remarkable ability to recreate movies from an fMRI pattern by applying a novel framework encompassing unique digital signal processing algorithms. Previous work applied Gabor filter models to lower visual areas to identify videos participant watched and simple pattern matching approaches to reconstruct a representation of the video. These models, however, have inherent limitations in the accuracy of identification and quality of reconstruction. We propose to improve decoding and reconstruction in three ways. First, we will expand the encoding models to beyond lower visual areas, extending to higher cortical regions that contain important semantic information. Encoding information in these higher areas will require the use of adaptive features that are capable of describing local as well as global image primitives. Second, we plan to reconstruct visual stimuli using local properties of lower visual areas. Rather than utilize a simple global template matching framework, we will piece-meal reconstruct visual input, from voxel to pixel. Third, we aim to ascertain the fundamental limits on the spatial and temporal resolution of the visual cortex in order to better understand the performance limits of encoding and decoding models. Specifically, we are interested in analyzing the *effective* spatial and temporal resolution, which also includes the acquisition (or measurement) process of the BOLD activity. With these three critical improvements, we will create a far more robust reconstruction framework, capable of deciphering the human visual system much more systematically.

9.4.2 Specific Aim 2: Characterize and Decode Human Visual Imagination

We will extend visual decoding into the imagination domain, where we will create the first true visual representation of an imagined scene using fMRI. We anticipate this challenge to be rather unique from the decoding visual input from the eyes in three distinct ways. First, neurons may encode an imagined thought in an entirely different method from visual input. Second, the areas of the brain utilized for imagination may be rather unique from the neural real-estate for watching videos. We will define functional regions-of-interest (ROIs) that characterize where key components of imagination occur and incorporate those regions into our encoding models. Third, as we build a robust encoding framework, imagination will also allow us to build a powerful new application: a neural search engine. Trained participants will be able to imagine any scene inside the scanner, and we will be able to decode and reconstruct that thought.

9.4.3 Specific Aim 3: Reconstruct the Visual Nature of Dreams

We aim to decode and reconstruct another distinct state of mind: dreaming. Just as imagination did, dreaming also likely possesses its own encoding models, neural real-estate, and applications. As such, we will iterate over a robust set of algorithms to find the optimal encoding model and the functional ROIs for dreaming. We will design novel methods for sleep-staging, including a purely video based technique, that will help identify REM sleep and greatly improve the accuracy of our decoding and reconstruction models. Our visual reconstruction approach aims to play back our dreams.

CHAPTER X

CONCLUSIONS

I had a great experience working on a broad array of projects with many great mentors. I tried to capture here the many ideas I attacked over the last 5 years in graduate school. The thrust of my thesis attacked three main topics: How we see, How we feel, and How we decide. Here, I will discuss the meaning of these results and what they mean for us next.

Mapping the polar angle representation of saccades in human SC was one of the most exciting projects I worked on in graduate school. It taught me how important every step of the process is to collect data. Participants need to be well-trained and happy in the scanner, data acquisition needs to be optimal and MR physics need to be well understood, and post-processing requires many approaches. Often this means you need to take the perspective of each aspect of a project, including being the participant! I was scanned 18 times in total on ~2 hour session of making 1000s of eye movements. At the end of some long sessions, my extraocular eye muscles would actually hurt! The topography of eye movements was similar to monkey SC, which made the approach more tangible. We could use the monkey maps as guidance to see if we were on the right track. However, this was not always the case. We also had tried to measure orientation columns in human SC. Orientation columns were recently discovered in mouse SC (Ahmadlou and Heimel, 2015; Feinberg and Meister, 2015) in *Nature*. The challenges in

mouse SC arise because it was hard to study SC without ablating portions of the visual cortex, which destroy top-down input to SC and alter physiological measurements. With advances in surgical approaches and optogenetic techniques, orientation columns were delineated in the mouse. We tried 5 scanning sessions on me to image orientation columns but were unsuccessful. This was another important lesson, that not every animal study indicates the functional organization of the human brain. In human SC, orientation columns may have completely migrated to the visual cortex. But now that the topography of saccadic eye movements has been vetted, we can study a whole host of vision science in humans that are much easier to perform than in monkey. For example, the most exciting project I am working on next is to measure ocular dominance columns in human SC. This will be a fun task of watching NBA videos in the scanner, while the video is being presented to one eye for 15 s and then to the other eye for 15 s via a 3D display. We just received a new 3D lens holder to place the filters in and can begin scanning soon!

I also enjoyed working on studying the ingroup biases associated with religions, especially working with the brilliant and very talented Don Vaughn. Donny performed a heroic task of scanning 135 participants (at a time were scanning was not billed hourly). This enabled us to resolve the empathy network and the ingroup biases, despite using a limited number of trials. A very interesting aspect I found in this study was the effect of repetition suppression. I quantified and observed a 40% decline in BOLD signal change from the first to last trial. I don’t expect this result to be unique to our study.

Parametrically modulating this effect helped to isolate well-defined brain regions responsible for the ingroup biases. This was an interesting approach, and I would be curious to see if would help several disciplines. As for the empathy, it was is one of the most remarkable human characteristics we hold. I was deeply moved by the following quote from Bill Bullard:

"*Opinion is really the lowest form of human knowledge. It requires no accountability, no understanding. The highest form of knowledge is empathy, for it requires us to suspend our egos and live in another's world. It requires profound purpose larger than the self kind of understanding.*"

I think this is an important lesson to take with me as a physician scientist, one that I hope to hold close to my chest.

The last main chapter, how we decide, was one of the most challenging projects I worked on. I found the work of Soon et al. 2008 to be very interesting, a novel finding and a mechanism of how the brain might function. However, as scientists, we are challenged to question every finding and every result we encounter. This meant spending many months trying to replicate the original result of John Dylan Haynes' group. Replicability in science is very challenging, often with less than half of the results in psychology repeating by independent scientists (Collaboration, 2015). Functional MRI likely also faces similar challenges, as so many decision points from data collection to

data analysis can be made. In fact, even using the same structural processing software on different operating systems has resulted in differing results (Gronenschild et al., 2012). That's not to say that software developed for mass usage in the community is a bad approach; communities develop software and tools that no single individual could develop in an academic lifetime. Rather, it suggests we need to be vigilant and open about our practices. This is beginning to become standard practice, but most labs still do not make the raw datasets publicly available. Hopefully, it will become standard practice to place all data collected in online databases publicly available for all to use. If such a system was in place, I would have personally saved many months and many research dollars trying to replicate a result. Nonetheless, I was only partially able to replicate the Soon et al. 2008 result. What does this mean? Well, scanning acquisition was different (3mm voxels vs 2 mm in my data), participants themselves were different (button presses were faster in my data), and exact analysis pipeline had to be inferred from the paper and built with my own software. I did see positive predictive decoding in PCC/Precuneous but not in the exact frontopolar locations. I also decoding elsewhere. An open question is how do we report these differences? Journals would likely not be interested in publishing a pure replication experiment, but it should be known to the next student how else the data might look when the experiment was run again independently. Many interpretations have been cast on the Libet et al. 1985 and the Soon et al. 2008 studies (Bode et al., 2014). The most extreme, often portrayed by the media, suggest that free will does not exist if the brain is making decisions before conscious awareness. However, it is important to discuss this claim for two reasons. First, conscious awareness

is likely not a white line. You could be more (or less) aware of an upcoming decision, but we are often asked to make the decision of when precisely conscious awareness arose (Miller and Schwarz, 2014). This means that the decoding is occurring just prior to the declared conscious awareness. Second, the interesting part for me is the cascade of activity that leads to decision-making. This conversation seems very useful to understand better how the brain makes decisions. Lastly, I thoroughly enjoyed the many talks and debates with advisor Dr. David Eagleman who guided me through many of these ideas.

Despite the many topics spanned in the other chapters, there were still many more that were not included. I spent ~1 year working on trying to build machine learning models to predict mTBI patients from controls in the veteran population. This was a tricky challenge as it was all based on self-report and the type and severity of the injuries were so heterogeneous. It is unclear to me that any spatially aligned normalization approaches would ever yield predictive diagnostic value. Individual measures are essential. Further, most models in this field are significant on the aggregate but vary for individuals dramatically. This implies that measures like brain age or TBI status could not be inferred from an individual scan with current predictive power of any model. This is an interesting challenge that will likely require strong collaborations with computer scientists, MR physicists, and neuropsychologists alike. Secondly, I spent many months analyzing EEG data from musicians and controls. Data were acquired via a portable Emotive 14-channel EEG head set. Several (> 40) previous studies have been published

using this hardware. However, our dataset faced two challenges that revealed important lessons to me. First, we were trying to see if time perception and the underlying neural correlates were different in musicians compared to controls. This meant running participants on a number of timing tasks (e.g., beat matching, sound oddball). During these tasks, musicians would often bob their heads in rhythm to the beat of the music. Unfortunately, this introduced motion artifacts into the data that could have corrupted the signal. Second, the number of trials run on this experiment was very small (on the order of 10 – 25 trials). Typical EEG studies run 100s to 1000s of trials to elicit enough SNR to resolve questions, especially with lower-grade portable hardware. We did not observe significant effects between musicians and controls. However, the challenge is that we do not know if this was limited to quantity and quality of the data. This was an important, recurring theme during my thesis. Working with existing datasets has many advantages and can be fruitful and productive for all members involved. However, often no matter how much effort is put in post-hoc, limitations like the number of trials sampled or experimental manipulations cannot be altered after data collection is complete. There is a great feeling when something doesn't work to alter and run the experiment again. Had I solely worked with existing data on saccadic eye movements, we would have never resolved the polar angle representation of saccades in SC because there were critical manipulations of the experiment design that needed to be made. This was a very valuable lesson for me, to be aware of the quality of the data are prior to initiating analyses and understand the limitations of the data. As a physician, the data acquisition will be even less likely to be altered manually, and I will very likely receive

data on my desk that is not of the highest quality. These experiences will be a lesson well served!

Graduate school is a highly non-linear path. When I received my first project, I thought, “Great, I’ll finish this in one week. What should I do next week?” Five years later, I am still tackling some of those problems. The idea though is not to be discouraged, to persevere and continue to discover. Just don’t be surprised that on your path from A to B that you may discover C and never reach B and then forget what A was all about!

REFERENCES

Ahmadlou, M., Heimel, J.A., 2015. Preference for concentric orientations in the mouse superior colliculus. Nat. Commun. 6. doi:10.1038/ncomms7773

Allefeld C., S.C.S., Bogler C., Heinzle J., Haynes J. D. 2013. Sequential dependencies between trials in free choice tasks. In ArXiv.

Allman, M.J., and Meck, W.H. 2012. Pathophysiological distortions in time perception and timed performance. Brain 135, 656-677.

Altemeyer, B., 1981. Right-wing authoritarianism. University of Manitoba Press.

Amodio, D.M., and Frith, C.D. 2006. Meeting of minds: the medial frontal cortex and social cognition. Nat Rev Neurosci 7, 268-277.

Andersson, J.L.R.J., M.; Smith, S. 2007a. Non-linear optimisation. . FMRIB technical report TR07JA1.

Andersson, J.L.R.J., M.; Smith, S. 2007b. Non-linear registration, aka Spatial normalisation FMRIB technical report TR07JA2

Avants, B.B., Tustison, N.J., Song, G., Cook, P.A., Klein, A., Gee, J.C., 2011. A reproducible evaluation of ANTs similarity metric performance in brain image registration. NeuroImage 54, 2033–2044. doi:10.1016/j.neuroimage.2010.09.025

Avants, B.B., Yushkevich, P., Pluta, J., Minkoff, D., Korczykowski, M., Detre, J., Gee, J.C., 2010. The optimal template effect in hippocampus studies of diseased populations. NeuroImage 49, 2457–2466. doi:10.1016/j.neuroimage.2009.09.062

Azevedo, R.T., Macaluso, E., Avenanti, A., Santangelo, V., Cazzato, V., Aglioti, S.M., 2013. Their pain is not our pain: brain and autonomic correlates of empathic

resonance with the pain of same and different race individuals. Hum. Brain Mapp. 34, 3168–3181. doi:10.1002/hbm.22133

Bagarinao, E., Nakai, T., Tanaka, Y., 2006. Real-time functional MRI: development and emerging applications. Magn Reson Med Sci 5, 157–65.

Balfour, D.J. 2002. Neuroplasticity within the mesoaccumbens dopamine system and its role in tobacco dependence. Current drug targets CNS and neurological disorders 1, 413-421.

Balfour, D.J. 2004. The neurobiology of tobacco dependence: a preclinical perspective on the role of the dopamine projections to the nucleus accumbens [corrected]. Nicotine & tobacco research : official journal of the Society for Research on Nicotine and Tobacco 6, 899-912.

Barros-Loscertales, A., Bustamante, J.C., Ventura-Campos, N., Llopis, J.J., Parcet, M.A., Avila, C., 2011a. Lower activation in the right frontoparietal network during a counting Stroop task in a cocaine-dependent group. Psychiatry Res 194, 111–8. doi:10.1016/j.pscychresns.2011.05.001

Barros-Loscertales, A., Garavan, H., Bustamante, J.C., Ventura-Campos, N., Llopis, J.J., Belloch, V., Parcet, M.A., Avila, C., 2011b. Reduced striatal volume in cocaine-dependent patients. NeuroImage 56, 1021–6. doi:10.1016/j.neuroimage.2011.02.035

Beauchamp, M.S., Lee, K.E., Haxby, J.V., and Martin, A. 2003. FMRI responses to video and point-light displays of moving humans and manipulable objects. J Cogn Neurosci 15, 991-1001.

Behrens, T.E., Berg, H.J., Jbabdi, S., Rushworth, M.F., and Woolrich, M.W. 2007. Probabilistic diffusion tractography with multiple fibre orientations: What can we gain? Neuroimage 34, 144-155.

Behrens, T.E., Woolrich, M.W., Jenkinson, M., Johansen-Berg, H., Nunes, R.G., Clare, S., Matthews, P.M., Brady, J.M., Smith, S.M., 2003. Characterization and propagation of uncertainty in diffusion-weighted MR imaging. Magn. Reson. Med. Off. J. Soc. Magn. Reson. Med. Soc. Magn. Reson. Med. 50, 1077–88. doi:10.1002/mrm.10609

Belhumeur, P., Hespanha, J., Kriegman, D. 1997. Eigenfaces vs. Fisherfaces: Recognition Using Class Specific Linear Projection. IEEE Transactions on Pattern Analysis and Machine Intelligence, 711-720.

Bell, R.P., Foxe, J.J., Ross, L.A., Garavan, H., 2013. Intact inhibitory control processes in abstinent drug abusers (I): A functional neuroimaging study in former cocaine addicts. Neuropharmacology. doi:10.1016/j.neuropharm.2013.02.018

Bell, R.P., Garavan, H., Foxe, J.J., 2014. Neural correlates of craving and impulsivity in abstinent former cocaine users: Towards biomarkers of relapse risk. Neuropharmacology 85, 461–470. doi:10.1016/j.neuropharm.2014.05.011

Biotti, D., Barbieux, M., Brassat, D., 2016. Teaching Video NeuroImages: Alternating skew deviation with abducting hypertropia following superior colliculus infarction. Neurology 86, e93–94. doi:10.1212/WNL.0000000000002425

Bode, S., Bogler, C., Haynes, J.-D., 2013. Similar neural mechanisms for perceptual guesses and free decisions. NeuroImage 65, 456–465. doi:10.1016/j.neuroimage.2012.09.064

Bode, S., Bogler, C., Soon, C.S., Haynes, J.-D., 2012. The neural encoding of guesses in the human brain. NeuroImage 59, 1924–1931. doi:10.1016/j.neuroimage.2011.08.106

Bode, S., He, A.H., Soon, C.S., Trampel, R., Turner, R., Haynes, J.-D., 2011. Tracking the unconscious generation of free decisions using ultra-high field fMRI. PloS One 6, e21612. doi:10.1371/journal.pone.0021612

Bode, S., Murawski, C., Soon, C.S., Bode, P., Stahl, J., Smith, P.L., 2014. Demystifying "free will": The role of contextual information and evidence accumulation for predictive brain activity. Neurosci. Biobehav. Rev. 47C, 636–645. doi:10.1016/j.neubiorev.2014.10.017

Bonnet, M.H., and Arand, D.L. 1997. Heart rate variability: sleep stage, time of night, and arousal influences. Electroencephalogr Clin Neurophysiol 102, 390-396.

Bonson, K.R., Grant, S.J., Contoreggi, C.S., Links, J.M., Metcalfe, J., Weyl, H.L., Kurian, V., Ernst, M., London, E.D., 2002. Neural systems and cue-induced cocaine craving. Neuropsychopharmacology 26, 376–86. doi:10.1016/S0893-133X(01)00371-2

Born H. A., Kim J. Y., Savjani R. R., Das P., Dabaghian Y. A., Guo Q., et al., 2014. Genetic suppression of transgenic APP rescues Hypersynchronous network

activity in a mouse model of Alzeimer's disease. J. Neurosci Off. J. Soc. Neurosci. 34, 3826–3840. doi:10.1523/JNEUROSCI.5171-13.2014

Botvinick, M., Jha, A.P., Bylsma, L.M., Fabian, S.A., Solomon, P.E., Prkachin, K.M., 2005. Viewing facial expressions of pain engages cortical areas involved in the direct experience of pain. NeuroImage 25, 312–319. doi:10.1016/j.neuroimage.2004.11.043

Brainard, D.H., 1997. The Psychophysics Toolbox. Spat. Vis. 10, 433–436.

Bruck, C., Wildgruber, D., Kreifelts, B., Kruger, R., and Wachter, T. 2011. Effects of subthalamic nucleus stimulation on emotional prosody comprehension in Parkinson's disease. PLoS One 6, e19140.

Brühl, A.B., Scherpiet, S., Sulzer, J., Stämpfli, P., Seifritz, E., Herwig, U., 2014. Real-time neurofeedback using functional MRI could improve down-regulation of amygdala activity during emotional stimulation: a proof-of-concept study. Brain Topogr. 27, 138–148. doi:10.1007/s10548-013-0331-9

Buckholtz, J.W., Asplund, C.L., Dux, P.E., Zald, D.H., Gore, J.C., Jones, O.D., and Marois, R. 2008. The neural correlates of third-party punishment. Neuron 60, 930-940.

Buckner, R.L., Krienen, F.M., Castellanos, A., Diaz, J.C., and Yeo, B.T. 2011. The organization of the human cerebellum estimated by intrinsic functional connectivity. J Neurophysiol 106, 2322-2345.

Bullmore, E.T., Suckling, J., Overmeyer, S., Rabe-Hesketh, S., Taylor, E., and Brammer, M.J. 1999. Global, voxel, and cluster tests, by theory and permutation, for

a difference between two groups of structural MR images of the brain. IEEE Trans Med Imaging 18, 32-42.

Camprodon, J.A., Martinez-Raga, J., Alonso-Alonso, M., Shih, M.C., Pascual-Leone, A., 2007. One session of high frequency repetitive transcranial magnetic stimulation (rTMS) to the right prefrontal cortex transiently reduces cocaine craving. Drug Alcohol Depend 86, 91–4. doi:S0376-8716(06)00222-5 10.1016/j.drugalcdep.2006.06.002

Canavan, S.V., Forselius, E.L., Bessette, A.J., Morgan, P.T., 2014. Preliminary evidence for normalization of risk taking by modafinil in chronic cocaine users. Addict. Behav. 39, 1057–1061. doi:10.1016/j.addbeh.2014.02.015

Canterberry, M., Hanlon, C.A., Hartwell, K.J., Li, X., Owens, M., LeMatty, T., Prisciandaro, J.J., Borckardt, J., Saladin, M.E., Brady, K.T., George, M.S., 2013. Sustained reduction of nicotine craving with real-time neurofeedback: exploring the role of severity of dependence. Nicotine Tob. Res. Off. J. Soc. Res. Nicotine Tob. 15, 2120–2124. doi:10.1093/ntr/ntt122

Cao, J., Dwyer, J.B., Gautier, N.M., Leslie, F.M., and Li, M.D. 2013a. Central myelin gene expression during postnatal development in rats exposed to nicotine gestationally. Neuroscience letters 553, 115-120.

Cao, J., Wang, J., Dwyer, J.B., Gautier, N.M., Wang, S., Leslie, F.M., and Li, M.D. 2013b. Gestational nicotine exposure modifies myelin gene expression in the brains of adolescent rats with sex differences. Translational psychiatry 3, e247.

Caria, A., Sitaram, R., Birbaumer, N., 2012. Real-time fMRI: a tool for local brain regulation. Neuroscientist 18, 487–501. doi:10.1177/1073858411407205

Casebeer, W., and Churchland, P. 2003. The Neural Mechanisms of Moral Cognition: A Multiple-Aspect Approach to Moral Judgment and Decision-Making. Biology and Philosophy 18, 169-194.

Caskey, N.H., Jarvik, M.E., Wirshing, W.C., Madsen, D.C., Iwamoto-Schaap, P.N., Eisenberger, N.I., Huerta, L., Terrace, S.M., and Olmstead, R.E. 2002. Modulating tobacco smoking rates by dopaminergic stimulation and blockade. Nicotine & tobacco research : official journal of the Society for Research on Nicotine and Tobacco 4, 259-266.

Chang, D.H.F., Hess, R.F., Mullen, K.T., 2016. Color responses and their adaptation in human superior colliculus and lateral geniculate nucleus. NeuroImage. doi:10.1016/j.neuroimage.2016.04.067

Chein, J., Albert, D., O'Brien, L., Uckert, K., Steinberg, L., 2011. Peers increase adolescent risk taking by enhancing activity in the brain's reward circuitry. Dev. Sci. 14, F1–10. doi:10.1111/j.1467-7687.2010.01035.x

Chen, B.T., Yau, H.J., Hatch, C., Kusumoto-Yoshida, I., Cho, S.L., Hopf, F.W., Bonci, A., 2013. Rescuing cocaine-induced prefrontal cortex hypoactivity prevents compulsive cocaine seeking. Nature 496, 359–62. doi:10.1038/nature12024

Cherek, D.R., 1981. Effects of smoking different doses of nicotine on human aggressive behavior. Psychopharmacology (Berl.) 75, 339–345.

Childress, A.R., Mozley, P.D., McElgin, W., Fitzgerald, J., Reivich, M., O'Brien, C.P., 1999. Limbic activation during cue-induced cocaine craving. Am J Psychiatry 156, 11–8.

Cid, J., 2009. Is imprisonment criminogenic? A comparative study of recidivism rates between prison and suspended prison sanctions. Eur. J. Criminol. 6, 459–480.

Cikara, M., Botvinick, M.M., Fiske, S.T., 2011. Us versus Them: Social Identity Shapes Neural Responses to Intergroup Competition and Harm. Psychol. Sci. 22. doi:10.1177/0956797610397667

Cikara, M., Eberhardt, J.L., and Fiske, S.T. 2011. From agents to objects: sexist attitudes and neural responses to sexualized targets. J Cogn Neurosci 23, 540-551.

Citizens United v. Federal Election Commission, 558 U.S. 310. 2010.

Coffey, S.F., Gudleski, G.D., Saladin, M.E., Brady, K.T., 2003. Impulsivity and rapid discounting of delayed hypothetical rewards in cocaine-dependent individuals. Exp Clin Psychopharmacol 11, 18–25.

Cole, J.H., Leech, R., Sharp, D.J., Alzheimer's Disease Neuroimaging Initiative, 2015. Prediction of brain age suggests accelerated atrophy after traumatic brain injury. Ann. Neurol. 77, 571–581. doi:10.1002/ana.24367

Collaboration, O.S., 2015. Estimating the reproducibility of psychological science. Science 349, aac4716. doi:10.1126/science.aac4716

Condy, C., Rivaud-Péchoux, S., Ostendorf, F., Ploner, C.J., Gaymard, B., 2004. Neural substrate of antisaccades: role of subcortical structures. Neurology 63, 1571–1578.

Connolly, A.C., Guntupalli, J.S., Gors, J., Hanke, M., Halchenko, Y.O., Wu, Y.C., Abdi, H., and Haxby, J.V. 2012. The representation of biological classes in the human brain. J Neurosci 32, 2608-2618.

Connolly, J.D., Vuong, Q.C., Thiele, A., 2015. Gaze-dependent topography in human posterior parietal cortex. Cereb. Cortex N. Y. N 1991 25, 1519–1526. doi:10.1093/cercor/bht344

Contreras-Huerta, L.S., Baker, K.S., Reynolds, K.J., Batalha, L., Cunnington, R., 2013. Racial bias in neural empathic responses to pain. PloS One 8, e84001. doi:10.1371/journal.pone.0084001

Corbo, V., Salat, D.H., Amick, M.M., Leritz, E.C., Milberg, W.P., McGlinchey, R.E., 2014. Reduced cortical thickness in veterans exposed to early life trauma. Psychiatry Res. 223, 53–60. doi:10.1016/j.pscychresns.2014.04.013

Costafreda, S.G., Fu, C.H., Lee, L., Everitt, B., Brammer, M.J., and David, A.S. 2006. A systematic review and quantitative appraisal of fMRI studies of verbal fluency: role of the left inferior frontal gyrus. Hum Brain Mapp 27, 799-810.

Coutanche, M.N., and Thompson-Schill, S.L. 2012. The advantage of brief fMRI acquisition runs for multi-voxel pattern detection across runs. Neuroimage 61, 1113-1119.

Cox, R.W. 1996. AFNI: software for analysis and visualization of functional magnetic resonance neuroimages. Comput Biomed Res 29, 162-173.

Cox, R.W., Jesmanowicz, A., Hyde, J.S., 1995. Real-time functional magnetic resonance imaging. Magn. Reson. Med. Off. J. Soc. Magn. Reson. Med. Soc. Magn. Reson. Med. 33, 230–6.

Curran, J.M., 2013. Hotelling: Hotelling's T-squared test and variants.

Dash, S., Nazari, S.A., Yan, X., Wang, H., Crawford, J.D., 2016. Superior Colliculus Responses to Attended, Unattended, and Remembered Saccade Targets during Smooth Pursuit Eye Movements. Front. Syst. Neurosci. 10, 34. doi:10.3389/fnsys.2016.00034

Davis, M., 1980. A multidimensional approach to individual differences in empathy. JSAS Catalog of Selected Documents in Psychology 10.

Dawkins, R., 2008. The God Delusion, Reprint edition. ed. Mariner Books, Boston.

de Borst, A.W., Sack, A.T., Jansma, B.M., Esposito, F., de Martino, F., Valente, G., Roebroeck, A., di Salle, F., Goebel, R., and Formisano, E. 2012. Integration of "what" and "where" in frontal cortex during visual imagery of scenes. Neuroimage 60, 47-58.

Dean, P.J.A., Sato, J.R., Vieira, G., McNamara, A., Sterr, A., 2015. Long-term structural changes after mTBI and their relation to post-concussion symptoms. Brain Inj. 1–8. doi:10.3109/02699052.2015.1035334

Decety, J., and Lamm, C. 2006. Human empathy through the lens of social neuroscience. ScientificWorldJournal 6, 1146-1163.

deCharms, R.C., 2007. Reading and controlling human brain activation using real-time functional magnetic resonance imaging. Trends Cogn. Sci. 11, 473–81. doi:10.1016/j.tics.2007.08.014

deCharms, R.C., 2008. Applications of real-time fMRI. Nat. Rev. Neurosci. 9, 720–9. doi:10.1038/nrn2414

deCharms, R.C., Maeda, F., Glover, G.H., Ludlow, D., Pauly, J.M., Soneji, D., Gabrieli, J.D., Mackey, S.C., 2005. Control over brain activation and pain learned by using real-time functional MRI. Proc. Natl. Acad. Sci. U. S. A. 102, 18626–31. doi:10.1073/pnas.0505210102

Demanet, J., De Baene, W., Arrington, C.M., and Brass, M. 2013. Biasing free choices: the role of the rostral cingulate zone in intentional control. Neuroimage 72, 207-213.

D'Esposito, M., Postle, B.R., and Rypma, B. 2000. Prefrontal cortical contributions to working memory: evidence from event-related fMRI studies. Exp Brain Res 133, 3-11.

Di Chiara, G., Bassareo, V., Fenu, S., De Luca, M.A., Spina, L., Cadoni, C., Acquas, E., Carboni, E., Valentini, V., and Lecca, D. 2004. Dopamine and drug addiction: the nucleus accumbens shell connection. Neuropharmacology 47 Suppl 1, 227-241.

Ding, Y.S., Fowler, J.S., Logan, J., Wang, G.J., Telang, F., Garza, V., Biegon, A., Pareto, D., Rooney, W., Shea, C., et al. 2004. 6-[18F]Fluoro-A-85380, a new PET tracer for the nicotinic acetylcholine receptor: studies in the human brain and in vivo demonstration of specific binding in white matter. Synapse 53, 184-189.

Eagleman, D.M., Correro, M.A., 2010. Why neuroscience matters for a rational drug policy. Minn. J. Law Sci. Technol.

Ehrman, R.N., Robbins, S.J., Childress, A.R., O'Brien, C.P., 1992. Conditioned responses to cocaine-related stimuli in cocaine abuse patients. Psychopharmacology (Berl.) 107, 523–529.

Ellmore, T.M., Castriotta, R.J., Hendley, K.L., Aalbers, B.M., Furr-Stimming, E., Hood, A.J., Suescun, J., Beurlot, M.R., Hendley, R.T., and Schiess, M.C. 2013. Altered nigrostriatal and nigrocortical functional connectivity in rapid eye movement sleep behavior disorder. Sleep 36, 1885-1892.

Ersche, K.D., Barnes, A., Jones, P.S., Morein-Zamir, S., Robbins, T.W., Bullmore, E.T., 2011. Abnormal structure of frontostriatal brain systems is associated with aspects of impulsivity and compulsivity in cocaine dependence. Brain J. Neurol. 134, 2013–24. doi:10.1093/brain/awr138

Ersche, K.D., Jones, P.S., Williams, G.B., Smith, D.G., Bullmore, E.T., Robbins, T.W., 2013. Distinctive personality traits and neural correlates associated with stimulant drug use versus familial risk of stimulant dependence. Biol. Psychiatry 74, 137–44. doi:10.1016/j.biopsych.2012.11.016

Feinberg, E.H., Meister, M., 2015. Orientation columns in the mouse superior colliculus. Nature 519, 229–232. doi:10.1038/nature14103

Fernandez-Serrano, M.J., Perales, J.C., Moreno-Lopez, L., Perez-Garcia, M., Verdejo-Garcia, A., 2012. Neuropsychological profiling of impulsivity and compulsivity in

cocaine dependent individuals. Psychopharmacol. Berl 219, 673–83. doi:10.1007/s00213-011-2485-z

Fischl, B., Dale, A.M., 2000. Measuring the thickness of the human cerebral cortex from magnetic resonance images. Proc Natl Acad Sci U A 97, 11050–5. doi:10.1073/pnas.200033797

Fjell, A.M., Westlye, L.T., Amlien, I., Espeseth, T., Reinvang, I., Raz, N., Agartz, I., Salat, D.H., Greve, D.N., Fischl, B., Dale, A.M., Walhovd, K.B., 2009. Minute effects of sex on the aging brain: a multisample magnetic resonance imaging study of healthy aging and Alzheimer's disease. J Neurosci 29, 8774–83. doi:10.1523/JNEUROSCI.0115-09.2009

Folkes, V.S., and Kamins, M.A. 1999. Effects of information about firms' ethical and unethical actions on consumers' attitudes. Journal of Consumer Psychology 8, 243-259.

Forstmann, B.U., Brass, M., Koch, I., and von Cramon, D.Y. 2006. Voluntary selection of task sets revealed by functional magnetic resonance imaging. J Cogn Neurosci 18, 388-398.

Fotenos, A.F., Snyder, A.Z., Girton, L.E., Morris, J.C., Buckner, R.L., 2005. Normative estimates of cross-sectional and longitudinal brain volume decline in aging and AD. Neurology 64, 1032–1039. doi:10.1212/01.WNL.0000154530.72969.11

Fowler, S.W., Chiang, A.C., Savjani, R.R., Larson, M.E., Sherman, M.A., Schuler, D.R., Cirrito, J.R., Lesne´ , S.E., and Jankowsky, J.L., 2014. Genetic modulation of soluble Ab rescues cognitive and synaptic impairment in a mouse model of Alzheimer's

disease. J. Neurosci Off. J. Soc. Neurosci. 34, 7871–7885. doi:10.1523/JNEUROSCI.0572-14.2014

Franklin, T.R., Acton, P.D., Maldjian, J.A., Gray, J.D., Croft, J.R., Dackis, C.A., O'Brien, C.P., Childress, A.R., 2002. Decreased gray matter concentration in the insular, orbitofrontal, cingulate, and temporal cortices of cocaine patients. Biol. Psychiatry 51, 134–42.

Friederici, A.D., Ruschemeyer, S.A., Hahne, A., and Fiebach, C.J. 2003. The role of left inferior frontal and superior temporal cortex in sentence comprehension: localizing syntactic and semantic processes. Cereb Cortex 13, 170-177.

Frith, C.D., Friston, K., Liddle, P.F., and Frackowiak, R.S. 1991. Willed action and the prefrontal cortex in man: a study with PET. Proceedings Biological sciences / The Royal Society 244, 241-246.

Garavan, H., Kaufman, J.N., Hester, R., 2008. Acute effects of cocaine on the neurobiology of cognitive control. Philos. Trans. R. Soc. Lond. B. Biol. Sci. 363, 3267–76. doi:10.1098/rstb.2008.0106

Garavan, H., Pankiewicz, J., Bloom, A., Cho, J.K., Sperry, L., Ross, T.J., Salmeron, B.J., Risinger, R., Kelley, D., Stein, E.A., 2000. Cue-induced cocaine craving: neuroanatomical specificity for drug users and drug stimuli. Am J Psychiatry 157, 1789–98.

Garcia Dominguez, L., Kostelecki, W., Wennberg, R., and Perez Velazquez, J.L. 2011. Distinct dynamical patterns that distinguish willed and forced actions. Cognitive neurodynamics 5, 67-76.

Glover, G.H., 1999. Simple analytic spiral K-space algorithm. Magn. Reson. Med. 42, 412–415.

Glover, G.H., Lai, S., 1998. Self-navigated spiral fMRI: interleaved versus single-shot. Magn. Reson. Med. 39, 361–368.

Goddeyne, C., Nichols, J., Wu, C., Anderson, T., 2015. Repetitive mild traumatic brain injury induces ventriculomegaly and cortical thinning in juvenile rats. J. Neurophysiol. 113, 3268–3280. doi:10.1152/jn.00970.2014

Goldstein, R.Z., Tomasi, D., Alia-Klein, N., Honorio Carrillo, J., Maloney, T., Woicik, P.A., Wang, R., Telang, F., Volkow, N.D., 2009. Dopaminergic response to drug words in cocaine addiction. J. Neurosci. Off. J. Soc. Neurosci. 29, 6001–6. doi:10.1523/JNEUROSCI.4247-08.2009

Goldstein, R.Z., Tomasi, D., Rajaram, S., Cottone, L.A., Zhang, L., Maloney, T., Telang, F., Alia-Klein, N., Volkow, N.D., 2007. Role of the anterior cingulate and medial orbitofrontal cortex in processing drug cues in cocaine addiction. Neuroscience 144, 1153–9. doi:10.1016/j.neuroscience.2006.11.024

Gons, R.A., van Norden, A.G., de Laat, K.F., van Oudheusden, L.J., van Uden, I.W., Zwiers, M.P., Norris, D.G., and de Leeuw, F.E. 2011. Cigarette smoking is associated with reduced microstructural integrity of cerebral white matter. Brain 134, 2116-2124.

Gorgolewski, K., Burns, C.D., Madison, C., Clark, D., Halchenko, Y.O., Waskom, M.L., Ghosh, S.S., 2011. Nipype: a flexible, lightweight and extensible neuroimaging data

processing framework in python. Front Neuroinform 5, 13. doi:10.3389/fninf.2011.00013

Gorsuch, R.L., Venable, G.D., 1983. Development of an "Age Universal" I-E Scale. J. Sci. Study Relig. 22, 181–187. doi:10.2307/1385677

Grahn, J.A., and Brett, M. 2007. Rhythm and beat perception in motor areas of the brain. J Cogn Neurosci 19, 893-906.

Grant, S., London, E.D., Newlin, D.B., Villemagne, V.L., Liu, X., Contoreggi, C., Phillips, R.L., Kimes, A.S., Margolin, A., 1996. Activation of memory circuits during cue-elicited cocaine craving. Proc. Natl. Acad. Sci. U. S. A. 93, 12040–5.

Greene, J., and Haidt, J. 2002. How (and where) does moral judgment work? Trends Cogn Sci 6, 517-523.

Greene, J.D., Sommerville, R.B., Nystrom, L.E., Darley, J.M., and Cohen, J.D. 2001. An fMRI investigation of emotional engagement in moral judgment. Science 293, 2105-2108.

Gronenschild, E.H., Habets, P., Jacobs, H.I., Mengelers, R., Rozendaal, N., van Os, J., Marcelis, M., 2012. The effects of FreeSurfer version, workstation type, and Macintosh operating system version on anatomical volume and cortical thickness measurements. PLoS One 7, e38234. doi:10.1371/journal.pone.0038234

Grossman, E., Donnelly, M., Price, R., Pickens, D., Morgan, V., Neighbor, G., and Blake, R. 2000. Brain areas involved in perception of biological motion. J Cogn Neurosci 12, 711-720.

Grossman, E.D., and Blake, R. 2001. Brain activity evoked by inverted and imagined biological motion. Vision Res 41, 1475-1482.

Guo, X., Zheng, L., Zhang, W., Zhu, L., Li, J., Wang, Q., Dienes, Z., Yang, Z., 2012. Empathic neural responses to others' pain depend on monetary reward. Soc. Cogn. Affect. Neurosci. 7, 535–541. doi:10.1093/scan/nsr034

Hanes, D.P., Smith, M.K., Optican, L.M., Wurtz, R.H., 2005. Recovery of saccadic dysmetria following localized lesions in monkey superior colliculus. Exp. Brain Res. 160, 312–325. doi:10.1007/s00221-004-2013-z

Hanke, M., Halchenko, Y.O., Sederberg, P.B., Hanson, S.J., Haxby, J.V., and Pollmann, S. 2009a. PyMVPA: A python toolbox for multivariate pattern analysis of fMRI data. Neuroinformatics 7, 37-53.

Hanke, M., Halchenko, Y.O., Sederberg, P.B., Olivetti, E., Frund, I., Rieger, J.W., Herrmann, C.S., Haxby, J.V., Hanson, S.J., and Pollmann, S. 2009b. PyMVPA: A Unifying Approach to the Analysis of Neuroscientific Data. Front Neuroinform 3, 3.

Hanlon, C.A., Hartwell, K.J., Canterberry, M., Li, X., Owens, M., Lematty, T., Prisciandaro, J.J., Borckardt, J., Brady, K.T., George, M.S., 2013. Reduction of cue-induced craving through realtime neurofeedback in nicotine users: The role of region of interest selection and multiple visits. Psychiatry Res 213, 79–81. doi:10.1016/j.pscychresns.2013.03.003

Harris, L.T., and Fiske, S.T. 2006. Dehumanizing the lowest of the low: neuroimaging responses to extreme out-groups. Psychol Sci 17, 847-853.

Hartwell, K.J., Prisciandaro, J.J., Borckardt, J., Li, X., George, M.S., Brady, K.T., 2013. Real-time fMRI in the treatment of nicotine dependence: a conceptual review and pilot studies. Psychol. Addict. Behav. J. Soc. Psychol. Addict. Behav. 27, 501–509. doi:10.1037/a0028215

Harvey, A.H., Kirk, U., Denfield, G.H., and Montague, P.R. 2010. Monetary favors and their influence on neural responses and revealed preference. J Neurosci 30, 9597-9602.

Hein, G., Silani, G., Preuschoff, K., Batson, C., Singer, T., 2010. Neural responses to ingroup and outgroup members' suffering predict individual differences in costly helping. Neuron 68, 149–60.

Hein, G., Singer, T., 2008. I feel how you feel but not always: the empathic brain and its modulation. Curr. Opin. Neurobiol. 18, 153–8.

Hester, R., Garavan, H., 2004. Executive dysfunction in cocaine addiction: evidence for discordant frontal, cingulate, and cerebellar activity. J Neurosci 24, 11017–22.

Himmelbach, M., Erb, M., Karnath, H.-O., 2007. Activation of superior colliculi in humans during visual exploration. BMC Neurosci. 8, 66. doi:10.1186/1471-2202-8-66

Himmelbach, M., Linzenbold, W., Ilg, U.J., 2013. Dissociation of reach-related and visual signals in the human superior colliculus. NeuroImage 82, 61–67. doi:10.1016/j.neuroimage.2013.05.101

Hirshorn, E.A., and Thompson-Schill, S.L. 2006. Role of the left inferior frontal gyrus in covert word retrieval: neural correlates of switching during verbal fluency. Neuropsychologia 44, 2547-2557.

Hofstetter, S., Tavor, I., Tzur Moryosef, S., and Assaf, Y. 2013. Short-term learning induces white matter plasticity in the fornix. The Journal of neuroscience : the official journal of the Society for Neuroscience 33, 12844-12850.

Hudkins, M., O'Neill, J., Tobias, M.C., Bartzokis, G., and London, E.D. 2012. Cigarette smoking and white matter microstructure. Psychopharmacology 221, 285-295.

Hulka, L.M., Eisenegger, C., Preller, K.H., Vonmoos, M., Jenni, D., Bendrick, K., Baumgartner, M.R., Seifritz, E., Quednow, B.B., 2014. Altered social and non-social decision-making in recreational and dependent cocaine users. Psychol. Med. 44, 1015–1028. doi:10.1017/S0033291713001839

Hyder, F., Phelps, E.A., Wiggins, C.J., Labar, K.S., Blamire, A.M., and Shulman, R.G. 1997. "Willed action": a functional MRI study of the human prefrontal cortex during a sensorimotor task. Proc Natl Acad Sci U S A 94, 6989-6994.

Inciardi, J.A., Surratt, H.L., 2001. Drug use, street crime, and sex-trading among cocaine-dependent women: implications for public health and criminal justice policy. J Psychoact. Drugs 33, 379–89.

Jack, A.I., Dawson, A.J., Begany, K.L., Leckie, R.L., Barry, K.P., Ciccia, A.H., and Snyder, A.Z. 2012. fMRI reveals reciprocal inhibition between social and physical cognitive domains. Neuroimage 66C, 385-401.

Jacoby, N., Bruneau, E., Koster-Hale, J., Saxe, R., 2015. Localizing Pain Matrix and Theory of Mind networks with both verbal and non-verbal stimuli. NeuroImage 126, 39–48. doi:10.1016/j.neuroimage.2015.11.025

Jarvik, M., 1990. The drug dilemma: manipulating the demand. Science 250, 387–92.

Jbabdi, S., Behrens, T.E., and Smith, S.M. 2010. Crossing fibres in tract-based spatial statistics. Neuroimage 49, 249-256.

Jenkinson, M., and Smith, S. 2001. A global optimisation method for robust affine registration of brain images. Med Image Anal 5, 143-156.

Jenkinson, M., Bannister, P., Brady, M., and Smith, S. 2002. Improved optimization for the robust and accurate linear registration and motion correction of brain images. Neuroimage 17, 825-841.

Jenkinson, M., Beckmann, C.F., Behrens, T.E., Woolrich, M.W., and Smith, S.M. 2012. Fsl. Neuroimage 62, 782-790.

Jenkinson, M., Smith, S., 2001. A global optimisation method for robust affine registration of brain images. Med Image Anal 5, 143–56. doi:S1361841501000366 [pii]

Jernigan, T.L., Archibald, S.L., Berhow, M.T., Sowell, E.R., Foster, D.S., Hesselink, J.R., 1991. Cerebral structure on MRI, Part I: Localization of age-related changes. Biol. Psychiatry 29, 55–67.

Kahnt, T., Grueschow, M., Speck, O., Haynes, J., 2011. Perceptual learning and decision-making in human medial frontal cortex. Neuron 70, 549–59.

Kang, M.S. 2010. After Citizens United. Indiana Law Review 44, 243-254.

Kao, Y.C., Davis, E.S., and Gabrieli, J.D. 2005. Neural correlates of actual and predicted memory formation. Nat Neurosci 8, 1776-1783.

Katyal, S., Greene, C.A., Ress, D., 2012. High-resolution functional magnetic resonance imaging methods for human midbrain. J. Vis. Exp. JoVE e3746. doi:10.3791/3746

Katyal, S., Ress, D., 2014. Endogenous attention signals evoked by threshold contrast detection in human superior colliculus. J. Neurosci. Off. J. Soc. Neurosci. 34, 892–900. doi:10.1523/JNEUROSCI.3026-13.2014

Katyal, S., Zughni, S., Greene, C., Ress, D., 2010. Topography of covert visual attention in human superior colliculus. J. Neurophysiol. 104, 3074–3083. doi:10.1152/jn.00283.2010

Kaufman, J.N., Ross, T.J., Stein, E.A., Garavan, H., 2003. Cingulate hypoactivity in cocaine users during a GO-NOGO task as revealed by event-related functional magnetic resonance imaging. J. Neurosci. Off. J. Soc. Neurosci. 23, 7839–43.

Khalki, H., Khalki, L., Aboufatima, R., Ouachrif, A., Mountassir, M., Benharref, A., and Chait, A. 2012. Prenatal exposure to tobacco extract containing nicotinic alkaloids produces morphological and behavioral changes in newborn rats. Pharmacol Biochem Behav 101, 342-347.

Kilts, C.D., Schweitzer, J.B., Quinn, C.K., Gross, R.E., Faber, T.L., Muhammad, F., Ely, T.D., Hoffman, J.M., Drexler, K.P., 2001. Neural activity related to drug craving in cocaine addiction. Arch Gen Psychiatry 58, 334–41. doi:yoa9048 [pii]

Klein, A., Tourville, J., 2012. 101 labeled brain images and a consistent human cortical labeling protocol. Front. Neurosci. 6, 171. doi:10.3389/fnins.2012.00171

Knabb, J.J., Welsh, R.K., Ziebell, J.G., and Reimer, K.S. 2009. Neuroscience, moral reasoning, and the law. Behavioral sciences & the law 27, 219-236.

Knapp, W.P., Soares, B.G., Farrel, M., Lima, M.S., 2007. Psychosocial interventions for cocaine and psychostimulant amphetamines related disorders. Cochrane Database Syst Rev CD003023. doi:10.1002/14651858.CD003023.pub2

Kochunov, P., Du, X., Moran, L.V., Sampath, H., Wijtenburg, S.A., Yang, Y., Rowland, L.M., Stein, E.A., and Hong, L.E. 2013. Acute nicotine administration effects on fractional anisotropy of cerebral white matter and associated attention performance. Frontiers in pharmacology 4, 117.

Konen, C.S., Kastner, S., 2008. Representation of eye movements and stimulus motion in topographically organized areas of human posterior parietal cortex. J. Neurosci. Off. J. Soc. Neurosci. 28, 8361–8375. doi:10.1523/JNEUROSCI.1930-08.2008

Konova, A.B., Moeller, S.J., Tomasi, D., Parvaz, M.A., Alia-Klein, N., Volkow, N.D., Goldstein, R.Z., 2012. Structural and behavioral correlates of abnormal encoding of money value in the sensorimotor striatum in cocaine addiction. Eur J Neurosci 36, 2979–88. doi:10.1111/j.1460-9568.2012.08211.x

Kostelecki, W., Mei, Y., Garcia Dominguez, L., and Perez Velazquez, J.L. 2012. Patterns of brain activity distinguishing free and forced actions: contribution from sensory cortices. Front Integr Neurosci 6, 84.

Krauss, R. 2010. Neuroscience and Institutional Choice in Federal Sentencing Law. Yale Law Journal 120, 367-378.

Lages, M., Boyle, S.C., and Jaworska, K. 2013. Flipping a coin in your head without monitoring outcomes? Comments on predicting free choices and a demo program. Frontiers in psychology 4, 925.

Lane, S.D., Moeller, F.G., Steinberg, J.L., Buzby, M., Kosten, T.R., 2007. Performance of cocaine dependent individuals and controls on a response inhibition task with varying levels of difficulty. Am J Drug Alcohol Abuse 33, 717–26. doi:10.1080/00952990701522724

Lang, P.J., Bradley, M.M., Cuthbert, B.N., 2008. International affective picture system (IAPS): Affective ratings of pictures and instruction manual., Technical Report A-8. University of Florida, Gainesville, Fl.

Lang, P.J., Bradley,. M. M., Cuthbert, B.N. 1999. International Affective Digitzed Sounds (IADS. In International Affective Digitzed Sounds (IADS) (Gainesville, FL.

Lazar, N.A., 2009. Discussion of "Puzzlingly High Correlations in fMRI Studies of Emotion, Personality, and Social Cognition" by Vul et al. 2009. Perspect. Psychol. Sci. J. Assoc. Psychol. Sci. 4, 308–309. doi:10.1111/j.1745-6924.2009.01129.x

Leemans, A., Jones, D.K., 2009. The B-matrix must be rotated when correcting for subject motion in DTI data. Magn. Reson. Med. Off. J. Soc. Magn. Reson. Med. Soc. Magn. Reson. Med. 61, 1336–49. doi:10.1002/mrm.21890

Li, S., Huang, X., Li, L., Du, F., Li, J., Bi, F., Lui, S., Turner, J.A., Sweeney, J.A., Gong, Q., 2016. Posttraumatic Stress Disorder: Structural Characterization with 3-T MR Imaging. Radiology 150477. doi:10.1148/radiol.2016150477

Li, X., Hartwell, K.J., Borckardt, J., Prisciandaro, J.J., Saladin, M.E., Morgan, P.S., Johnson, K.A., Lematty, T., Brady, K.T., George, M.S., 2012. Volitional reduction of anterior cingulate cortex activity produces decreased cue craving in smoking cessation: a preliminary real-time fMRI study. Addict Biol. doi:10.1111/j.1369-1600.2012.00449.x

Liao, Y., Tang, J., Deng, Q., Deng, Y., Luo, T., Wang, X., Chen, H., Liu, T., Chen, X., Brody, A.L., and Hao, W. 2011. Bilateral fronto-parietal integrity in young chronic cigarette smokers: a diffusion tensor imaging study. PloS one 6, e26460.

Libet, B., 1985. Unconscious cerebral initiative and the role of conscious will in voluntary action. Behav. BRAIN Sci. 8, 529–566.

Lieberman, M.D., Berkman, E.T., Wager, T.D., 2009. Correlations in Social Neuroscience Aren't Voodoo: Commentary on Vul et al. 2009. Perspect. Psychol. Sci. J. Assoc. Psychol. Sci. 4, 299–307. doi:10.1111/j.1745-6924.2009.01128.x

Lin, F., Wu, G., Zhu, L., and Lei, H. 2013. Heavy smokers show abnormal microstructural integrity in the anterior corpus callosum: a diffusion tensor imaging study with tract-based spatial statistics. Drug and alcohol dependence 129, 82-87.

Lindemer, E.R., Salat, D.H., Leritz, E.C., McGlinchey, R.E., Milberg, W.P., 2013. Reduced cortical thickness with increased lifetime burden of PTSD in OEF/OIF Veterans and the impact of comorbid TBI. NeuroImage Clin. 2, 601–611. doi:10.1016/j.nicl.2013.04.009

Linden, D.E., Habes, I., Johnston, S.J., Linden, S., Tatineni, R., Subramanian, L., Sorger, B., Healy, D., Goebel, R., 2012. Real-time self-regulation of emotion networks in patients with depression. PloS One 7, e38115. doi:10.1371/journal.pone.0038115

Linzenbold, W., Himmelbach, M., 2012. Signals from the deep: reach-related activity in the human superior colliculus. J. Neurosci. Off. J. Soc. Neurosci. 32, 13881–13888. doi:10.1523/JNEUROSCI.0619-12.2012

Linzenbold, W., Lindig, T., Himmelbach, M., 2011. Functional neuroimaging of the oculomotor brainstem network in humans. NeuroImage 57, 1116–1123. doi:10.1016/j.neuroimage.2011.05.052

List, J., Ott, S., Bukowski, M., Lindenberg, R., Flöel, A., 2015. Cognitive function and brain structure after recurrent mild traumatic brain injuries in young-to-middle-aged adults. Front. Hum. Neurosci. 9, 228. doi:10.3389/fnhum.2015.00228

Liu, Y., Li, Y.-J., Luo, E.-P., Lu, H.-B., Yin, H., 2012. Cortical thinning in patients with recent onset post-traumatic stress disorder after a single prolonged trauma exposure. PloS One 7, e39025. doi:10.1371/journal.pone.0039025

Maas, L.C., Lukas, S.E., Kaufman, M.J., Weiss, R.D., Daniels, S.L., Rogers, V.W., Kukes, T.J., Renshaw, P.F., 1998. Functional magnetic resonance imaging of human brain activation during cue-induced cocaine craving. Am J Psychiatry 155, 124–6.

Madhyastha, T., Merillat, S., Hirsiger, S., Bezzola, L., Liem, F., Grabowski, T., and Jancke, L. 2014. Longitudinal reliability of tract-based spatial statistics in diffusion tensor imaging. Hum Brain Mapp.

Mar, R.A. 2011. The neural bases of social cognition and story comprehension. Annu Rev Psychol 62, 103-134.

Martin, A., and Weisberg, J. 2003. Neural foundations for understanding social and mechanical concepts. Cogn Neuropsychol 20, 575-587.

Maxwell, W.L., MacKinnon, M.-A., Stewart, J.E., Graham, D.I., 2010. Stereology of cerebral cortex after traumatic brain injury matched to the Glasgow outcome score. Brain J. Neurol. 133, 139–160. doi:10.1093/brain/awp264

Mayer, A.R., Wilcox, C.E., Teshiba, T.M., Ling, J.M., and Yang, Z. 2013. Hyperactivation of the cognitive control network in cocaine use disorders during a multisensory Stroop task. Drug and alcohol dependence 133, 235-241.

McKee, A.C., Cantu, R.C., Nowinski, C.J., Hedley-Whyte, E.T., Gavett, B.E., Budson, A.E., Santini, V.E., Lee, H.-S., Kubilus, C.A., Stern, R.A., 2009. Chronic traumatic encephalopathy in athletes: progressive tauopathy after repetitive head injury. J. Neuropathol. Exp. Neurol. 68, 709–735. doi:10.1097/NEN.0b013e3181a9d503

Mehrabian, A., 2000. Manual for the Balanced Emotional Empathy Scale (BEES. Available Albert Mehrabian 1130 Alta Mesa Road, Monterey, CA 93940.

Merchant, H., Luciana, M., Hooper, C., Majestic, S., and Tuite, P. 2008. Interval timing and Parkinson's disease: heterogeneity in temporal performance. Exp Brain Res 184, 233-248.

Miller, J., Schwarz, W., 2014. Brain signals do not demonstrate unconscious decision making: an interpretation based on graded conscious awareness. Conscious. Cogn. 24, 12–21. doi:10.1016/j.concog.2013.12.004

Mitchell, J.P., Banaji, M.R., and Macrae, C.N. 2005. The link between social cognition and self-referential thought in the medial prefrontal cortex. J Cogn Neurosci 17, 1306-1315.

Mitra, J., Shen, K., Ghose, S., Bourgeat, P., Fripp, J., Salvado, O., Pannek, K., Taylor, D.J., Mathias, J.L., Rose, S., 2016. Statistical machine learning to identify traumatic brain injury (TBI) from structural disconnections of white matter networks. NeuroImage 129, 247–259. doi:10.1016/j.neuroimage.2016.01.056

Moeller, F.G., Hasan, K.M., Steinberg, J.L., Kramer, L.A., Dougherty, D.M., Santos, R.M., Valdes, I., Swann, A.C., Barratt, E.S., Narayana, P.A., 2005. Reduced anterior corpus callosum white matter integrity is related to increased impulsivity and reduced discriminability in cocaine-dependent subjects: diffusion tensor imaging. Neuropsychopharmacology 30, 610–7. doi:10.1038/sj.npp.1300617

Mohler, C.W., Wurtz, R.H., 1976. Organization of monkey superior colliculus: intermediate layer cells discharging before eye movements. J. Neurophysiol. 39, 722–744.

Moll, J., De Oliveira-Souza, R., and Zahn, R. 2008. The neural basis of moral cognition: sentiments, concepts, and values. Ann N Y Acad Sci 1124, 161-180.

Moll, J., de Oliveira-Souza, R., Eslinger, P.J., Bramati, I.E., Mourao-Miranda, J., Andreiuolo, P.A., and Pessoa, L. 2002. The neural correlates of moral sensitivity: a functional magnetic resonance imaging investigation of basic and moral emotions. J Neurosci 22, 2730-2736.

Moll, J., de Oliveira-Souza, R., Moll, F.T., Ignacio, F.A., Bramati, I.E., Caparelli-Daquer, E.M., and Eslinger, P.J. 2005. The moral affiliations of disgust: a functional MRI study. Cognitive and behavioral neurology 18, 68-78.

Moll, J., de Oliveira-Souza, R., Passman, L.J., Cunha, F.C., Souza-Lima, F., and Andreiuolo, P.A. 2000. Functional MRI correlates of real and imagined tool-use pantomimes. Neurology 54, 1331-1336.

Moss, H.E., Abdallah, S., Fletcher, P., Bright, P., Pilgrim, L., Acres, K., and Tyler, L.K. 2005. Selecting among competing alternatives: selection and retrieval in the left inferior frontal gyrus. Cereb Cortex 15, 1723-1735.

Naqvi, N.H., Bechara, A., 2009. The hidden island of addiction: the insula. Trends Neurosci 32, 56–67. doi:10.1016/j.tins.2008.09.009

Nestares, O., Heeger, D.J., 2000. Robust multiresolution alignment of MRI brain volumes. Magn. Reson. Med. 43, 705–715.

Nichols, T.E., and Holmes, A.P. 2002. Nonparametric permutation tests for functional neuroimaging: a primer with examples. Hum Brain Mapp 15, 1-25.

Nichols, T.E., Poline, J.-B., 2009. Commentary on Vul et al.'s 2009) "Puzzlingly High Correlations in fMRI Studies of Emotion, Personality, and Social Cognition." Perspect. Psychol. Sci. J. Assoc. Psychol. Sci. 4, 291–293. doi:10.1111/j.1745-6924.2009.01126.x

Nishimoto, S., Vu, A.T., Naselaris, T., Benjamini, Y., Yu, B., and Gallant, J.L. 2011. Reconstructing visual experiences from brain activity evoked by natural movies. Curr Biol 21, 1641-1646.

Office of National Drug Control Policy, 2012. FY 2013 Budget and Performance Summary. Companion Natl. Drug Control Strategy.

Office of National Drug Control Policy, 2014. 2013 Annual Report, Arrestee Drug Abuse Monitoring Program II. Executive Office of the President, Washington, DC.

Omalu, B., Bailes, J., Hamilton, R.L., Kamboh, M.I., Hammers, J., Case, M., Fitzsimmons, R., 2011. Emerging histomorphologic phenotypes of chronic traumatic encephalopathy in American athletes. Neurosurgery 69, 173–183; discussion 183. doi:10.1227/NEU.0b013e318212bc7b

Opanashuk, L.A., Pauly, J.R., and Hauser, K.F. 2001. Effect of nicotine on cerebellar granule neuron development. The European journal of neuroscience 13, 48-56.

Orr, J.M., and Banich, M.T. 2014. The neural mechanisms underlying internally and externally guided task selection. Neuroimage 84, 191-205.

Parvaz, M.A., Alia-Klein, N., Woicik, P.A., Volkow, N.D., Goldstein, R.Z., 2011. Neuroimaging for drug addiction and related behaviors. Rev Neurosci 22, 609–24. doi:10.1515/RNS.2011.055

Pasalar, S., Ro, T., and Beauchamp, M.S. 2010. TMS of posterior parietal cortex disrupts visual tactile multisensory integration. The European journal of neuroscience 31, 1783-1790.

Paul, R.H., Grieve, S.M., Niaura, R., David, S.P., Laidlaw, D.H., Cohen, R., Sweet, L., Taylor, G., Clark, R.C., Pogun, S., and Gordon, E. 2008. Chronic cigarette smoking and the microstructural integrity of white matter in healthy adults: a diffusion tensor

imaging study. Nicotine & tobacco research : official journal of the Society for Research on Nicotine and Tobacco 10, 137-147.

Peirce, J.W., 2008. Generating Stimuli for Neuroscience Using PsychoPy. Front. Neuroinformatics 2, 10. doi:10.3389/neuro.11.010.2008

Pelli, D.G. 1997. The VideoToolbox software for visual psychophysics: transforming numbers into movies. Spatial vision 10, 437-442.

Pessoa, L., Gutierrez, E., Bandettini, P., and Ungerleider, L. 2002. Neural correlates of visual working memory: fMRI amplitude predicts task performance. Neuron 35, 975-987.

Pimlott, S.L., Piggott, M., Owens, J., Greally, E., Court, J.A., Jaros, E., Perry, R.H., Perry, E.K., and Wyper, D. 2004. Nicotinic acetylcholine receptor distribution in Alzheimer's disease, dementia with Lewy bodies, Parkinson's disease, and vascular dementia: in vitro binding study using 5-[(125)i]-a-85380. Neuropsychopharmacology : official publication of the American College of Neuropsychopharmacology 29, 108-116.

Poldrack, R.A., Wagner, A.D., Prull, M.W., Desmond, J.E., Glover, G.H., and Gabrieli, J.D. 1999. Functional specialization for semantic and phonological processing in the left inferior prefrontal cortex. Neuroimage 10, 15-35.

Quiroga, R.Q., Nadasdy, Z., and Ben-Shaul, Y. 2004. Unsupervised spike detection and sorting with wavelets and superparamagnetic clustering. Neural Comput 16, 1661-1687.

Raz, N., Gunning, F.M., Head, D., Dupuis, J.H., McQuain, J., Briggs, S.D., Loken, W.J., Thornton, A.E., Acker, J.D., 1997. Selective aging of the human cerebral cortex observed in vivo: differential vulnerability of the prefrontal gray matter. Cereb. Cortex 7, 268–282. doi:10.1093/cercor/7.3.268

Ress, D., Glover, G.H., Liu, J., Wandell, B., 2007. Laminar profiles of functional activity in the human brain. NeuroImage 34, 74–84. doi:10.1016/j.neuroimage.2006.08.020

Rigoard, P., Buffenoir, K., Jaafari, N., Giot, J.P., Houeto, J.L., Mertens, P., Velut, S., Bataille, B., 2011. The accumbofrontal fasciculus in the human brain: a microsurgical anatomical study. Neurosurgery 68, 1102–1111; discussion 1111. doi:10.1227/NEU.0b013e3182098e48

Rilling, J., Gutman, D., Zeh, T., Pagnoni, G., Berns, G., and Kilts, C. 2002. A neural basis for social cooperation. Neuron 35, 395-405.

Robbins, S.J., Ehrman, R.N., Childress, A.R., O'Brien, C.P., 1997. Relationships among physiological and self-report responses produced by cocaine-related cues. Addict. Behav. 22, 157–167.

Robertson, D., Snarey, J., Ousley, O., Harenski, K., DuBois Bowman, F., Gilkey, R., and Kilts, C. 2007. The neural processing of moral sensitivity to issues of justice and care. Neuropsychologia 45, 755-766.

Robinson, D.A., 1972. Eye movements evoked by collicular stimulation in the alert monkey. Vision Res. 12, 1795–1808.

Ruckmann, J., Bodden, M., Jansen, A., Kircher, T., Dodel, R., Rief, W., 2015. How pain empathy depends on ingroup/outgroup decisions: A functional magnet resonance imaging study. Psychiatry Res. 234, 57–65. doi:10.1016/j.pscychresns.2015.08.006

Rueckert, D., Sonoda, L.I., Hayes, C., Hill, D.L., Leach, M.O., and Hawkes, D.J. 1999. Nonrigid registration using free-form deformations: application to breast MR images. IEEE Trans Med Imaging 18, 712-721.

Salas, R., Sturm, R., Boulter, J., and De Biasi, M. 2009. Nicotinic receptors in the habenulo-interpeduncular system are necessary for nicotine withdrawal in mice. J Neurosci 29, 3014-3018.

Salat, D.H., Buckner, R.L., Snyder, A.Z., Greve, D.N., Desikan, R.S., Busa, E., Morris, J.C., Dale, A.M., Fischl, B., 2004. Thinning of the cerebral cortex in aging. Cereb Cortex 14, 721–30. doi:10.1093/cercor/bhh032

Savjani, R.R., Velasquez, K.M., Thompson-Lake, D.G.Y., Baldwin, P.R., Eagleman, D.M., De La Garza Ii, R., Salas, R., 2014. Characterizing white matter changes in cigarette smokers via diffusion tensor imaging. Drug Alcohol Depend. 145, 134–142. doi:10.1016/j.drugalcdep.2014.10.006

Schaich Borg, J., Lieberman, D., and Kiehl, K.A. 2008. Infection, incest, and iniquity: investigating the neural correlates of disgust and morality. J Cogn Neurosci 20, 1529-1546.

Scherfler, C., Seppi, K., Mair, K.J., Donnemiller, E., Virgolini, I., Wenning, G.K., and Poewe, W. 2012. Left hemispheric predominance of nigrostriatal dysfunction in Parkinson's disease. Brain 135, 3348-3354.

Schiller, P.H., Stryker, M., 1972. Single-unit recording and stimulation in superior colliculus of the alert rhesus monkey. J. Neurophysiol. 35, 915–924.

Schlaepfer, T.E., Lancaster, E., Heidbreder, R., Strain, E.C., Kosel, M., Fisch, H.U., Pearlson, G.D., 2006. Decreased frontal white-matter volume in chronic substance abuse. Int J Neuropsychopharmacol 9, 147–53. doi:10.1017/S1461145705005705

Schluppeck, D., Glimcher, P., Heeger, D.J., 2005. Topographic organization for delayed saccades in human posterior parietal cortex. J. Neurophysiol. 94, 1372–1384. doi:10.1152/jn.01290.2004

Schurger, A., Sitt, J.D., and Dehaene, S. 2012. An accumulator model for spontaneous neural activity prior to self-initiated movement. Proc Natl Acad Sci U S A 109, E2904-2913.

Sereno, A.B., Briand, K.A., Amador, S.C., Szapiel, S.V., 2006. Disruption of reflexive attention and eye movements in an individual with a collicular lesion. J. Clin. Exp. Neuropsychol. 28, 145–166. doi:10.1080/13803390590929298

Sereno, A.B., Briand, K.A., Amador, S.C., Szapiel, S.V., 2006. Disruption of reflexive attention and eye movements in an individual with a collicular lesion. J. Clin. Exp. Neuropsychol. 28, 145–166. doi:10.1080/13803390590929298

Sereno, M.I., Pitzalis, S., Martinez, A., 2001. Mapping of contralateral space in retinotopic coordinates by a parietal cortical area in humans. Science 294, 1350–1354. doi:10.1126/science.1063695

Singer, T., Seymour, B., O'Doherty, J., Kaube, H., Dolan, R.J., Frith, C.D., 2004. Empathy for pain involves the affective but not sensory components of pain. Science 303, 1157–1162. doi:10.1126/science.1093535

Singer, T., Seymour, B., O'Doherty, J., Stephan, K., Dolan, R., Frith, C., 2006. Empathic neural responses are modulated by the perceived fairness of others. Nature 439, 466–9.

Smith, S.M., 2002. Fast robust automated brain extraction. Hum. Brain Mapp. 17, 143–55. doi:10.1002/hbm.10062

Smith, S.M., Jenkinson, M., Johansen-Berg, H., Rueckert, D., Nichols, T.E., Mackay, C.E., Watkins, K.E., Ciccarelli, O., Cader, M.Z., Matthews, P.M., and Behrens, T.E. 2006. Tract-based spatial statistics: voxelwise analysis of multi-subject diffusion data. Neuroimage 31, 1487-1505.

Smith, S.M., Jenkinson, M., Woolrich, M.W., Beckmann, C.F., Behrens, T.E., Johansen-Berg, H., Bannister, P.R., De Luca, M., Drobnjak, I., Flitney, D.E., et al. 2004. Advances in functional and structural MR image analysis and implementation as FSL. Neuroimage 23 Suppl 1, S208-219.

Sommer, M., Rothmayr, C., Dohnel, K., Meinhardt, J., Schwerdtner, J., Sodian, B., and Hajak, G. 2010. How should I decide? The neural correlates of everyday moral reasoning. Neuropsychologia 48, 2018-2026.

Song, S.K., Sun, S.W., Ju, W.K., Lin, S.J., Cross, A.H., and Neufeld, A.H. 2003. Diffusion tensor imaging detects and differentiates axon and myelin degeneration in mouse optic nerve after retinal ischemia. Neuroimage 20, 1714-1722.

Song, S.K., Sun, S.W., Ramsbottom, M.J., Chang, C., Russell, J., and Cross, A.H. 2002. Dysmyelination revealed through MRI as increased radial (but unchanged axial) diffusion of water. Neuroimage 17, 1429-1436.

Song, S.K., Yoshino, J., Le, T.Q., Lin, S.J., Sun, S.W., Cross, A.H., and Armstrong, R.C. 2005. Demyelination increases radial diffusivity in corpus callosum of mouse brain. Neuroimage 26, 132-140.

Soon, C.S., Brass, M., Heinze, H.J., and Haynes, J.D. 2008. Unconscious determinants of free decisions in the human brain. Nat Neurosci 11, 543-545.

Soon, C.S., He, A.H., Bode, S., and Haynes, J.D. 2013. Predicting free choices for abstract intentions. Proc Natl Acad Sci U S A 110, 6217-6222.

Sowell, E.R., Peterson, B.S., Thompson, P.M., Welcome, S.E., Henkenius, A.L., Toga, A.W., 2003. Mapping cortical change across the human life span. Nat. Neurosci. 6, 309–315. doi:10.1038/nn1008

Stojanoski, B., Cusack, R., 2014. Time to wave good-bye to phase scrambling: creating controlled scrambled images using diffeomorphic transformations. J. Vis. 14. doi:10.1167/14.12.6

Sulzer, J., Haller, S., Scharnowski, F., Weiskopf, N., Birbaumer, N., Blefari, M.L., Bruehl, A.B., Cohen, L.G., Decharms, R.C., Gassert, R., Goebel, R., Herwig, U., Laconte, S., Linden, D., Luft, A., Seifritz, E., Sitaram, R., 2013. Real-time fMRI neurofeedback: Progress and challenges. NeuroImage 76, 386–99. doi:10.1016/j.neuroimage.2013.03.033

Tagliazucchi, E., von Wegner, F., Morzelewski, A., Borisov, S., Jahnke, K., and Laufs, H. 2012. Automatic sleep staging using fMRI functional connectivity data. Neuroimage 63, 63-72.

Tate, D.F., York, G.E., Reid, M.W., Cooper, D.B., Jones, L., Robin, D.A., Kennedy, J.E., Lewis, J., 2014. Preliminary findings of cortical thickness abnormalities in blast injured service members and their relationship to clinical findings. Brain Imaging Behav. 8, 102–109. doi:10.1007/s11682-013-9257-9

Teki, S., Grube, M., and Griffiths, T.D. 2011. A unified model of time perception accounts for duration-based and beat-based timing mechanisms. Front Integr Neurosci 5, 90.

Thielscher, A., and Pessoa, L. 2007. Neural correlates of perceptual choice and decision making during fear-disgust discrimination. J Neurosci 27, 2908-2917.

Thimm, M., Weidner, R., Fink, G.R., and Sturm, W. 2012. Neural mechanisms underlying freedom to choose an object. Hum Brain Mapp 33, 2686-2693.

Thompson, P.M., Lee, A.D., Dutton, R.A., Geaga, J.A., Hayashi, K.M., Eckert, M.A., Bellugi, U., Galaburda, A.M., Korenberg, J.R., Mills, D.L., Toga, A.W., Reiss, A.L., 2005. Abnormal cortical complexity and thickness profiles mapped in Williams syndrome. J. Neurosci. Off. J. Soc. Neurosci. 25, 4146–4158. doi:10.1523/JNEUROSCI.0165-05.2005

Tremblay, S., De Beaumont, L., Henry, L.C., Boulanger, Y., Evans, A.C., Bourgouin, P., Poirier, J., Théoret, H., Lassonde, M., 2013. Sports concussions and aging: a

neuroimaging investigation. Cereb. Cortex N. Y. N 1991 23, 1159–1166. doi:10.1093/cercor/bhs102

Tustison, N.J., Cook, P.A., Klein, A., Song, G., Das, S.R., Duda, J.T., Kandel, B.M., van Strien, N., Stone, J.R., Gee, J.C., Avants, B.B., 2014. Large-scale evaluation of ANTs and FreeSurfer cortical thickness measurements. NeuroImage 99, 166–179. doi:10.1016/j.neuroimage.2014.05.044

Umene-Nakano, W., Yoshimura, R., Kakeda, S., Watanabe, K., Hayashi, K., Nishimura, J., Takahashi, H., Moriya, J., Ide, S., Ueda, I., et al. 2014. Abnormal white matter integrity in the corpus callosum among smokers: tract-based spatial statistics. PLoS One 9, e87890.

UNODC, U.N.O. on D. and C., 2012. World Drug Report. United Nations, New York.

Valeriani, M., Betti, V., Le Pera, D., De Armas, L., Miliucci, R., Restuccia, D., Avenanti, A., Aglioti, S.M., 2008. Seeing the pain of others while being in pain: a laser-evoked potentials study. NeuroImage 40, 1419–1428. doi:10.1016/j.neuroimage.2007.12.056

Van Boven, R.W., Ingeholm, J.E., Beauchamp, M.S., Bikle, P.C., and Ungerleider, L.G. 2005. Tactile form and location processing in the human brain. Proc Natl Acad Sci U S A 102, 12601-12605.

Velasquez, K.M., Molfese, D.L., and Salas, R. 2014. The role of the habenula in drug addiction. Frontiers in human neuroscience 8, 174.

Vieraitis, L.M., Kovandzic, T.V., Marvell, T.B., 2007. THE CRIMINOGENIC EFFECTS OF IMPRISONMENT: EVIDENCE FROM STATE PANEL DATA,

1974–2002. Criminol. Public Policy 6, 589–622. doi:10.1111/j.1745-9133.2007.00456.x

Vizi, E.S., and Lendvai, B. 1999. Modulatory role of presynaptic nicotinic receptors in synaptic and non-synaptic chemical communication in the central nervous system. Brain research Brain research reviews 30, 219-235.

Volkow, N.D., Fowler, J.S., 2000. Addiction, a disease of compulsion and drive: involvement of the orbitofrontal cortex. Cereb. Cortex 10, 318–25.

Volkow, N.D., Fowler, J.S., Wang, G.J., Telang, F., Logan, J., Jayne, M., Ma, Y., Pradhan, K., Wong, C., Swanson, J.M., 2010. Cognitive control of drug craving inhibits brain reward regions in cocaine abusers. NeuroImage 49, 2536–43. doi:10.1016/j.neuroimage.2009.10.088

Vul, E., Harris, C., Winkielman, P., Pashler, H., 2009a. Puzzlingly High Correlations in fMRI Studies of Emotion, Personality, and Social Cognition. Perspect. Psychol. Sci. J. Assoc. Psychol. Sci. 4, 274–290. doi:10.1111/j.1745-6924.2009.01125.x

Vul, E., Harris, C., Winkielman, P., Pashler, H., 2009b. Reply to Comments on "Puzzlingly High Correlations in fMRI Studies of Emotion, Personality, and Social Cognition." Perspect. Psychol. Sci. J. Assoc. Psychol. Sci. 4, 319–324. doi:10.1111/j.1745-6924.2009.01132.x

Wang, H., Suh, J.W., Das, S.R., Pluta, J.B., Craige, C., Yushkevich, P.A., 2013. Multi-Atlas Segmentation with Joint Label Fusion. IEEE Trans. Pattern Anal. Mach. Intell. 35, 611–623. doi:10.1109/TPAMI.2012.143

Wang, X., Xie, H., Cotton, A.S., Tamburrino, M.B., Brickman, K.R., Lewis, T.J., McLean, S.A., Liberzon, I., 2015. Early cortical thickness change after mild traumatic brain injury following motor vehicle collision. J. Neurotrauma 32, 455–463. doi:10.1089/neu.2014.3492

Wechsberg, W.M., Golin, C., El-Bassel, N., Hopkins, J., Zule, W., 2012. Current interventions to reduce sexual risk behaviors and crack cocaine use among HIV-infected individuals. Curr HIVAIDS Rep 9, 385–93. doi:10.1007/s11904-012-0131-y

Weiskopf, N., Scharnowski, F., Veit, R., Goebel, R., Birbaumer, N., Mathiak, K., 2004. Self-regulation of local brain activity using real-time functional magnetic resonance imaging (fMRI. J Physiol Paris 98, 357–73. doi:10.1016/j.jphysparis.2005.09.019

Weiskopf, N., Sitaram, R., Josephs, O., Veit, R., Scharnowski, F., Goebel, R., Birbaumer, N., Deichmann, R., Mathiak, K., 2007. Real-time functional magnetic resonance imaging: methods and applications. Magn Reson Imaging 25, 989–1003. doi:10.1016/j.mri.2007.02.007

Weiskopf, N., Veit, R., Erb, M., Mathiak, K., Grodd, W., Goebel, R., Birbaumer, N., 2003. Physiological self-regulation of regional brain activity using real-time functional magnetic resonance imaging (fMRI): methodology and exemplary data. NeuroImage 19, 577–86.

Wexler, B.E., Gottschalk, C.H., Fulbright, R.K., Prohovnik, I., Lacadie, C.M., Rounsaville, B.J., Gore, J.C., 2001. Functional magnetic resonance imaging of cocaine craving. Am J Psychiatry 158, 86–95.

Wilde, E.A., Bouix, S., Tate, D.F., Lin, A.P., Newsome, M.R., Taylor, B.A., Stone, J.R., Montier, J., Gandy, S.E., Biekman, B., Shenton, M.E., York, G., 2015. Advanced neuroimaging applied to veterans and service personnel with traumatic brain injury: state of the art and potential benefits. Brain Imaging Behav. 9, 367–402. doi:10.1007/s11682-015-9444-y

Winkler, A.M., Ridgway, G.R., Webster, M.A., Smith, S.M., Nichols, T.E., 2014. Permutation inference for the general linear model. NeuroImage 92, 381–397. doi:10.1016/j.neuroimage.2014.01.060

Wolf, E.J., Sadeh, N., Leritz, E.C., Logue, M.W., Stoop, T.B., McGlinchey, R., Milberg, W., Miller, M.W., 2015. Posttraumatic Stress Disorder as a Catalyst for the Association Between Metabolic Syndrome and Reduced Cortical Thickness. Biol. Psychiatry. doi:10.1016/j.biopsych.2015.11.023

Woolrich, M.W., Jbabdi, S., Patenaude, B., Chappell, M., Makni, S., Behrens, T., Beckmann, C., Jenkinson, M., and Smith, S.M. 2009. Bayesian analysis of neuroimaging data in FSL. Neuroimage 45, S173-186.

Woolrich, M.W., Ripley, B.D., Brady, M., Smith, S.M., 2001. Temporal autocorrelation in univariate linear modeling of FMRI data. NeuroImage 14, 1370–1386. doi:10.1006/nimg.2001.0931

Xu, G., Pan, Q., Bajaj, C.L., 2006. Discrete Surface Modelling Using Partial Differential Equations. Comput. Aided Geom. Des. 23, 125–145. doi:10.1016/j.cagd.2005.05.004

Xu, X., Zuo, X., Wang, X., Han, S., 2009. Do you feel my pain? Racial group membership modulates empathic neural responses. J. Neurosci. Off. J. Soc. Neurosci. 29, 8525–8529. doi:10.1523/JNEUROSCI.2418-09.2009

Young, L., Cushman, F., Hauser, M., and Saxe, R. 2007. The neural basis of the interaction between theory of mind and moral judgment. Proc Natl Acad Sci U S A 104, 8235-8240.

Yushkevich, P.A., Piven, J., Hazlett, H.C., Smith, R.G., Ho, S., Gee, J.C., Gerig, G., 2006. User-guided 3D active contour segmentation of anatomical structures: significantly improved efficiency and reliability. NeuroImage 31, 1116–1128. doi:10.1016/j.neuroimage.2006.01.015

Zeki, S., Romaya, J.P., 2008. Neural correlates of hate. PloS One 3, e3556. doi:10.1371/journal.pone.0003556

Zhang, X., Salmeron, B.J., Ross, T.J., Geng, X., Yang, Y., and Stein, E.A. 2011. Factors underlying prefrontal and insula structural alterations in smokers. Neuroimage 54, 42-48.

APPENDIX

IMAGE PROCESSING*

1. Genetic Suppression of Transgenic APP Rescues Hypersynchronous Network Activity in a Mouse Model of Alzheimer's Disease

1.1 Methods

Sagittal sections located ~1–1.5 mm from midline were selected for analysis based on landmarks in hippocampus, lateral ventricle, and striatum. A total of 4–5 sections were imaged per animal. Fluorescent images were collected from nonoverlapping fields within cortex (L2/3 above CA1 and L5 above lateral ventricle). A single optical plane of 0.977 μm in depth was collected in red (vGAT) and green (vGLUT) channels using an ApoTome structured illumination device (Carl Zeiss) at 40× magnification (222.2 × 166.4 μm per field). We used a custom script written in MATLAB (R2012b) to batch process two-channel fluorescence images in an unbiased and automated way. Grayscale images were binarized using Otsu's method to divide the dataset into signal and background so that the variance in each of the resulting subsets is mimimized.

---

* Reprinted with permission from "Genetic suppression of transgenic APP rescues Hypersynchronous network activity in a mouse model of Alzeimer's disease." by Born HA, Kim JY, Savjani RR, Das P, Dabaghian YA, Guo Q, Yoo JW, Schuler DR, Cirrito JR, Zheng H, Golde TE, Noebels JL, Jankowsky JL, 2014. *Journal of Neuroscience*. 12, 3826-3840, Copyright 2014 by Society of Neuroscience.

* Reprinted with permission from "Genetic modulation of soluble Aβ rescues cognitive and synaptic impairment in a mouse model of Alzheimer's disease." by Fowler SW, Chiang AC, Savjani RR, Larson ME, Sherman MA, Schuler DR, Cirrito JR, Lesné SE, Jankowsky JL, 2014. *Journal of Neuroscience*. 34, 7871-7885, Copyright 2014 by Society of Neuroscience.

In this case, the method uses variance minimization to define the cutoff between immunopositive pixels and background. The script then calculates the area occupied by vGLUT- or vGAT-positive pixels in each image normalized to the total area of the field. We have posted a modified version of the script on MATLAB's file exchange site (http://www.mathworks.com/matlabcentral/fileexchange/39591).

1.2 Results

The sensitivity of APP/TTA mice to both spontaneous SWDs and acute GABAergic inhibition prompted us to test whether there may be underlying changes in the excitatory to inhibitory balance. We examined the relative levels of glutamatergic to GABAergic innervation by measuring the density of synaptic immunostaining for their respective vesicular neurotransmitter transporters, vGLUT and vGAT. Because our EEG recordings were taken above parietal cortex, we focused our histological analyses on this region and specifically on the main neuronal cell body layers 2/3 and 5. Within layer 5, the area occupied by vGLUT staining was significantly lower in APP/TTA mice than in controls ($p < 0.05$; $n = 4–5$ mice/group; **Figure A.1**). vGLUT density was restored to control levels by 4–5 weeks of transgene suppression, but was not rescued by GSI treatment, which is consistent with our EEG findings. In contrast, vGLUT staining within layer 2/3 was not significantly altered by transgene expression or treatment.

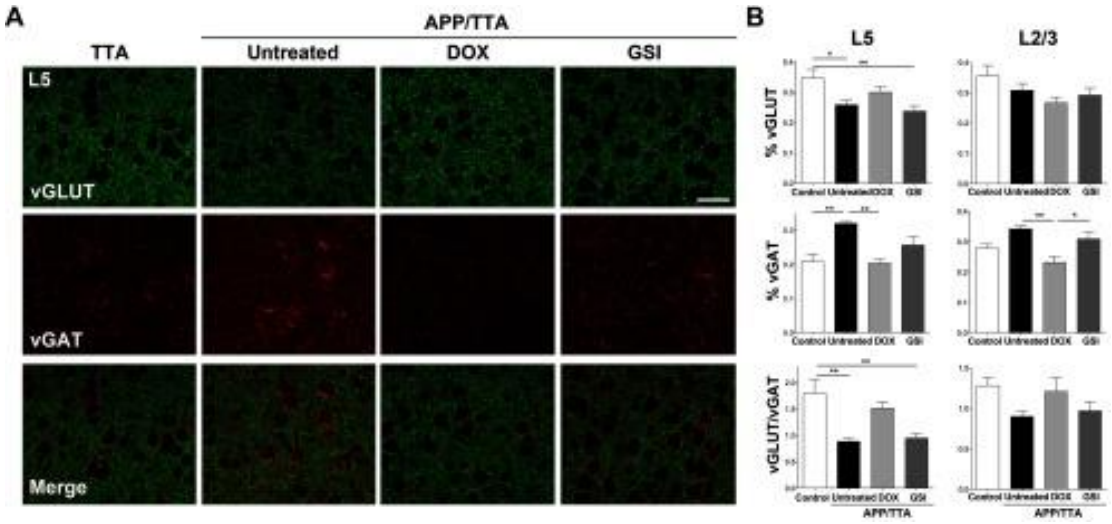

Figure A.1 Restored Glutamatergic and GABAergic Cortical Markers

Transgene suppression restores cortical markers of glutamatergic and GABAergic innervation to control levels. ***A***, Tissue from TTA and APP/TTA mice used for EEG recording was coimmunostained for vGLUT1 and vGAT. Images show cortex layer 5 from untreated TTA (control) mice along with untreated, DOX-treated, and GSI-treated APP/TTA mice. Scale bar, 50 μm. ***B***, Percent area occupied by vGLUT1 and vGAT staining within layers 2/3 and 5 was measured using a custom MATLAB script. Untreated APP/TTA mice had a lower density of vGLUT1 and higher density of vGAT in layer 5 than control animals, with a similar trend in layer 2/3. Transgene suppression restored these excitatory/inhibitory markers to control levels, whereas GSI had no effect. *$p < 0.05$, **$p < 0.01$.

Changes in vGAT staining were opposite to those in vGLUT. In layer 5, the area of vGAT staining increased with APP overexpression ($p < 0.01$ vs control) but decreased to control levels after transgene suppression. vGAT staining in layer 2/3 showed a similar pattern: although the increase in vGAT with transgene expression was not significant, the drop after suppression was ($p < 0.01$ vs untreated). vGAT levels after GSI treatment fell in between those of untreated and DOX-treated animals, but were not significantly changed from untreated APP/TTA mice.

Together, these analyses revealed that continued overexpression of APP caused a significant reduction in the ratio of vGLUT:vGAT within layer 5 ($p < 0.01$ vs control) and a parallel trend in layer 2/3. Transgene suppression restored the excitatory/inhibitory ratio to control levels, whereas GSI treatment did not.

2. Genetic Modulation of Soluble Aβ Rescues Cognitive and Synaptic Impairment in a Mouse Model of Alzheimer's Disease

2.1 Methods

The area of synaptophysin immunostaining surrounding thioflavine-S-positive fibrillar plaques was measured using a custom script written in MATLAB (R2012b) to batch process two-channel fluorescence images in an unbiased and automated way. Two tissue sections spanning the frontal cortex were selected for analysis from each animal. Two nonoverlapping fields of view each centered on an isolated plaque of 43.56 μm average diameter were photographed for each section. A single optical plane of 0.98 μm in depth was collected from each field in the red (synaptophysin) and green (thioflavine) channels using an ApoTome structured illumination device (Carl Zeiss). At 40× magnification each field spanned an area of 222.2 × 166.4 μm.

The first step in the automated script removed the area occupied by the thioflavine-positive plaque from the region of interest that would be used be used to measure synaptophysin. To accomplish this in an unbiased fashion, we binarized the grayscale thioflavine images using Otsu's method. The Otsu method works by calculating the threshold at which to divide the dataset into signal and background so that the variance in each of the resulting subsets is minimized. In this case, the method uses variance minimization to define the cutoff between thioflavine-positive pixels and thioflavine-negative pixels. Pixels above background defined the area of the plaque and were used

as a mask to remove this region from the corresponding synaptophysin image. The masked synaptophysin images were then also binarized, again applying Otsu's method for determining the optimal threshold between signal and background. The script then calculated the area occupied by synaptophysin-positive pixels in each image, normalizing to the total area remaining after the region of thioflavine staining was removed. We have posted the script on MATLAB's File Exchange (http://www.mathworks.com/matlabcentral/fileexchange/39591).

2.2 Results

Synaptic recovery despite sustained amyloid.

Past work has shown that exposure to oligomeric Aβ is rapidly synaptotoxic *in vitro*, which led us to test whether synaptic markers were also reduced in untreated APP/TTA mice as they are in several other amyloid-bearing AD models. Moreover, we wanted to determine whether synaptic recovery accompanied the decrease in oligomeric Aβ with transgene suppression, which might support their behavioral improvement. We quantified the levels of both postsynaptic PSD95 and presynaptic synapsin Ia/b in cortical extracts from behaviorally tested mice (**Figure A.2A-C**). Western blotting confirmed that untreated APP/TTA mice have less PSD95 than TTA controls ($F_{(1,28)}$ = 25.80, $p < 0.01$; **Figure A.2B**) as well as lower levels of synapsin ($F_{(1,27)}$ = 6.20, p = 0.05; **Figure A.2C**). Dox treatment to suppress transgenic APP increased the amount of both proteins in APP/TTA mice, but did not affect their levels in TTA controls ($F_{(1,28)}$ = 11.80, p = 0.002 for PSD95 and $F_{(1,27)}$ = 3.70, p = 0.04 for synapsin).

While these changes in synapsin and PSD95 are consistent with synapse loss throughout the cortex of untreated APP/TTA mice, past work has shown that the greatest decrease in synapse density occurs in the immediate vicinity of amyloid plaques. Knowing that dox-treated mice showed behavioral improvements despite the persistence of amyloid plaques, we tested whether plaque-associated synapse loss was rescued by lowering Aβ production. We manually selected thioflavine-positive plaques from the rostral forebrain ranging in size from 2500–11,000 μm^2 so that the distribution of plaque sizes was no different between dox-treated and untreated mice (unpaired Student's *t* test, $p > 0.05$). We then measured the area of synaptophysin immunostaining in a 0.036 mm^2 region surrounding each plaque (one field of view at 40× magnification) to compare the density of synapses in untreated and dox-treated APP/TTA mice (**Figure A.2D**). The area of synaptophysin staining in the vicinity of fibrillar deposits was markedly higher in the dox-treated animals than in their untreated siblings ($t = 3.34$, $p < 0.01$; **Figure A.2E**). This suggests that synaptic loss is reversible, as were cognitive deficits, once APP and Aβ are reduced.

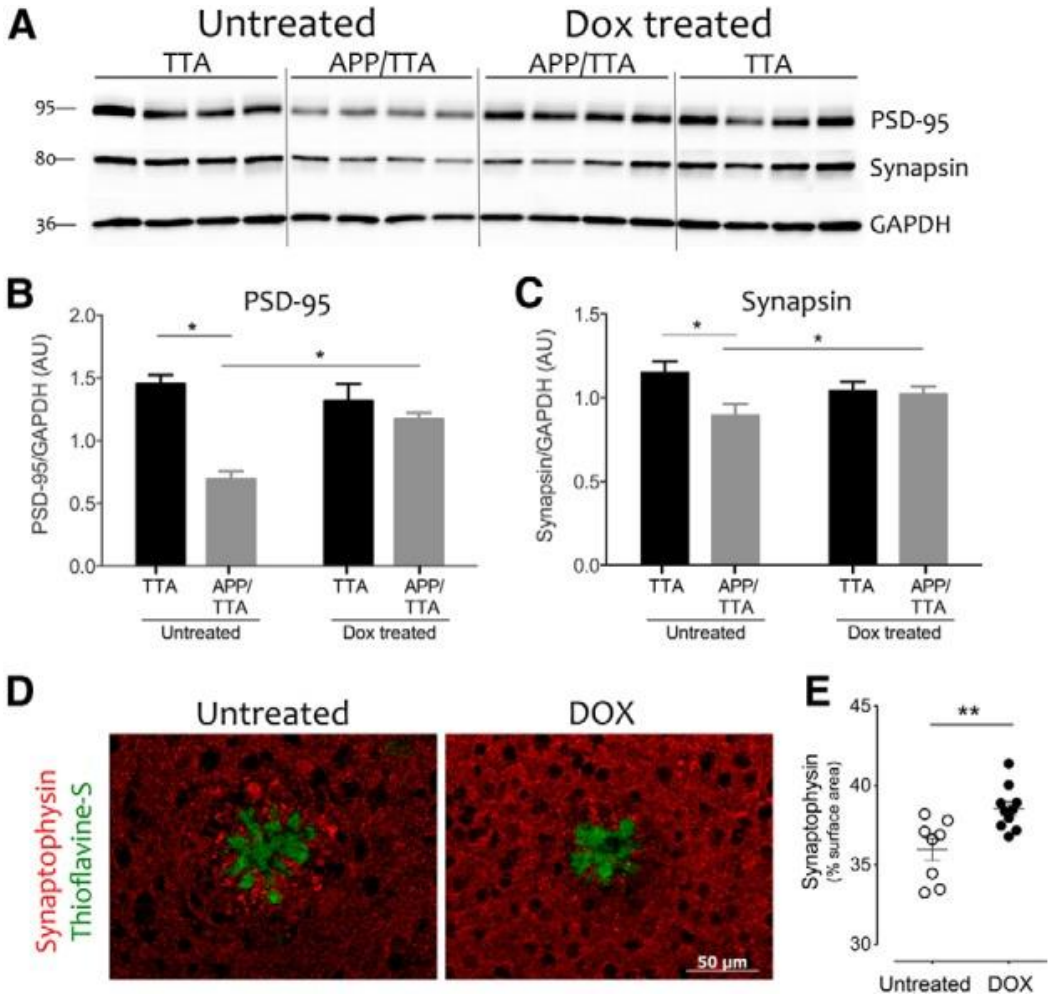

Figure A.2 Restored Synaptic Protein Levels

Synaptic protein levels and synaptic area are restored by suppression of transgenic APP/Aβ. ***A***, Immunoblotting was used to measure the levels of presynaptic and postsynaptic proteins synapsin and PSD95 in cortical homogenates from behaviorally tested animals. ***B***, ***C***, The signal intensity revealed significant deficits in both synapsin and PSD95 between untreated APP/TTA mice ($n = 8$) and TTA controls ($n = 8$; $^{*}p < 0.05$). Levels of both proteins were increased by dox treatment in APP/TTA mice ($n = 8$; $^{*}p < 0.05$) to levels that were indistinguishable from TTA controls ($n = 8$). ***D***, Synaptophysin immunostaining (red) was used to estimate the area occupied by synaptic terminals in the vicinity of thioflavine-positive fibrillar plaques (green) at the conclusion of behavioral testing. ***E***, Consistent with the recovery of synaptic proteins, the area of synaptophysin immunostaining was significantly greater in dox-treated APP/TTA mice than in untreated controls ($^{**}p < 0.01$; $n = 8$ untreated; $n = 10$ dox).